DELINEATION AND ANALYSIS OF ACTIVE GEOMORPHOLOGICAL PROCESSES USING HIGH RESOLUTION SPATIAL SURVEYS

DELINEATION AND ANALYSIS OF ACTIVE GEOMORPHOLOGICAL PROCESSES USING HIGH RESOLUTION SPATIAL SURVEYS

By REBECCA E. LEE, M.Sc.

A Thesis
Submitted to the School of Graduate Studies in
Partial Fulfilment of the Requirements for the Degree
Doctor of Philosophy

McMaster University

DOCTOR OF PHILOSOPHY (2021) McMaster University
(School of Earth, Environment & Society) Hamilton, Ontario, Canada

TITLE: **DELINEATION AND ANALYSIS OF ACTIVE GEOMORPHOLOGICAL PROCESSES USING HIGH RESOLUTION SPATIAL SURVEYS**

AUTHOR: Rebecca Lee, M.Sc. (McMaster University, 2016)

SUPERVISOR: Professor C.H. Eyles

NUMBER OF PAGES: xvii, 233

Abstract

The past few decades have seen rapid improvement in technologies related to remote sensing, specifically in digital photogrammetry and the use of unmanned aerial vehicles (UAVs). This has presented new opportunities to collect imagery at both a high temporal and spatial resolution to create detailed digital elevation models (DEMs) and investigate small-scale geomorphological features and their development over time. The high-resolution capacity of this methodology is well-suited to the study of a variety of terrains in which many critical geomorphological features are low relief and difficult or impossible to delineate using traditional remote sensing datasets. This study utilizes UAV-based imagery collection and data analysis, in conjunction with sedimentological analysis, of two study sites in Iceland and southern Ontario. The primary objective of this work is to explore the utility of integrating high-resolution spatial surveys with more traditional field techniques to identify geomorphological features, interpret their depositional origin, and quantify temporal changes in their form.

The first study was completed on the forefields of Öldufellsjökull and western Sléttjökull, two surge-type outlet glaciers of the Mýrdalsjökull Ice Cap in southeast Iceland. Glacial deposits are important sources of paleoclimatic information but not all deposits are formed by processes that reflect the overall climatic conditions of a region; surge-type (fast-flowing) glaciers undergo periodic episodes of rapid ice movement, often unrelated to ambient climatic conditions. Remotely sensed data and field investigations were combined to complete a landsystem analysis of the forefields at each of Öldufellsjökull and western Sléttjökull, and an unmanned aerial vehicle (UAV) was used to collect high-resolution imagery of areas of particular interest. The forefields of Öldufellsjökull and western Sléttjökull, lack many of the characteristics typical of surge-type landsystems and instead are more similar to the active temperate landsystem common in Iceland. The identification of landforms considered to be diagnostic of surge-type glacier behaviour was only possible through a targeted high-resolution UAV survey suggesting that small-scale diagnostic landforms may be overlooked in many investigations.

The second study area focused on the Niagara Escarpment in Hamilton, Ontario, a major landform resulting from extensive glacial and fluvial erosion of Paleozoic sedimentary rocks during the late Quaternary. In Hamilton, the Niagara Escarpment is a steep faced cuesta composed of Ordovician and Silurian sedimentary rocks. Recent rockfalls onto roads crossing the escarpment have raised serious concerns about its stability. To address these concerns, and to provide more information on erosional processes active along the escarpment in Hamilton, a comprehensive study of the Niagara Escarpment was completed including the collection of multi-temporal photogrammetric surveys of select rock faces, and detailed sedimentological and fracture analysis. A comprehensive lithological investigation was completed of all accessible rock outcrops in Hamilton to identify areas most likely to experience erosion based on site characteristics. A second component of this investigation was to evaluate the utility of using high-resolution imagery combined with Structure from Motion (SfM) software to detect temporal changes on the escarpment face. A staged erosion study was conducted in which lithological blocks of a known size were removed from the escarpment face at a selected site, to determine the lower limits of detection of erosion using this methodology. The study found that the location of block removal (erosion) was consistently identified, but the calculated volume of blocks removed was less accurately determined, differing by an average of 175% from the known volume of the block. A further study using this same methodology tested its ability to identify areas of natural loss (erosion) from the escarpment face. Based on multiple surveys taken 14 months apart at a selected study site, approximately one third of the area of interest experienced either loss (erosion) or gain (deposition) of material. There appear to be clear connections between lithology, density of fracturing, and the location of material loss (erosion); areas of the outcrop characterised by interbedded shales, and those areas exposing densely fractured sandstone or dolostone, were most likely to erode. The lithological characteristics of the Niagara Escarpment, including the strength of individual stratigraphic units, their vertical arrangement, and their density of fracturing, as well as climatic and hydrological factors (e.g., groundwater flow, location of surficial water

features, mean annual temperature, mean annual precipitation etc.), all contribute to the amount and types of erosion active on the exposed rock face.

The studies reported in this thesis have integrated high-resolution, close-range imagery with traditional field techniques to explore the characteristics and development of geomorphological forms in different terrain types. In each of the studies, the importance of collecting high-resolution imagery (<10 cm) to map geomorphological features of various scales is highlighted.

Acknowledgements

To say that completing my doctoral work has been a long journey would be an understatement, but it has definitely been a journey worth taking. The people that have been with me through this ride, those that I have known a lifetime and those that I met along the way, have encouraged me through all the setbacks, pushed me to do better and made this process rewarding in every way.

Firstly, I would like to thank everyone in the Glacial Lab. Chimira, Riley, Allie; you all have been there for me, even though I dragged you into the field for "just one more thing", asked you to read my work or bounced ideas off of you, each of you has helped me though this process. Rodrigo, thanks for all your help in the field, for sticking with me in the worst conditions (except that time you left me in the Andes and a cow attacked me!) and making sure that the field process was fun (mostly). Thanks for all your insightful comments on my research, they always helped me see the problem from a new light and thanks for just being there, I know that having you encourage me through this journey has made me a more confident and capable person. I know that going forward we will be friends for a long time!

My family have been here throughout this process, helping me through some of my hardest moments and politely pretending to know what I was talking about when I went on extended rock-based rants, thanks for that! Mom and Dad, thanks for helping me find my path through this. Ian, my brother, you have been one of my biggest supports through this, helping to keep things in perspective and making sure that I took some breaks and remembered to relax. Theo and Mille, your warmth and constant support for me made some of the most difficult moments a little easier. Katrina, Daynian and Ryley you have been my biggest cheerleaders and always make me smile!

To my Nana, who isn't with us anymore, I want to thank you for providing me with nothing but love, support and delicious dinners throughout my graduate degrees. I know I get my resiliency and stubbornness from you, traits that have helped me push through any barriers I faced during this.

I would like to thank all of my friends who have been constantly supportive, even when I randomly blurt out a thought about my research in the middle of dinner or need some help talking through a problem. Vicki, Torie and Kayla our Tuesday Euchre nights were always a ray of sunshine in a difficult week! Nick, Logan, Sue, Robbyn, Sam, Lauren, I appreciate all the days we spent talking about my research and all the times that you helped me decompress from a hard day or week, it's these times that I think helped me stay focused.

Yorgan, you have been the most amazing partner during this time. I appreciate all the support you give me, whether it is sitting with me in silence while I try to think through a problem, helping me with my Agisoft issues or building me a computer, your help has been immeasurable. Even through my rants, my constant need to be working and my many difficult moments, thanks for sticking with me!

I would like to thank my committee members for their insightful feedback on my work which has helped strengthen it. Dr. Joe Boyce, thank you for being on my committee, you encouraged me to think more critically about some of my assumptions and that has made my work more impactful. My external examiner, Dr. John Johnston, thank you for being a part of my committee. I thoroughly enjoyed reading your comments and they made me consider some fundamentals of stratigraphy that were critical to my work. Finally, thanks to Dr. Alex Peace for being the chair to my committee. Alex, I have enjoyed working with you on our various project together and I hope we can continue to collaborate in the future.

Thank you to Dr. John Maclachlan! You have been one of my biggest mentors throughout my graduate degrees, always taking time to advise me on what to do (even when I wasn't ready to hear it). I credit you with getting me into earth sciences when I took your first-year geology course (though I am sure you don't remember that). Thank you for being such a big support for me, helping me pursue different learning opportunities and agreeing to be my master's supervisor which lead me here. You were the person I turned to when I was confused and in need of direction and you always helped get me back on course, your encouragement throughout the years has been so important to me and any success I have will be in large part due to you. Thanks for taking time to talk to me about my research, for editing it over and over, and for coming and helping me in the field in southern Ontario. Thank you for giving me opportunities to help research in other areas, the work in Kentucky was some of my favourite and my interest in SoTL was ignited by you. I don't think I could ever say it enough but thank you so much for all the help and encouragement that you have given me over the years!

Finally, I would like to thank my supervisor, Dr. Carolyn Eyles, who has seen me through this difficult process, I cannot fully say how thankful I am. You have been a constant source of support, encouraging me to follow my own interests and passions, to try out new techniques and explore new areas of research. You taught me how to think critically about my work and about what I read, how to formulate my thoughts into coherent ideas and that the figures should tell the story of your research. You have been a great role-model, not only in how to research and how to teach, but also how to conduct myself and how to interact with others to make a productive team. I have cherished every moment that I have been with the Glacial Lab, every secret Santa, lunch at the Pheonix, tea in the lab, and day in the field; each moment working with you has been important to me and I will miss the lab and the family atmosphere that you create with your warmth. You have provided me with all the tools, the knowledge and the confidence to pursue my own passions and dreams, and as I continue my career, I know that your teaching, mentorship and friendship are the source of my success. Thank you for everything that you have done for me, I will be eternally grateful!

Thank you to everyone, it has been quite the ride!

Table of Contents

List of Figures

List of Tables

Chapter One: Introduction

1. 1 Introduction

The past few decades have seen the rapid development of technologies related to remote sensing, specifically in digital photogrammetry, and the use of unpiloted aerial vehicles (UAVs) for high-resolution spatial surveys. The use of UAVs allows rapid collection of close-range imagery with a high spatial and temporal resolution that was not achievable using more traditional remote sensing technologies (Clark, 2017; Ely et al., 2017). At the same time, structure from motion (SfM) modelling workflows were developed that allowed the integration of overlapping imagery to create high-resolution point datasets. These datasets can be used to create models, such as digital elevation models (DEMs), commonly used in geomorphological studies (Lowe, 2004; Snavely et al., 2008; Westoby et al., 2012; Aber et al., 2019). The ability to collect and model with high spatial and temporal resolution has allowed the investigation of evolving geomorphological features, and enhanced understanding of how these forms are developing. This technological advancement has been applied to better understand processes operating in a wide variety of physical environments including glacial forefields (e.g. Tonkin et al., 2016; Dąbski et al., 2017; Ely et al., 2017; Chandler et al., 2020), eroding coastlines and soils (e.g. D'Oleire-Oltmanns et al., 2012; Kaiser et al., 2014; Eltner et al., 2015; Harwin et al., 2015; Turner et al., 2016; Clark, 2017), and features such as active faults and landslides (e.g. Turner et al., 2015; Bi et al., 2017). UAVs can rapidly capture spatial data, allowing the creation of high-quality landscape models that can also be used to address concerns regarding geological hazards, such as landslides, rockfalls, and flooding (Niethammer et al., 2012; Langhammer & Vacková, 2018; Giordan et al., 2020).

This thesis will explore different applications of high-resolution spatial surveys, including the use of UAV technology in conjunction with traditional field methods, to explore modern glacial forefields and an actively eroding rocky escarpment. The capacity for high-resolution imagery makes this approach well-suited to the study of glaciated terrains, in which many critical geomorphological features are low relief and difficult or impossible to delineate using most traditional remote sensing datasets. UAV imagery is

also extremely valuable for the identification of areas of erosion and material loss on vertical outcrops that may be otherwise inaccessible. While UAV images provide high quality data, it is still critical to collect additional data types, including sedimentological and in-field geomorphological measurements, to verify and complement the remotely sensed data.

The utility of high spatial and temporal datasets has become increasingly important for policy planning as climate change results in more rapid, and unexpectedly large scale, geological hazards. Glacial environments have been especially impacted by recent climate warming. For example, there have been multiple glacier collapse events in recent years which have destroyed infrastructure and impacted thousands of people (BBC, 2020; Biswas, 2021). Ongoing climate change may lead to more of these catastrophic events, as well as to associated slope failures, landslides, and floods as temperature and precipitation patterns vary. Understanding modern glacial environments will provide insight into how these environments will change in the future, as well as their utility for paleoclimatic reconstructions. In this study, the modern forefields of surge-type glaciers located in Iceland, were examined as they undergo periodic rapid movement and are particularly sensitive to changes in temperature and precipitation (Ingólfsson et al., 2016). Modern surge-type glaciers can also be used as analogues of former fast-flowing ice streams that affected the growth and movement of large continental ice sheets that covered North America and Europe in the past (Evans & Rea, 1999).

A second application of high-resolution spatial surveys that may be used for policy and planning purposes, relates to the quantification of change that occurs in natural landscapes. Quantification of erosion processes and rates is particularly difficult and previous studies have involved time consuming, and often invasive, field measurement of material loss from exposed rock faces (Hooke, 1979; Sirvent et al., 1997; Jugie et al., 2018). In this thesis, the detection of change on exposed rock outcrop faces over time, using high-resolution UAV imagery and SfM modelling, is used to identify areas of erosion on the Niagara Escarpment. Erosion of the Niagara Escarpment, which transects the city of Hamilton, Ontario, poses infrastructure and safety challenges due to its proximity to

buildings and roads. The use of UAVs to collect data quickly, up to multiple times per year, permits the identification of areas of high erosion potential along the escarpment. When such high-resolution surveys are conducted over extended time periods (years, decades) they have the potential to provide an approximate erosion rate for the escarpment. The ability to collect and analyse high-resolution information, which can be used to identify the location and rates of change of natural landscapes as a result of both erosional and depositional processes, is critical for timely decisions and policy planning at all governmental levels.

1. 2 Rationale and objectives

This thesis will report on the use of high-resolution spatial surveys in the investigation of the changing geomorphological characteristics of modern and ancient glaciated terrains. The use of UAVs permits the rapid collection of spatial imagery which can be used to create high-resolution (1 cm – 5 cm) orthomosaics, digital elevation models, and 3-D models (Eltner et al., 2015; Ely et al., 2017; Chandler et al., 2020). Models of both high temporal and spatial resolution can be generated from these data to investigate geomorphological features and their evolution over time. In this study, two contrasting sites were selected for investigation, an active glacial forefield located at the margin of two surge-type glaciers in southern Iceland, and the Niagara Escarpment, a remnant erosional feature created, in part, during the last glaciation of southern Ontario.

The first study, conducted in Iceland, utilized UAV imagery to create planform models of specific areas within the forefield of a surge-type glacier to identify geomorphic features which may be diagnostic of fast ice flow. Surge-type glaciers are commonly used as analogues for paleo-ice streams which were active in the Laurentide Ice Sheet (LIS), and affected both the erosion and deposition of glacial sediments across southern Ontario (Margold et al., 2015; Sookhan et al., 2018; Stokes, 2018; Sookhan et al., 2021). In modern glacial forefields, many important landforms are below the detection limit of most traditional remotely sensed data and require extensive and time-consuming field work to accurately map. Recent surveys using UAVs have identified an abundance of small-scale landforms, for example flutes of ~2 cm relief (Ely et al., 2017); these small-scale forms

may have significant implications for the reconstruction of landform development and past glacier dynamics. This purpose of this study is to use high-resolution UAV-based imagery, in conjunction with traditional remotely sensed and sedimentological data, to analyze the forefields of the two glaciers. This will facilitate the identification of small-scale landforms that potentially record conditions of fast-ice flow and will allow comparison with the established surge-type landsystems model of Evans and Rea (2003).

The second study focuses on an evolving geomorphological feature, the Niagara Escarpment, which was initially created through fluvial and glacial erosion during the Paleogene, Neogene and Quaternary and continues to develop (Straw, 1968; Gross & Engelder, 1991; Gao, 2011). The escarpment is a significant geomorphological feature in southern Ontario which is undergoing constant change that impacts urban infrastructure in the city of Hamilton. This study provides a unique opportunity to investigate erosion processes on an exposed rock face in an urban environment and to study geomorphological processes over short periods of time. The Niagara Escarpment bisects the city of Hamilton and its location within the city has required the construction of access roads that cross the escarpment face, dating back to the mid 1800s. There are 19 access roads that traverse the escarpment, all of which are under threat of major slope failures and rockfalls each year (Figure 1.1A; CBC, 2014; Van Dongen, 2017). Multiple attempts to control rockfalls have required the construction of rock fences, metal retaining walls, scaling of the rock face, and widening of road shoulders. Abundant waterfalls also cross the escarpment face in Hamilton, which range in size from seasonal small cascades to large waterfalls greater than 30 m tall (Figure 1.1A). Of particular concern is the location of more than 1000 buildings within 50 m of the escarpment edge, including homes, businesses, and hospitals (Figure 1.1B). As the escarpment continues to erode, the structural integrity of these structures is compromised and several properties lying close to the edge have been lost (Spectator, 2017). Erosion of the escarpment has caused millions of dollars in infrastructure repairs, threatened the safety of the adjoining roads and trails, as well as caused personal property damage (CBC, 2014; Van Dongen, 2017). Thus, the ability to readily monitor changes,

quantify the rate of erosion, and predict areas at high risk of failure is critical for policy planning and for helping to preserve this important natural feature.

Three separate studies were conducted on the Niagara Escarpment in Hamilton. The first examined the lithological variability of the escarpment to determine how vertical and lateral variability in lithological characteristics impacts erosion potential. The second study tested a methodology for quantifying the rate of erosion of a rock face by removing blocks and utilizing a change detection process involving 3-D models created through Structure from Motion (SfM). The third study aimed to determine the location and amount of erosion occurring naturally on a rock face over a 14-month period. This study compared the known areas of erosion with lithological characteristics to determine the factors that impact erosion processes at the site.

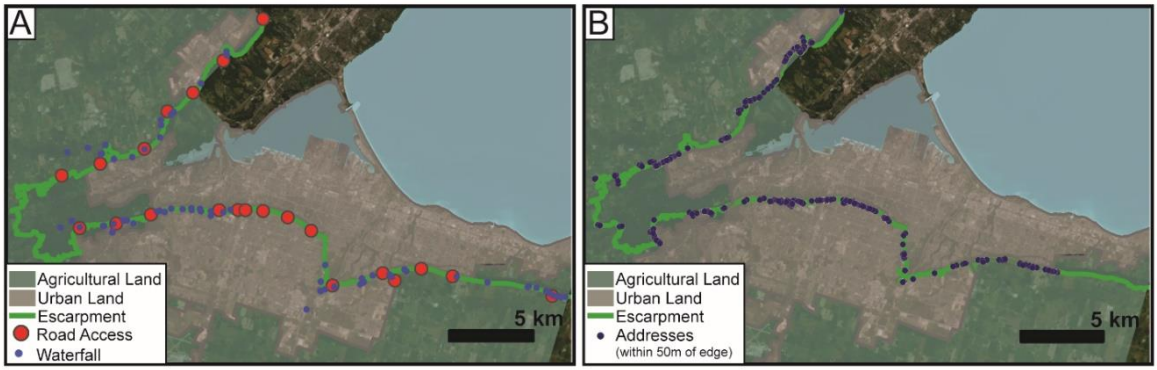

Figure 1.1: A) Road accesses that connect the lower city and the upper city of Hamilton (red circles) and waterfalls that cascade over its edge (blue circles); B) Buildings located within 50 m of the escarpment edge, highlighting the amount of infrastructure at risk from erosion of the escarpment. Data retrieved from City of Hamilton (2021).

The overall objective of the studies reported in this thesis is to apply modern spatial analytical techniques to analyse geomorphological features and quantify their development over time. This work reports findings from modern glacial settings in Iceland, which record recent geomorphic change, and from an area affected by current erosion processes in southern Ontario. Study areas

1.2.1 Mýrdalsjökull, Iceland

Iceland is located on the Mid Atlantic Ridge with the formation of the island attributed to volcanic activity associated with plate spreading and the presence of a hot spot (Thordarson & Larsen, 2007; Brandsdóttir & Menke, 2008; Howell et al., 2014). Despite its location in the north Atlantic, Iceland has a relatively mild oceanic climate due to the influence of the warm Irminger Current (Björnsson & Pálsson, 2008). This temperate climate allows for the ice caps developed on volcanic peaks within Iceland to be considered warm-based or temperate, resulting dynamic glacier systems with high meltwater outputs (Björnsson & Pálsson, 2008; Hannesdóttir et al., 2015). Iceland has five major ice caps which cover almost 11% of the country; these include Vatnajökull, the largest of the ice caps, Mýrdalsjökull, Langjökull, Hofsjökull and Drangajökull (Figure 1.2A). The study area selected within Iceland is focused on two outlet glaciers, Sléttjökull and Öldufellsjökull on the northern margin of the Mýrdalsjökull Ice Cap (Figure 1.2B).

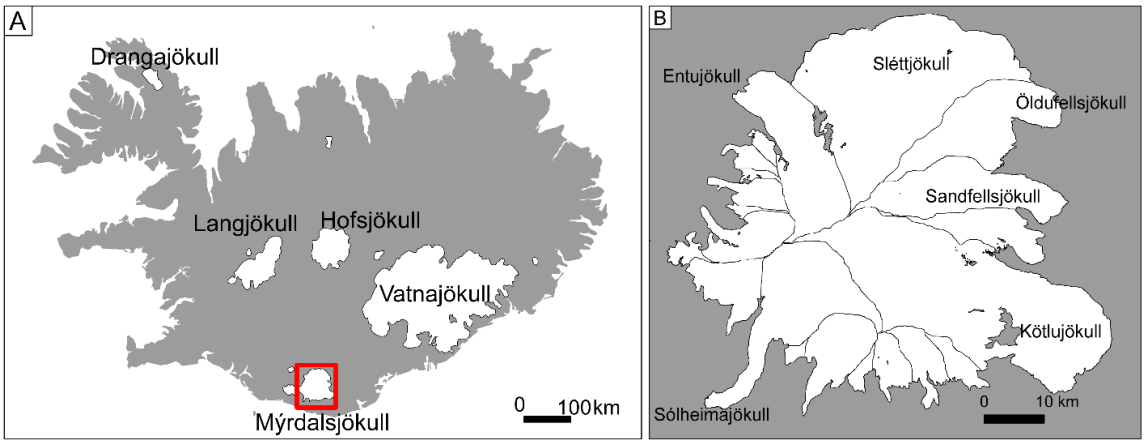

Figure 1.2: A) Distribution of the five major ice caps in Iceland including Mýrdalsjökull in southern Iceland; B) Ice drainage basins of the Mýrdalsjökull Ice Cap, the two surge type glaciers in this study are Sléttjökull and Öldufellsjökull located on the northern margin.

1.2.1.1. Mýrdalsjökull Ice Cap

The Mýrdalsjökull Ice Cap is located on Katla, a large composite volcano up to 1500 m in elevation (Sturkell & Sigmundsson, 2003). Mýrdalsjökull is the second smallest ice cap in Iceland with an area of approximately 590 km^2 and, in 2004, had an average thickness of 240 m (Óladóttir et al., 2008; Mayer et al., 2017). It is located in southern Iceland, an area which experiences the highest mean annual temperature within the country, as well as high rates of precipitation (Sigurðsson, 2010). The main glacial outlets for the ice cap are Kötlujökull, Entujökull, Sólheimajökull and Sléttjökull (Figure 1.2B; Sturkell et al., 2010).

Sléttjökull is fed by three tributary basins and has a total area of 112 km^2 (WGMS, 2017). Öldufellsjökull is a smaller glacier, located to the east of Sléttjökull and has an area of 43 km^2 (WGMS, 2017). The boundaries of Öldufellsjökull and Sléttjökull are not clearly defined, allowing these two ice masses to be considered as a singular outlet glacier, or as separate glaciers, in different studies (Björnsson et al., 2000; Mayer et al., 2017). For this research, the two glaciers will be considered as separate outlet glaciers of the Mýrdalsjökull Ice Cap. Öldufellsjökull and the western basin of Sléttjökull are the only outlet glaciers known to exhibit surging behaviour (intermittent rapid flow) in the Mýrdalsjökull Ice Cap (Björnsson et al., 2003). The western basin of Sléttjökull is recorded to have surged in 1992 and Öldufellsjökull in 1974, 1984 and 1992 (Ingólfsson et al., 2016).

Surging glaciers are of particular interest as they account for a disproportionately high amount of ice movement, impacting the hydrological systems and morphology of the ice caps they drain (Björnsson et al., 2003). Surge-type glaciers are considered as analogues for the modern fast-flowing ice streams that operate in Antarctica and previously drained large volumes of ice from the LIS (Evans & Rea, 1999; Schomacker et al., 2014; Ingólfsson et al., 2016). This thesis will explore the impact of surging glaciers on the landscape through the application of UAV-based photogrammetry and the creation of high-resolution spatial models that can be used to delineate landforms below the resolution of many traditional remotely sensed data.

1.2.1.2. Characteristics of surging glaciers

A surging glacier is defined as one "which periodically (every 15 to 100 or more years) discharges an ice reservoir by means of a sudden, brief, large-scale ice displacement, which moves 10 to 100 or more times faster than the glacier's normal flow rate between surges" (Post, 1969, pg 229). For example, during a surge event, the flow rate at Brúarjökull, an Icelandic glacier, has been recorded to be as high as 100 m/day for short periods of three to four months (Ingólfsson et al., 2016). Surging glaciers account for approximately 1-4% of the total number of glaciers worldwide, with a highly clustered distribution in certain areas (Sharp, 1988; Jiskoot, 2011). Most surging glaciers are found within Iceland (Thorarinsson, 1969; Björnsson et al., 2003), Svalbard (Jiskoot et al., 2000; Flink et al., 2017), select ranges in western North America including the St. Elias Range (Post, 1969; Sevestre & Benn, 2015), areas of central Asia such as the Pamirs (Hewitt, 1969, 2011), and the Canadian Arctic (Copland et al., 2003; Sevestre & Benn, 2015); few examples of surging glaciers are found outside of these regions (Figure 1.3).

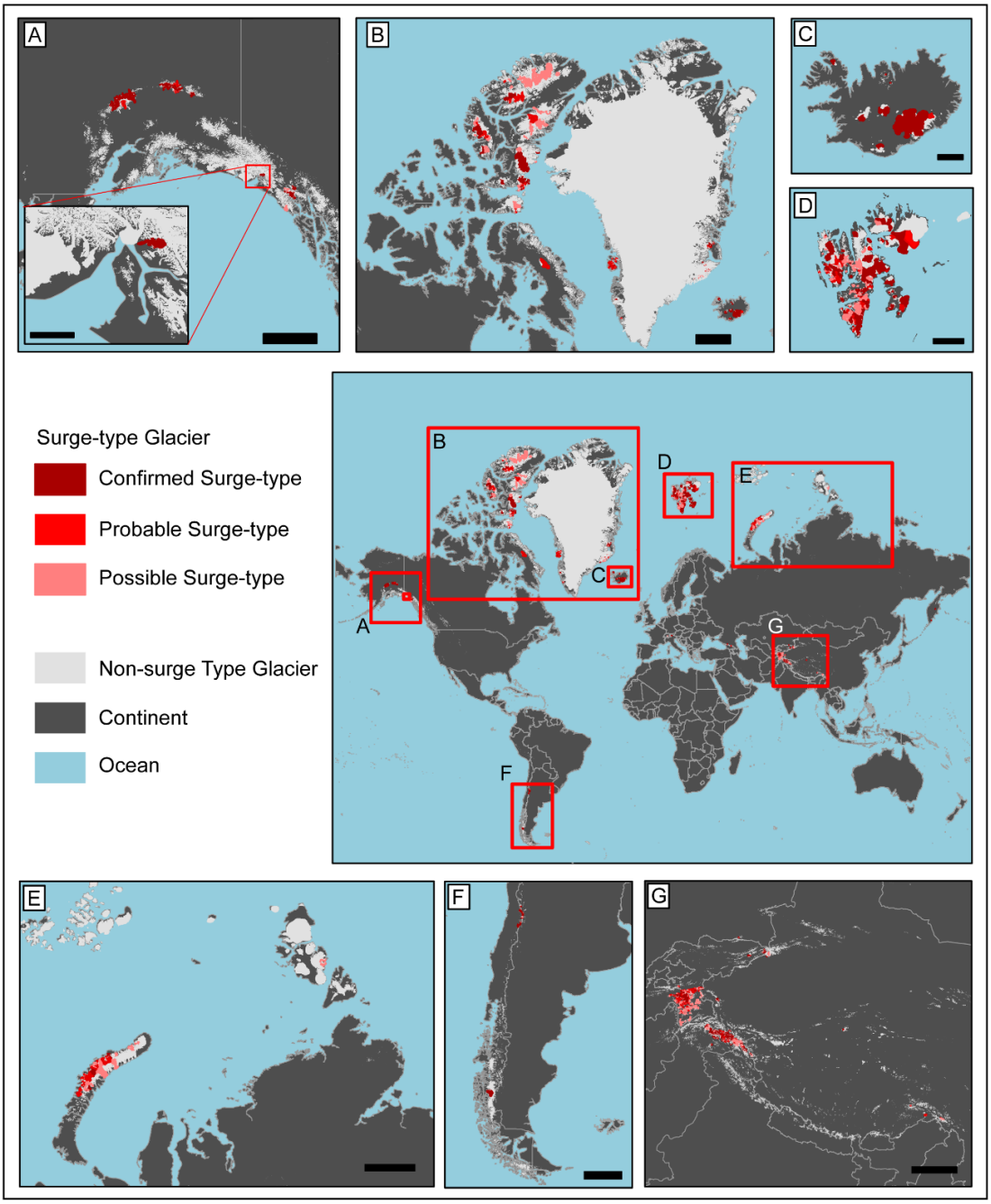

Figure 1.3: Clustered geographic distribution of surging glaciers globally shown in central world map. Surge-type clusters found in Western Canada and Alaska (A); Northern Canada and Greenland (B); Iceland (C); Svalbard (D); Northern Russia (E); Southern Andes (F); and the Pamirs, in the Himalayas (G). Scale bars represent 200 km (C); 500 km (A, D, F, G); 1000 km (B, E). Surge type glaciers are divided into confirmed surge-type, probable surge-type and possible surge-type based on the surge-index from Sevestre and Benn (2015). Data obtained from the Randolph Glacier Index 6.0 (2017).

Similar to ice streams, surging glaciers represent an important method of ice drainage from a large ice body. In Iceland during the 1990's, surges accounted for 25% of ice mass flux and resulted in thinning of the accumulation area of the major ice caps by 25-100m (Björnsson et al., 2003). Surging can increase the rate of erosion and sediment transfer within the proglacial field and can impact the timing and magnitude of meltwater runoff due to changes in the subglacial hydrological system during surge periods furthering their importance in the geological record (Carrivick et al., 2017).

Surging glaciers have been proposed as analogues for paleo-ice streams, specifically land-terminating streams (Evans & Rea, 1999; Schomacker et al., 2014; Ingólfsson et al., 2016). A study completed by Andreassen et al. (2014) in the Barents Sea, where a paleo-ice stream is believed to have existed, showed similarities in the suite of landforms observed to that found in surge-type glaciers. Enhancing the spatial resolution of geomorphic models describing the landforms generated by surging glaciers will therefore aid in the interpretation of the location, dynamics, and sedimentary deposits of paleo-ice streams.

Many investigations into the geomorphology and sedimentology of surging glacier forefields have been conducted (Björnsson et al., 2003; Grant et al., 2009; Benediktsson et al., 2010; Jónsson et al., 2014; Ingólfsson et al., 2016). Based on the geomorphology of proglacial fields found in Iceland, Canada, the USA and Svalbard, Evans and Rea (1999; 2003) proposed a landsystems model for surging glaciers (Figure 1.4). They propose that the landsystem produced by a surging glacier consists of three distinct zones: Zone A, distal zone of thrust block moraines; Zone B, an area composed of hummocky moraines; and Zone C, an inner zone of subglacial landforms (Figure 1.4; Evans & Rea, 2003; Evans et al., 2009). Interzonal elements found throughout the forefield include ice-cored lake sediments, outwash, and overridden moraines (Evans & Rea, 2003). An objective of this study was to verify the characteristics of this proposed landsystem using high-resolution spatial data from Sléttjökull and Öldufellsjökull.

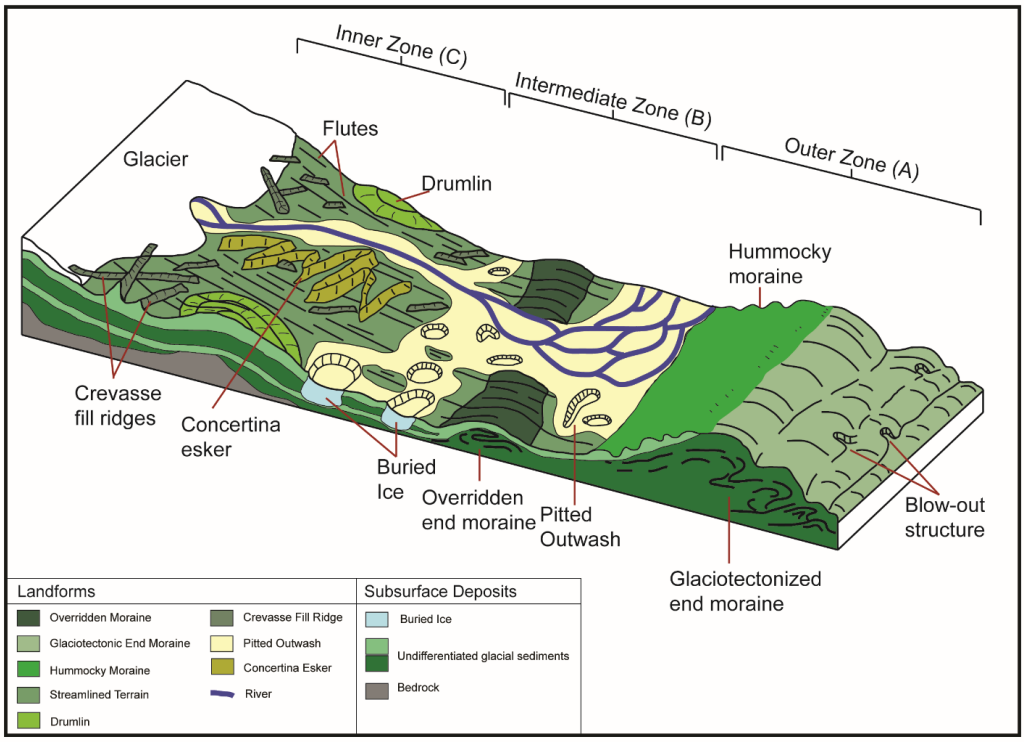

Figure 1.4: Idealized model of the surge-type landsystem which includes an outer zone (A) defined by a glaciotectonized end moraine. The intermerdiate zone (B) includes hummocky moraine on the up-ice side of the moraine. The inner zone (C) is primarily subglacial in origin, and includes crevasse fill ridges, flutes, drumlins, and concertina eskers. This figure is adapted from Ingólfsson et al. (2016); based on work by Schomacker et al. (2014) and Evans and Rea (2003).

1.2.1.3. Geomorphology and Sedimentology of Sléttjökull and Öldufellsjökull

Previous studies of Sléttjökull have focussed on the central and eastern basins, where the pattern of retreat, and landforms generated within the proglacial field, reflect deposition by ice that does not experience periodic rapid flow rates (i.e. a non-surge type glacier). The forefield of the eastern side of Sléttjökull is composed primarily of unlithified glacial and glaciofluvial deposits as well as some minor bedrock ridges (Krüger, 1988; Kruger, 1995; Kjær et al., 2004). The proglacial field is composed of a proximal streamlined till plain up to 2 km wide which exhibits flutes and drumlins and is surrounded by a series of more distal end moraines (Kjær et al., 2004; Schomacker et al., 2010). The moraines are interpreted as end moraines, deposited at the LIA maximum of Sléttjökull at

the end of the 19th century (Krüger et al., 2010). Beyond the end moraines is an extensive outwash plain (Krüger, 1988; Kjær et al., 2003; Schomacker et al., 2010).

This study examines the forefields of the western basin of Sléttjökull and Öldufellsjökull using a landsystem approach combining sedimentological and geomorphological information to understand process-form relationships. The use of high-resolution spatial imagery collected in areas impacted by known surges allows connections between landscape features of varying size to be made to areas of fast-ice flow. The use of high-resolution imagery provides an opportunity to identify small scale features which may be particularly diagnostic of fast ice flow regimes.

1.2.2 Niagara Escarpment

The Niagara Escarpment is a prominent landscape feature of southern Ontario, stretching over 725 km from Niagara Falls in the east to Manitoulin Island in the northwest (Figure 1.5A). The feature also extends eastward into New York State and into Michigan and Wisconsin to the west (Figure 1.5A). In the Hamilton and Niagara Region, is composed of gently southwest dipping (5.5 m/km) sedimentary deposits of late Ordovician to Silurian age (Figure 1.5B; Brigham, 1971; Feenstra, 1981; Tepper et al., 1987). The sedimentary rocks now exposed along the escarpment were deposited in shallow epeiric seas in the Michigan and Appalachian basins, separated by the Algonquin Arch, an anticlinal feature located north of Lake Ontario (Bolton, 1957; Brett et al., 1990). The lithological units exposed along the escarpment are highly variable along its length with significant changes occurring in the Hamilton area of southern Ontario. The cause of this variation is commonly attributed to the influence of the uplifting Algonquin Arch, as well as local variations in sea level and the impact of growing reefs and other obstructions changing the dynamics of the seaway (Crowley, 1973; Brett et al., 1990). Ten lithologic units, or formations, are exposed along the Niagara Escarpment in the Hamilton region, these include: at the base, the Queenston Formation followed by the Whirlpool, the Manitoulin, the Cabot Head, the Grimsby, the Thorold, the Reynales, the Irondequoit, and the Rochester formations and the caprock formed by the Lockport Group, which in this location includes the Gasport Formation and the Ancaster Member of the Goat Island Formation (Figure 1.6).

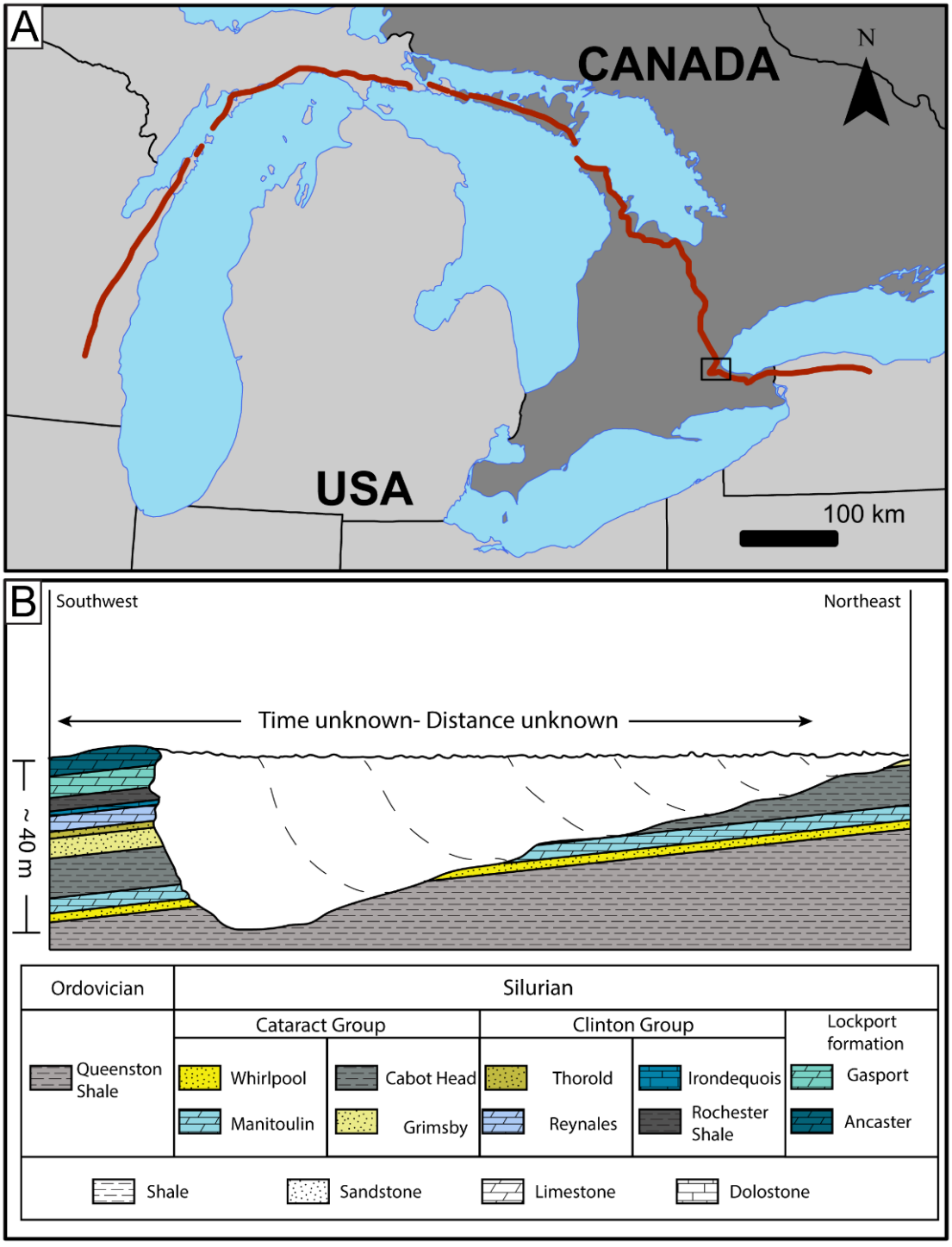

Figure 1.5: A) Total extent of the Niagara Escarpment, from New York State to Wisconsin, with 725 km within southern Ontario; B) Schematic diagram showing overall stratigraphy and southwestward recession of the Niagara Escarpment (adapted from Tovell, 1992).

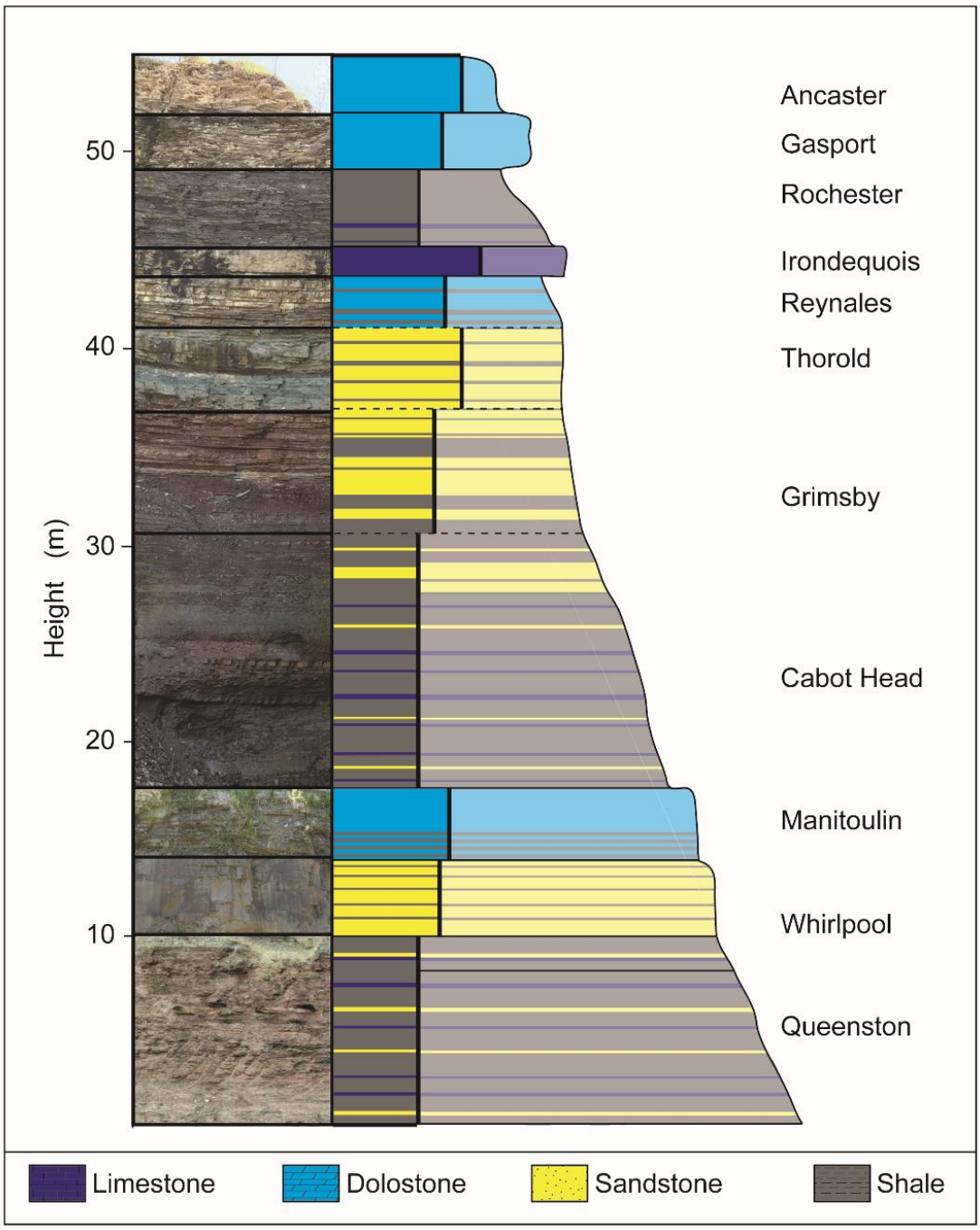

Figure 1.6: Generalized stratigraphy of the Niagara Escarpment in the Hamilton Region showing images of the lithologic units (left), stratigraphic log (centre) and the profile of the escarpment (right).

The initial form of the escarpment was created through fluvial and glacial erosion of the Paleozoic bedrock during the Paleogene, Neogene and Quaternary (Figure 1.5B; Straw, 1968; Gao, 2011; Brunton & Brintnell, 2020). The orientation and density of pre-existing fracture sets in the Paleozoic bedrock likely played an important role in the formation of the escarpment, controlling the rate of quarrying and the overall trajectory of escarpment retreat. Multiple bedrock valleys that penetrate the escarpment in Ontario, for example the Dundas Valley located beneath Hamilton, are believed to have been excavated during the Quaternary (Straw, 1968; Karrow, 1974; Eyles et al., 1997; Gao, 2011). The location of the bedrock valleys may also be related to pre-glacial weaknesses in the bedrock that allowed enhanced erosion by ice sheets and glacial meltwater during this time (Straw, 1968; Gao, 2011). However, the actual rate of retreat of the escarpment is only known along the Niagara Gorge, where fluvial erosion by the Niagara River has caused a relatively rapid retreat rate averaging 1 m/year since deglaciation (Hewitt, 1971; Hayakawa & Matsukura, 2009).

There are many factors that are known or believed to impact the rate of erosion of the escarpment and the dominant method by which it erodes (e.g. block toppling, raveling, slope failure) (Erguler & Shakoor, 2009; Dühnforth et al., 2010; Naylor & Stephenson, 2010; Portenga & Bierman, 2011; Gautam & Shakoor, 2013; Perras et al., 2014; Scott & Wohl, 2019; Selen et al., 2020). Some key factors that impact erosion include the lithological properties of the rock face such as rock type, the vertical distribution of rock types, rock strength and composition (Franklin, 1981; Budetta et al., 2000; Moore & Blenkinsop, 2006; Agustawijaya, 2007; Niemann, 2009; Naylor & Stephenson, 2010; Gautam & Shakoor, 2013), the fracture characteristics of the rock face including the orientation, density, aperture and intensity of fractures (Kirby & Ouimet, 2011; Loye et al., 2012; Scott & Wohl, 2019), and the hydrological properties of the region such the degree of saturation, timing and duration of precipitation, water chemistry and proximity to rivers (Reddy et al., 1986; Cooper et al., 2002; Agustawijaya, 2007; Kanji, 2014). Additional climatic factors can also impact erosion as freeze-thaw and wetting-drying cycles can reduce rock strength and increase fracturing (Lautridou & Ozouf, 1982; Okamoto, 1993;

Owen et al., 2011; Portenga & Bierman, 2011; Eyssautier-Chuine et al., 2016; Selen et al., 2020).

1. 3 Methodologies

This study applies several new, and recently enhanced methodologies to the investigation of geomorphic processes and terrains including photogrammetry using UAVs, Structure from Motion (SfM) modeling, and change detection to determine erosion rates. The data obtained from these investigative methodologies are integrated into landsystem analyses that combine sedimentological and high-resolution geomorphological information to connect landscapes with the processes that formed them.

1.3.1 Photogrammetry

1.3.1.1. Basics of photogrammetric methods

Photogrammetry is an investigative method in which imagery is analyzed to determine reliable quantitative information about the physical environment, whether single objects or entire landscapes (Wolf et al., 2014; Aber et al., 2019). It has been utilized in many different disciplines (e.g., Hagan, 1980; Fussell, 1982; Barker et al., 1997; Jauregui & Jauregui, 2000; Letortu et al., 2018) and has evolved with continuously improving technology, passing from analogue methods to computer modelling. The primary focus of photogrammetry is to determine 3-D coordinates of features using imagery of the area; these coordinates are then used to facilitate measurements of the geomorphometry of landforms and permit quantitative analysis of these features (Linder, 2009; Aber et al., 2019). The methodology is nearly as old as photography itself and was first employed by Laussedat in the 1860s, who used photography and perspective from multiple points to create a topographic map (Ragey, 1952; Granshaw, 2019). Since that time, there have been many improvements in photogrammetry facilitating more complex and high-resolution mapping of various features.

Photogrammetry is based on the concepts of perspective geometry and stereoscopic vision, to perceive the world as three-dimensional. Using two or more photographs taken at different locations, the size and location of an object in 3-D space is calculated using triangulation, as the lines of sight, relative distance and size differ (Linder, 2009; Aber et

al., 2019). Related to this phenomenon is parallax, the apparent displacement of an object caused by a change in the location of observation (Haldar, 2018); there is a larger parallax for closer objects, and it lessens further from the point of observation (Aber et al., 2019). In stereo pairs, where two images are viewed stereoscopically, the parallax gives the three-dimensional effect. These basic principles form the foundation of the wide-ranging field of photogrammetric analysis. Critical to this analysis is knowing the location of the camera and the internal properties of the camera, as these are necessary to calculate the location of the objects (Aber et al., 2019). This need for high level understanding of camera placement and geometry of the camera has made the application of photogrammetry difficult for non-experts.

1.3.1.2. Structure from Motion (SfM)

Structure from Motion (SfM) is an extension of photogrammetry and is a more reliable, faster, and more highly automated system for determining the coordinates of an object based on imagery.

The basic workflow of SfM begins with the collection of overlapping images, with an overlap exceeding 75% (Figure 1.7, stage 1; James & Robson, 2012; Micheletti et al., 2015; Letortu et al., 2018). Using an SfM software, the images are compared to extract features in common; this is usually completed using the scale invariant feature transform (SIFT) (Lowe, 2004; Snavely et al., 2008; Westoby et al., 2012). SIFT identifies key point features in each image which are invariant to changes in scale, rotation and illumination (Westoby et al., 2012), and uses these points to establish the spatial relationship between images in an arbitrary 3-D coordinate system (Figure 1.7, stage 2; Lowe, 2004; Micheletti et al., 2015). The ‘sparse bundle adjustment’ is then used to find points near the key points and is used to create a 3-D point cloud that covers the area of interest (Figure 1.7, stage 3; Snavely et al., 2008; Aber et al., 2019); the output of this is the sparse point cloud, composed of tie points in an arbitrary 3-D space (Figure 1.7, stage 4). At this stage, the tie points can be filtered based on user-defined parameters, removing those that have high error in their projection, and areas that are not of interest.

Up to this point, the entire workflow has been completed in an arbitrary 3-D coordinate system, and for most purposes it is necessary to translate this into a real-world coordinate system. To accomplish this, it is necessary to insert high quality ground control points (GCPs) (Figure 1.7, stage 5; Westoby et al., 2012; Fonstad et al., 2013; Clark, 2017); GCPs should be located throughout the area of study, using easily identifiable markers or natural locations. GCPs may have a degree of error at time of collection, dependent on the area of collection, the amount of interference of the satellite signal, and the type of system used to collect the data (Micheletti et al., 2015).

The next stage in the workflow is to take the established camera locations and computed sparse point cloud and use these to create a high-resolution dataset where the algorithm determines new matched points surrounding the established key points and tie points from the sparse cloud, while also filtering and removing errors (Figure 1.7, stage 6; Micheletti et al., 2015; Stumpf et al., 2015;). The output of this step is the dense point cloud (Figure 1.7, stage 7) which is used to create any final product models of interest, including digital elevation models (DEMs), orthophotos, or triangulated irregular network (TIN) models (Figure 1.7, stage 8).

This entire workflow is completed using a SfM software, such as commercial options of Agisoft Metashape or Pix4D or freeware versions such as VisualSfM and Regard3-D. For this methodology to be optimized, each location of interest in the survey must be captured in a minimum of 3 clear and detailed images, optimally taken at different distances from the area of interest; changes in lighting should be minimized as well as the number of shadows, as they can obscure details (James & Robson, 2012; Westoby et al., 2012; Micheletti et al., 2015; Letortu et al., 2018; Aber et al., 2019).

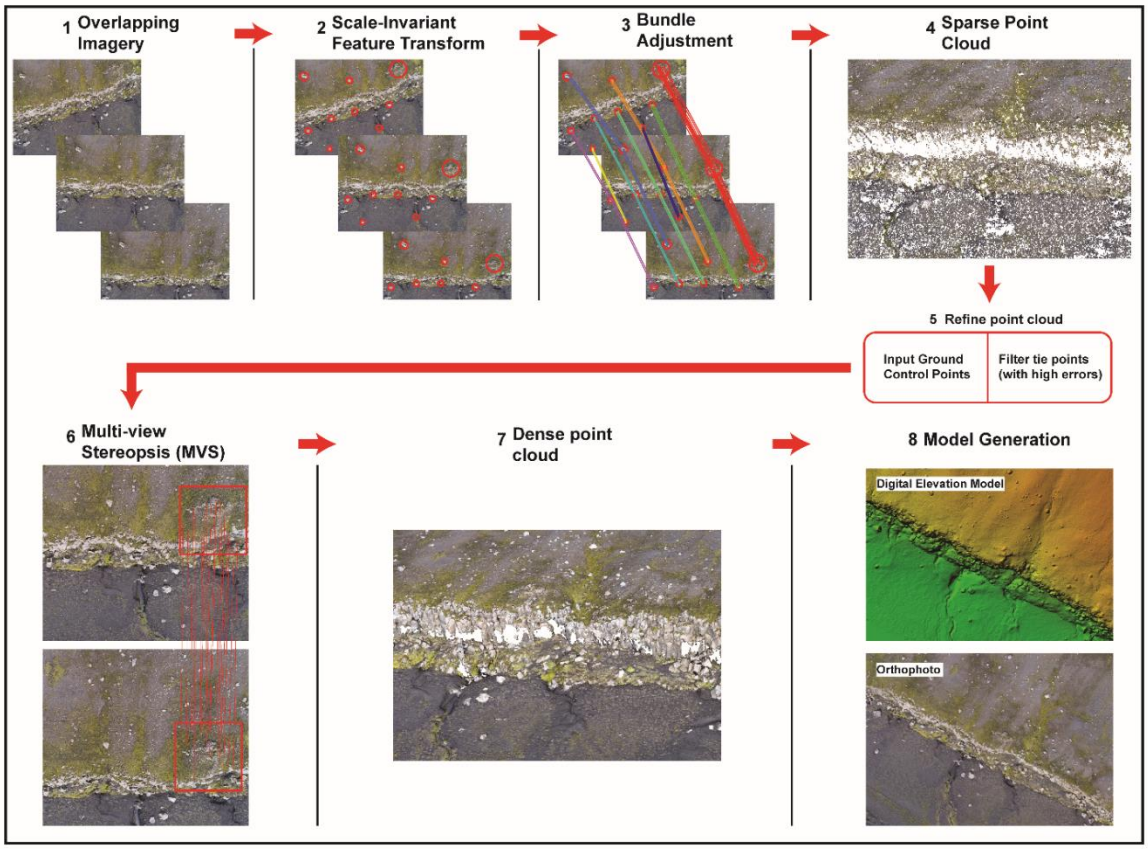

Figure 1.7: Standard workflow used in most Structure from Motion (SfM) software, including Agisoft Metashape, which was used in this thesis. Stage 1: Overlapping images collected during field work. Stage 2: Scale-invariant Feature Transform where the overlapping images are compared and key points extracted, key points are noted with red circles in the diagram. Stage 3: Sparse bundle adjustment finds more points near the key points which can be identified in the overlapping images and used to create a 3-D point cloud, denoted using coloured lines. Stage 4: Sparse point cloud. Stage 5: Refine the point cloud using ground control points and filtering. Stage 6: Using the key points and tie point from the sparse cloud, further neighbouring points are identified and filtered denoted using red lines above. Stage 7: Dense point cloud. Stage 8: Create models based on the dense cloud for analysis. For further details, see text.

1.3.1.3. Unmanned Aerial Vehicles (UAVs)

A further development in the utility of SfM for research purposes has been the rapid increase in unmanned aerial vehicle (UAV) technology. In the past two decades, UAVs have become more affordable, with increased flight time, improved sensors (including cameras) and increased positioning capabilities and maneuvering controls (Hugenholtz et

al., 2013; Bi et al., 2017; Clark, 2017). The ability to automate the flight paths of UAVs has further enabled them to be used as a research tool, as consistent and optimized imagery collection can be conducted (Tonkin et al., 2014; Eltner et al., 2015; Bi et al., 2017). There are many benefits to using drones (UAVs) in the field; for example, imagery of large areas can be collected in relatively short amounts of time, at a high spatial and temporal resolution, allowing for the analysis of processes and landscapes on a scale that was difficult to complete using more traditional remote sensing techniques (Clark, 2017; Ely et al., 2017). When working on vertical outcrops, using a drone permits the collection of imagery close to the face at high elevations, facilitating the creation of more accurate models. This ability to collect close range photogrammetric data has facilitated the development of methodologies to create high-resolution (<10 cm) models quickly and at low cost (Chandler et al., 2015; Ely et al., 2017)

1.3.1.4. Change detection methodologies

When multiple surveys are completed of the same region at different times (days, weeks, or multiple years apart) the resultant models can be compared to determine how the landscape or feature of interest has evolved; this is commonly known as change detection. To facilitate change detection, it is critical to minimize the error between models generated using SfM. Co-registration of the point clouds must be conducted, to minimize the difference in the point clouds or models caused by errors in the spatial location of points that is unrelated to real world change. This is commonly completed using the Iterative Closest Points (ICP) algorithm, which iteratively transforms the point clouds based on the proximity of its neighbours and is one of the most common methodologies of point cloud registration (Zhang, 1994; Rajendra et al., 2014). ICP can be applied to full datasets, or if changes are expected, can be applied to subsets of the datasets where no change was observed (Micheletti et al., 2015; Stumpf et al., 2015).

The ability to quantify geomorphic change is a focus of many geomorphological studies and has been facilitated by comparing multiple DEMs taken at different times in the past (Williams, 2012). Comparing multiple DEMs of planform landscapes is relatively

common and quantifies the volumetric change between two DEMs. This can be completed in any GIS program, such as ArcGIS or QGIS.

The Multiscale Model to Model Cloud Comparison (M3C2) algorithm is used to analyze changes of more complex topography. This algorithm computes the local distance between two point clouds along the normal surface direction based on the surface orientation (Lague et al., 2013). The M3C2 is effective at determining change in complex topography as it acts on each point, or a subset of key points, and also provides an estimate of uncertainty (Barnhart & Crosby, 2013; Lague et al., 2013; Stumpf et al., 2015). In addition to calculating areas of change, based on two 3-D point clouds, the algorithm provides a confidence interval for each of the distance measurements based on the cloud roughness and the registration error (Lague et al., 2013); this allows users to filter out change with a confidence interval below a chosen threshold to ensure all identified change is real.

Based on the distances computed using the M3C2 algorithm the approximate volume of change can also be calculated. There are many methods of determining volume, two of the most common are the alpha-shape and power crust algorithms (Amenta et al., 2001; van Veen et al., 2017; Bonneau et al., 2019; DiFrancesco et al., 2020, 2021;). These can be used to reconstruct the approximate shape of the area of change, as a modeled block from which a volume can be calculated.

An alpha shape is a generalization of the convex hull of a point set which is defined as the union of all simplices covered by its alpha complex. The alpha complex is a subcomplex of the Delaunay triangulation of the point set which includes all Delaunay tetrahedra (including faces, edges, and points) which have empty spheres with radii less than the set alpha radius. Alpha radii were determined separately for each of the defined clusters in order to find the smallest radius that creates a manifold, watertight model to provide more accurate volume measurements.

The power crust algorithm computes an approximate medial axis transform (MAT) based on a subset of Voronoi vertices of the point set (Amenta et al., 2001; Bonneau et al.,

2019). From the MAT a piecewise-linear approximation of the surface is created (Amenta et al., 2001; Bonneau et al., 2019) and the volume calculated.

1.3.2 Landsystem analysis

Landsystem analysis was applied in the planform landscape investigation of the forefield in Iceland. This methodology allows for the integration of high spatial and temporal remotely sensed data collected using the UAV to be integrated with sedimentological data to better understand the characteristics and possible origin of landforms to interpret past glacial dynamics. Landsystem analysis is a hierarchical method of classifying terrain into genetically related landform-sediment assemblages (Evans, 2003). It focuses on integrating the spatial distribution, morphological characteristics, and sedimentological characteristics of a suite of landforms to diagnose the former environment of deposition (Schomacker et al., 2014; Evans et al., 2016). Landsystem analysis has been applied to a variety of glacial environments and deposits within modern glaciated regions (Eyles & Menzies, 1983; Evans & Twigg, 2002; Bennett & Evans, 2012) and paleo-glaciated regions (Evans et al., 1999; Kehew et al., 2012; Lane et al., 2016).

It is a valuable tool for understanding and mapping both surface and subsurface deposits (Eyles, 1983; Cooke & Doornkamp, 1990). However, due to the focus on geomorphological characteristics it is most effective when applied to deposits with surficial expression of landforms (Eyles, 1983). It also facilitates identification of connections between landscape features on a variety of scales (small to large) to fully encapsulate the complexity of glacial landscapes. The integration of high-resolution imagery with this method allows for the delineation of smaller scale landsystem elements, which facilitates enhanced understanding of the full range of processes that have operated in a particular region in the past.

1. 4 Organization of the thesis

This thesis is presented as a series of four manuscripts intended for submission to international scientific journals for publication. These four substantive chapters (Chapters 2-5) are placed between an introductory (Chapter 1) and concluding chapter (Chapter 6).

Chapter 2 investigates the forefields of two modern surge-type glaciers in southern Iceland, Sléttjökull and Öldufellsjökull, on the northern margin of Mýrdalsjökull. Each of the glaciers is known to have surged in the last 50 years, implying there should be an imprint of this fast ice flow in the area deglaciated since that time. The study combines sedimentological and geomorphological field data with UAV-based DEMs and orthophotos to analyze the landform-sediment assemblages present. These assemblages are then compared with that of the established surge-type landsystem tracts, to determine whether these glaciers have similar distribution of landsystem tracts or differ from the conventional fast-ice flow regime. The results of this study show that these two forefields, when considered in their entirety, lack any expected indicators of fast ice flow. However, on high-resolution models of smaller areas of the forefields some indicators of fast-ice flow can be identified. Additionally, the high-resolution surveys show a circular feature, believed to be a water escape structure caused by fluctuations in groundwater pressure during and after the active phase of the surge. This chapter explores the use of UAV based imagery in conjunction with sedimentology to determine past depositional processes. The following chapters focus on the use of UAVs to collect datasets for spatial and temporal comparative analyses.

Chapters 3, 4 and 5 focus on the erosion of the Niagara Escarpment, taking a multi-faceted approach to identify and examine factors influencing processes and rates of erosion. Chapter 3 focuses on a detailed sedimentological analysis of the lithological units exposed along the Niagara Escarpment in Hamilton, Ontario. This work was completed through the creation and analysis of field-based sedimentological logs, core logs, and UAV-based imagery to supplement data in areas where field-based logs were infeasible. Previous work on the area, including lithological data from additional exposures within the city limits were incorporated to provide a comprehensive view of the lithological characteristics of the escarpment. Based on previous sedimentological studies, and the new sedimentological data collected for this study, variations in lithological properties, unit geometry, and thickness are evident across the 22 km of escarpment exposed within Hamilton. Rock strength properties, specifically unconfined compressive strength, relative fracture density,

and the proportion of fine-grained (shale) layers, were considered for each lithologic unit to give a preliminary determination of the relative susceptibility of each to erosion.

Chapter 4 uses UAV-based imagery and SfM software to create a dense point cloud of a chosen rock outcrop located at Albion Falls, Hamilton. Two surveys were completed over two field seasons; the first one (Survey 1) in which there was no change to the rock face; and a second survey (Survey 2) where rocks of a known size were removed. Survey 1 and Survey 2 for each field season were compared using the M3C2 algorithm, to determine whether this methodology can reliably determine the location of erosional events, and the size of erosional event that is below the threshold of detection. Volume calculations were completed based on the M3C2 model to determine the accuracy of the volume of change when compared with the known volume of the removed rock samples. The M3C2 algorithm reliably identified the location of >90% of the removed blocks. However, the volume calculations both over and underestimated the volume of the removed rock. The size of the sample was not the determining factor in the accuracy of the methodology, rather shadows, vegetation, and contrast of the removed block with the surrounding rock face, were associated with the inaccurate results.

Chapter 5 builds on the methodology utilized in chapter 4, to investigate the location and rate of change (i.e., erosion) of the rock face at Albion Falls in relation to its lithological properties. Using the same UAV-based models and change detection methodology, outcrop surveys from 2018 and 2020 were compared to determine the total change over the 14-month period. The lithology of the outcrop was mapped using the UAV-based model, as well as manually logged in the field. Fractures were mapped on the model using the CloudCompare Compass Plugin and analyzed using FracPaQ, a Matlab toolbox for fracture distribution analysis. This outcrop showed significant change, with 33% of the rock face experiencing erosion and 2.5% of the face showing accumulation of released debris. Areas of the outcrop dominated by shale and sandstone, or shale and dolostone interbeds, underwent a greater amount of erosion compared with other areas. The amount of erosion within a single formation was not constant across the length of the outcrop indicating that erosion processes are both spatially and temporally complex. For example, the propagation

of fractures and the development of undercutting take multiple years to occur, eventually destabilizing the rock face and creating failures. Further surveys completed over multiple years may provide more information on the processes occurring at this site.

The final chapter summarizes the findings of the four substantive chapters of the thesis and highlights some areas for future work pertaining to the utility of drones, erosion monitoring, and planform mapping in glaciated terrains. The body of this thesis provides an understanding of the current utility of consumer-grade UAVs in research in glaciated terrains, their limitations, and benefits within geomorphological studies. This study demonstrates the importance of utilizing high spatial and temporal resolution imagery to investigate low-relief small-scale landforms (Chapter 2) and processes (Chapter 3 – 5) to inform studies and policies related to erosion and landform genesis in glaciated terrains.

1. 5 Preface

This thesis consists of 4 chapters containing research that was led by the author. Chapter 2 examines the impact of fast-ice flow on two outlet glaciers in southern Iceland and will be submitted to *Earth Surface Processes and Landforms*. R. Lee is the primary author completing the field work, literature review, writing, and figure drafting. Co-author R. Narro Perez conducted fieldwork with the author and provided discussions on the results and editing of the paper. Co-author C. H. Eyles (supervisor) assisted in literature review, provided essential discussion, and manuscript editing.

Chapter 3 focuses on the lithology of the Niagara Escarpment in Hamilton, Ontario and how its composition will impact erosion of the feature. This paper will be submitted to the *Canadian Journal of Earth Sciences.* R. Lee is the primary author completing the field work, literature review, writing, and figure drafting. Co-author R. Narro Perez conducted fieldwork with the author, provided discussions on the results and editing of the paper. Co-author C. H. Eyles (supervisor), conducted fieldwork with the author, assisted in literature review, provided essential discussion, and editing.

Chapter 4 focuses on the accuracy of change detection as applied to a sample outcrop on the Niagara Escarpment. This paper will be submitted to *Earth Surface Processes and Landforms*. R. Lee is the primary author completing the field work, literature

review, writing, and figure drafting. Co-author J. C. Maclachlan conducted fieldwork with the author, provided discussion of the results and editing of the manuscript. Co-author C. H. Eyles (supervisor), assisted in literature review, provided essential discussion, and editing.

Chapter 5 quantifies the rate of erosion of the Niagara Escarpment at a selected site in Hamilton and explores how the outcrop evolved between surveys. This paper will be submitted to *Physical Progress in Geography*. R. Lee is the primary author completing the field work, literature review, writing, and figure drafting. Co-author J. C. Maclachlan conducted fieldwork with the author, provided discussion of the results and editing of the manuscript. Co-author C. H. Eyles (supervisor), assisted in literature review, provided essential discussion, and editing.

1. 6 References

Aber, J. S., Marzolff, I., Ries, J. B., & Aber, S. E. W. (2019). Principles of Photogrammetry. In Small-format aerial photography and UAS imagery: Principles, techniques and geoscience applications (2nd ed., pp. 19–38). Elsevier.

Agustawijaya, D. S. (2007). The uniaxial compressive strength of soft rock. Civil Engineering Dimension, 9(1), 9–14.

Amenta, N., Choi, S., & Kolluri, R. K. (2001). The power crust. Proceedings of the Symposium on Solid Modeling and Applications, 249–260. https://doi.org/10.1145/376957.376986

Andreassen, K., Winsborrow, M. C. M., Bjarnadóttir, L. R., & Rüther, D. C. (2014). Ice stream retreat dynamics inferred from an assemblage of landforms in the northern Barents Sea. Quaternary Science Reviews, 92, 246–257. https://doi.org/10.1016/j.quascirev.2013.09.015

Barker, R., Dixon, L., & Hooke, J. (1997). Use of terrestrial photogrammetry for monitoring and measuring bank erosion. Earth Surface Processes and Landforms, 22(13), 1217–1227. https://doi.org/10.1002/(SICI)1096-9837(199724)22:13<1217::AID-ESP819>3.0.CO;2-U

Barnhart, T. B., & Crosby, B. T. (2013). Comparing two methods of surface change detection on an evolving thermokarst using high-temporal-frequency terrestrial laser scanning, Selawik River, Alaska. Remote Sensing, 5(6), 2813–2837. https://doi.org/10.3390/rs5062813

BBC. (2020). Mont Blanc: Glacier collapse risk forces Italy Alps evacuation. BBC. https://www.bbc.co.uk/news/world-europe-53692476

Benediktsson, Í. Ö., Schomacker, A., Lokrantz, H., & Ingólfsson, Ó. (2010). The 1890 surge end moraine at Eyjabakkajökull, Iceland: a re-assessment of a classic glaciotectonic locality. Quaternary Science Reviews, 29, 484–506. https://doi.org/10.1016/j.quascirev.2009.10.004

Bennett, G. L., & Evans, D. J. A. (2012). Glacier retreat and landform production on an overdeepened glacier foreland: The debris-charged glacial landsystem at Kviárjökull, Iceland. *Earth Surface Processes and Landforms*, *37*, 1584–1602. https://doi.org/10.1002/esp.3259

Bi, H., Zheng, W., Ren, Z., Zeng, J., & Yu, J. (2017). Using an unmanned aerial vehicle for topography mapping of the fault zone based on structure from motion photogrammetry. *International Journal of Remote Sensing*, *38*(8–10), 2495–2510. https://doi.org/10.1080/01431161.2016.1249308

Biswas, S. (2021). *"Hanging" glacier broke off to trigger India flood*. BBC News. https://www.bbc.com/news/world-asia-india-56007448

Björnsson, H., & Pálsson, F. (2008). Icelandic glaciers. *Jökull*, *58*(58), 365–386.

Björnsson, H., Palsson, F., & Gudmundsson, M. T. (2000). Surface and bedrock topography of the Mýrdalsjökull ice cap, Iceland: The Katla caldera, eruption sites and routes of jökulhlaups. *Jökull*, *49*(49), 29–46.

Björnsson, H., Pálsson, F., Sigurdsson, O., & Flowers, G. E. (2003). Surges of glaciers in Iceland. *Annals of Glaciology*, *36*, 82–90. https://doi.org/10.3189/172756403781816365

Bolton, T. E. (1957). Silurian stratigraphy and palaeontology of the Niagara Escarpment in Ontario.

Bonneau, D., Hutchinson, D. J., DiFrancesco, P.-M., Coombs, M., & Sala, Z. (2019). Three-dimensional rockfall shape back analysis: Methods and implications. *Natural Hazards and Earth System Sciences*, *19*(12), 2745–2765. https://doi.org/10.5194/nhess-19-2745-2019

Brandsdóttir, B., & Menke, W. H. (2008). The seismic structure of Iceland. *Jökull*, *58*, 17–34.

Brett, C. E., Goodman, W. M., & LoDuca, S. T. (1990). Sequences, cycles, and basin dynamics in the Silurian of the Appalachian Foreland Basin. *Sedimentary Geology*, *69*(3–4), 191–244. https://doi.org/10.1016/0037-0738(90)90051-T

Brigham, R. J. (1971). *Structural geology of southwestern Ontario and southeastern Michigan*. Ontario Department of Mines and Northern Affairs.

Brunton, F. R., & Brintnell, C. (2020). Early Silurian Sequence Stratigraphy and Geological Controls on Karstic Bedrock Groundwater-Flow Zones, Niagara Escarpment Region and the Subsurface of Southwestern Ontario.

Budetta, P., Galietta, G., & Santo, A. (2000). A methodology for the study of the relation between coastal cliff erosion and the mechanical strength of soils and rock masses. *Engineering Geology*, *56*(3–4), 243–256. https://doi.org/10.1016/S0013-7952(99)00089-7

Carrivick, J., Tweed, F. S., James, W., & Jóhannesson, T. (2017). Surface and geometry changes during the first documented surge of Kverkjökull, central Iceland. *Jökull*, *66*, 27–49.

CBC. (2014, May 23). The escarpment is falling and it's costing Hamilton thousands. *CBC News*. https://www.cbc.ca/news/canada/hamilton/headlines/the-escarpment-is-falling-and-it-s-costing-hamilton-thousands-1.2622273

Chandler, B. M. P., Evans, D. J. A., Chandler, S. J. P., Ewertowski, M. W., Lovell, H., Roberts, D. H., Schaefer, M., & Tomczyk, A. M. (2020). The glacial landsystem of Fjallsjökull, Iceland: Spatial and temporal evolution of process-form regimes at an active temperate glacier. *Geomorphology*, *361*, 107192. https://doi.org/10.1016/j.geomorph.2020.107192

Chandler, B. M. P., Evans, D. J. A., Roberts, D. H., Ewertowski, M., & Clayton, A. I. (2015). Glacial geomorphology of the Skálafellsjökull foreland, Iceland: A case study of 'annual' moraines. *Journal of Maps*, 1–13. https://doi.org/10.1080/17445647.2015.1096216

City of Hamilton (2021). *Open Hamilton: GIS Database.* Retreived from: https://open.hamilton.ca/, September, 2021.

Clark, A. (2017). Small unmanned aerial systems comparative analysis for the application to coastal erosion monitoring. *GeoResJ*, *13*, 175–185. https://doi.org/10.1016/j.grj.2017.05.001

Cooke, R. V., & Doornkamp, J. C. (1990). *Geomorphology in environmental management: a new introduction*. Oxford University Press (OUP).

Cooper, R. J., Wadham, J. L., Tranter, M., Hodgkins, R., & Peters, N. E. (2002). Groundwater hydrochemistry in the active layer of the proglacial zone, Finsterwalderbreen, Svalbard. *Journal of Hydrology*, *269*(3–4), 208–223. https://doi.org/10.1016/S0022-1694(02)00279-2

Copland, L., Sharp, M. J., & Dowdeswell, J. A. (2003). The distribution and flow characteristics of surge-type glaciers in the Canadian High Arctic. *Annals of Glaciology*, *36*(March 2014), 73–81. https://doi.org/10.3189/172756403781816301

Crowley, D. J. (1973). Middle Silurian Patch Reefs in Gasport Member (Lockport Formation), New York. *AAPG Bulletin*, *57*(2), 283–300. https://doi.org/10.1306/819a426a-16c5-11d7-8645000102c1865d

D'Oleire-Oltmanns, S., Marzolff, I., Peter, K. D., & Ries, J. B. (2012). Unmanned aerial vehicle (UAV) for monitoring soil erosion in Morocco. *Remote Sensing*, *4*(11), 3390–3416. https://doi.org/10.3390/rs4113390

Dąbski, M., Zmarz, A., Pabjanek, P., Korczak-Abshire, M., Karsznia, I., & Chwedorzewska, K. J. (2017). UAV-based detection and spatial analyses of periglacial landforms on Demay Point (King George Island, South Shetland Islands, Antarctica). *Geomorphology*, *290*(March), 29–38. https://doi.org/10.1016/j.geomorph.2017.03.033

DiFrancesco, P. M., Bonneau, D. A., & Hutchinson, D. J. (2021). Computational Geometry-Based Surface Reconstruction for Volume Estimation: A Case Study on Magnitude-Frequency Relations for a LiDAR-Derived Rockfall Inventory. *ISPRS International Journal of Geo-Information*, *10*(3), 157. https://doi.org/10.3390/ijgi10030157

DiFrancesco, P. M., Bonneau, D., & Hutchinson, D. J. (2020). The implications of M3C2 projection diameter on 3D semi-automated rockfall extraction from sequential terrestrial laser scanning point clouds. *Remote Sensing*, *12*(11). https://doi.org/10.3390/rs12111885

Dühnforth, M., Anderson, R. S., Ward, D., & Stock, G. M. (2010). Bedrock fracture control of glacial erosion processes and rates. *Geology*, *38*(5), 423–426. https://doi.org/10.1130/G30576.1

Eltner, A., Baumgart, P., Maas, H. G., & Faust, D. (2015). Multi-temporal UAV data for automatic measurement of rill and interrill erosion on loess soil. *Earth Surface Processes and Landforms*, *40*(6), 741–755. https://doi.org/10.1002/esp.3673

Ely, J. C., Graham, C., Barr, I. D., Rea, B. R., Spagnolo, M., & Evans, J. (2017). Using UAV acquired photography and structure from motion techniques for studying glacier landforms: application to the glacial flutes at Isfallsglaciären. *Earth Surface Processes and Landforms*, *42*(6), 877–888. https://doi.org/10.1002/esp.4044

Erguler, Z. A., & Shakoor, A. (2009). Quantification of fragment size distribution of clay-bearing rocks after slake durability testing. *Environmental and Engineering Geoscience*, *15*(2), 81–89. https://doi.org/10.2113/gseegeosci.15.2.81

Evans, David J.A. (2003). Introduction to Glacial Landsystems. In *Glacial Landsystems*. Hodder Arnold.

Evans, David J.A., Ewertowski, M., Orton, C., & Graham, D. J. (2018). The glacial geomorphology of the ice cap piedmont lobe landsystem of east mýrdalsjökull, Iceland. *Geosciences (Switzerland)*, *8*(6). https://doi.org/10.3390/geosciences8060194

Evans, David J.A., Lemmen, D. S., & Rea, B. R. (1999). Glacial landsystems of the southwest Laurentide Ice Sheet: modern Icelandic analogues. *Journal of Quaternary Science*, *14*(7), 673–691. https://doi.org/10.1002/(SICI)1099-1417(199912)14:7<673::AID-JQS467>3.0.CO;2-#

Evans, David J.A., & Rea, B. R. (1999). Geomorphology and sedimentology of surging glaciers: A land-systems approach. *Annals of Glaciology*, *28*(1995), 75–82. https://doi.org/10.3189/172756499781821823

Evans, David J.A., & Rea, B. R. (2003). Surging glacier landsystem. In D. J.A. Evans (Ed.), *Glacial Landsystems* (pp. 259–288). Hodder Arnold.

Evans, David J.A., Roberts, D. H., & Evans, S. C. (2016). Multiple subglacial till deposition: A modern exemplar for Quaternary palaeoglaciology. *Quaternary Science Reviews*, *145*, 183–203. https://doi.org/10.1016/j.quascirev.2016.05.029

Evans, David J.A., & Twigg, D. R. (2002). The active temperate glacial landsystem: A model based on Breiðamerkurjökull and Fjallsjökull, Iceland. *Quaternary Science Reviews*, *21*, 2143–2177. https://doi.org/10.1016/S0277-3791(02)00019-7

Evans, David J.A., Twigg, D. R., Rea, B. R., & Orton, C. (2009). Surging glacier landsystem of tungnaárjökull, iceland. *Journal of Maps*, *5*(1), 134–151. https://doi.org/10.4113/jom.2009.1064

Eyles, N. (1983). Glacial Geology: A landsystems approach. In N. Eyles (Ed.), *Glacial Geology: An Introduction for engineers and earth scientists* (1st ed., pp. 1–18). Pergamon Press Canada Ltd.

Eyles, N., Arnaud, E., Scheidegger, A. E., & Eyles, C. H. (1997). Bedrock jointing and geomorphology in southwestern Ontario, Canada: An example of tectonic predesign. *Geomorphology*, *19*(1–2), 17–34. https://doi.org/10.1016/s0169-555x(96)00050-5

Eyles, N., & Menzies, J. (1983). The subglacial landsystem. In N. Eyles (Ed.), *Glacial Geology: An Introduction for engineers and Earth Scientists* (pp. 19–70). Pergamon Press Canada Ltd.

Eyssautier-Chuine, S., Marin, B., Thomachot-Schneider, C., Fronteau, G., Schneider, A., Gibeaux, S., & Vazquez, P. (2016). Simulation of acid rain weathering effect on natural and artificial carbonate stones. *Environmental Earth Sciences*, *75*(748), 1–19. https://doi.org/10.1007/s12665-016-5555-z

Feenstra, B. H. (1981). Quaternary geology and industrial minerals of the Niagara-Welland Area, southern Ontario (p. 260). Ontario Geological Survey - Open File Report 5361.

Flink, A. E., Noormets, R., Fransner, O., Hogan, K. A., ÓRegan, M., & Jakobsson, M. (2017). Past ice flow in Wahlenbergfjorden and its implications for late Quaternary ice sheet dynamics in northeastern Svalbard. *Quaternary Science Reviews*, *163*, 162–179. https://doi.org/10.1016/j.quascirev.2017.03.021

Fonstad, M. A., Dietrich, J. T., Courville, B. C., Jensen, J. L., & Carbonneau, P. E. (2013). Topographic structure from motion: A new development in photogrammetric

measurement. *Earth Surface Processes and Landforms*, *38*(4), 421–430. https://doi.org/10.1002/esp.3366

Franklin, J. A. (1981). A shale rating system and tentative applications to shale performance. *Transportation Research Record*, *790*(3), 2–12.

Fussell, A. (1982). Terrestrial photogrammetry in archaeology. *World Archaeology*, *14*(2), 157–172.

Gao, C. (2011). Buried bedrock valleys and glacial and subglacial meltwater erosion in Southern Ontario, Canada. *Canadian Journal of Earth Sciences*, *48*(5), 801–818. https://doi.org/10.1139/e10-104

Gautam, T. P., & Shakoor, A. (2013). Slaking behavior of clay-bearing rocks during a one-year exposure to natural climatic conditions. *Engineering Geology*, *166*, 17–25. https://doi.org/10.1016/j.enggeo.2013.08.003

Giordan, D., Adams, M. S., Aicardi, I., Alicandro, M., Allasia, P., Baldo, M., De Berardinis, P., Dominici, D., Godone, D., Hobbs, P., Lechner, V., Niedzielski, T., Piras, M., Rotilio, M., Salvini, R., Segor, V., Sotier, B., & Troilo, F. (2020). The use of unmanned aerial vehicles (UAVs) for engineering geology applications. *Bulletin of Engineering Geology and the Environment*, *79*(7), 3437–3481. https://doi.org/10.1007/s10064-020-01766-2

Granshaw, S. I. (2019). Laussedat bicentenary: origins of photogrammetry. *The Photogrammetric Record*, *34*(166), 128–147.

Grant, K. L., Stokes, C. R., & Evans, I. S. (2009). Identification and characteristics of surge-type glaciers on Novaya Zemlya, Russian Arctic. *Journal of Glaciology*, *55*(194), 960–972. https://doi.org/10.3189/002214309790794940

Gross, M. R., & Engelder, T. (1991). A case for neotectonic joints along the Niagara Escarpment. *Tectonics*, *10*(3), 631–641. https://doi.org/10.1029/90TC02702

Hagan, T. O. (1980). A case for terrestrial photogrammetry in deep-mine rock structure studies. *International Journal of Rock Mechanics and Mining Sciences & Geomechanics Abstracts*, *17*(4), 191–198.

Haldar, S. K. (2018). Chapter 3 - Photogeology, Remote Sensing, and Geographic Information System in Mineral Exploration. In S. K. Haldar (Ed.), *Mineral Exploration (Second Edition)* (Second Edi, pp. 47–68). Elsevier. https://doi.org/https://doi.org/10.1016/B978-0-12-814022-2.00003-4

Hannesdóttir, H., Björnsson, H., Pálsson, F., Aðalgeirsdóttir, G., & Guðmundsson, S. S. (2015). Changes in the southeast Vatnajökull ice cap, Iceland, between ~ 1890 and 2010. *The Cryosphere*, *9*(2), 565–585. https://doi.org/10.5194/tc-9-565-2015

Harwin, S., Lucieer, A., & Osborn, J. (2015). The impact of the calibration method on the accuracy of point clouds derived using unmanned aerial vehicle multi-view stereopsis. *Remote Sensing*, *7*(9), 11933–11953. https://doi.org/10.3390/rs70911933

Hayakawa, Y. S., & Matsukura, Y. (2009). Factors influencing the recession rate of Niagara Falls since the 19th century. *Geomorphology*, *110*(3–4), 212–216. https://doi.org/10.1016/j.geomorph.2009.04.011

Hewitt, D. F. (1971). *The Niagara Escarpment* (Industrial). Ontario Department of Mines and Northern Affairs - Report No. 35.

Hewitt, K. (1969). Glacier surges in the Karakoram Himalaya (Central Asia). *Canadian Journal of Earth Sciences*, *6*(4), 1009–1018. https://doi.org/10.1139/e69-106

Hewitt, K. (2011). Glaciers of the Karakoram Himalaya. In *Encyclopedia of Snow, Ice and Glaciers* (pp. 415–428). Springer Netherlands.

Hooke, J. M. (1979). An analysis of the processes of river bank erosion. *Journal of Hydrology*, *42*(1–2), 39–62. https://doi.org/10.1016/0022-1694(79)90005-2

Howell, S. M., Ito, G., Breivik, A. J., Rai, A., Mjelde, R., Hanan, B., Sayit, K., & Vogt, P. (2014). The origin of the asymmetry in the Iceland hotspot along the Mid-Atlantic Ridge from continental breakup to present-day. *Earth and Planetary Science Letters*, *392*, 143–153. https://doi.org/10.1016/j.epsl.2014.02.020

Hugenholtz, C. H., Whitehead, K., Brown, O. W., Barchyn, T. E., Moorman, B. J., LeClair, A., Riddell, K., & Hamilton, T. (2013). Geomorphological mapping with a small unmanned aircraft system (sUAS): Feature detection and accuracy assessment of a photogrammetrically-derived digital terrain model. *Geomorphology*, *194*, 16–24. https://doi.org/10.1016/j.geomorph.2013.03.023

Ingólfsson, Ó., Benediktsson, Í. Ö., Schomacker, A., Kjær, K. H., Brynjólfsson, S., Jónsson, S. A., Korsgaard, N. J., & Johnson, M. D. (2016). Glacial geological studies of surge-type glaciers in Iceland - Research status and future challenges. *Earth-Science Reviews*, *152*, 37–69. https://doi.org/10.1016/j.earscirev.2015.11.008

James, M. R., & Robson, S. (2012). Straightforward reconstruction of 3D surfaces and topography with a camera: Accuracy and geoscience application. *Journal of Geophysical Research: Earth Surface*, *117*(3), 1–17. https://doi.org/10.1029/2011JF002289

Jauregui, L., & Jauregui, M. (2000). Terrestrial photogrammetry applied to architectural restoration and archaeological surveys. *International Archives of Photogrammetry and Remote Sensing*, *XXXIII*, 401–405. http://www.isprs.org/proceedings/xxxiii/congress/part5/401_XXXIII-part5.pdf

Jiskoot, H., Murray, T., & Boyle, P. (2000). Controls on the distribution of surge-type glaciers in Svalbard. *Journal of Glaciology*, *46*(154), 412–422. https://doi.org/10.3189/172756500781833115

Jiskoot, Hester. (2011). Glacier Surging. In *Encyclopedia of Snow, Ice and Glaciers* (pp. 415–428). SpringerNetherlands.

Jónsson, S. A., Schomacker, A., Benediktsson, Í. Ö., Ingólfsson, Ó., & Johnson, M. D. (2014). The drumlin field and the geomorphology of the Múlajökull surge-type glacier, central Iceland. *Geomorphology*, *207*(March), 213–220. https://doi.org/10.1016/j.geomorph.2013.11.007

Jugie, M., Gob, F., Virmoux, C., Brunstein, D., Tamisier, V., Le Coeur, C., & Grancher, D. (2018). Characterizing and quantifying the discontinuous bank erosion of a small low energy river using Structure-from-Motion Photogrammetry and erosion pins. *Journal of Hydrology*, *563*(February), 418–434. https://doi.org/10.1016/j.jhydrol.2018.06.019

Kaiser, A., Neugirg, F., Rock, G., Müller, C., Haas, F., Ries, J. B., & Schmidt, J. (2014). Small-scale surface reconstruction and volume calculation of soil erosion in complex

Moroccan gully morphology using structure from motion. *Remote Sensing*, *6*(8), 7050–7080.

Kanji, M. A. (2014). Critical issues in soft rocks. *Journal of Rock Mechanics and Geotechnical Engineering*, *6*(3), 185–195.

Karrow, P. F. (1974). Till stratigraphy in Parts of Southwestern Ontario. *Bulletin of the Geological Society of America*, *85*(5), 761–768. https://doi.org/10.1130/0016-7606(1974)85<761:TSIPOS>2.0.CO;2

Kehew, A. E., Esch, J. M., Kozlowski, A. L., & Ewald, S. K. (2012). Glacial landsystems and dynamics of the Saginaw Lobe of the Laurentide Ice Sheet, Michigan, USA. *Quaternary International*, *260*, 21–31. https://doi.org/10.1016/j.quaint.2011.07.021

Kirby, E., & Ouimet, W. (2011). Tectonic geomorphology along the eastern margin of Tibet: Insights into the pattern and processes of active deformation adjacent to the Sichuan Basin. *Geological Society Special Publication*, *353*, 165–188. https://doi.org/10.1144/SP353.9

Kjær, K. H., Krüger, J., & van der Meer, J. J. M. (2003). What causes till thickness to change over distance? Answers from Mýrdalsjökull, Iceland. *Quaternary Science Reviews*, *20*(15), 1687–1700. https://doi.org/10.1016/S0277-3791(03)00162-8

Kjær, K. H., Sultan, L., Krüger, J., & Schomacker, A. (2004). Architecture and sedimentation of outwash fans in front of the Mýrdalsjökull ice cap, Iceland. *Sedimentary Geology*, *172*(1), 139–163. https://doi.org/10.1016/j.sedgeo.2004.08.002

Kruger, J. (1995). Origin, chronology and climatological significance of annual-moraine ridges at Myrdalsjokull, Iceland. *Holocene*, *5*(4), 420–427. https://doi.org/10.1177/095968369500500404

Krüger, J. (1988). Glacial geomorphological research at Mýrdalsjökull , Iceland, 1977-86. I: the northern margin. *Geografisk Tidsskrift*, *88*, 68–77.

Krüger, J., Kjær, K. H., & Schomacker, A. (2010). Dead-Ice Environments: A Landsystems Model for a Debris-Charged, Stagnant Lowland Glacier Margin, Kötlujökull. *Developments in Quaternary Sciences*, *13*, 105–126. https://doi.org/http://dx.doi.org/10.1016/S1571-0866(09)01307-4

Lague, D., Brodu, N., & Leroux, J. (2013). Accurate 3D comparison of complex topography with terrestrial laser scanner: Application to the Rangitikei canyon (N-Z). *ISPRS Journal of Photogrammetry and Remote Sensing*, *82*, 10–26. https://doi.org/10.1016/j.isprsjprs.2013.04.009

Lane, T. P., Roberts, D. H., Ó Cofaigh, C., Rea, B. R., & Vieli, A. (2016). Glacial landscape evolution in the Uummannaq region, West Greenland. *Boreas*, *45*(2), 220–234. https://doi.org/10.1111/bor.12150

Langhammer, J., & Vacková, T. (2018). Detection and Mapping of the Geomorphic Effects of Flooding Using UAV Photogrammetry. *Pure and Applied Geophysics*, *175*(9), 3223–3245. https://doi.org/10.1007/s00024-018-1874-1

Lautridou, J. P., & Ozouf, J. C. (1982). Experimental frost shattering. *Progress in Physical Geography: Earth and Environment*, *6*(2), 215–232. https://doi.org/10.1177/030913338200600202

Letortu, P., Jaud, M., Grandjean, P., Ammann, J., Costa, S., Maquaire, O., Davidson, R., Le Dantec, N., & Delacourt, C. (2018). Examining high-resolution survey methods

for monitoring cliff erosion at an operational scale. *GIScience and Remote Sensing*, *55*(4), 457–476. https://doi.org/10.1080/15481603.2017.1408931

Linder, W. (2009). Digital photogrammetry: A Practical Course (3rd ed.). Springer.

Lowe, D. G. (2004). Distinctive image features from scale-invariant keypoints. *International Journal of Computer Vision*, *60*(2), 91–110.

Loye, A., Pedrazzini, A., Theule, J. I., Jaboyedoff, M., Liébault, F., & Metzger, R. (2012). Influence of bedrock structures on the spatial pattern of erosional landforms in small alpine catchments. *Earth Surface Processes and Landforms*, *37*(13), 1407–1423. https://doi.org/10.1002/esp.3285

Margold, M., Stokes, C. R., & Clark, C. D. (2015). Ice streams in the Laurentide Ice Sheet: Identification, characteristics and comparison to modern ice sheets. *Earth-Science Reviews*, *143*, 117–146. https://doi.org/10.1016/j.earscirev.2015.01.011

Mayer, C., Jaenicke, J., Lambrecht, A., Braun, L., Völksen, C., Minet, C., & Münzer, U. (2017). Local surface mass-balance reconstruction from a tephra layer - A case study on the northern slope of Mýrdalsjökull, Iceland. *Journal of Glaciology*, *63*(237), 79–87. https://doi.org/10.1017/jog.2016.119

Micheletti, N., Chandler, J. H., & Lane, S. N. (2015). Structure from Motion (SfM) Photogrammetry (Section 2.1.3). In L. E. Clarke & J. M. Nield (Eds.), *Geomorphological Techniques (Online Edition)*. British Society for Geomorphology. https://doi.org/10.1002/esp.3767

Moore, A., & Blenkinsop, T. (2006). Scarp retreat versus pinned drainage divide in the formation of the Drakensberg escarpment, southern Africa. *South African Journal of Geology*, *109*(4), 599–610. https://doi.org/10.2113/gssajg.109.4.599

Naylor, L. A., & Stephenson, W. J. (2010). On the role of discontinuities in mediating shore platform erosion. *Geomorphology*, *114*(1–2), 89–100. https://doi.org/10.1016/j.geomorph.2008.12.024

Niemann, W. L. (2009). Lessons learned from rates of mudrock undercutting measured over two time periods. *Environmental and Engineering Geoscience*, *15*(3), 117–131. https://doi.org/10.2113/gseegeosci.15.3.117

Niethammer, U., James, M. R., Rothmund, S., Travelletti, J., & Joswig, M. (2012). UAV-based remote sensing of the Super-Sauze landslide: Evaluation and results. *Engineering Geology*, *128*, 2–11. https://doi.org/10.1016/j.enggeo.2011.03.012

Okamoto, T. (1993). Testing methods of indurated soils and soft rocks - suggestions and recommendations. In *Techincal committee on indurated soils and soft rocks*. International Society for Soil Mechanics and Foundation Engineering.

Óladóttir, B. A., Sigmarsson, O., Larsen, G., & Thordarson, T. (2008). Katla volcano, Iceland: Magma composition, dynamics and eruption frequency as recorded by Holocene tephra layers. *Bulletin of Volcanology*, *70*(4), 475–493. https://doi.org/10.1007/s00445-007-0150-5

Owen, J. J., Amundson, R., Dietrich, W. E., Nishiizumi, K., Sutter, B., & Chong, G. (2011). The sensitivity of hillslope bedrock erosion to precipitation. *Earth Surface Processes and Landforms*, *36*, 117–135. https://doi.org/10.1002/esp.2083

Perras, M. A., Diederichs, M. S., & Besaw, D. (2014). Geological and geotechnical observations from the Niagara Tunnel Project. *Bulletin of Engineering Geology and the Environment*, *73*, 1303–1323. https://doi.org/10.1007/s10064-014-0633-5

Portenga, E. W., & Bierman, P. R. (2011). Understanding earth's eroding surface with 10Be. *GSA Today*, *21*(8), 4–10. https://doi.org/10.1130/G111A.1

Post, A. (1969). Distribution of surging glaciers in western North America. *Journal of Glaciology*, *8*(53), 229–240.

RGI Consortium (2017). Randolph Glacier Inventory – A Dataset of Global Glacier Outlines: Version 6.0: Technical Report, Global Land Ice Measurements from Space, Colorado, USA. Digital Media. DOI: **https://doi.org/10.7265/N5-RGI-60**

Ragey, L. (1952). The work of Laussedat and education in photogrammetry at the National School of Arts and Crafts, Paris. *Photogrammetric Engineering*, *1*(18), 21–26.

Rajendra, Y. D., Mehrotra, S. C., Kale, K. V., Manza, R. R., Dhumal, R. K., Nagne, A. D., & Vibhute, A. D. (2014). Evaluation of Partially Overlapping 3D Point Cloud's Registration by using ICP variant and CloudCompare. *The International Archives of Photogrammetry, Remote Sensing and Spatial Information Sciences*, *40*(8), 891–897.

Reddy, M. M., Sherwood, S. I., & Doe, B. R. (1986). Limestone and marble dissolution by acid rain: an onsite weathering experiment. In R. Baboiam (Ed.), *Materials Degradation Caused by Acid Rain* (Vol. 318, pp. 226–238). American Chemical Society.

Schomacker, A., Benediktsson, Í. Ö., & Ingólfsson, Ó. (2014). The Eyjabakkajökull glacial landsystem, Iceland: Geomorphic impact of multiple surges. *Geomorphology*, *218*, 98–107. https://doi.org/10.1016/j.geomorph.2013.07.005

Schomacker, A., Kjær, K. H., & Krüger, J. (2010). Subglacial Environments, Sediments and Landforms at the Margins of Mýrdalsjökull. *Developments in Quaternary Sciences*, *13*, 127–144.

Scott, D. N., & Wohl, E. E. (2019). Bedrock fracture influences on geomorphic process and form across process domains and scales. *Earth Surface Processes and Landforms*, *44*(1), 27–45. https://doi.org/10.1002/esp.4473

Selen, L., Panthi, K. K., & Vistnes, G. (2020). An analysis on the slaking and disintegration extent of weak rock mass of the water tunnels for hydropower project using modified slake durability test. 1919–1937.

Sevestre, H., & Benn, D. I. (2015). Climatic and geometric controls on the global distribution of surge-type glaciers: Implications for a unifying model of surging. *Journal of Glaciology*, *61*(228), 646–662. https://doi.org/10.3189/2015JoG14J136

Sharp, M. J. (1988). Surging glaciers: Behaviour and mechanisms. *Progress in Physical Geography*, *12*(3), 349–370. https://doi.org/10.1177/030913338801200302

Sigurðsson, O. (2010). Variations of Mýrdalsjökull during postglacial and historical times. *Developments in Quaternary Sciences*, *13*, 69–78.

Sirvent, J., Desir, G., Gutierrez, M., Sancho, C., & Benito, G. (1997). Erosion rates in badland areas recorded by collectors, erosion pins and profilometer techniques (Ebro Basin, NE-Spain). *Geomorphology*, *18*(2), 61–75. https://doi.org/10.1016/S0169-555X(96)00023-2

Snavely, N., Seitz, S. M., & Szeliski, R. (2008). Modeling the world from internet photo collections. *International Journal of Computer Vision*, *80*, 189–210.

Sookhan, S., Eyles, N., & Arbelaez-Moreno, L. (2018). Converging ice streams: A new paradigm for reconstructions of the laurentide ice sheet in southern Ontario and deposition of the Oak Ridges moraine. *Canadian Journal of Earth Sciences*, *55*(4), 373–396. https://doi.org/10.1139/cjes-2017-0180

Sookhan, S., Eyles, N., Bukhari, S., & Paulen, R. C. (2021). LiDAR-based quantitative assessment of drumlin to mega-scale glacial lineation continuums and flow of the paleo Seneca-Cayuga paleo-ice stream. *Quaternary Science Reviews*, *263*, 107003. https://doi.org/10.1016/j.quascirev.2021.107003

Spectator. (2017, October 13). Cracks in the foundation: The price of living on the edge. *The Hamilton Spectator*. https://www.thespec.com//news/hamilton-region/2017/10/13/cracks-in-the-foundation-the-price-of-living-on-the-edge.html

Stokes, C. R. (2018). Geomorphology under ice streams: Moving from form to process. *Earth Surface Processes and Landforms*, *43*(1), 85–123. https://doi.org/10.1002/esp.4259

Straw, A. (1968). Late Pleistocene glacial erosion along the Niagara Escarpment of southern Ontario. *Geological Society of America Bulletin*, *79*(7), 889–910.

Stumpf, A., Malet, J. P., Allemand, P., Pierrot-Deseilligny, M., & Skupinski, G. (2015). Ground-based multi-view photogrammetry for the monitoring of landslide deformation and erosion. *Geomorphology*, *231*, 130–145. https://doi.org/10.1016/j.geomorph.2014.10.039

Sturkell, E., Einarsson, P., Sigmundsson, F., Hooper, A., Ófeigsson, B. G., Geirsson, H., & Ólafsson, H. (2010). Katla and Eyjafjallajökull Volcanoes. *Developments in Quaternary Sciences*, *13*, 5–21.

Sturkell, E., & Sigmundsson, F. (2003). Recent unrest and magma movements at Eyjafjallajökull and Katla volcanoes, Iceland. *Journal of Geophysical Research*, *108*(B8), 1–13. https://doi.org/10.1029/2001jb000917

Tepper, D. H., York, N., Goodman, W. M., York, N., Gross, M. R., Kappel, W. M., York, N., & Yager, R. M. (1990). *Stratigraphy , structural geology, and hydrogeology of the Lockport Group : Niagara Falls area , New York* (pp. 1–25). Field Trip Guidebook.

Thorarinsson, S. (1969). Glacier surges in Iceland, with special reference to the surges of Brúarjökull. *Canadian Journal of Earth Sciences*, *6*(4), 875–882. https://doi.org/10.1139/e69-089

Thordarson, T., & Larsen, G. (2007). Volcanism in Iceland in historical time: Volcano types, eruption styles and eruptive history. *Journal of Geodynamics*, *43*(1), 118–152. https://doi.org/10.1016/j.jog.2006.09.005

Tonkin, T. N., Midgley, N. G., Cook, S. J., & Graham, D. J. (2016). Ice-cored moraine degradation mapped and quantified using an unmanned aerial vehicle: A case study from a polythermal glacier in Svalbard. *Geomorphology*, *258*, 1–10. https://doi.org/10.1016/j.geomorph.2015.12.019

Tonkin, T. N., Midgley, N. G., Graham, D. J., & Labadz, J. C. (2014). The potential of small unmanned aircraft systems and structure-from-motion for topographic surveys:

A test of emerging integrated approaches at Cwm Idwal, North Wales. *Geomorphology*, *226*, 35–43. https://doi.org/10.1016/j.geomorph.2014.07.021

Tovell, W. M. (1992). *Guide to the geology of the Niagara Escarpment: with field trips*. Niagara Escarpment Commission with the assistance of the Ontario Heritage Foundation.

Turner, D., Lucieer, A., & de Jong, S. M. (2015). Time series analysis of landslide dynamics using an Unmanned Aerial Vehicle (UAV). *Remote Sensing*, *7*(2), 1736–1757. https://doi.org/10.3390/rs70201736

Turner, I. L., Harley, M. D., & Drummond, C. D. (2016). UAVs for coastal surveying. *Coastal Engineering*, *114*, 19–24. https://doi.org/10.1016/j.coastaleng.2016.03.011

Van Dongen, M. (2017, December 28). Experts begin 'painstaking' study of failing Claremont Access walls. *The Hamilton Spectator*. https://www.thespec.com/news-story/7040741-experts-begin-painstaking-study-of-failing-claremont-access-walls/

van Veen, M., Hutchinson, D. J., Kromer, R., Lato, M., & Edwards, T. (2017). Effects of sampling interval on the frequency - magnitude relationship of rockfalls detected from terrestrial laser scanning using semi-automated methods. *Landslides*, *14*(5), 1579–1592. https://doi.org/10.1007/s10346-017-0801-3

Westoby, M. J., Brasington, J., Glasser, N. F., Hambrey, M. J., & Reynolds, J. M. (2012). "Structure-from-Motion" photogrammetry: A low-cost, effective tool for geoscience applications. *Geomorphology*, *179*, 300–314. https://doi.org/10.1016/j.geomorph.2012.08.021

WGMS. (2017). *Fluctuations of Glaciers Database*. World Glacier Monitoring Service. https://doi.org/10.5904/wgms-fog-2017-10

Williams, R. D(2012). DEMs of Difference. *Geomorphological Techniques*, *2*, 1–17.

Wolf, P. R., Dewitt, B. A., & Wilkinson, B. E. (2014). Terrestrial and Close-Range Photogrammetry. *Elements of Photogrammetry with Applications in GIS*, *114*.

Zhang, Z. (1994). Iterative point matching for registration of free-form curves and surfaces. *International Journal of Computer Vision*, *13*(2), 119–152.

Chapter Two: Detecting the imprint of fast ice flow on modern proglacial fields: an example from Mýrdalsjökull Ice Cap, southern Iceland

Abstract

Glacial deposits are important sources of paleoclimatic information but not all deposits are formed by processes that reflect the overall climatic conditions of a region; surge-type (fast-flowing) glaciers undergo periodic episodes of rapid ice movement, often unrelated to ambient climatic conditions. This study focuses on the identification of landscape features resulting from rapid ice flow on the forefields of Öldufellsjökull and western Sléttjökull, two surge-type outlet glaciers of the Mýrdalsjökull Ice Cap in southeast Iceland. Remotely sensed data and field investigations were combined to complete a landsystem analysis of the forefields at each of these glaciers and an uncrewed aerial vehicle (UAV) was used to collect high-resolution imagery of areas of particular interest. Two assemblages of landsystems are identified on each forefield, which pass from streamlined landforms containing abundant flutes close to the glacier, to spatially restricted bands of arcuate moraines with associated glaciofluvial and glaciolacustrine deposits more distally. This distribution of landsystem tracts has limited similarity to the current surge-type glacier landsystem model, suggesting that other processes are controlling the development of landform-sediment assemblages. Using a high-resolution digital elevation model of an area within the 1984 surge limit, three distinct landform types were identified that were not apparent on the coarse resolution imagery: hummocky moraine; a zig-zag sediment ridge interpreted as a concertina esker; and a circular feature hypothesized to have formed as a result of water escape caused by changing hydrological regimes during and after the active surge phase. The forefields of Öldufellsjökull and western Sléttjökull, lack many of the characteristics typical of surge-type landsystems and instead are more similar to the active temperate landsystem common in Iceland. The identification of landforms considered to be diagnostic of surge-type glaciers was only possible through a high-

resolution targeted survey and suggests that landforms may be overlooked in many investigations.

Keywords: Glacial geomorphology; Surge-type glacier; close-range photogrammetry; Iceland; landsystem analysis

2. 1 Introduction

The study of glacial deposits has provided important information for the reconstruction of past changes in climate and can provide critical information for understanding and refining models of future climate change. As climate continues to warm, it is important to have the ability to predict the response of modern ice sheets and ice caps to temperature change and to changes in ocean circulation patterns (Stokes et al., 2016). However, not all glacier types respond to external climatic forcing alone and their behavior may not accurately record climatic fluctuations (Meier and Post, 1969; Raymond, 1987; Carrivick et al., 2017). While many glaciers have steady flow rates that change in response to external forcing factors such as climate, some ice masses show differential and episodic changes in their rates of movement which are, at times, particularly fast and can be triggered by intrinsic factors (Hart, 1999; Farnsworth et al., 2016; Ingólfsson et al., 2016).

Surge-type glaciers, which periodically undergo sudden large-scale ice displacement resulting in glacier flow rates 10 or 100s of times faster than normal, and ice streams, narrow zones within an ice sheet that continuously flow much faster (>300 m/year) than the surrounding ice, are two examples of ice masses in which changes in velocity and extent are not always triggered by external factors (Raymond, 1987; Stokes and Clark, 1999; Stokes, 2018). It is therefore necessary to differentiate glacial landforms and sediments created from fast ice flow regimes, such as surge-type glaciers, from those created by glaciers responding to changes in climate, in order to better interpret the historical climatic and glaciological record (Sharp, 1988; Ingólfsson et al., 2016).

In a surge-type glacier, the surge cycle can be divided into two parts, the quiescence phase and the active surge phase. Each of these two phases has a relatively consistent

periodicity within a single glacier, although the periodicity varies widely between glaciers (Meier and Post, 1969; Sharp, 1988). The active phase of a surging glacier during which the ice moves rapidly, can last for less than one year up to 10 years, depending on the glacier (Raymond, 1987; Jiskoot et al., 2000; Striberger et al., 2011; Sevestre and Benn, 2015). The rate of ice flow during a surge can also vary dramatically depending on the glacier, with velocities of up to 100m/day having been recorded at multiple glaciers (Kamb et al., 1985; Ingólfsson et al., 2016). Surging glaciers represent an important mechanism for rapid ice drainage from an ice sheet or ice cap. Surge-type glaciers account for approximately 1% to 4% of the glaciers currently on Earth; their distribution is restricted to a few geographic regions, including Iceland, Svalbard, select ranges in western North America, areas of central Asian such as the Pamirs, and the Canadian Arctic (Jiskoot et al., 1998; Copland et al., 2003; Sevestre and Benn, 2015; Flink et al., 2017; Chudley and Willis, 2019).

In Iceland during the 1990's, glacial surges accounted for 25% of ice mass flux, despite the fact that only 14 glaciers experienced surges during that period (Ingólfsson et al., 2016); this resulted in thinning of the accumulation area of the major ice caps by 25-100m (Björnsson et al., 2003). The surging of an outlet glacier can result in significant changes to the geometry of the ice cap including changes to the location of ice divides as well as to the size and shape of the ice cap itself (Adalgeirsdóttir et al., 2005; Ingólfsson et al., 2016). Surging can also increase the rate of erosion and sediment transfer within the proglacial field and can impact the timing and magnitude of meltwater runoff due to changes in the subglacial hydrological system during surge periods (Carrivick et al., 2017).

The precise mechanism causing glaciers to surge is unknown, with many competing theories proposed (Clarke et al., 1984; Fowler, 1987; Kamb, 1987; Benn et al., 2019). It is evident from previous studies that basal sliding is an important mechanism by which surging glaciers move (Hambrey et al. 1996; Ingólfsson et al. 2016) and factors that affect rates of basal sliding are a focus of many of these theories. Hence, mechanisms for surge initiation are commonly linked to factors such as changing thermal regime (Sharp 1988; Jiscoot et al. 2000), changes in basal hydrology causing ice-bed decoupling (Kamb 1987;

Fuller and Murray 2002), and/or deformation of the substrate (Clarke et al. 1984; Fuller and Murray 2002; Ingólfsson et al. 2016). While basal sliding and basal ice characteristics are linked to surging behaviour there is no clear connection to climatic controls, although the periodicity of surges may be impacted by climatic variables (Sevestre and Benn 2015; Carrivick et al. 2016).

To better understand the physical processes occurring during a surge event many studies have investigated the geomorphological and sedimentological characteristics of the proglacial fields of surging glaciers. Some of the most commonly noted landforms resulting from surging behaviour include thrust block moraines, hummocky moraines, concertina eskers, crevasse squeeze ridges, flutes, and drumlins (Sharp, 1985b; Evans and Rea, 1999; Hart, 1999; Johnson et al., 2010; Schomacker et al., 2014; Farnsworth et al., 2016). With the exception of concertina eskers, each of these landforms can also be found within the proglacial fields of non-surging glaciers and therefore a single landform cannot be considered diagnostic of surging behaviour (Evans and Rea, 1999; Schomacker et al., 2014). However, a suite of landforms has been proposed as a landsystem representative of a surging glacier forefield (Evans and Rea, 1999; Schomacker et al., 2006, 2014; Jónsson et al., 2014). This landsystem consists of three distinct zones: Zone A, distal to the ice margin, comprises a zone of thrust block moraines; Zone B, is an intermediate zone dominated by glaciofluvial deposits including pitted outwash; and Zone C forms an inner zone of subglacial landforms (Schomacker et al., 2014; Ingólfsson et al., 2016). Interzonal elements found throughout the surging glacier forefield include ice-cored lake sediments, outwash, and overridden moraines (Evans and Rea, 2003).

Ice streams within ice sheets also exhibit rapid ice flow, similar to that of surging glaciers; however, ice streams also differ as they are continuously fast flowing and can maintain these rates for centuries, although some ice streams may switch periodically between fast and slow ice flow rates (Clarke, 1987; Stokes and Clark, 1999; Andreassen et al., 2014). As a consequence of their high rates of ice flow, ice streams provide an important mechanism for the rapid removal of ice and sediment from ice sheets, and account for 90% of the sediment and ice that is discharged from Antarctica (Stokes and Clark, 1999; Bennett,

2003; Winsborrow et al., 2010; Kyrke-Smith et al., 2015). It is expected that a similar proportion of ice and sediment discharge from the Laurentide Ice Sheet (LIS) and Scandinavian Ice Sheets (SIS) would have been caused by such ice streams in the past (Stokes et al., 2016). In order to reconstruct the impact of ice streams on paleo-ice sheet dynamics it is critical to identify and locate the former position of ice streams. Unfortunately, it is difficult to directly study the nature of proglacial and subglacial landform sediment-assemblages associated with modern ice streams due to the inaccessible environments in which they are generated. The use of accessible surge-type glaciers as analogues for paleo-ice streams can help identify features to delimit their extent and dynamics, especially in the study of land terminating paleo-ice streams (Evans and Rea, 1999; Schomacker et al., 2014; Ingólfsson et al., 2016).

This paper examines the sediments and landforms produced by two surge-type modern Icelandic glaciers, Sléttjökull and Öldufellsjökull, the only two glaciers on the Mýrdalsjökull Ice Cap that have recorded surge behaviour. Using high-resolution surveying techniques, the landform-sediment assemblages identified across the proglacial fields and within distinctive surge zones produced by each glacier, will be compared in order to discriminate distinctive signatures and diagnostic landforms of the surge events.

2.1.1 Study Area

The study area is focused on two outlet glaciers, Sléttjökull and Öldufellsjökull on the northern margin of the Mýrdalsjökull Ice Cap, in southern Iceland (Figure 2.1A-D). Iceland has a relatively mild oceanic climate, due to the influence of the warm Irminger Current, which has allowed the development of warm-based or temperate ice caps. These ice masses have high meltwater outputs and more dynamic changes in glacier form and extent in comparison with ice masses developed in areas with more severe polar climates (Björnsson and Pálsson, 2008; Hannesdóttir et al., 2015).

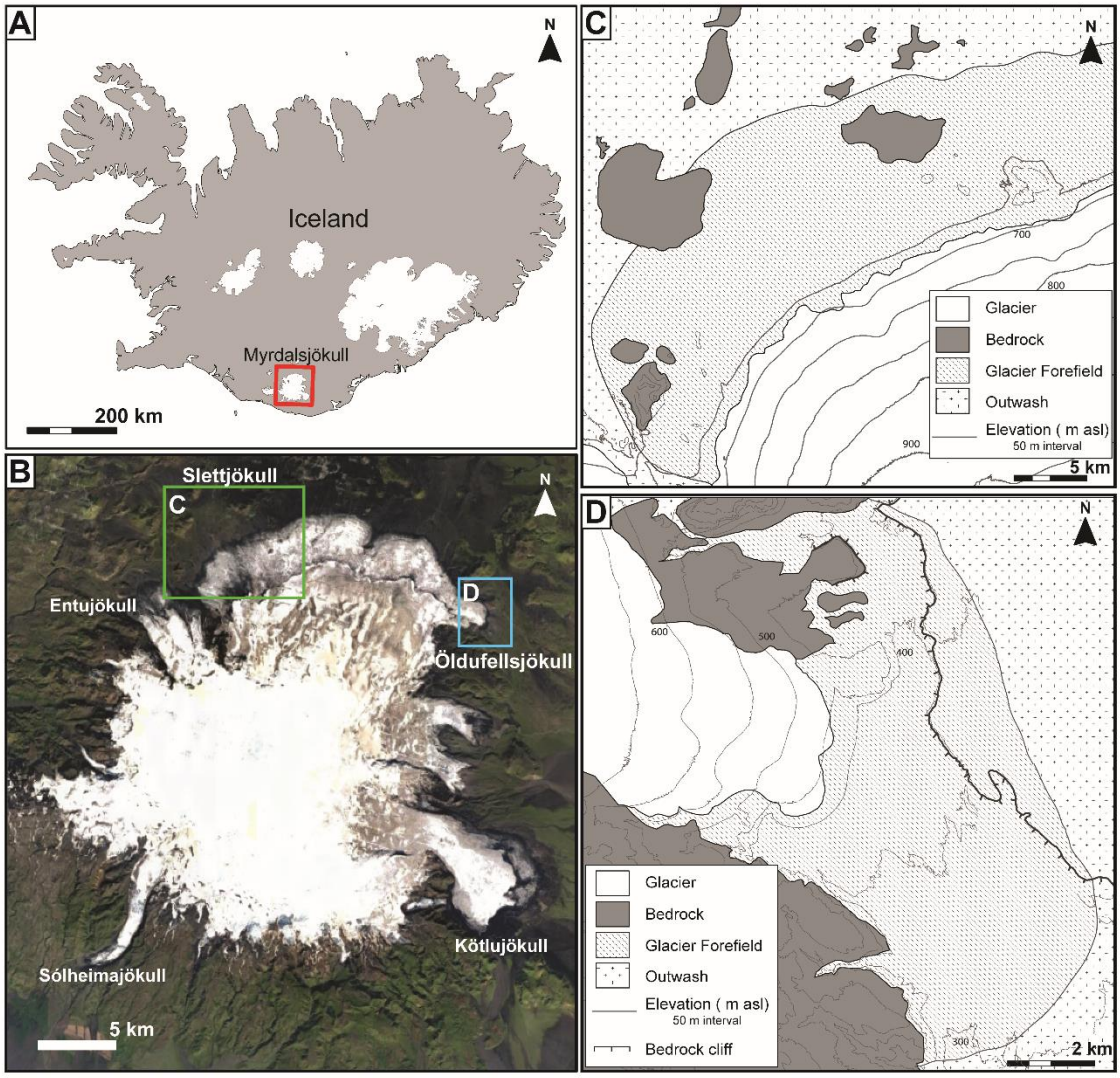

Figure 2.1: A) Location of the Mýrdalsjökull Ice Cap (red box) in southern Iceland; B) Sléttjökull (box C) and Öldufellsjökull (box D), outlet glaciers located on the northern margin of Mýrdalsjökull; Detailed maps of the study areas at Sléttjökull (C) and Öldufellsjökull (D).

Mýrdalsjökull is the second smallest ice cap in Iceland with an area of approximately 590 km^2 and an average thickness of 240 m in 2004 (Óladóttir et al., 2008; Mayer et al., 2017). It is underlain by Katla, a large composite volcano which is up to 1500 m in elevation (Sturkell and Sigmundsson, 2003). Its location in southern Iceland has the highest mean annual temperature within the country as well as high rates of precipitation (Sigurðsson, 2003). The main outlets for the Mýrdalsjökull glacier are Kötlujökull, Entujökull, Sólheimajökull and Sléttjökull (Figure 2.1B; Sturkell et al., 2010)

Table 2.1: Glacier characteristics of Sléttjökull and Öldufellsjökull. The metrics of Sléttjökull include the entire glacier, while the western margin is the area of interest in this study (WGMS, 2017).

	Sléttjökull	**Öldufellsjökull**
Area (km^2)	112	43
Maximum elevation (m asl)	1362	1395
Minimum elevation (m asl)	340	340
Slope (º)	5.5	7.9

Sléttjökull drains the northwestern margin of the Mýrdalsjökull Ice Cap and has a total area of 112 km^2 (Table 2.1 and Figure 2.1C; WGMS, 2017). It is a complex outlet glacier, consisting of a single lobe with a margin 21 km in length that is fed by three drainage sub-basins (Mayer et al., 2017). Öldufellsjökull is a smaller glacier, located to the east of Sléttjökull and has an area of only 43 km^2 (Table 2.1 and Figure 2.1D; WGMS, 2017). The lateral margins of Öldufellsjökull and Sléttjökull are not clearly defined and the ice masses have been considered as a single outlet glacier or as separate glaciers in different studies (Björnsson et al., 2000; Mayer et al., 2017); for this research, the two glaciers are considered to be separate outlet glaciers of the ice cap. Öldufellsjökull and the western sub-basin of Sléttjökull are the only outlet glaciers of the Mýrdalsjökull Ice Cap to have documented surges (Björnsson et al., 2003), although Kötlujökull is proposed to have surged in the past (Þórarinsson, 1957; Evans et al., 2018).

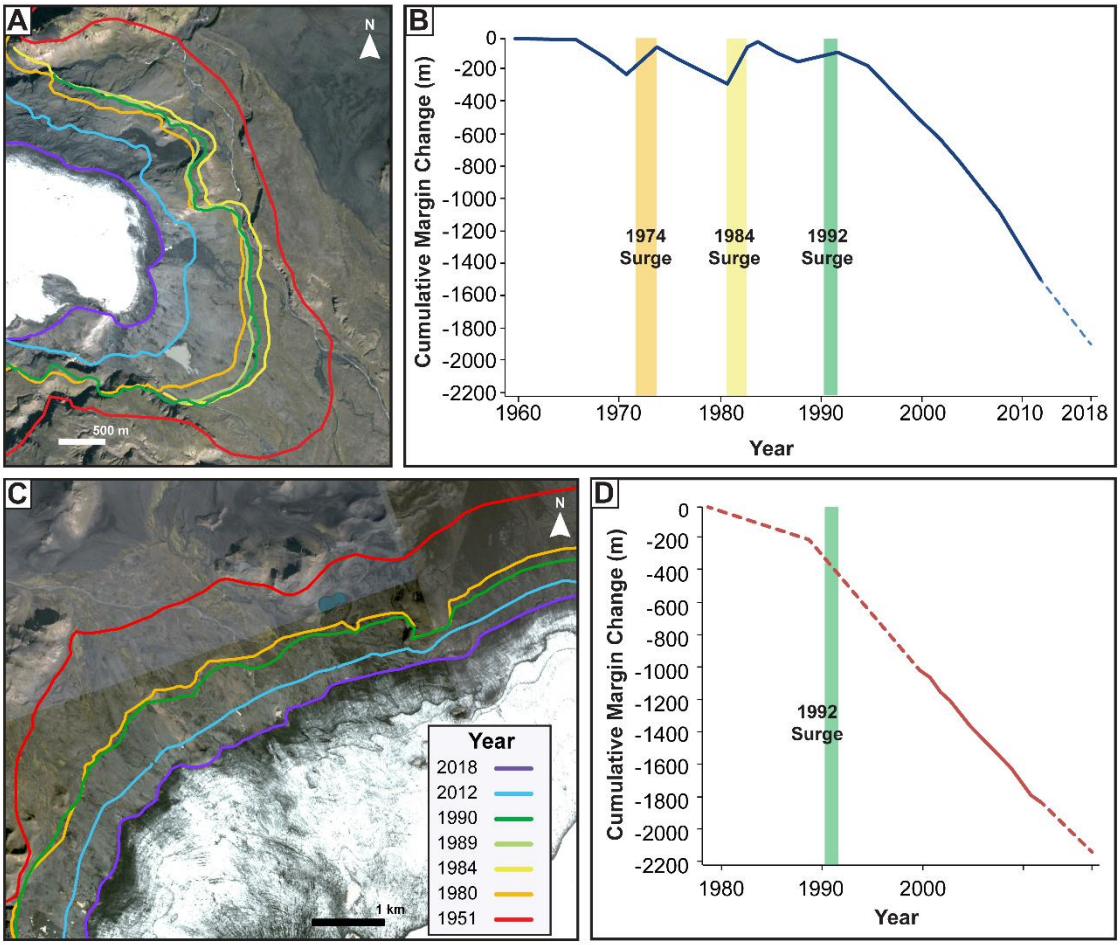

Figure 2.2: A) Map of margin change at Öldufellsjökull based on aerial imagery; B) Graph of the change in the margin at Öldufellsjökull showing the overall retreat of the glacier margin since the early 1960s. The timing of known surges are highlighted; note change in margin position immediately after each surge. Data obtained from the WGMS (2017); C) Map of margin change at Sléttjökull based on aerial imagery (Army Map Service, 1951; Landmælingar Islands, 1980a, 1980b, 1984, 1989, 1990; Google Earth, 2019); D) Graph of the change in the margin at Sléttjökull showing the overall retreat of the glacier margin since the early 1980s. The time of the known surge is shown by a green bar although no margin advance is evident in the recorded data. Data obtained from the WGMS (2017).

The margins of both Sléttjökull and Öldufellsjökull have shown an overall retreat since observations of the glaciers began in the early 19th century, a similar trend to that shown by other glaciers in southern Iceland (Hannesdóttir et al., 2015; Evans et al., 2018; Lee et al., 2018). Öldufellsjökull has relatively well documented records of ice margin

position, beginning in 1961. From these records, the 3 recorded surges in 1974, 1984 and 1992 can be identified on a temporal map of glacier margin position, as well as on graphs showing the cumulative margin changes (Figure 2.2A,B). It can be noted that the ice margin remained in a similar position for multiple decades, in part as a result of the forward movement of the margin generated by the 3 surges (Figure 2.2A,B). The velocity of the 3 surging events at Öldufellsjökull is unknown but can be estimated from the change in margin position to be at least 200 m/year during the 1984 surge. Additionally, there are aerial images of Öldufellsjökull prior to and during this surge event, which show the characteristic changes in the glacier surface topography from relatively smooth to highly crevassed (Figure 2.3; Meier and Post, 1969; Farnsworth et al., 2016; Evans et al., 2018). Relatively little is known about the margin changes at Sléttjökull during surge events (Figure 2.2C,D); the only known surge at the glacier occurred in 1992 and the impact on the position of the margin is not reflected on the margin change graph or maps due to a lack of measurements at this glacier.

The focus of previous studies of Sléttjökull have been on the central and eastern sub-basins where the pattern of retreat and landforms within the forefield reflect a non-surge type glacier. The forefield generated by the non-surging ice consists of a proximal streamlined till plain up to 2 km wide which exhibits flutes and drumlinized features and is surrounded by a series of more distal end moraines (Kjær et al., 2004; Schomacker et al., 2010). The moraines are interpreted to record the LIA maximum of Sléttjökull at the end of the 19th century (Krüger et al., 2010). Beyond the end moraines is an extensive outwash plain (Krüger, 1988; Kjær et al., 2003; Schomacker et al., 2010). Unfortunately, no studies have examined the proglacial field of the western basin of Sléttjökull. The proglacial field of Öldufellsjökull is reported to be composed of two areas of densely spaced moraines, divided by large regions of fluted terrain (Evans et al., 2018).

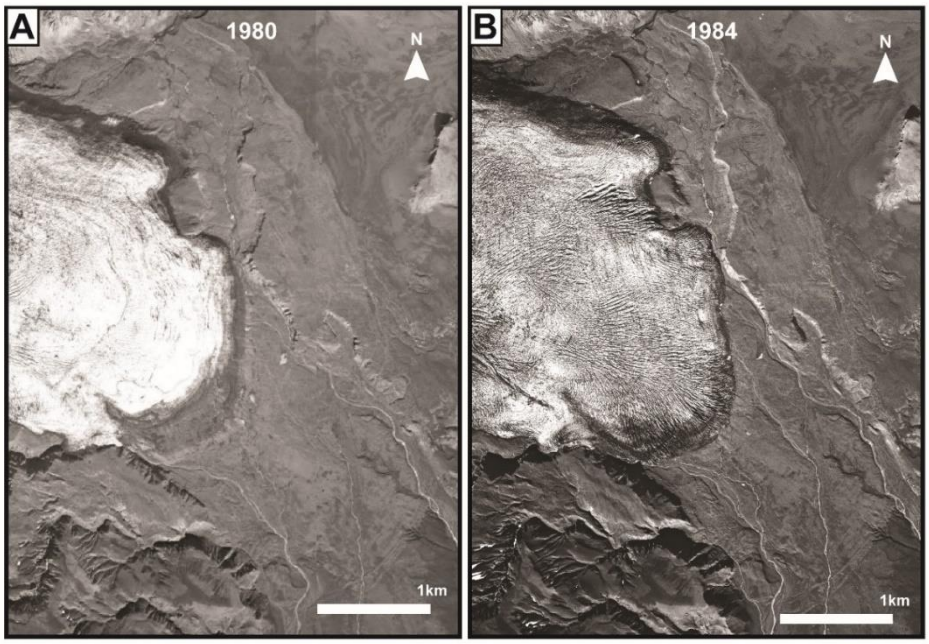

Figure 2.3: Aerial imagery collected of Öldufellsjökull in 1980 before the surging event (A) and in 1984 during the surging event (B) (Landmælingar Islands, 1980b, 1984). The imagery clearly shows the change from a relatively smooth glacial surface in 1980 to a highly crevassed glacial surface in 1984, a feature characteristic of actively surging glaciers.

2. 2 Methods

Documentation of the sediments and landforms on the glacial forefields of Sléttjökull and Öldufellsjökull was conducted using a combination of remotely sensed and sedimentological data collected in the summer 2018 field season. Initial planning for field work was completed using historical imagery (Figure 2.4; (AMS, 1951; Landmælingar Islands, 1980a, 1980b, 1984, 1989, 1990) and modern aerial photography (Planet Team, 2017; Google Earth, 2019). Preliminary geomorphological maps were compiled for each of the glacier forefields using these data, and areas of interest for field investigation were identified. Field data collection included sedimentological and geomorphological observations and measurements, as well as the collection of Uncrewed Aerial Vehicle (UAV) based aerial surveys.

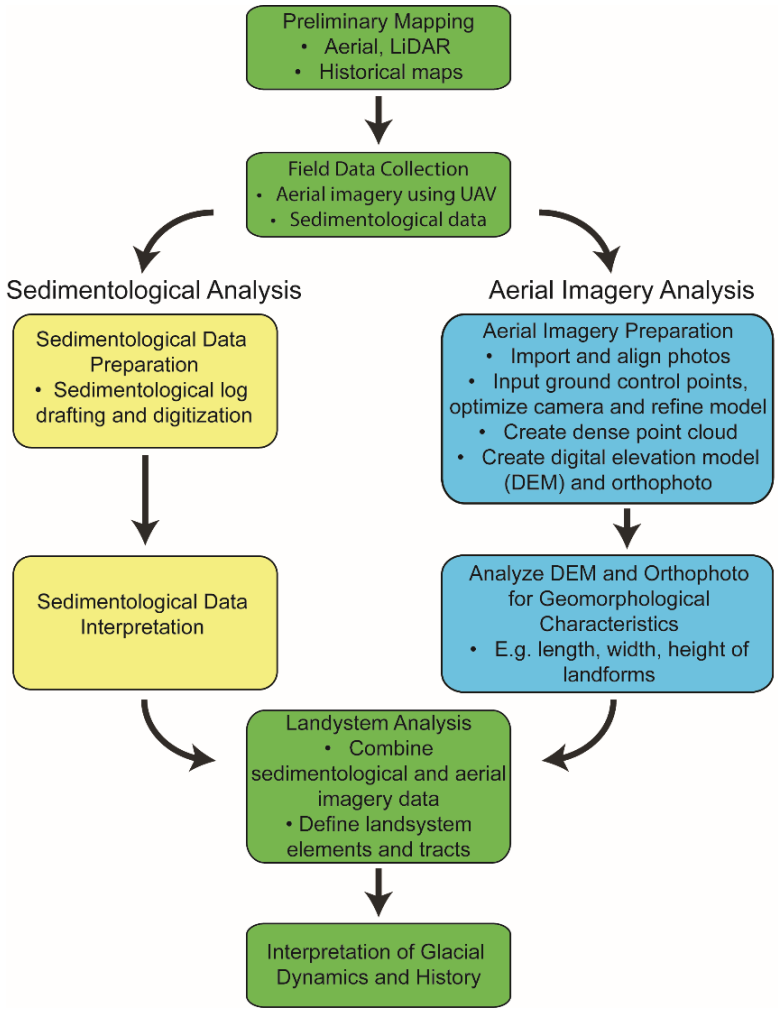

Figure 2.4: Depiction of the workflow applied in this study to analyze the glacial forefields of Sléttjökull and Öldufellsjökull.

Sediment characteristics, such as sediment type, grain size, bed thickness, and sedimentary structures were identified during field work from surface exposures and stream cuts on the proglacial fields. Where feasible, sedimentological logs were documented in areas of interest and where sufficient exposures were available or where pits could be dug (Figure 2.5). Ground-truthing of the preliminary mapped geomorphology was completed, and the location and dimensions of the morphological characteristics of landforms recorded.

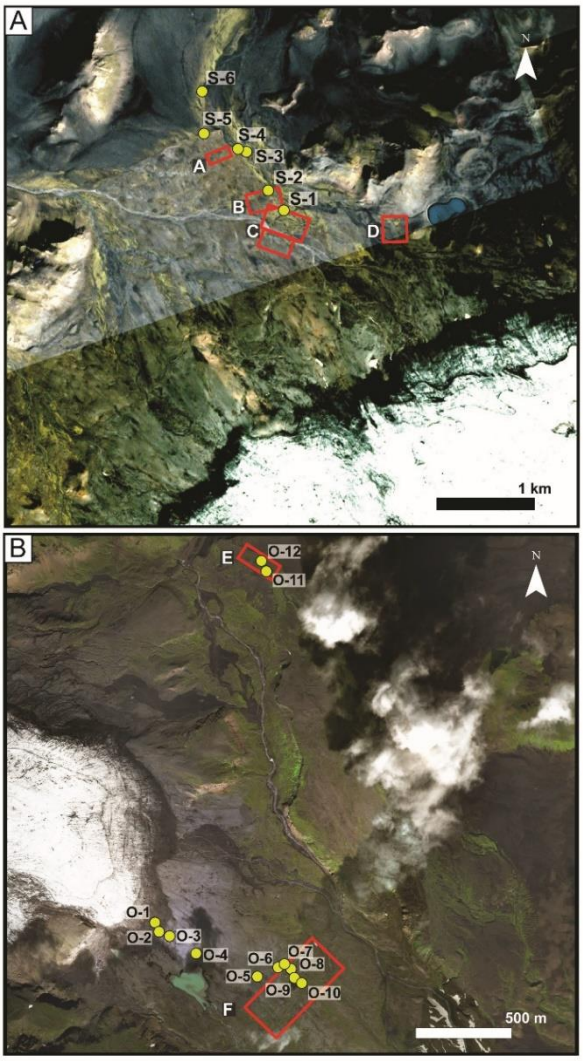

Figure 2.5: Map of the location of UAV-based aerial surveys (outlined in red) and sedimentological logs (yellow dots) at Sléttjökull (A) and Öldufellsjökull (B) (imagery from ESRI 2019).

The focus of the UAV derived aerial surveys was to document the characteristics of the proglacial field that were impacted by and/or were proximal to the known surge events identified from the historical aerial imagery. At Sléttjökull five UAV survey sites were documented and at Öldufellsjökull two UAV surveys were completed (Figure *2.5*). Aerial imagery was collected using a DJI Phantom 4 Advanced with an attached 24-megapixel camera which allowed geotagging of each of the images using the internal GPS

of the UAV which has an error of up to 1.5 m. The surveys were planned and completed using Pix4D capture, flying grid surveys to ensure sufficient overlap of imagery for model creation. The UAV was flown at a height of 30 m above the home point, collecting imagery with an approximate resolution of 1.8 cm. Ground control points (Table 2.2) were collected using an SX Blue II GNSS receiver (average error on site less than ~0.5 m) prior to the UAV imagery collection for each survey to improve accuracy of the final models.

Table 2.2: Description of the location and size of UAV-based surveys completed in the proglacial fields of Öldufellsjökull and Sléttjökull. Location of surveys indicated on Figure 2.5.

		Location	Approximate Size	Number of GCPs
Sléttjökull	**Survey A**	Region proximal to the LIA moraine	0.026 km^2 (260 m by 100 m)	6
	Survey B	Located in the streamlined region between the LIA moraines and the surge moraines	0.07 km^2 (350 m by 200 m)	8
	Survey C	Located in the streamlined region and outwash between the LIA moraines and the surge moraines	0.17 km^2 (325 m by 175 m and 450 m by 250 m)	8
	Survey D	Area located just beyond the 1990 glacier margin location, likely an area that experienced the ~1992 surge	0.063 km^2 (250 m by 250m)	8
Öldufellsjökull	**Survey E**	Area located just beyond the recorded surge maximums	0.32 km^2 (800 m by 400 m)	12
	Survey F	Region that was impacted by the 1978 and 1984 surge events	0.12 km^2 (400 m by 300 m)	10

Data processing was completed using Agisoft Metashape Professional (Agisoft Metashape, 2020), one of the most commonly used Structure from Motion modelling software packages (Ely et al., 2017; Hart et al., 2018). The data processing methodology used was similar to that of other studies and the established Agisoft workflow for terrain model generation (Figure 2.4; e.g. Westoby et al., 2012; Evans et al., 2015a; Ely et al., 2017). For each of the surveys, images were input into Metashape as a single unit and aligned using the highest accuracy settings. Ground control points (GCPs) were identified on the images and the images were aligned again, using the GCPs to increase accuracy. The final set of aligned points were refined, removing any points with a reprojection error greater than 0.5 pixels, and were used to create a dense point cloud. From the dense point cloud, a mesh, DEM and orthophoto were created to be used in the analysis (Figure ??). The DEM and orthophoto each have a resolution of 2 cm and the approximate vertical resolution of the DEM is 2 -3 cm. These relatively high-resolution DEMs were critical for mapping relatively small landsystem elements in areas of known surge activity that were not visible on the coarser resolution DEM created from historical imagery.

A final geomorphological map of the entire proglacial field was compiled using the LiDAR derived DEM (Figure 2.6 and Figure *2.7*; Icelandic Meteorological Office and Institute of Earth Sciences, 2013) and included observations of geomorphological features and their underlying sedimentary characteristics obtained during the field season. High-resolution mapping was completed in the areas of the UAV-based surveys (Figure 2.8). The higher resolution of the UAV-based imagery allows for the delineation of smaller, lower relief landforms which were undetectable using the LiDAR-derived DEM (Figure 2.9). Hillshade images were created from each of the DEMs at different azimuths (225° and 315°) and using Multi-directional Oblique Weighting (MDOW) to reduce azimuth bias when mapping landforms (Smith and Clark, 2005). Landform morphology characteristics (e.g., length, height) were calculated from the DEM, when resolution allowed.

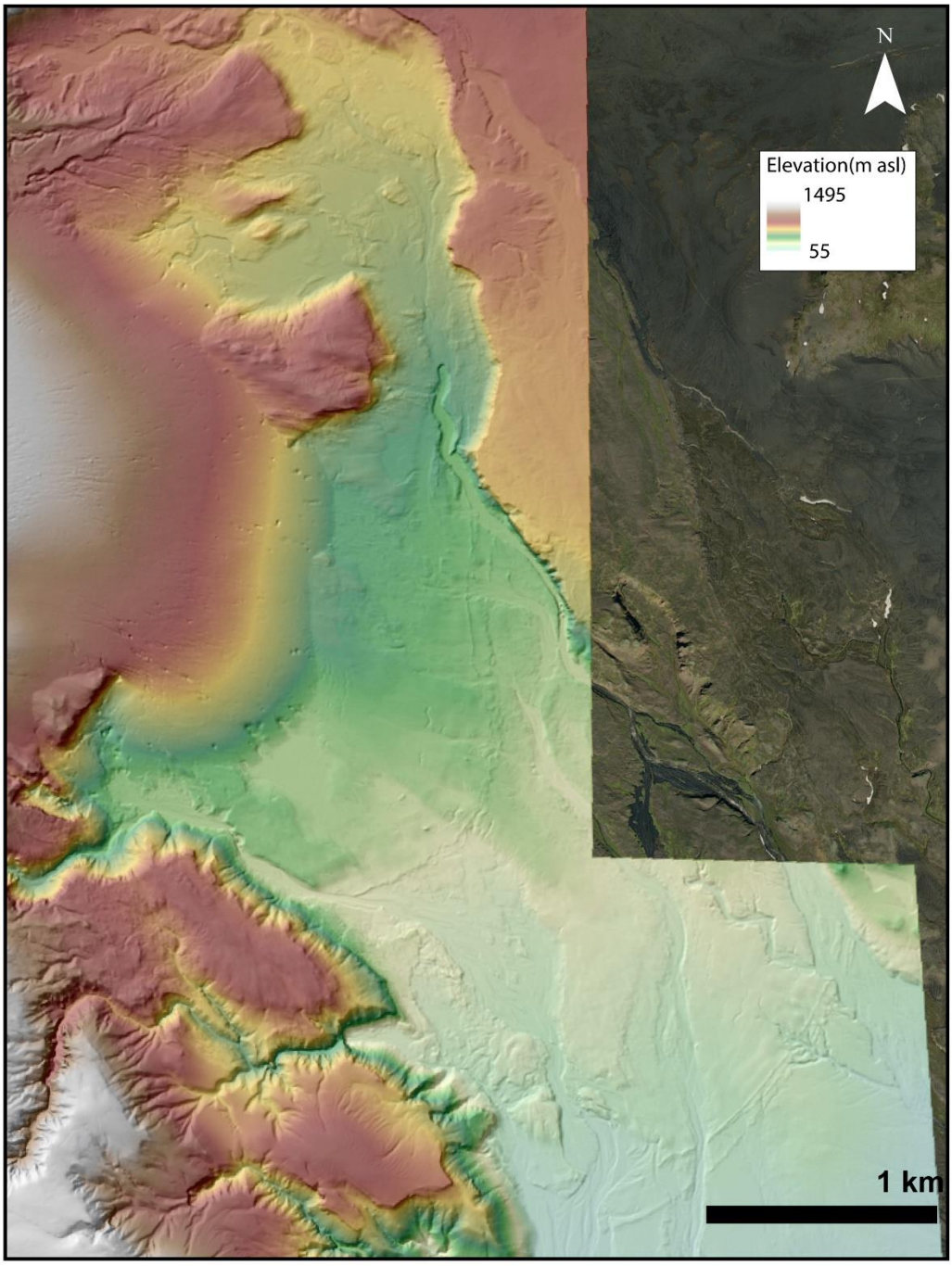

Figure 2.6: LiDAR derived DEM (5 m resolution) overlain on a hillshade model of the Öldufellsjökull proglacial field (Icelandic Meteorological Office and Institute of Earth Sciences, 2013). Aerial imagery (ESRI 2019) shown in areas where LiDAR cover was not present.

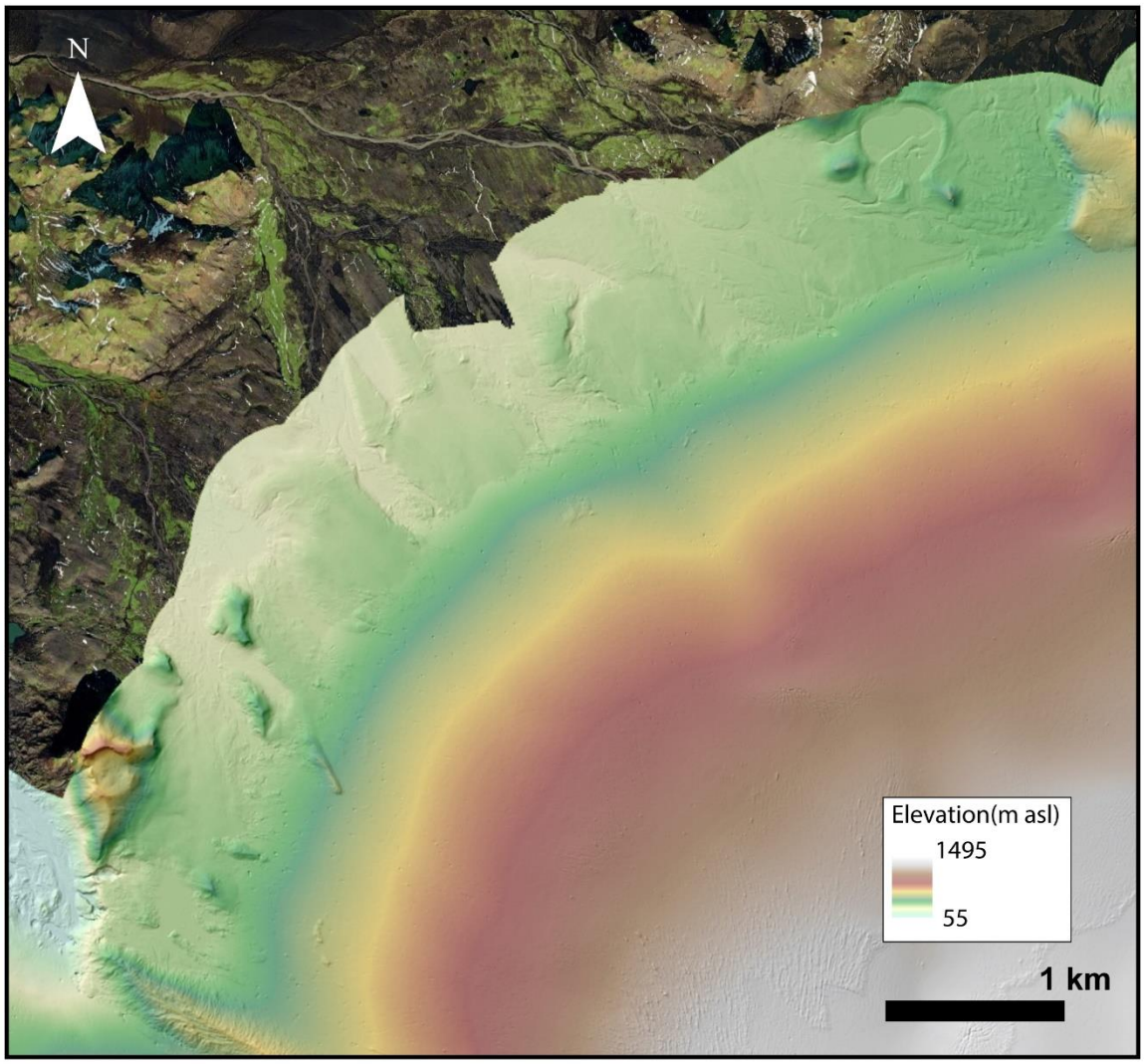

Figure 2.7: LiDAR derived DEM (5 m resolution) overlain on a hillshade model of the Sléttjökull proglacial field (Icelandic Meteorological Office and Institute of Earth Sciences, 2013). Aerial imagery (ESRI 2019) shown in areas where LiDAR cover was not present.

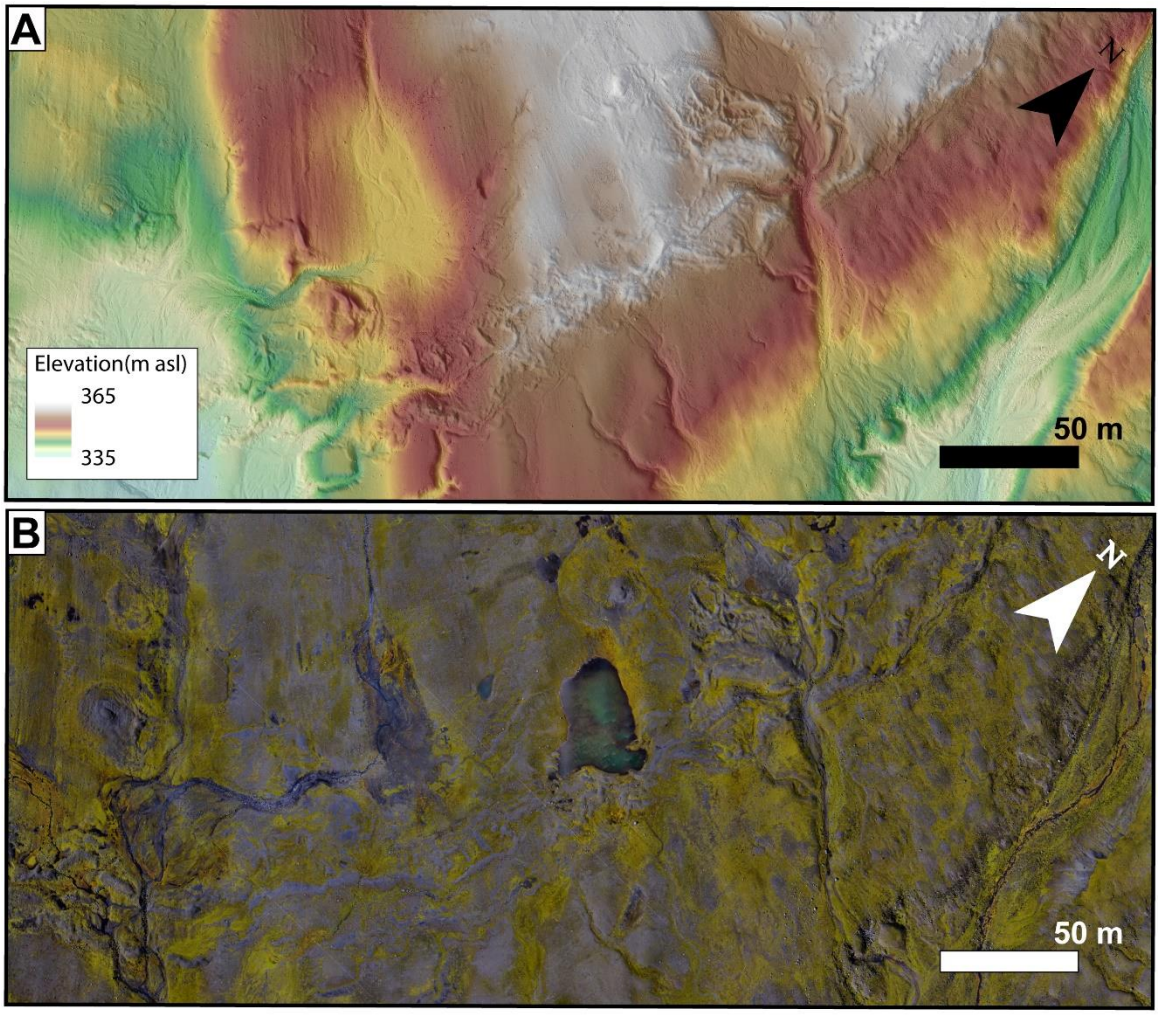

Figure 2.8: Survey F, Öldufellsjökull; an example of a high-resolution (2 cm) DEM overlain on a hillshade model (Icelandic Meteorological Office and Institute of Earth Sciences, 2013) (A) and orthophoto (B) produced using UAV-based photogrammetry of the forefield. Each of the UAV-based surveys had the same 2 cm resolution.

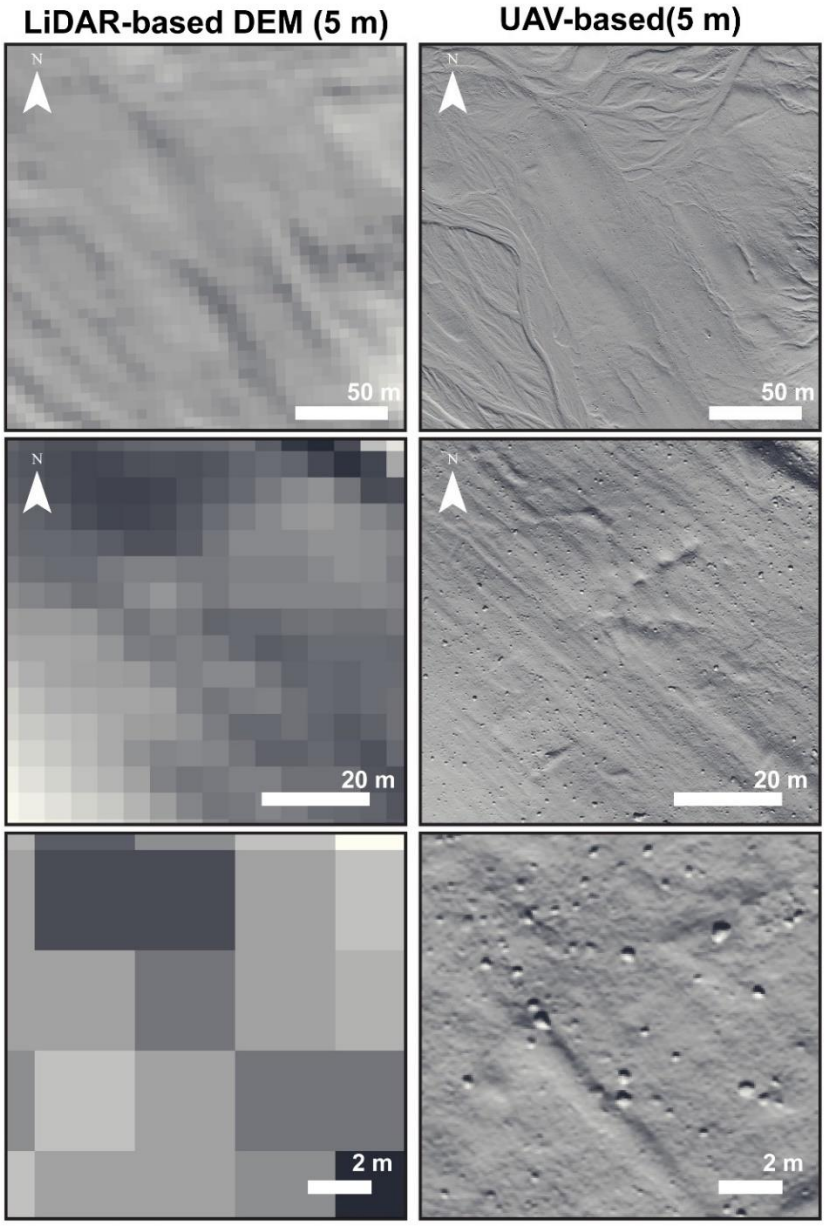

Figure 2.9: Comparison of the resolution and interpretability of landforms using hillshade models derived from the 5 m LiDAR-based DEM (Icelandic Meteorological Office and Institute of Earth Sciences, 2013) and the 2 cm UAV-based DEM. The UAV-based imagery is able to delineate much smaller landforms and as the zoom increases, the legibility remains when the LiDAR-based hillshade models become pixelated. The upper image shows the majority of Survey E and the middle and lower images show parts of Survey F of the Öldufellsjökull forefield (see Figure 2.5B).

Using a landsystems approach, the geomorphological and sedimentological data were combined, to determine landsystem elements, process-form relationships, and to identify the imprint of fast ice flow at these glacier margins. Landsystem analysis is a hierarchical method of analysis that utilizes geomorphological and sedimentological information to develop a holistic understanding of process-form relationships and landscape development (Eyles, 1983; Evans, 2003). Using this methodology, landform-sediment assemblages can be grouped into landsystem tracts which record larger suites of processes occurring within the system. The distribution and type of landsystem tracts can then combined to define a landsystem that represents the overall dynamics of the glacial system. The landsystem approach has been widely applied in glacial geomorphological studies and a repository of landsystems representing differing glacial dynamics, such as active temperate (e.g. Evans & Twigg, 2002; Chandler et al., 2015, 2020), surging (e.g. Evans & Rea, 2003; Kjær et al., 2008), and the margins of the paleo ice sheets (Alexanderson et al., 2002; Colgan et al., 2003; Kehew et al., 2012) have been created. This study will determine whether the existing surge-type glacier landsystem is identifiable at the Sléttjökull and Öldufellsjökull margins, and if there are additional small-scale landforms identifiable on high-resolution imagery which can be included in the surge-type landsystem model to enhance its diagnostic features.

2. 3 Results

The forefields of Öldufellsjökull (Figure 2.10) and Sléttjökull (Figure 2.11) can each be divided into five main landsystem tracts comprising arcuate moraines, streamlined terrain, hummocky topography, glaciofluvial, and glaciolacustrine. The distribution of these tracts is similar on both glacier forefields and will be discussed together. The UAV-based survey conducted within the limits of the three surges at Öldufellsjökull (survey F) will be discussed separately as it exhibits characteristics with significant implications for fast ice flow imprint.

2.3.1 Landsystem Tracts

2.3.1.1. Arcuate Moraine Landsystem Tract

The arcuate moraine landsystem tract is found primarily in two distinct bands within the two glacier forefields (Figure 2.10 and Figure 2.11). The distal band of arcuate moraines delimits the extent of the glacier forefield and is likely related to maximum glacier advance during the Little Ice Age (LIA). Although there are no specific dates associated with these glacial landforms, the terminal moraines in many, if not most of the glacier forefields in Iceland, are associated with the LIA maximum (e.g. Schomacker et al., 2014; Hannesdóttir et al., 2015; Lee et al., 2018). The second band of arcuate moraines on each forefield is located more proximal to the glaciers and is related to the maximum extent of the known surges at both glaciers. Across the rest of the forefield there are scattered small moraines up to 4 m in height and less than 100 m in length (Figure 2.10 and Figure 2.11).

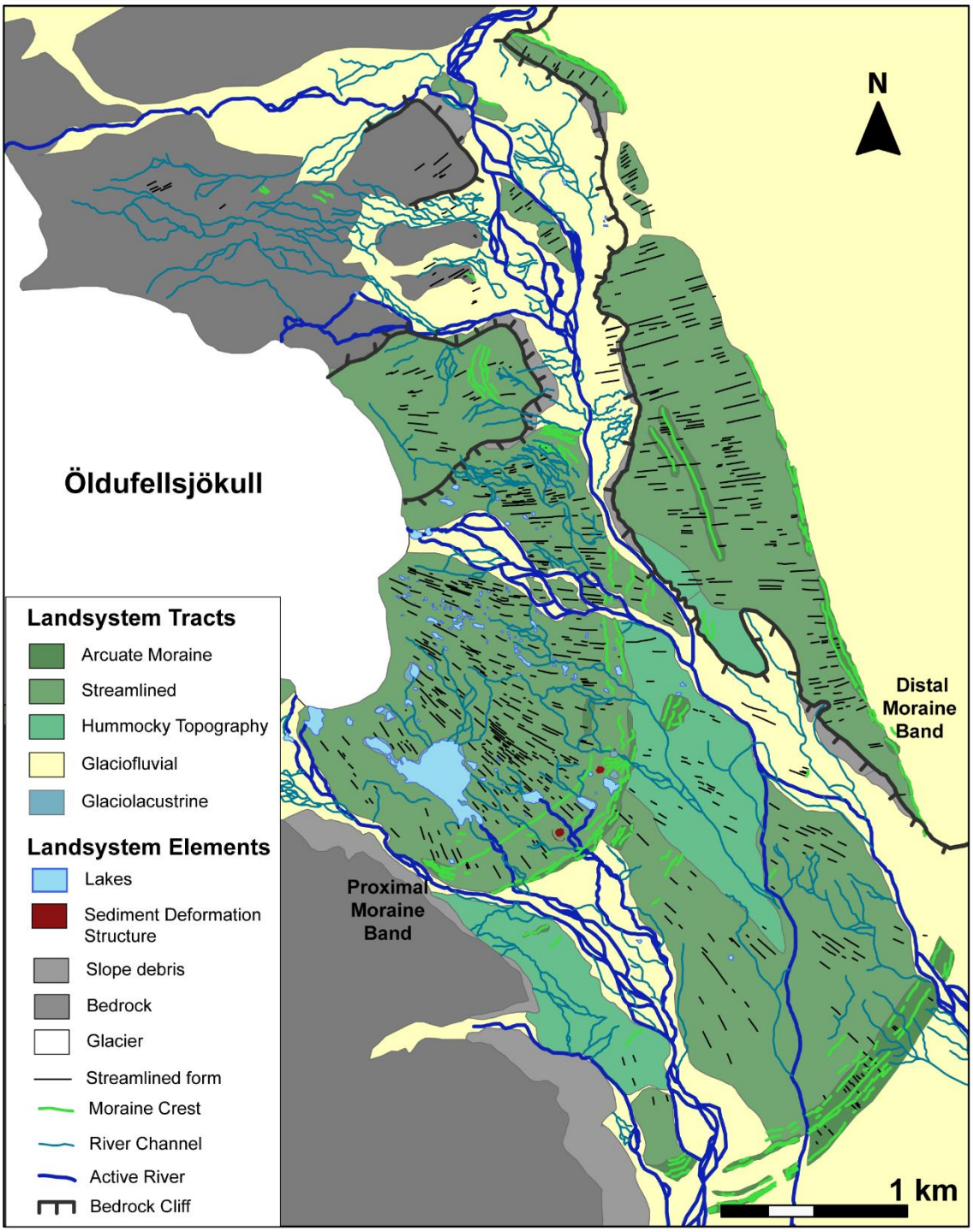

Figure 2.10: Geomorphological map of the forefield of Öldufellsjökull based on interpretations of LiDAR-based 5 m DEM (Icelandic Meteorological Office and Institute of Earth Sciences, 2013), recent aerial imagery (Google Earth 2019; ESRI 2019), and field observations.

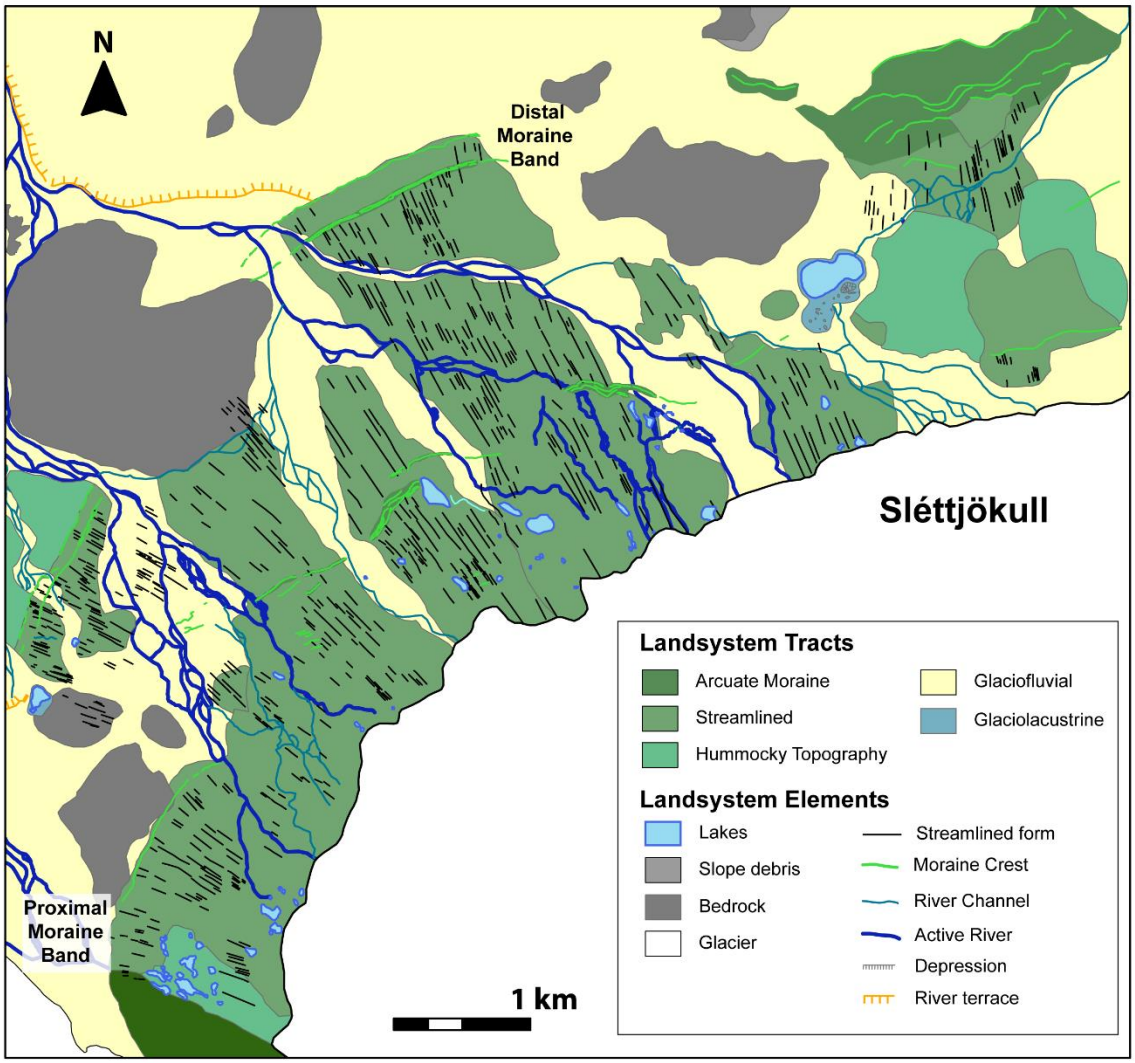

Figure 2.11: Geomorphological map of the forefield of western Sléttjökull based on interpretations of LiDAR-based 5 m DEM (Icelandic Meteorological Office and Institute of Earth Sciences, 2013), recent aerial imagery (Google Earth 2019; ESRI 2019), and field observations.

Table 2.3: Geomorphological characteristics recorded at each glacier in the streamlined and moraine landsystem tracts. The metrics were recorded using the 5 m LiDAR based DEM and Google Earth imagery and from the high-resolution UAV-based imagery.

			Sléttjökull				Öldufellsjökull			
Landsystem Tract	**Landform**		**Dataset**	**Mean**	**Min**	**Max**	**Dataset**	**Mean**	**Min**	**Max**
Arcuate Moraine	Distal Moraine Band	Height	5 m DEM and Google Imagery	2.9	1.1	5.2	5 m DEM and Google Imagery	---	---	---
		Length		233.02	9.16	1650.26		78.07	3.34	497.43
		Width		---	---	---		---	---	---
		Shape		Asymmetrical, steep down ice				Asymmetrical, steep down ice		
		Height		---	---	---	UAV Surveys E – F	1.35	0.23	2.92
		Length		---	---	---		74.83	26.13	170.29
		Width		---	---	---		---	---	---
		Shape		---				Asymmetrical, steep down ice		
	Proximal Moraine Band	Height	5 m DEM and Google Imagery	2.1	0.9	7	5 m DEM and Google Imagery	1	0.8	4.2
		Length		166.75	13.99	885.46		75.56	3.79	766.27
		Width		---	---	---		---	---	---
		Shape		Asymmetrical, steep down ice				Asymmetrical, steep down ice		
		Height		---	---	---	UAV Surveys E – F	0.94	0.11	2.79
		Length		---	---	---		22.02	1.82	79.01
		Width		---	---	---		---	---	---
		Shape		---				Asymmetrical, steep down ice		
Streamlined	Flutes	Height	5 m DEM and Google Imagery	N/A	N/A	N/A	5 m DEM and Google Imagery	N/A	N/A	N/A
		Length		96.72	12.60	392.86		53.21	5.99	262.76
		Width		N/A	N/A	N/A		N/A	N/A	N/A
		Shape		Parallel sided				Parallel sided		
		Height	UAV Surveys A – D	0.10	0.025	0.93	UAV Surveys E – F	0.16	0.01	7.14
		Length		40.41	3.68	152.65		19.42	1.20	225.76
		Width		3.05	0.21	14.88		1.83	0.18	7.59
		Elongation Ratio		17.07	1.28	119.64		15.44	1.81	276.18
		Shape		Parallel sided; 20% up-ice boulder				Parallel sided; 55% up-ice boulder		
	Moraine	Height	UAV Surveys A – D	0.43	0.14	2.60		---	---	---
		Length		31.14	8.09	73.28		---	---	---
		Shape		Asymmetrical, steep up ice				---	---	---

At both Sléttjökull and Öldufellsjökull the arcuate moraines located in the distal bands are generally 2 – 3 m in height, but can reach up to 7 m, and exhibit an arcuate planform shape and an asymmetrical cross section, steeper down-ice (Figure 2.12A; Table 2.3). The moraines are composed predominantly of sand, with thin upper layers of diamict. At Sléttjökull, the 4 m high terminal moraine is composed of massive medium-grained sand (Sm) interbedded with thin gravel layers (Gm) overlain by multiple fining upwards sequences of horizontally laminated coarse- and fine-grained sands (Sh) (Log S-5, Figure 2.13A). The uppermost unit at this location is a massive to crudely stratified, matrix-supported diamict (Dmm, Dms) with bullet-shaped boulders embedded in the moraine surface (Figure 2.13A). The sediment observed in a more proximal moraine at Sléttjökull (S-2) in this landsystem tract is composed of interbeds of clay, fine to medium grained sand, and gravel (Fm(d), Sm, Gm; Figure 2.13B). The upper part of the moraine is composed of a fining upwards, coarse- to medium-grained sand (Sg) with a few larger clasts near the base (Figure 2.13B).

The more ice-proximal arcuate moraine landsystem tract identified on the forefields of both glaciers, is composed of lower amplitude moraines averaging 1 m and reaching a maximum of 4 m in height (Table 2.3). These moraines also have an arcuate planform shape and an asymmetrical cross-sectional profile with a steep down-ice slope (Figure 2.12B). The moraines are frequently streamlined, and bullet-shaped boulders are common on the up-ice side (Figure 2.12C).

An exposure through the end moraine of the ice-proximal arcuate moraine band at Öldufellsjökull is composed primarily of massive and crudely stratified matrix-supported diamicts with interbeds of sand containing poorly sorted rounded clasts close to the base (Figure 2.13C). The diamicts contain poorly sorted subrounded clasts which commonly show striations.

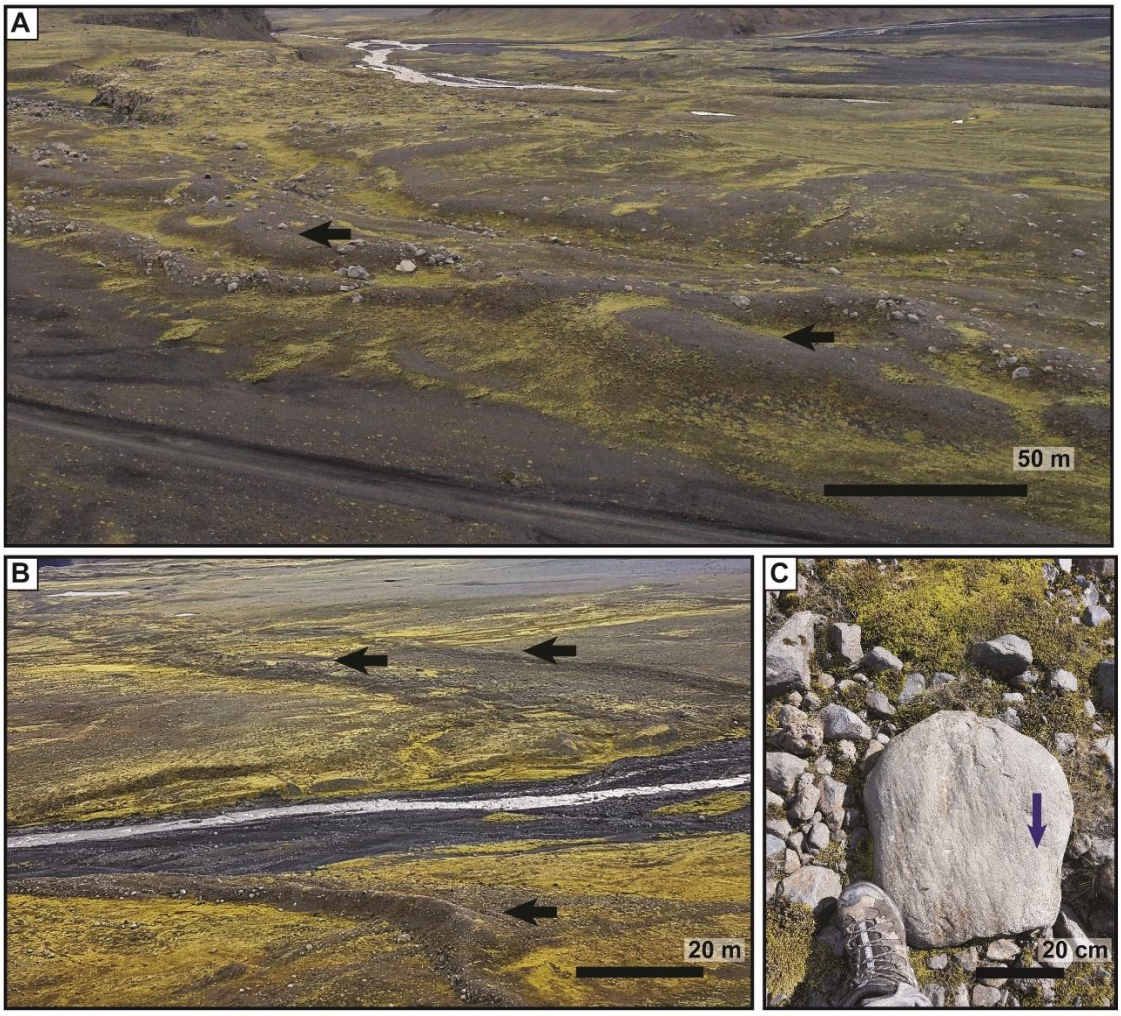

Figure 2.12: Images highlighting features of the arcuate moraine landsystems tract. A) Moraines in the distal moraine band located in the Öldufellsjökull forefield; B) Moraines in the proximal moraine band at Öldufellsjökull resulting from the known surging events; C) Bullet-shaped boulder found in the proximal moraine landsystem tract. Direction of ice flow indicated with the black arrows.

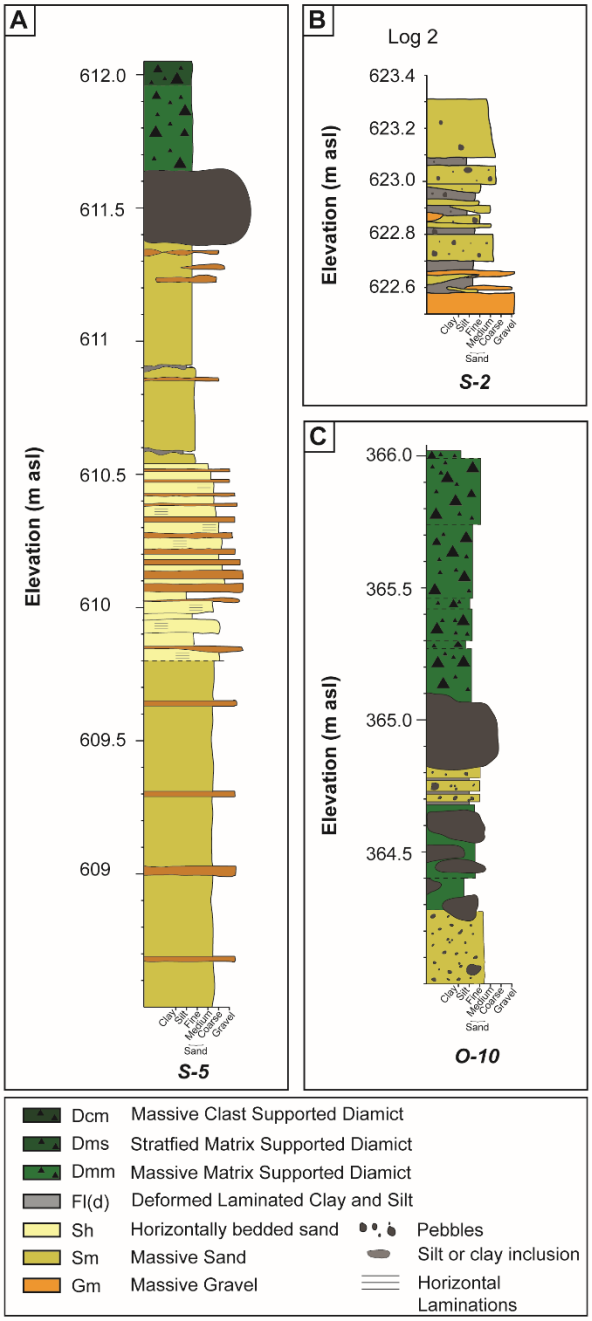

Figure 2.13: Sedimentological logs of exposures through the arcuate moraine landsystem tract. A) Sedimentological log from the terminal moraine in the western Sléttjökull forefield illustrating the predominance of interbedded sands and gravels with a veneer of diamict at surface; B) Sedimentological log through a smaller moraine in the distal moraine band at Sléttjökull showing interbedded sands, gravels, and clays; C) Sedimentological log of a moraine exposure in the proximal moraine band in the Öldufellsjökull forefield showing greater thicknesses of diamict. Location of logs is shown in Figure 2.5.

2.3.1.2. Streamlined Landsystem Tract

The streamlined landsystem tract dominates both glacier forefields, with more than half of the area displaying streamlined landforms dominated by flutes (Figure 2.10 and Figure 2.11). This landsystem tract has an overall smooth and low relief appearance, containing some features interpreted as overridden moraines, based on their flattened, ridge-like appearance and transverse to flow orientation (Figure 2.14A). Parallel sided flutes dominate and have an average length of 100 m and 53 m at Sléttjökull and Öldufellsjökull respectively; unfortunately, reliable widths and heights are not measurable using the 5 m resolution LiDAR-based DEM (Table 2.3). Using the high-resolution (2 cm DEM) imagery obtained with the UAV, the average length, height, and elongation ratio of the flutes at Sléttjökull are 40.4 m, 0.11 m and 17.1 respectively (Table 2.3), and approximately 20% of these flutes have identifiable up-ice boulders (Figure 2.14B; Table 2.3). At Öldufellsjökull, the flutes are, on average, slightly higher at 0.16 m, and the average length and elongation ratio are smaller at 19.42 m and 15.43 respectively; about half of these flutes have up-ice boulders.

When the glacier forefields are mapped using the 5 m resolution LiDAR-based DEM, few arcuate moraine ridges can be identified within the streamlined landsystem tract (Figure 2.10 and Figure 2.11). However, when high-resolution UAV surveys and geomorphological mapping was completed at Sléttjökull, low amplitude moraine ridges averaging only 0.44 m in height and 30 m in length can be identified (Table 2.3; Figure 2.9 and Figure 2.15A-D). The moraines are superimposed on the streamlined features and likely represent push moraines formed during the recession of the glacier margin. In general, these are arcuate in shape and exhibit primarily an asymmetrical cross-sectional profile, with a steeper up-ice slope. The low amplitude of these moraines makes them difficult or impossible to see on the coarser resolution imagery.

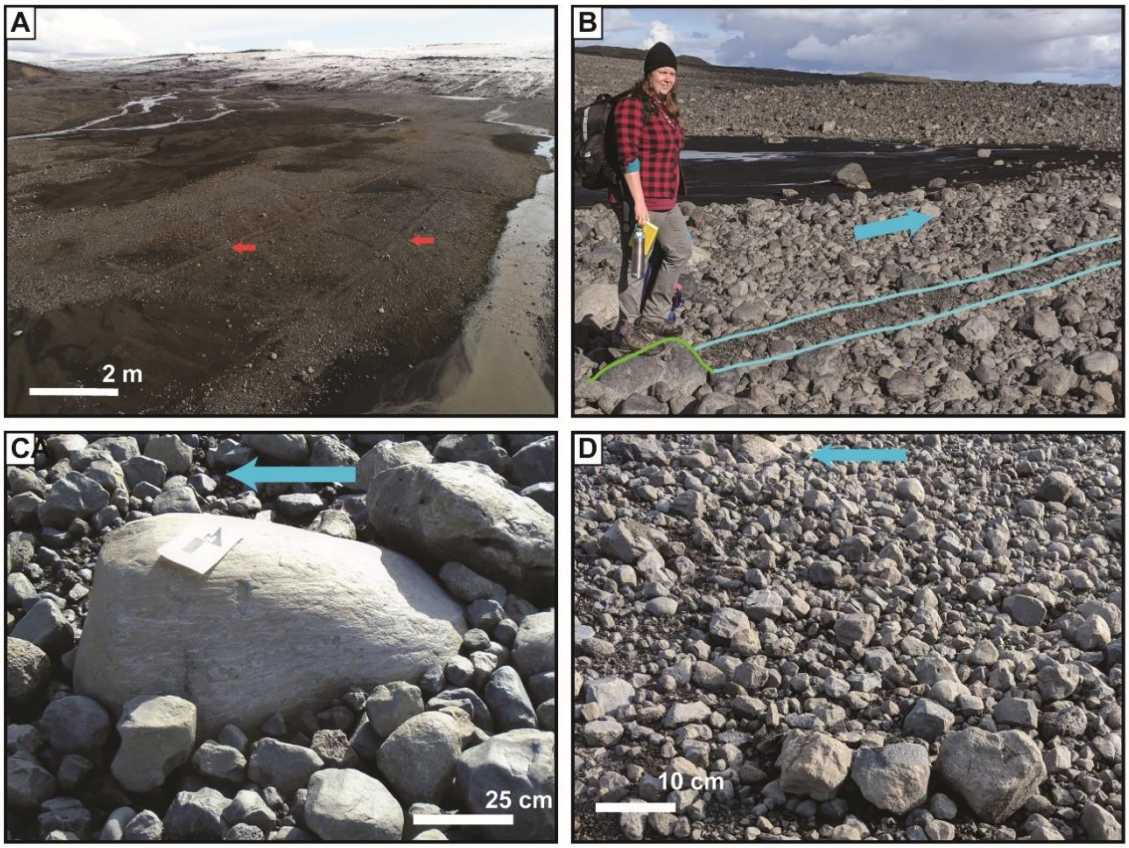

Figure 2.14: Features of the streamlined landsystem tract. A) Long flutes, indicated by the red arrows, found near the margin of western Sléttjökull; B) Parallel sided flute (outlined in blue) with an up-ice boulder (outlined in green) located in the Öldufellsjökull forefield. Direction of ice flow is indicated with the blue arrow; C) Bullet shaped boulder found in the streamlined landsystem tract. Direction of ice flow is indicated with the blue arrow; D) Boulder dominated area located more proximal to the ice margin at Öldufellsjökull. Direction of ice flow is indicated with the blue arrow.

Figure 2.15: Detailed geomorphological maps based on UAV surveys of the forefields of western Sléttjökull (A, B, C, D) and of the bedrock terrace at Öldufellsjökull (E). Location of the surveys is shown in Figure 2.5. An example of the high-resolution DEM and imagery of Survey F is shown in Figure 2.8.

The streamlined landsystem tracts of Sléttjökull and Öldufellsjökull are composed primarily of diamict interspersed with gravel and sand beds (Figure 2.16). A series of exposures through the streamlined landsystem tract proximal to the ice margin at Öldufellsjökull reveal four distinct diamict units (Unit O-D1 logs O-3, O-4, and O-5, Figure 2.16*C*) which vary in both clast and matrix content and the degree of stratification they show. Two of the diamict units (O-D2 and O-D3; Figure 2.16C) are separated by a unit of interbedded gravel and sand that thickens away from the ice margin. The surface of the streamlined landsystem tract at Öldufellsjökull is covered with boulders up to 0.5 m in size, some of which are bullet shaped (Figure 2.14C,D). Shallow pits dug into the streamlined landsystem tract located on top of the bedrock cliff at Öldufellsjökull expose massive matrix supported diamict (Dmm) with a fine sand matrix which is similar to Unit O-D2 in logs O-3, O-4 and O-5 (Figure 2.16B, C).

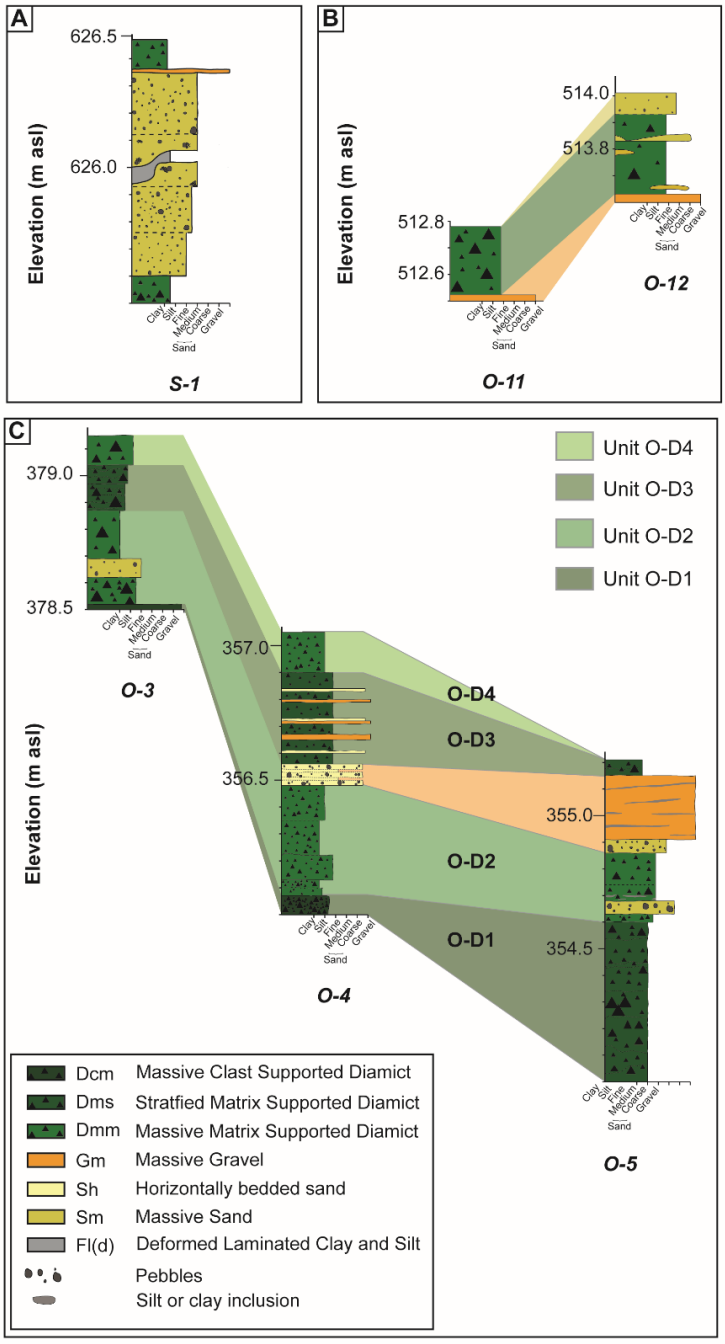

Figure 2.16: Sedimentological logs taken from outcrops in the streamlined landsystem tract. A) Log taken through a flute in the western Sléttjökull forefield composed primarily of sand; B) Correlation of facies between two logs recorded in the streamlined landsystem tract of the upper terrace area of the Öldufellsjökull forefield; C) Correlation of sedimentary units identified within 3 exposures through the streamlined landsystem tract at Öldufellsjökull showing the lateral continuity of diamict facies from ice proximal (0-3) to more distal (0-5) locations. Location of logs is shown in Figure 2.5.

2.3.1.3. Hummocky Topography Landsystem Tract

The hummocky topography landsystem tract is less extensive than either the arcuate moraine or streamlined landsystem tracts. At both Sléttjökull and Öldufellsjökull this tract is located just beyond the limits of the known surges, down-ice of the proximal moraine band (Figure 2.10 and Figure 2.11). Areas of hummocky topography are found most often within spatially restricted areas within 1 km of bedrock cliffs, medial moraines, or streamlined bedrock and sediment mounds, where supraglacial debris may have been sourced (Figure 2.10 and Figure 2.11).

The hummocks within this landsystem tract are low amplitude, primarily < 1 m in height (Figure 2.17A, B), and randomly distributed, although in some areas they form bands, crudely aligned parallel to ice flow direction (Figure 2.17A). Abundant waterfilled depressions occur within the hummocky topography landsystem tract, most notably in areas proximal to the modern glacier margin as can be seen on the western edge of Sléttjökull (Figure 2.11).

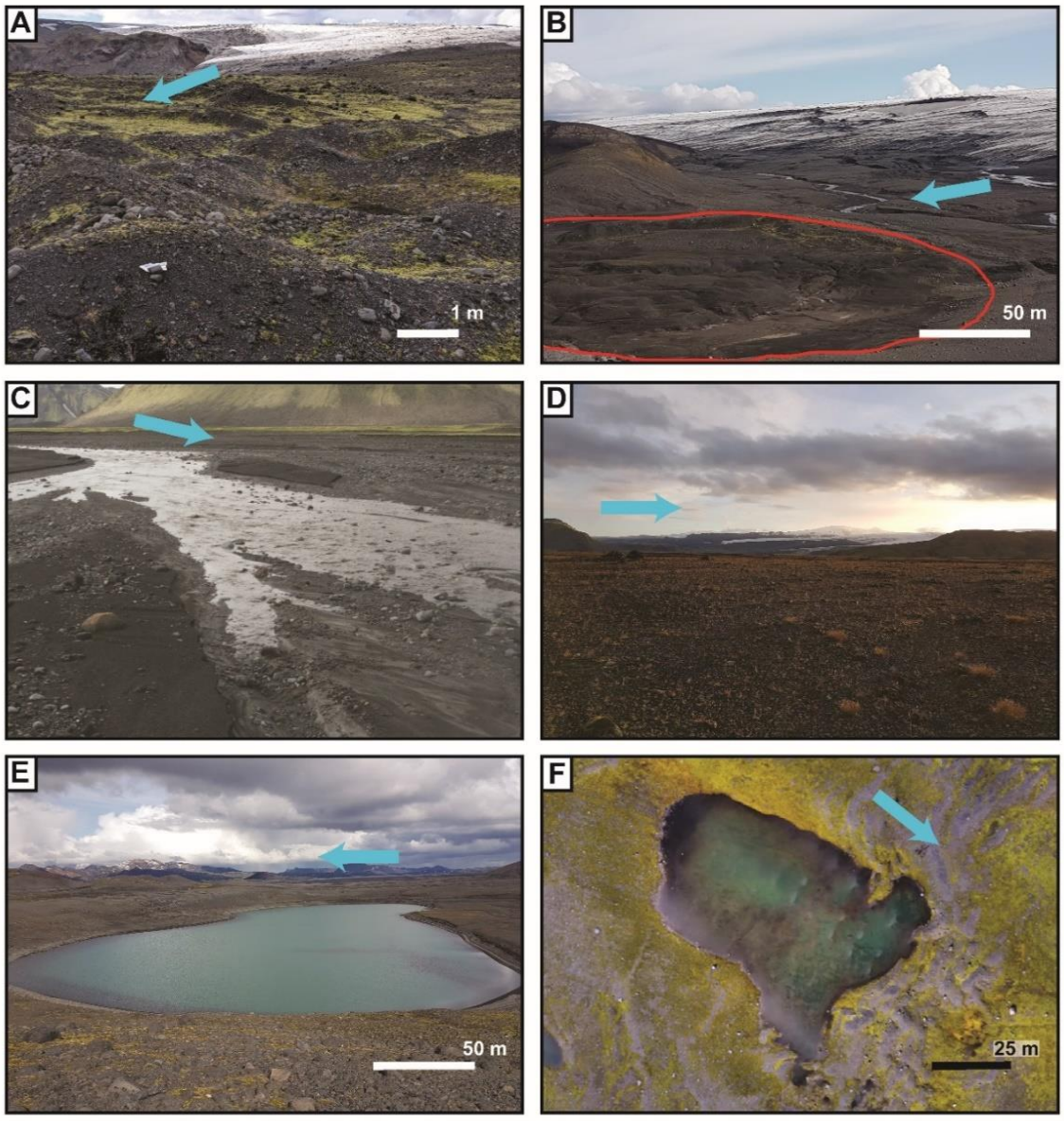

Figure 2.17: A) Hummocky topography observed near the bedrock cliffs at Öldufellsjökull. B) A former glaciolacustrine area outlined in red which shows some pitted and hummocky features; C) Outwash plain in the Sléttjökull forefield with developing river; D) Sparsely vegetated outwash plain located beyond the terminal moraine at Öldufellsjökull; E) Isolated lake at Sléttjökull; F) Lake in the surge zone at Öldufellsjökull. Direction of ice flow is indicated with the blue arrows.

2.3.1.4. Glaciofluvial Landsystem Tract

In each of the forefields of Sléttjökull and Öldufellsjökull the glaciofluvial landsystem tract includes landsystem elements that incorporate extensive outwash plains, active and abandoned channels, and terraces (Figure 2.10, Figure 2.11, and Figure 2.17C, D). At Öldufellsjökull, four main fluvial channels drain the glacier (Figure 2.10). These have deposited large areas of outwash, particularly in locations proximal to the bedrock terrace where most of the streamlined landsystem appears to have been removed by erosion (Figure 2.10 and Figure 2.11). At Sléttjökull, the glacier is drained by many active channels, although the areas dominated by glaciofluvial landforms and outwash deposits are not always associated with the currently active channels, suggesting there may have been changes in the overall drainage pattern of this glacier (Figure 2.11). At each of the two glacier forefields, the glaciofluvial landsystem tract extends across the forefield to intersect with the large, heavily vegetated outwash plain located beyond the terminal moraine (Figure 2.17D). At Sléttjökull, a small discrete area of pitted outwash is visible in Survey C, suggesting the presence of buried ice (Figure 2.15C).

The characteristics of sediments recorded in the three logs taken from exposures through the glaciofluvial landsystems tract on the Sléttjökull forefield show significant differences (Figure 2.18A). Sediments recorded proximal to the ice margin (S-3, Figure 2.18A) consist of stacked successions of clay and fine- to medium-grained massive sand (Sm) and gravel (Gm), overlain by massive matrix supported diamict (Dmm; Figure 2.18A). This sediment stratigraphy is similar to that contained within the streamlined landform at Sléttjökull (Figure 2.16C; 13). Further away from the ice margin (Log S-4; Figure 14A) the sediments are dominated by multiple fining upwards sequences of crudely bedded coarse- to medium-grained sands (Sh) and lack the diamict units observed in more proximal locations (S-3, Figure 14A). Sediments exposed in a small pit beyond the terminal moraine (S-6; Figure 14A), are characterized by laminated interbeds of fine, medium and coarse sand (Sh). The diamict facies identified in locations proximal to the current ice margin have likely been eroded and reworked by the fluvial systems and are therefore absent in more distal locations.

At Öldufellsjökull, sediments exposed within the glaciofluvial landsystem tract (Figure 14B) are also composed predominantly of interbedded sands and gravels and show an overall fining of sediment grain size moving distally from the glacier margin (e.g. logs O-6 to O-9; Figure 2.18B).

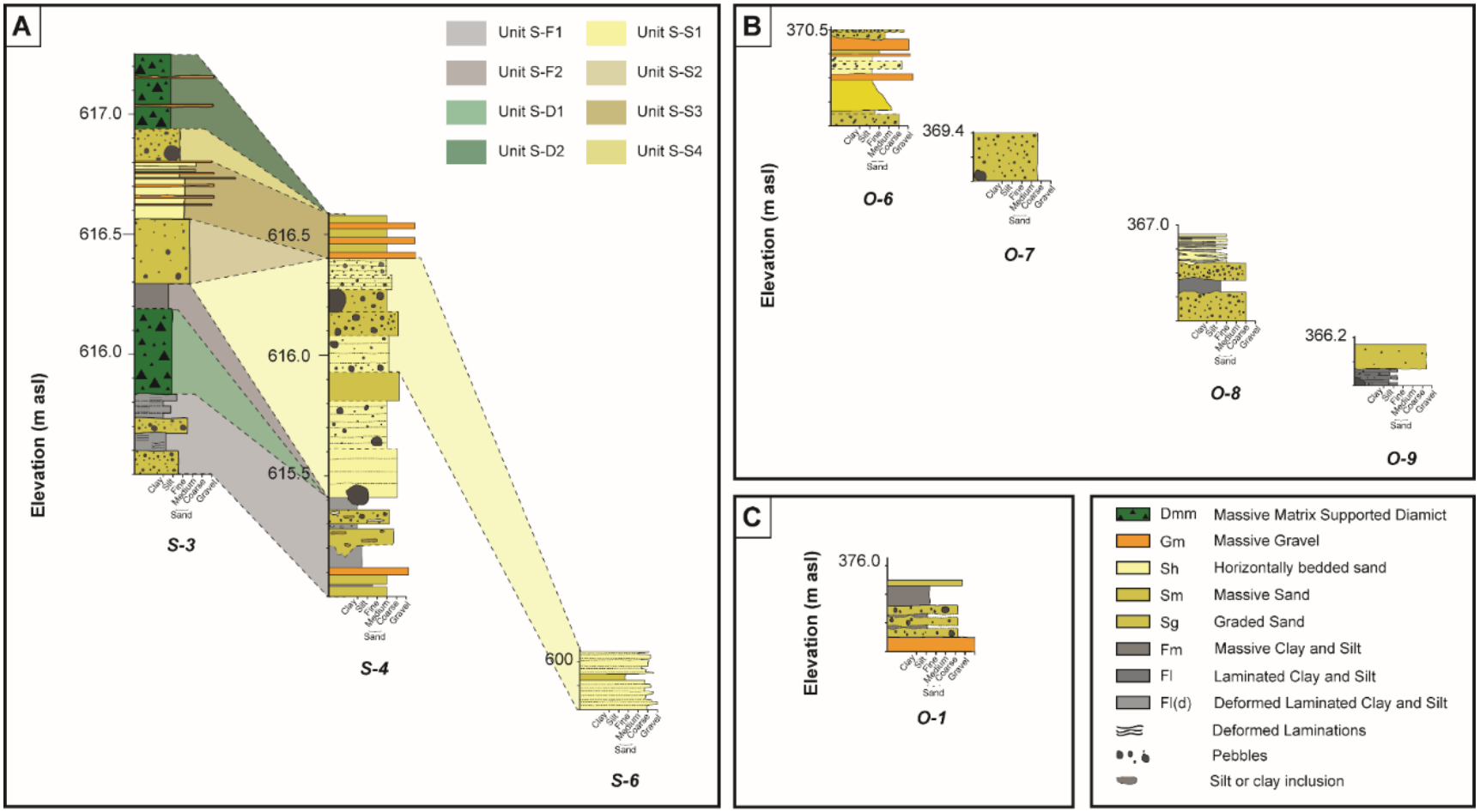

Figure 2.18: Sedimentological logs taken through the glaciofluvial and glaciolacustrine landsystem tracts. A) Correlation of logs in the western Sléttjökull forefield depicting the change from diamict dominated facies (S-3) to gravels and sands (S-4, S-6) moving distally in the forefield; B) Sedimentological logs of exposures through the fluvial landsystem in the Öldufellsjökull forefield; C) Sediment logs taken in the location of former lakes, showing interbeds of clay, silt, sand and gravel. These logs depict the overall distal fining of these deposits. Location of logs is shown in Figure 2.5.

2.3.1.5. Glaciolacustrine Landsystem Tract

The forefields of Sléttjökull and Öldufellsjökull lack the large proglacial lakes that are commonly observed at Icelandic glaciers (Figure 2.10 and Figure 2.11). However, there are many small lakes in the forefields, particularly within the limits of the proximal moraine band. Most of these lakes are relatively small, averaging 0.001 km^2 and 0.003 km^2 at Öldufellsjökull and Sléttjökull respectively (Figure 2.17E, F).

Sediment pits were dug and logs were taken in areas which were believed to have previously contained glacial lakes, based on their location and shape (Figure 2.10). These glaciolacustrine sediments consist of interbedded clay, silt, sand, and gravel (Fl, Sh, Gm; Figure 2.18C)

2.3.2 Surge Zone (Survey F)

To identify the impact of fast ice flow on glacier forefields, a detailed UAV survey was completed at Öldufellsjökull in the region that was inferred to have been overridden during the three recorded surges in 1978 and 1984 and should have landforms reflecting these processes (Figure 2.19). The most distal moraine in this area is streamlined on the up-ice side but shows no evidence of complete glacier overriding, suggesting that the surges terminated in this region. The landform tracts identified within this area include the streamlined, arcuate moraine, glaciofluvial and glaciolacustrine tracts (Figure 2.19).

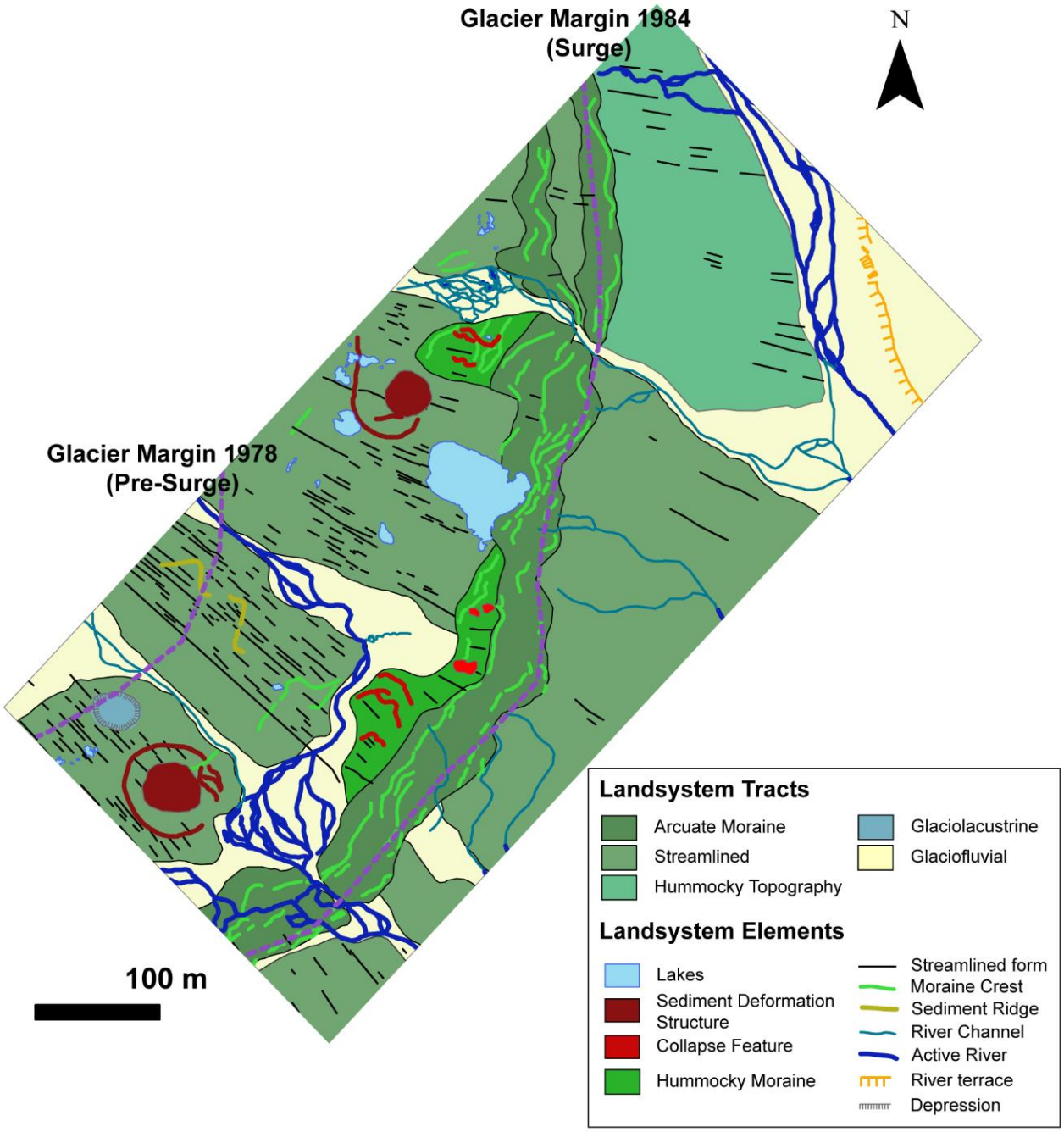

Figure 2.19: Geomorphological map of the area impacted by the known surges at Öldufellsjökull. Known location of the margin in 1980 prior to the surge and in 1984 during the active surge is noted by the purple dashed line. Location of the survey is shown in Figure 2.5 (Survey F).

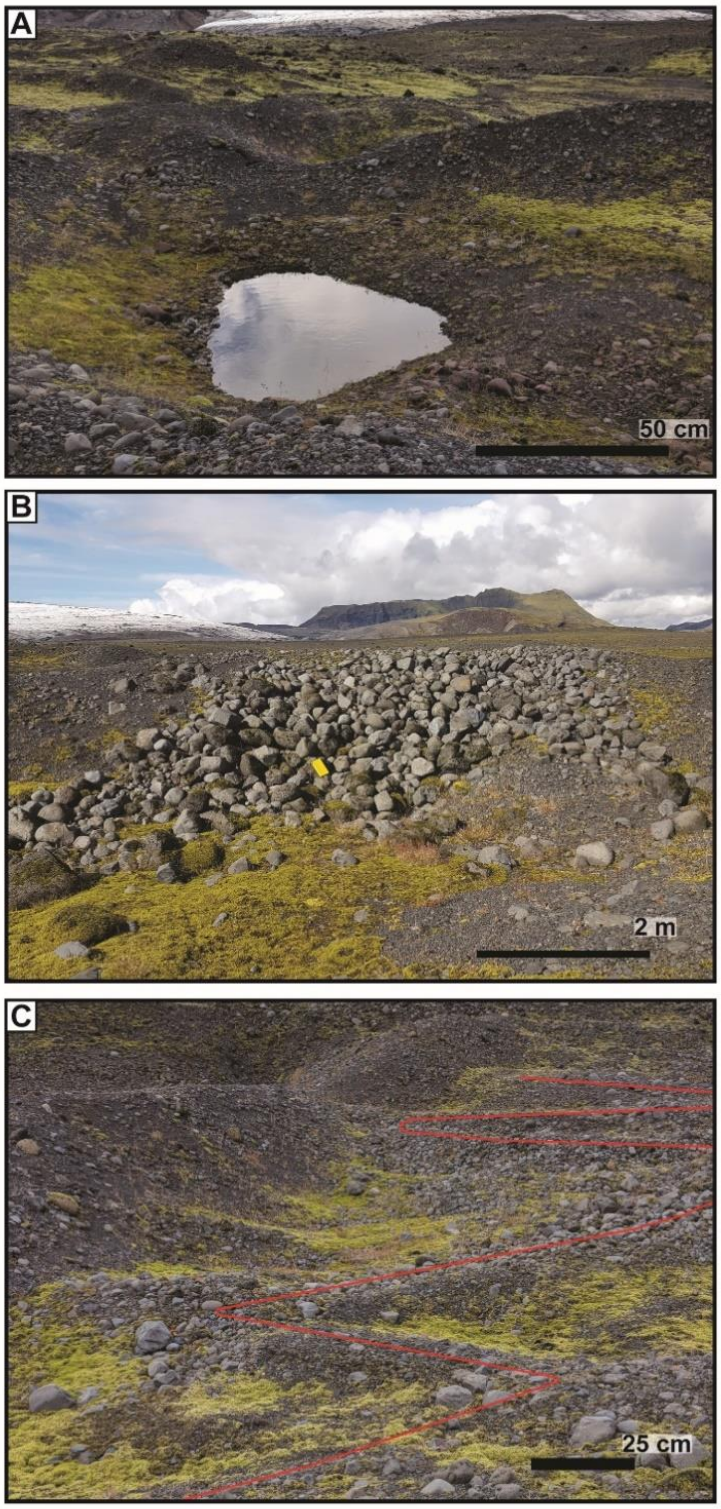

Figure 2.20: Hummocky moraine found on the up-ice side of the moraine in the surge zone with frequent water filled depressions (A) and areas of sorted boulders (B). C) Low amplitude zig-zag sediment ridge found in the streamlined landsystem tract.

There are three specific landform types observed in this detailed UAV survey that were not apparent on the LiDAR-based 5 m DEM at this location (Figure 2.9). The high-resolution of this imagery allows the identification of multiple areas of irregular, hummocky topography on the up-ice side of the distal moraine containing water filled depressions and areas of sorted boulders (Figure 2.19 and Figure 2.20A, B). Secondly, a zig-zag sediment ridge composed of subrounded to rounded gravel, overlying and running approximately parallel to fluting, can be identified in the streamlined landsystem tract area (Figure 2.19 and Figure 2.20C). This zig-zag ridge is 95 m long, up to 3 m wide and 0.25 m tall. The final feature that is unique to this area consists of a central sediment mound surrounded by concentric low relief ridges (Figure 2.19 and Figure 2.21A, B). The central mound is approximately 1 m in height and is symmetrical both perpendicular and parallel to the direction of ice flow (Figure 2.21C, D); the surrounding ridges are lower amplitude with a maximum height of 0.15 m. The entire structure, including all the concentric circular ridges, is 90 m in diameter. The upper surface of this circular feature dips towards the small fluvial channel to the east (Figure 17C, D) but is generally conformable with the overall topography of the area. The whole area is located in a relative topographic low, in comparison to the streamlined terrain that lies to the northeast (Figure 2.21C, D); the circular feature appears to disrupt the streamlined flutes visible on both the up-ice and down-ice sides (Figure 17, C,D).

A second, less well-developed circular structure, approximately 55 m in diameter is located on a relative topographic high, 300 m to the northeast (Figure 2.21E). The central mound at this second location is 2.8 m high and is also symmetrical both parallel and perpendicular to ice flow. However, at this location the concentric circular ridges have been disturbed and are not as clearly defined around the central mound. Both of the circular structures at Öldufellsjökull are located in areas underlain by medium to coarse sands, and gravels similar to that shown in logs O-6 to O-9 of Figure 2.18.

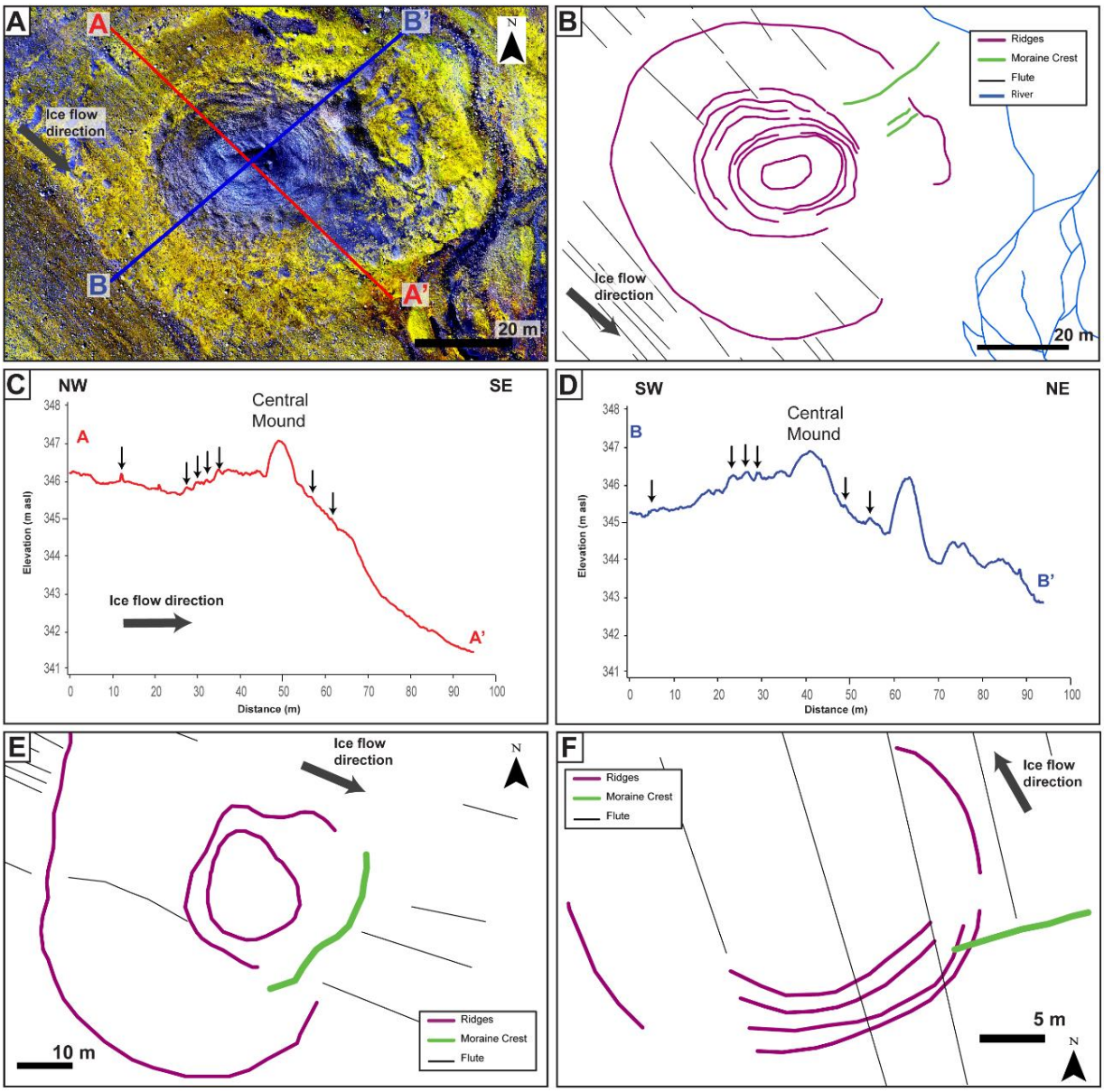

Figure 2.21: A) High contrast aerial image of the circular feature found within the Öldufellsjökull surge area. Current ice margin is located approximately 1.1 km to the northwest; B) Schematic geomorphological drawing of the circular feature depicting the central high and concentric circular ridges; C) Elevation profile of the feature parallel to ice flow, note the symmetrical form of the central mound, concentric circles surrounding the feature indicated by black arrows; D) Elevation profile of the feature perpendicular to ice flow, note the symmetrical form of the central mound, concentric ridges indicated by black arrows; E) Schematic geomorphological drawing of the less well developed circular feature in the Öldufellsjökull surge area; F) Schematic geomorphological drawing of remnant circular ridges in the forefield of Sléttjökull located in Survey B (refer to Figure 2.15B).

A similar circular form can also be identified on high-resolution imagery of the Sléttjökull forefield (Survey B, Figure 2.15) where multiple concentric half circular ridges are visible, although these are very low amplitude (< 5 cm) and more difficult to identify (Figure 2.15B and Figure 2.21F). This circular feature lacks the central mound observed in the two examples found at Öldufellsjökull. There is greater vegetation cover in this region, and the area was overridden by ice less recently, during the late 1950s or early 1960s (Figure 2.2C), allowing the topography of the structure to become subdued over time.

2. 4 Discussion

2.4.1 Geomorphology of the forefields

The landsystem tracts identified at Öldufellsjökull and Sléttjökull (Figure 2.10 and Figure 2.11) lack most of the geomorphic indicators ascribed to surge-type glaciers in Iceland (Evans and Rea, 1999; Benediktsson et al., 2010; Jónsson et al., 2014; Schomacker et al., 2014; Ingólfsson et al., 2016). The typical surge-type glacier landsystem is composed of three zones (distal to proximal): Zone A consisting of glaciotectonized end moraines composed of folded and thrusted pre-surge sediments with hummocky moraine on the up-ice slope; Zone B consisting of active channels and pitted outwash; and Zone C consisting of flutes, drumlins, crevasse squeeze ridges and concertina eskers (Figure 18; Evans and Rea, 1999; Schomacker et al., 2014; Ingólfsson et al., 2016).

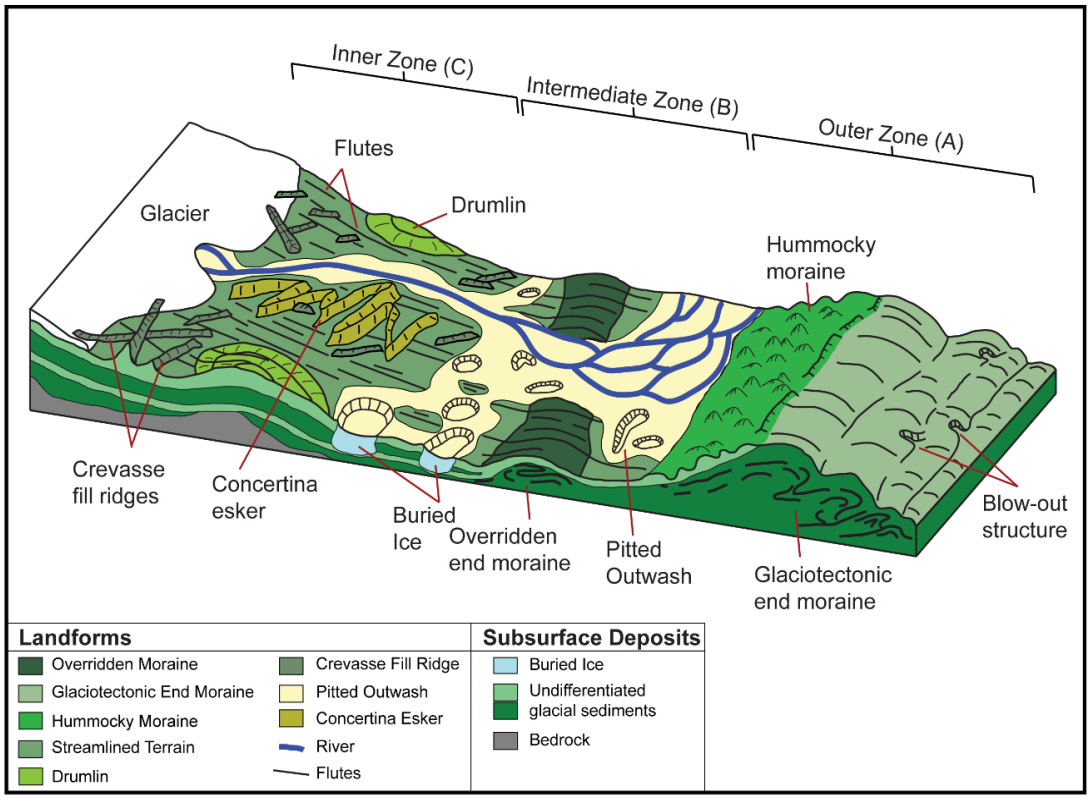

Figure 2.22: Idealized version of the surge type landsystem with includes an outer zone (A) defined by a glaciotectonic end moraine with hummocky moraine on the up-ice slope. The intermediate zone (B) is dominated by fluvial deposits included channelized outwash and pitted outwash. The inner zone (C) is primarily subglacial in origin, included crevasse fill ridges, flutes, drumlins, and concertina eskers. Figure is modified from Ingólfsson et al. (2016); based on work by Schomacker et al. (2014) and Evans and Rea (2003).

In comparison, the forefields at Sléttjökull and Öldufellsjökull consist of two repetitions of the same or groupings of similar landsystem tracts, termed herein landsystem tract assemblages (LTA). The LTA at Öldufellsjökull and Sléttjökull consist of the heavily streamlined landsystem tract in proximal positions followed by the arcuate moraine landsystem tract more distally; the glaciofluvial landsystem tract occurs throughout the forefield (Figure 2.23). There is no indication of glaciotectonism or thrust sheets in the moraines at Öldufellsjökull or Sléttjökull as is reported widely in other surging glacier landsystems (Figure 2.13C). Between the two repetitions of the streamlined/arcuate moraine LTA is an area dominated by hummocky topography with limited areas of pitted outwash (Figure 2.23). This landform distribution shares more similarities with the active temperate glacial landsystem commonly reported in Iceland (Spedding and Evans, 2002; Evans and Orton, 2015; Chandler et al., 2015, 2020; Evans et al., 2016b; Lee et al., 2018) than

with that described for surge-type glaciers. The active temperate glacier landsystem is composed of three main landsystem tracts, namely arcuate moraines, streamlined terrain including flutes and overridden moraines, and glaciofluvial terrain, including active channels and kame terraces (Evans and Twigg, 2002; Chandler et al., 2015, 2020; Evans et al., 2016a; Lee et al., 2018).

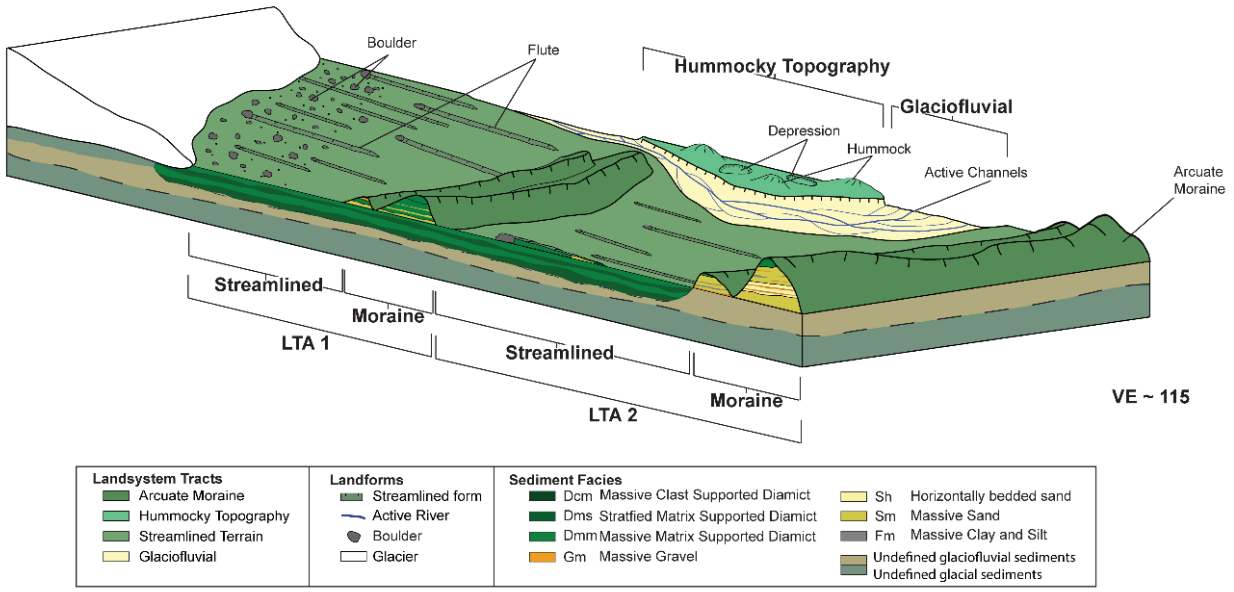

Figure 2.23: Model of the distribution of landforms found in the glacial forefields of western Sléttjökull and Öldufellsjökull. The forefield can be divided into two main landsystem tract assemblages which are composed of a large area of streamlined landsystem tract followed by a band of arcuate moraines (LTA 1 and LTA 2). Interspersed throughout the forefields are hummocky topography and glaciofluvial landsystems. This model shows similar characteristics to those of active temperate glacier forefields common in Iceland (e.g. Evans and Twigg 2002; Chandler et al. 2015) and shows limited similarity to the forefields of surge-type glaciers (e.g. Schomacker, Benediktsson, and Ingólfsson 2014; Ingólfsson et al. 2016).

The absence of the 'typical' surge-type glacier landsystem on the glacial forefields of Öldufellsjökull and Sléttjökull may be the result of the timing of surge events. The length of the surge cycles in Iceland can be on a time scale of centuries, limiting the imprint of the fast-ice flow on these fields (Raymond, 1987; Björnsson et al., 2003; Sevestre and Benn, 2015). Since there are no recorded surges prior to 1974 at Öldufellsjökull and prior to 1992 at Sléttjökull, there is a possibility these glaciers only developed surging behaviour recently. However, even the landsystem tracts within the limits of the known recent surge margins show limited similarity to

the surge-type glacier landsystem reported elsewhere (Evans et al., 2009; Benediktsson et al., 2010; Schomacker et al., 2014; Ingólfsson et al., 2016).

Within the surge margins, the arcuate moraine landsystem tract and the streamlined landsystem tract dominate and are incised by glaciofluvial deposits (Figure 2.10 and Figure 2.11). This landsystem distribution is somewhat similar to that of the surge-type landsystem although it lacks the distinctive characteristics of these zones. Zone A of the surge-type landsystem model (Figure 2.22) is a distal zone of glaciotectonized end moraines with hummocky topography commonly found on the up-ice side. While hummocky topography was identified on the Öldufellsjökull and Sléttjökull forefields it was rarely located within the known surge limits and appeared to have more consistent spatial association with bedrock and sediment highs, areas associated with a compressional regime and thrusting. Additionally, there is no evidence of glaciotectonism in the end moraines associated with known surges reported here, a typically diagnostic feature of rapidly emplaced moraines. The Öldufellsjökull and Sléttjökull forefields show abundant evidence of fluting, but there are none of the notable subglacial landforms found in Zone C of the surge-type landsystem model including crevasse fill ridges, drumlins, and concertina eskers (Figure 2.22). There are extensive areas of the glaciofluvial landsystem on these forefields, as included in Zone B of the surge-type landsystem; however, these areas lack the extensive pitted outwash indicative of stagnating ice (Figure 2.10 and Figure 2.11; Evans and Rea, 2003; Evans et al., 2009; Schomacker et al., 2014).

Due to the rapid forward movement and thinning of the surging glacier margin, common landform types in the surge zone are those associated with stagnation of the glacier margin and the melting of buried ice including pitted outwash and hummocky topography (Schomacker et al., 2006; Roberts et al., 2009; Ingólfsson et al., 2016). However, in the glaciofluvial deposits at Öldufellsjökull there are no areas of pitted outwash and at Sléttjökull the area of pitted outwash is small. There are distinct areas of hummocky topography in both of these forefields, however these are located adjacent to rock slopes and beyond the limits of the known surge margins (Figure 2.10 and Figure 2.11). The lack of extensive areas of hummocky topography or ice stagnation features at these glaciers may reflect their paucity of supraglacial debris (Figure 2.3; Van Der Meer et al., 1999); with limited amounts of insulating supraglacial debris there is less chance for the development of hummocky topography which is generally used to identify zones of ice stagnation at a surge-type margin.

Crevasse squeeze ridges (CSR) are also commonly associated with the surge-type glacier landsystem (Brynjólfsson et al., 2012; Schomacker et al., 2014; Evans et al., 2016c; Farnsworth et al., 2016). These ridges are between 0.5 and 2 m high, are usually composed of massive, matrix-supported diamict, and occur as networks on streamlined terrain oriented oblique or transverse to ice flow (Sharp, 1985b; Schomacker et al., 2014; Aradóttir et al., 2019). Although the precise method of their formation is not known, they are thought to develop as a result of the squeezing of saturated sediment into basal crevasses near the end of the active phase of the surge (Sharp, 1985a; Evans et al., 2016c; Farnsworth et al., 2016). CSR are not produced by all surge-type glaciers, although they are common and have been used as a diagnostic tool for determining the presence of surging behaviour (Farnsworth et al., 2016; Aradóttir et al., 2019). The aerial imagery of Öldufellsjökull taken during or recently after the surge in 1984, shows extensive crevassing of the glacier (Figure 2.3); however, there are no CSR evident on the glacier forefield. The absence of CSR may be related to the predominantly coarse-grained nature of the sediments on both the Öldufellsjökull and Sléttjökull glacier forefields. These sediments drain well and are not prone to saturation or deformation, even under conditions of high basal water pressure and meltwater input as expected near the end of a surge.

Table 2.4: Comparison of flute lengths recorded at different types of glaciers.

Reference	Glacier	Glacier Type	Average Length (m)	Maximum Length (m)
Schomacker et al. 2014	Eyjabakkajökull	Surge	41	550
Roberson et al. 2011	Midre Lovernbreen	Polythermal	22.5	99.85
Rose 1989	Austre Okstindbreen	Alpine	39	93
Ely et al. 2017	Isfallsglaciären	Polythermal	28	100
Hart et al. 2018	Skalafellsjökull	Active Temperate	11.48 – 18.75*	N/A
This study	Öldufellsjökull	Surge	53.21 (17.83 – 34.21) **	262.76 (61.35 – 225.76)**
	Sléttjökull	Surge	96.72 (29.58 – 47.06)**	392.86 (92.92 – 152.65)**

* Range of averages based on the averages from multiple study sites in the glacier forefield.

** Bracketed range based on high-resolution UAV surveys.

Certain geomorphological characteristics of flutes have been attributed to development under fast flowing ice, including high elongation ratios (Denis et al., 2007), increased length (Evans and Rea, 2003; Ives and Iverson, 2019), and parallel-sided flute geometry (Ives and Iverson, 2019). Previous work at Öldufellsjökull suggested that the elongate nature of the flutes in the forefield, compared with those of surrounding glaciers, may be indicative of its surging behaviour (Evans et al., 2018). The average flute length on the forefields of Sléttjökull and Öldufellsjökull, calculated using the 5 m DEM and ArcGIS base map aerial imagery, was 96.72 m and 53.21 m respectively. These flutes have a higher average and maximum length than those produced below alpine, polythermal, and active temperate non-surging glaciers reported in other studies (Table 2.4). However, when analyzing flute length using high-resolution imagery collected using the UAV, the average length drastically reduces to between 29.58 m – 47.06 m at Sléttjökull and 17.83 m to 34.21 m at Öldufellsjökull. The high-resolution imagery allows the identification of additional lower amplitude and narrower flutes, which tend to have shorter lengths, similar to those produced by non-surging glacier types (Figure 2.9 and Table 2.4). This suggests that flute length may be less diagnostic of surging behaviour. It can be surmised that the flutes at Öldufellsjökull and Sléttjökull are on average longer than those found in other glacier forefields not impacted by surges, but the significance of this characteristic and the impact of data collection biases is unclear.

2.4.2 Geomorphology of the surge zone

High-resolution analysis of the region identified to have been impacted by the most recent surges at Öldufellsjökull and Sléttjökull identifies features that are considered to be more characteristic of the surge-type landsystem (Figure 2.24). The presence of hummocky topography on the up-ice side of the moraine in this area is indicative of ice stagnation and is a common feature of Zone A of the surge-type landsystem (Figure 18; Evans and Rea, 1999; Kjær et al., 2008; Schomacker et al., 2014). Numerous parallel sided flutes, and a low relief zig zag ridge can be clearly identified in the streamlined landsystem tract (Figure 2.24). The zig-zag ridge drapes subglacial bedforms and is interpreted as a low relief concertina esker (Knudsen, 1995; Ingólfsson et al., 2016). Concertina eskers, with their characteristic crenulated form, are considered to be diagnostic of surge-type glaciers, formed as a result of ice margin compression associated with surging behaviour, (Ingólfsson et al., 2016). The relatively low relief of the concertina esker

identified here may reflect the good drainage capacity of the underlying clast- and sand-rich diamicts which facilitated water loss from the glacier base.

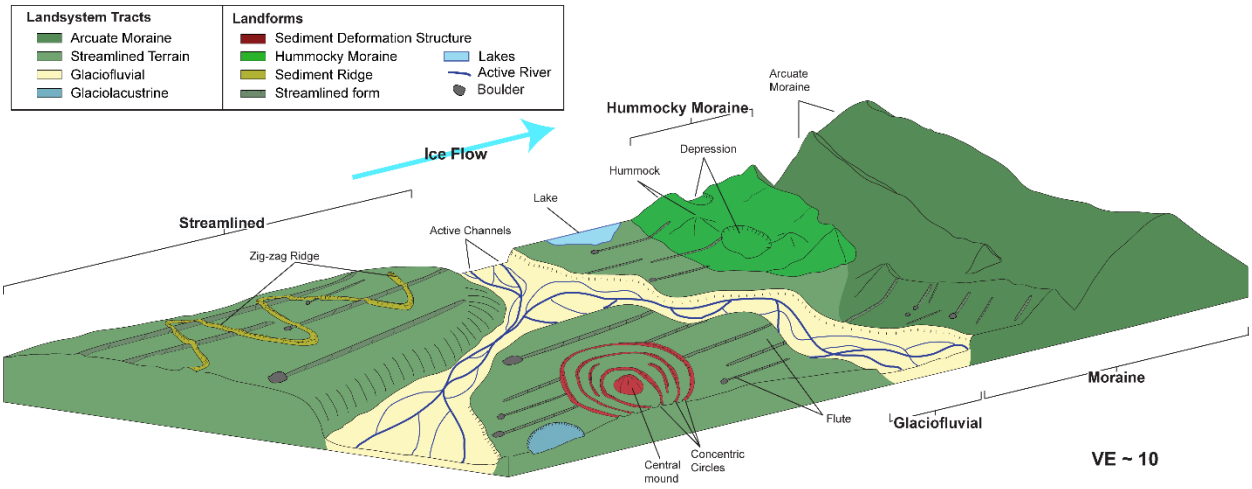

Figure 2.24: Model of the landform distribution identified in the surge area at Öldufellsjökull using high-resolution UAV imagery. The same landsystem tract assemblages observed across the entire forefield are present but more extensive areas of hummocky moraine, a zig-zag esker ridge and a circular mound can also be identified. Ice flow direction indicated with the blue arrow.

2.4.2.1. Circular structures

Of particular interest in the high-resolution survey areas of the Öldufellsjökull forefield are two previously unidentified circular structures, whose origins and implications for glacial dynamics are unclear. The larger and more distinct structure is found on the southwestern side of the UAV survey grid while the smaller structure is found on northeastern side (Figure 2.19). Each of these structures is composed of a low relief mound surrounded by a series of circular ridges and is symmetrical both parallel and perpendicular to ice flow; this suggests that it most likely formed after the surge ended and the ice margin stagnated (Figure 17A-D). Additionally, the structure appears to disrupt streamlining of the forefield, further supporting its development in a proglacial position after the active phase of surging.

Similar circular features are relatively common in periglacial environments and include perennial frost mounds, frost blisters, pingoes, palsas and lithalsas (Grosse and Jones, 2011). However, these forms are only known to develop in areas which have either continuous or discontinuous permafrost (Mackay, 1973; Morse and Burn, 2014; Wolfe et al., 2014). Permafrost

is generally associated with a mean annual air temperate (MAAT) below -2°C, (Washburn, 1980; Matsuoka, 2011). The nearest weather station to Öldufellsjökull, at Kirkjubæjarklaustur, shows an average MAAT from 1960 to 2000 of 4.58°C, with a low of 3.23°C in 1979 (Icelandic Meteorological Office, 2020), a value well above the temperature needed to create permafrost. Maps of permafrost extent in Iceland show a lower limit of permafrost around 460 m asl and even at higher elevations in southern Iceland (Etzelmüller and Frauenfelder, 2009; Czekirda et al., 2019). Therefore, it is unlikely that the circular features found in this high-resolution survey are related to permafrost.

It is possible that these features formed as a result of changing hydrological regimes during and following surge events. During the active phase of the surge, an increase in basal water pressure may cause ice-bed decoupling or saturation of the underlying sediments resulting in deformation (Clarke et al., 1984; Fuller and Murray, 2002; Sevestre and Benn, 2015; Ingólfsson et al., 2016). Water is driven into the subsurface by the weight of the overlying ice (Figure 2.25A) and will re-emerge at the ice margin (Figure 2.25B; Boulton and Caban, 1995).The upward flow of this water can cause overpressuring, particularly of coarse-grained sediment layers which may undergo dilation, causing them to expand upwards, producing a mound-like sediment diapir (Figure 2.25C; Boulton and Caban, 1995).

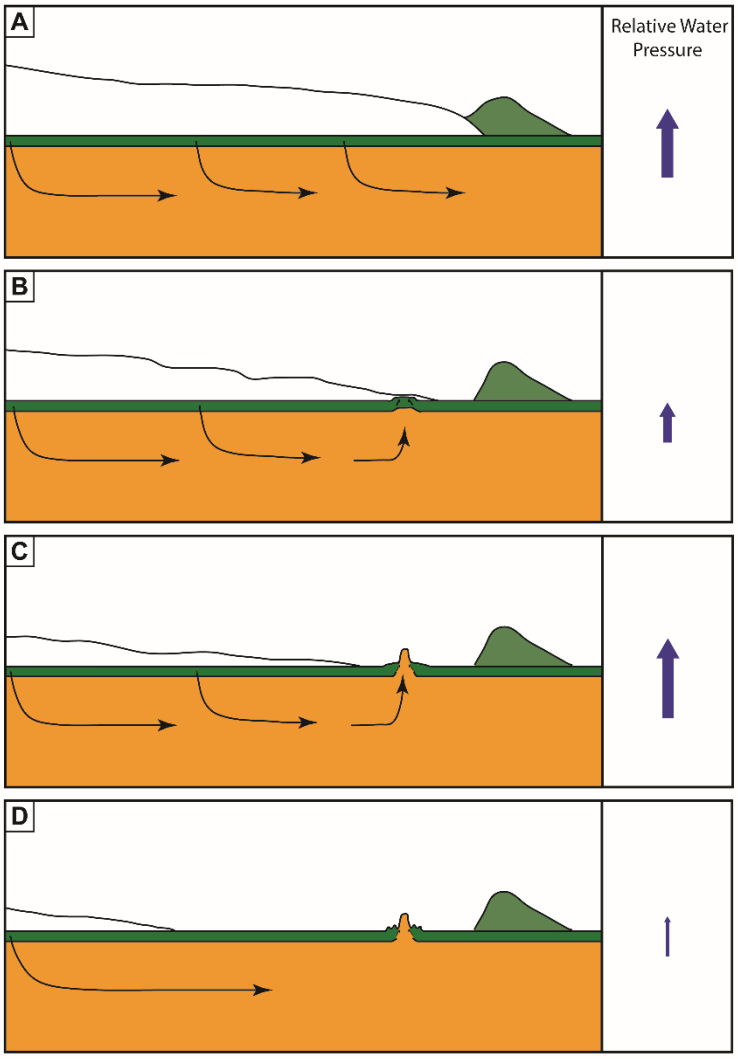

Figure 2.25: Proposed mechanism of formation of the circular feature interpreted as a sediment diapir. A) During the surge, high basal pressures force water downwards into underlying gravels and sands (orange); B) Following the main surge, the glacier thins and the basal water pressures decrease. Water escapes to the surface in areas where confining pressures are relatively low (e.g. where confining fine-grained units shown in green are relatively thin) and creates a bulge of the surface sediment; C) Bulging of the sediment causes weakness in the overlying sediment, and the overpressured sand breaks through the confining diamict, creating the central mound of the circular feature; D) Ice margin stagnates after the active surge phase and there is a return to the normal hydrologic regime allowing for dewatering of the sediment diapir causing deflation and the circular pattern of ridges to form. Sediment logs were not taken through the feature and sediment interpretations are based on logs taken in the forefield and observations of surficial sediments at this location.

At the location of the high-resolution surveys at Öldufellsjökull, the majority of the subsurface sediments are coarse-grained, consisting of interbedded gravel and coarse sand with a surficial cover of fine-grained, matrix rich diamict (Dmm; Figure 2.13C and Figure 2.16C) and occasional horizons of horizontally-laminated silty clay deposits (Fl; Figure 2.16 and Figure 2.18). This juxtaposition of coarse- and fine-grained sediment creates the ideal conditions for overpressuring of groundwaters and the formation of sediment diapirs in the manner described above (Figure 2.25; Boulton and Caban, 1995).The circular features may have developed in areas where underlying impermeable layers were relatively thin allowing groundwaters to escape to the surface during overpressuring events.

The superposition of the circular features on streamlined forms indicates that the features formed in the proglacial area after ice had receded. The concentric circular pattern of ridges surrounding the central high probably resulted from the deflation of the original diapir as it slowly dewatered during the quiescent phase of the surge when the ice margin stagnated, and hydrological conditions returned to their pre-surge state (Figure 2.25C). This is the first time such features have been documented on glacier forefields in Iceland and it will be interesting to see if additional examples are reported from subsequent high-resolution UAV surveys.

2.4.3 Utility of high-resolution UAV-based aerial surveys

It is apparent from the geomorphological analysis of the Öldufellsjökull and Sléttjökull forefields presented above, that the addition of UAV-based high-resolution surveys greatly enhances the quality of the data available for analysis. In particular, the use of UAV imagery allowed for the identification and inclusion of low amplitude landforms that are below the resolution of historical aerial imagery. The integration of data from large-scale mapping of the glacier forefields using historical aerial imagery with that from targeted high-resolution UAV surveys, was particularly beneficial as the overall landsystem patterns could be identified as well as site specific geomorphic characteristics. The high-resolution UAV survey of the Öldufellsjökull surge zone was especially valuable, as potentially diagnostic landforms of surge-type glacier behaviour were identified (e.g. areas of hummocky moraine, the zig-zag esker ridge, and circular features; Figure 2.19) that may have otherwise been missed. Each of these landforms have implications for reconstructing the former dynamics of the system and may have been omitted from the study if only the historical aerial imagery was utilized.

2. 5 Conclusions

This study has identified relatively few landscape features at Öldufellsjökull and Sléttjökull that are considered to be diagnostic of the surge-type glacial landsystem (Evans and Rea, 2003; Brynjólfsson et al., 2012; Ingólfsson et al., 2016). However, there are recently recorded surge events at both glacier margins (three at Öldufellsjökull and one at Sléttjökull). The paucity of diagnostic 'surge-type' landsystem elements at each of these glaciers may be a reflection of the relatively recent development of surging behaviour, allowing their forefields to show greater similarity to the active temperate landsystems identified for non-surging glaciers in Iceland (Spedding and Evans, 2002; Evans and Orton, 2015; Chandler et al., 2015, 2020; Evans et al., 2016b; Lee et al., 2018). However, analysis of high-resolution UAV-based imagery from small survey areas in the surge zone at Öldufellsjökull, has allowed identification of features that record the impact of the surges. Areas of hummocky moraine, a concertina esker, and circular feature related to hydrologic overpressuring most likely record the impact of surge-related processes on the forefield.

The circular features found in the high-resolution survey at Öldufellsjökull are unique to this glacier and may reflect the impact of the surges, although the exact implications for glacier dynamics are uncertain. These circular features are interpreted here as the surface expression of upward-moving sediment diapirs caused by overpressuring of groundwater during surge events (Figure 20). It is likely that similar structures exist in the surge zones of other fast-flowing glaciers but have not been recognized to date due to a lack of high-resolution imagery.

The use of a UAV to collect high-resolution imagery has allowed the identification of the imprint of fast ice flow on the geomorphology of the Öldufellsjökull and Sléttjökull forefields. Using high-resolution datasets, low relief landforms reflective of surging behaviour were identifiable. Enhanced use of high-resolution UAV surveys of glacial forefields will allow more comprehensive mapping of features at multiple scales and will provide more robust data sources with which to identify diagnostic landforms and sediments associated with various glacial regimes.

2. 6 References

Adalgeirsdóttir G, Björnsson H, Pálsson F, Magnússon E. 2005. Analyses of a surging outlet glacier of Vatnajökull ice cap, Iceland. Annals of Glaciology **42** : 23–28. DOI: 10.3189/172756405781812934

Agisoft Metashape. 2020. Agisoft Metashape Professional [online] Available from: https://www.agisoft.com/downloads/installer/

Alexanderson H, Adrielsson L, Hjort C, Möller P, Antonov O, Eriksson S, Pavlov M. 2002. Depositional history of the North Taymyr ice-marginal zone, Siberia - A landsystem approach. Journal of Quaternary Science **17** : 361–382. DOI: 10.1002/jqs.677

Andreassen K, Winsborrow MCM, Bjarnadóttir LR, Rüther DC. 2014. Ice stream retreat dynamics inferred from an assemblage of landforms in the northern Barents Sea. Quaternary Science Reviews **92** : 246–257. DOI: 10.1016/j.quascirev.2013.09.015

Aradóttir N, Ingólfsson Ó, Noormets R, Benediktsson ÍÖ, Ben-Yehoshua D, Håkansson L, Schomacker A. 2019. Glacial geomorphology of Trygghamna, western Svalbard - Integrating terrestrial and submarine archives for a better understanding of past glacial dynamics. Geomorphology **344** : 75–89. DOI: 10.1016/j.geomorph.2019.07.007

Army Map Service (AMS). 1951. Vestmannaeyjar, 1:250 000. AMS Series C562, NP 27, 28-2

Benediktsson ÍÖ, Schomacker A, Lokrantz H, Ingólfsson Ó. 2010. The 1890 surge end moraine at Eyjabakkajökull, Iceland: a re-assessment of a classic glaciotectonic locality. Quaternary Science Reviews **29** : 484–506. DOI: 10.1016/j.quascirev.2009.10.004

Benn DI, Fowler AC, Hewitt I, Sevestre H. 2019. A general theory of glacier surges. Journal of Glaciology **65** : 701–716. DOI: 10.1017/jog.2019.62

Bennett MR. 2003. Ice streams as the arteries of an ice sheet: Their mechanics, stability and significance. Earth-Science Reviews **61** : 309–339. DOI: 10.1016/S0012-8252(02)00130-7

Björnsson H, Pálsson F. 2008. Icelandic glaciers. Jökull **58** : 365–386.

Björnsson H, Palsson F, Gudmundsson MT. 2000. Surface and bedrock topography of the Mýrdalsjökull ice cap, Iceland: The Katla caldera, eruption sites and routes of jökulhlaups. Jökull **49** : 29–46.

Björnsson H, Pálsson F, Sigurdsson O, Flowers GE. 2003. Surges of glaciers in Iceland. Annals of Glaciology **36** : 82–90. DOI: 10.3189/172756403781816365

Boulton GS, Caban PE. 1995. Groundwater flow beneath ice sheets: Part II - Its impact on glacier tectonic structures and moraine formation. Quaternary Science Reviews **14** : 531–587.

Brynjólfsson S, Ingólfsson Ó, Schomacker A. 2012. Surge fingerprinting of cirque glaciers at the Tröllaskagi. Jökull **62** : 1–16.

Carrivick J, Tweed FS, James W, Jóhannesson T. 2017. Surface and geometry changes during the first documented surge of Kverkjökull, central Iceland. Jökull **66** : 27–49.

Chandler BMP, Evans DJA, Chandler SJP, Ewertowski MW, Lovell H, Roberts DH, Schaefer M, Tomczyk AM. 2020. The glacial landsystem of Fjallsjökull, Iceland: Spatial and temporal evolution of process-form regimes at an active temperate glacier. Geomorphology **361** : 107192. DOI: 10.1016/j.geomorph.2020.107192

Chandler BMP, Evans DJA, Roberts DH, Ewertowski M, Clayton AI. 2015. Glacial geomorphology of the Skálafellsjökull foreland, Iceland: A case study of 'annual' moraines. Journal of Maps : 1–13. DOI: 10.1080/17445647.2015.1096216

Chudley TR, Willis IC. 2019. Glacier surges in the north-west West Kunlun Shan inferred from 1972 to 2017 Landsat imagery. Journal of Glaciology **65** : 1–12. DOI: 10.1017/jog.2018.94

Clarke GKC. 1987. Fast glacier flow: ice streams, surging, and tidewater glaciers. Journal of Geophysical Research **92** : 8835–8841. DOI: 10.1029/JB092iB09p08835

Clarke GKC, Collins SG, Thompson DE. 1984. Flow, thermal structure, and subglacial conditions of a surge- type glacier. Canadian Journal of Earth Sciences **21** : 232–240. DOI: 10.1139/e84-024

Colgan PM, Mickelson DM, Cutler PM. 2003. Ice marginal terrestrial landsystems: southern laurentide ice sheet margin. In Glacial Landsystems , Evans DJA (ed). Hodder Arnold: London; 111–134.

Copland L, Sharp MJ, Dowdeswell JA. 2003. The distribution and flow characteristics of surge-type glaciers in the Canadian High Arctic. Annals of Glaciology **36** : 73–81. DOI: 10.3189/172756403781816301

Czekirda J, Westermann S, Etzelmüller B. 2019. Transient Modelling of Permafrost Distribution in Iceland. **7** : 1–23. DOI: 10.3389/feart.2019.00130

Denis M, Buoncristiani JF, Konaté M, Ghienne JF, Guiraud M. 2007. Hirnantian glacial and deglacial record in SW Djado Basin (NE Niger). Geodinamica Acta **20** : 177–195. DOI: 10.3166/ga.20.177-195

Ely JC, Graham C, Barr ID, Rea BR, Spagnolo M, Evans J. 2017. Using UAV acquired photography and structure from motion techniques for studying glacier landforms: application to the glacial flutes at Isfallsglaciären. Earth Surface Processes and Landforms **42** : 877–888. DOI: 10.1002/esp.4044

ESRI. 2019. Northern Margin of Mýrdalsjökull [basemap]

Etzelmüller B, Frauenfelder R. 2009. Factors Controlling The Distribution of Mountain Permafrost in The Northern Hemisphere and Their Influence on Sediment Transfer. Arctic, Antarctic, and Alpine Research **41** : 48–58. DOI: 10.1657/1938-4246(08-026)

Evans DJA. 2003. Introduction to Glacial Landsystems. In Glacial Landsystems , . Hodder Arnold: London;

Evans DJA, Ewertowski M, Orton C. 2015. Eiríksjökull plateau icefield landsystem, Iceland. Journal of Maps **12** : 747–756. DOI: 10.1080/17445647.2015.1072448

Evans DJA, Ewertowski M, Orton C. 2016a. Fláajökull (north lobe), Iceland: active temperate piedmont lobe glacial landsystem. Journal of Maps **12** : 777–789. DOI: 10.1080/17445647.2015.1073185

Evans DJA, Ewertowski M, Orton C, Graham DJ. 2018. The glacial geomorphology of the ice cap piedmont lobe landsystem of east mýrdalsjökull, Iceland. Geosciences (Switzerland) **8** DOI: 10.3390/geosciences8060194

Evans DJA, Ewertowski M, Orton C, Harris C, Guðmundsson S. 2016b. Snæfellsjökull volcano-centred ice cap landsystem, West Iceland. Journal of Maps **12** : 1128–1137. DOI: 10.1080/17445647.2015.1135301

Evans DJA, Orton C. 2015. Heinabergsjökull and Skalafellsjökull, Iceland: active temperate piedmont lobe and outwash head glacial landsystem. Journal of Maps **11** : 415–431. DOI: 10.1080/17445647.2014.919617

Evans DJA, Rea BR. 1999. Geomorphology and sedimentology of surging glaciers: A land-systems approach. Annals of Glaciology **28** : 75–82. DOI: 10.3189/172756499781821823

Evans DJA, Rea BR. 2003. Surging glacier landsystem. In Glacial Landsystems , Evans DJA (ed). Hodder Arnold: London; 259–288.

Evans DJA, Storrar RD, Rea BR. 2016c. Crevasse-squeeze ridge corridors: Diagnostic features of late-stage palaeo-ice stream activity. Geomorphology **258** : 40–50. DOI: 10.1016/j.geomorph.2016.01.017

Evans DJA, Twigg DR. 2002. The active temperate glacial landsystem: A model based on Breiðamerkurjökull and Fjallsjökull, Iceland. Quaternary Science Reviews **21** : 2143–2177. DOI: 10.1016/S0277-3791(02)00019-7

Evans DJA, Twigg DR, Rea BR, Orton C. 2009. Surging glacier landsystem of tungnaárjökull, iceland. Journal of Maps **5** : 134–151. DOI: 10.4113/jom.2009.1064

Eyles N. 1983. Glacial Geology: A landsystems approach. In Glacial Geology: An Introduction for engineers and earth scientists , Eyles N (ed). Pergamon Press Canada Ltd.: Toronto, Canada; 1–18.

Farnsworth WR, Ingólfsson Ó, Retelle M, Schomacker A. 2016. Over 400 previously undocumented Svalbard surge-type glaciers identified. Geomorphology **264** : 52–60. DOI: 10.1016/j.geomorph.2016.03.025

Flink AE, Noormets R, Fransner O, Hogan KA, ÓRegan M, Jakobsson M. 2017. Past ice flow in Wahlenbergfjorden and its implications for late Quaternary ice sheet dynamics in northeastern Svalbard. Quaternary Science Reviews **163** : 162–179. DOI: 10.1016/j.quascirev.2017.03.021

Fowler AC. 1987. A theory of glacier surges. Journal of Geophysical Research **92** : 9111–9120. DOI: 10.1029/JB092iB09p09111

Fuller S, Murray T. 2002. Sedimentological investigations in the forefield of an Icelandic surge-type glacier: Implications for the surge mechanism. Quaternary Science Reviews **21** : 1503–1520. DOI: 10.1016/S0277-3791(01)00099-3

Google Earth. 2019. Northeast margin of Mýrdalsjökull

Grosse G, Jones BM. 2011. Spatial distribution of pingos in northern Asia. Cryosphere **5** : 13–33. DOI: 10.5194/tc-5-13-2011

Hannesdóttir H, Björnsson H, Pálsson F, Aðalgeirsdóttir G, Guðmundsson SS. 2015. Changes in the southeast Vatnajökull ice cap, Iceland, between ~ 1890 and 2010. The Cryosphere **9** : 565–585. DOI: 10.5194/tc-9-565-2015

Hart JK. 1999. Identifying fast ice flow from landform assemblages in the geological record: A discussion. Annals of Glaciology **28** : 59–66. DOI: 10.3189/172756499781821887

Hart JK, Clayton AI, Martinez K, Robson BA. 2018. Erosional and depositional subglacial streamlining processes at Skálafellsjökull, Iceland: an analogue for a new bedform continuum model. Gff **140** : 153–169. DOI: 10.1080/11035897.2018.1477830

Icelandic Meteorological Office. 2020. Historical temperature measurements from Kirkjubæjarklaustur weather station (dataset) [online] Available from: https://www.vedur.is/Medaltalstoflur-txt/Stod_772_Kirkjubajarklaustur.ManMedal.txt

Icelandic Meteorological Office and Institute of Earth Sciences. 2013. DEMs of Icelandic glaciers (data set)

Ingólfsson Ó, Benediktsson ÍÖ, Schomacker A, Kjær KH, Brynjólfsson S, Jónsson SA, Korsgaard NJ, Johnson MD. 2016. Glacial geological studies of surge-type glaciers in Iceland - Research status and future challenges. Earth-Science Reviews **152** : 37–69. DOI: 10.1016/j.earscirev.2015.11.008

Ives LRW, Iverson NR. 2019. Genesis of glacial flutes inferred from observations at Múlajökull, Iceland. Geology **47** : 387–390. DOI: 10.1130/G45714.1

Jiskoot H, Boyle P, Murray T. 1998. The incidence of glacier surging in Svalbard: evidence from multivariate statistics. Computer Geosciences **24** : 387–399.

Jiskoot H, Murray T, Boyle P. 2000. Controls on the distribution of surge-type glaciers in Svalbard. Journal of Glaciology **46** : 412–422. DOI: 10.3189/172756500781833115

Johnson MD, Schomacker A, Benediktsson ÍÖ, Geiger AJ, Ferguson A, Ingólfsson Ó. 2010. Active drumlin field revealed at the margin of Múlajökull, Iceland: A surge-type glacier. Geology **38** : 943–946. DOI: 10.1130/G31371.1

Jónsson SA, Schomacker A, Benediktsson ÍÖ, Ingólfsson Ó, Johnson MD. 2014. The drumlin field and the geomorphology of the Múlajökull surge-type glacier, central Iceland. Geomorphology **207** : 213–220. DOI: 10.1016/j.geomorph.2013.11.007

Kamb B. 1987. Glacier surge mechanism based on linked cavity configuration of the basal water conduit system. Journal of Geophysical Research **92** : 9083–9100. DOI: 10.1029/JB092iB09p09083

Kamb B, Raymond CF, Harrison WD, Engelhardt H, Echelmeyer NH, Brugman MM, Pfeffer T. 1985. Glacier Surge Mechanism: 1982-1983 Surge of Variegated Glacier, Alaska. Science **227** : 469–479.

Kehew AE, Esch JM, Kozlowski AL, Ewald SK. 2012. Glacial landsystems and dynamics of the Saginaw Lobe of the Laurentide Ice Sheet, Michigan, USA. Quaternary International **260** : 21–31. DOI: 10.1016/j.quaint.2011.07.021

Kjær KH, Korsgaard NJ, Schomacker A. 2008. Impact of multiple glacier surges - a geomorphological map from Bruarjokull, East Iceland. Journal of Maps **4** : 5–20. DOI: 10.4113/jom.2008.91

Kjær KH, Krüger J, van der Meer JJM. 2003. What causes till thickness to change over distance? Answers from Mýrdalsjökull, Iceland. Quaternary Science Reviews **20** : 1687–1700. DOI: 10.1016/S0277-3791(03)00162-8

Kjær KH, Sultan L, Krüger J, Schomacker A. 2004. Architecture and sedimentation of outwash fans in front of the Mýrdalsjökull ice cap, Iceland. Sedimentary Geology **172** : 139–163. DOI: 10.1016/j.sedgeo.2004.08.002

Knudsen Ó. 1995. Concertina eskers, Brúarjökull, Iceland: An indicator of surge-type glacier behaviour. Quaternary Science Reviews **14** : 487–493. DOI: 10.1016/0277-3791(95)00018-K

Krüger J. 1988. Glacial geomorphological research at Mýrdalsjökull , Iceland, 1977-86. I: the northern margin. Geografisk Tidsskrift **88** : 68–77.

Krüger J, Kjær KH, Schomacker A. 2010. Dead-Ice Environments: A Landsystems Model for a Debris-Charged, Stagnant Lowland Glacier Margin, Kötlujökull. Developments in Quaternary Sciences **13** : 105–126. DOI: http://dx.doi.org/10.1016/S1571-0866(09)01307-4

Kyrke-Smith TM, Katz RF, Fowler AC. 2015. Subglacial hydrology as a control on emergence, scale, and spacing of ice streams. Journal of Geophysical Research: Earth Surface **120** : 1501–1514.

Landmælingar Islands. 1980a. Mælifell-Skaftárdalur, image F-8641 [aerial image] . National Land Survey of Iceland: Reykjavik [online] Available from: https://www.lmi.is/is/vefsjar/kortasjar/loftmyndasafn-1?fbclid=IwAR2ulEpjGF5QuRW2szjhL1QQQewB4pJAn_U16VtQMnWjcfHk2TngFpJ4qN4

Landmælingar Islands. 1980b. Nýja Eldhraun-Öldufellsjökull, image F-9339 [aerial image] . National Land Survey of Iceland: Reykjavik [online] Available from:

https://www.lmi.is/is/vefsjar/kortasjar/loftmyndasafn-1?fbclid=IwAR2ulEpjGF5QuRW2szjhL1QQQewB4pJAn_U16VtQMnWjcfHk2TngFpJ4qN4

Landmælingar Islands. 1984. Öldufellsjökull, image H-6416 [aerial image] . National Land Survey of Iceland: Reykjavik [online] Available from: https://www.lmi.is/is/vefsjar/kortasjar/loftmyndasafn-1?fbclid=IwAR3F5CrQLTK3y7pTQA6h2NKbd4px_LraVKKmQgnLgI2DOeawimL17s_vLs8

Landmælingar Islands. 1989. Mýrdalsjökull-Öldufellsjökull, image L-0909 [aerial image] . National Land Survey of Iceland: Reykjavik [online] Available from: https://www.lmi.is/is/vefsjar/kortasjar/loftmyndasafn-1?fbclid=IwAR2ulEpjGF5QuRW2szjhL1QQQewB4pJAn_U16VtQMnWjcfHk2TngFpJ4qN4

Landmælingar Islands. 1990. Hraun-Sléttjökull, image L-6129 [aerial image] . National Land Survey of Iceland: Reykjavik [online] Available from: https://www.lmi.is/is/vefsjar/kortasjar/loftmyndasafn-1?fbclid=IwAR2ulEpjGF5QuRW2szjhL1QQQewB4pJAn_U16VtQMnWjcfHk2TngFpJ4qN4

Lee RE, Maclachlan JC, Eyles CH. 2018. Landsystems of Morsárjökull, Skaftafellsjökull and Svínafellsjökull, outlet glaciers of the Vatnajökull Ice Cap, Iceland. Boreas **47** : 1199–1217. DOI: https://doi.org/10.1111/bor.12333

Mackay JR. 1973. The Growth of Pingos, Western Arctic Coast, Canada. Canadian Journal of Earth Sciences **10** : 979–1004. DOI: 10.1139/e73-086

Matsuoka N. 2011. Climate and material controls on periglacial soil processes: Toward improving periglacial climate indicators. Quaternary Research **75** : 356–365. DOI: 10.1016/j.yqres.2010.12.014

Mayer C, Jaenicke J, Lambrecht A, Braun L, Völksen C, Minet C, Münzer U. 2017. Local surface mass-balance reconstruction from a tephra layer - A case study on the northern slope of Mýrdalsjökull, Iceland. Journal of Glaciology **63** : 79–87. DOI: 10.1017/jog.2016.119

Van Der Meer JJM, Kjaer KH, Krüger J. 1999. Subglacial water-escape structures and till structures, Slettjokull, Iceland. Journal of Quaternary Science **14** : 191–205. DOI: 10.1002/(SICI)1099-1417(199905)14:3<191::AID-JQS436>3.0.CO;2-#

Meier MF, Post A. 1969. What are glacier surges? Canadian Journal of Earth Sciences **6** : 807–817.

Morse PD, Burn CR. 2014. Perennial frost blisters of the outer Mackenzie Delta, western Arctic coast, Canada. Earth Surface Processes and Landforms **39** : 200–213. DOI: 10.1002/esp.3439

Óladóttir BA, Sigmarsson O, Larsen G, Thordarson T. 2008. Katla volcano, Iceland: Magma composition, dynamics and eruption frequency as recorded by Holocene tephra layers. Bulletin of Volcanology **70** : 475–493. DOI: 10.1007/s00445-007-0150-5

Planet Team. 2017. Planet Application Program Interface: In Space for Life on Earth [online] Available from: https://api.planet.com

Raymond CF. 1987. How do glaciers surge? A review. Journal of Geophysical Research **92** : 9121–9134. DOI: 10.1029/JB092iB09p09121

Roberson S, Hubbard B, Coulson HR, Boomer I. 2011. Physical properties and formation of flutes at a polythermal valley glacier: Midre Lovénbreen, Svalbard. Geografiska Annaler, Series A: Physical Geography **93** : 71–88. DOI: 10.1111/j.1468-0459.2011.00420.x

Roberts DH, Yde JC, Knudsen NT, Long AJ, Lloyd JM. 2009. Ice marginal dynamics during surge activity, Kuannersuit Glacier, Disko Island, West Greenland. Quaternary Science Reviews **28** : 209–222. DOI: 10.1016/j.quascirev.2008.10.022

Rose J. 1989. Glacier stress patterns and sediment transfer associated with the formation of superimposed flutes. Sedimentary Geology **62** : 151–176. DOI: 10.1016/0037-0738(89)90113-9

Schomacker A, Benediktsson ÍÖ, Ingólfsson Ó. 2014. The Eyjabakkajökull glacial landsystem, Iceland: Geomorphic impact of multiple surges. Geomorphology **218** : 98–107. DOI: 10.1016/j.geomorph.2013.07.005

Schomacker A, Kjær KH, Krüger J. 2010. Subglacial Environments, Sediments and Landforms at the Margins of Mýrdalsjökull. Developments in Quaternary Sciences **13** : 127–144.

Schomacker A, Krüger J, Kjær KH. 2006. Ice-cored drumlins at the surge-type glacier Brúarjökull, Iceland: A transitional-state landform. Journal of Quaternary Science **21** : 85–93. DOI: 10.1002/jqs.949

Sevestre H, Benn DI. 2015. Climatic and geometric controls on the global distribution of surge-type glaciers: Implications for a unifying model of surging. Journal of Glaciology **61** : 646–662. DOI: 10.3189/2015JoG14J136

Sharp MJ. 1985a. " Crevasse-Fill " Ridges : A Landform Type Characteristic of Surging Glaciers ? Geografiska Annaler, Series A: Physical Geography **67** : 213–220.

Sharp MJ. 1985b. Sedimentation and stratigraphy at Eyjabakkajökull-An Icelandic surging glacier. Quaternary Research **24** : 268–284. DOI: 10.1016/0033-5894(85)90050-X

Sharp MJ. 1988. Surging glaciers: Behaviour and mechanisms. Progress in Physical Geography **12** : 349–370. DOI: 10.1177/030913338801200302

Sigurðsson O. 2003. Variations of Mýrdalsjökull during Postglacial and Historical Times. Developments in Quaternary Sciences **13** : 69–78.

Smith MJ, Clark CD. 2005. Methods for the visualization of digital elevation models for landform mapping. Earth Surface Processes and Landforms **30** : 885–900. DOI: 10.1002/esp.1210

Spedding N, Evans DJA. 2002. Sediments and landforms at Kvíárjökull, southeast Iceland: a reappraisal of the glaciated valley landsystem. Sedimentary Geology **149** : 21–42. DOI: 10.1016/S0037-0738(01)00242-1

Stokes CR. 2018. Geomorphology under ice streams: Moving from form to process. Earth Surface Processes and Landforms **43** : 85–123. DOI: 10.1002/esp.4259

Stokes CR, Clark CD. 1999. Geomorphological criteria for identifying Pleistocene ice streams.pdf. Annals of Glaciology **28** : 67–74.

Stokes CR, Margold M, Clark CD, Tarasov L. 2016. Ice stream activity scaled to ice sheet volume during Laurentide Ice Sheet deglaciation. Nature **530** : 322–326. DOI: 10.1038/nature16947 [online] Available from: http://dx.doi.org/10.1038/nature16947

Striberger J, Björck S, Benediktsson ÍÖ, Snowball I, Uvo CB, Ingólfsson Ó, Kjær KH. 2011. Climatic control of the surge periodicity of an Icelandic outlet glacier. Journal of Quaternary Science **26** : 561–565. DOI: 10.1002/jqs.1527

Sturkell E, Einarsson P, Sigmundsson F, Hooper A, Ófeigsson BG, Geirsson H, Ólafsson H. 2010. Katla and Eyjafjallajökull Volcanoes. Developments in Quaternary Sciences **13** : 5–21.

Sturkell E, Sigmundsson F. 2003. Recent unrest and magma movements at Eyjafjallajökull and Katla volcanoes, Iceland. Journal of Geophysical Research **108** : 1–13. DOI: 10.1029/2001jb000917

Washburn AL. 1980. Permafrost features as evidence of climatic change. Earth Science Reviews **15** : 327–402. DOI: 10.1016/0012-8252(80)90114-2

Westoby MJ, Brasington J, Glasser NF, Hambrey MJ, Reynolds JM. 2012. "Structure-from-Motion" photogrammetry: A low-cost, effective tool for geoscience applications. Geomorphology **179** : 300–314. DOI: 10.1016/j.geomorph.2012.08.021

WGMS. 2017. Fluctuations of Glaciers Database. DOI: 10.5904/wgms-fog-2017-10 [online] Available from: http://dx.doi.org/10.5904/wgms-fog-2017-10

Winsborrow MCM, Clark CD, Stokes CR. 2010. What controls the location of ice streams? Earth-Science Reviews **103** : 45–59. DOI: 10.1016/j.earscirev.2010.07.003 [online] Available from: http://dx.doi.org/10.1016/j.earscirev.2010.07.003

Wolfe SA, Stevens CW, Gaanderse AJ, Oldenborger GA. 2014. Lithalsa distribution, morphology and landscape associations in the Great Slave Lowland, Northwest Territories, Canada. Geomorphology **204** : 302–313. DOI: 10.1016/j.geomorph.2013.08.014

Þórarinsson S. 1957. The jökulhlaup from the Katla area in 1955 compared with other Jökulhlaups in Iceland. Jökull **7** : 21–25.

Chapter Three: Lithological controls on erosion processes and rates along the Niagara Escarpment in Hamilton, Ontario.

Abstract

The Niagara Escarpment is an actively forming landscape feature undergoing continual erosion resulting in catastrophic rock failures, particularly in areas where it presents as a steep rock face. Its erosion poses a threat to infrastructure and safety in urbanized areas, such as Hamilton in which the escarpment divides the city into its lower and upper regions. In Hamilton, there are 19 access roads and abundant trails that traverse the escarpment, as well as many houses and buildings located near the edge. Recent rock falls and slope movements have raised concerns on the stability of the feature necessitating a further understanding of the erosional processes occurring in the region. There are many factors which can influence the rate of erosion including the mechanical strength of the rock, distribution of rock types, fracture characteristics, hydrological properties of the site and climatological characteristics. Many of these factors are controlled or impacted by the lithology of the unit and therefore to understand erosion a detailed analysis of the lithology of a region is required. This study uses sedimentological analysis of 11 study sites in the Hamilton region to determine the vertical and horizontal lithological variability in the formations of the Niagara Escarpment. From this, the potential factors influencing erosion are discussed and the relative potential for erosion is determined. Lithological units exposed along the escarpment can be broadly divided into those that are shale-, sandstone- or dolostone-dominated, each type potentially impacted by different erosion processes. Shale-dominated formations are likely the most critical in establishing overall stability of the rock face as they erode most rapidly, undercutting the resistant lithologies and creating an unstable system which can cause rock falls. Dolostone-dominated formations are exposed frequently at the study sites and are more prominently located near the top of the escarpment face. These formations erode primarily through block toppling, controlled by their fracture characteristics, where greater density of fractures and the abundance of shale interbeds relates to higher potential for erosion.

Sandstone-dominated lithological units are less frequently exposed in Hamilton and are therefore not significant contributors to the overall erosion of the rock face. Erosion of these units is controlled in part by their fracture characteristics and abundance of shale. The stratigraphic juxtaposition of lithological types with different susceptibilities to erosion appears to be a critical

factor controlling the processes and rates of rock failure along the exposed rock face. Lateral variability of lithological characteristics along the escarpment results in a potential for greater amounts of rock failure and erosion in some areas of the city. Exposed rock faces containing significant amounts of shale interbedded with highly fractured dolostone and sandstone are likely to have the highest potential for erosion.

Key words; Erosion processes; Niagara Escarpment; Sedimentology

3. 1 Introduction

The Niagara Escarpment is a significant geomorphological feature, extending from New York State through southern Ontario, into Michigan and Wisconsin (Figure 3.1; Hewitt, 1971; Tinkler & Pengelly, 1994; Luczaj, 2013). It is an actively forming landscape feature with periodic catastrophic rock slope failures occurring particularly in areas where it forms a steep rock face (Philbrick, 1970; Hayakawa & Matsukura, 2009). The Niagara Escarpment bisects the city of Hamilton, located on the western edge of Lake Ontario, and separates the lower downtown core from upper residential and agricultural regions. Beginning in the mid 1800s, privately built access roads and inclined railways were constructed on the escarpment, in convenient locations with little consideration of their impact on the stability of the exposed rock face. Currently, nineteen access routes, ranging from one-way single lane roads to major highways, traverse the escarpment within the city of Hamilton, many of which have been developed on the foundations of the earlier constructed roadways.

Steep slopes on the sides of road cuts can fail for many reasons and may occur through continual and/or catastrophic events. Along road cuts crossing the Niagara Escarpment in Hamilton, such failures pose a threat to motorists, to houses and infrastructure located near the escarpment edge, and require continuous and costly repairs to retaining walls, fences, and barriers (Admassu et al., 2012; Miščević & Vlastelica, 2014). A considerable number of rock falls have occurred within the last decade, including major falls onto the Claremont and Sherman access routes (Figure 3.2A, B) and have raised public awareness and concern about the safety of the roads crossing the escarpment and disruption to traffic flow (CBC, 2014; Van Dongen, 2017; Mann, 2019). The continued retreat of the escarpment in Hamilton also impacts the stability and safety of more than 1000 homes that lie within 50 m of the escarpment face, as well as hospitals, apartment

buildings and other structures (Figure 3.2C). In some areas, fences, trees, and pipes can be observed hanging precariously over the escarpment edge (Figure 3.2D).

Figure 3.1: Location of the Niagara Escarpment (red line) extending from New York, through southern Ontario, Michigan, Wisconsin, and Illinois. Location of Hamilton at the western edge of Lake Ontario indicated with a star.

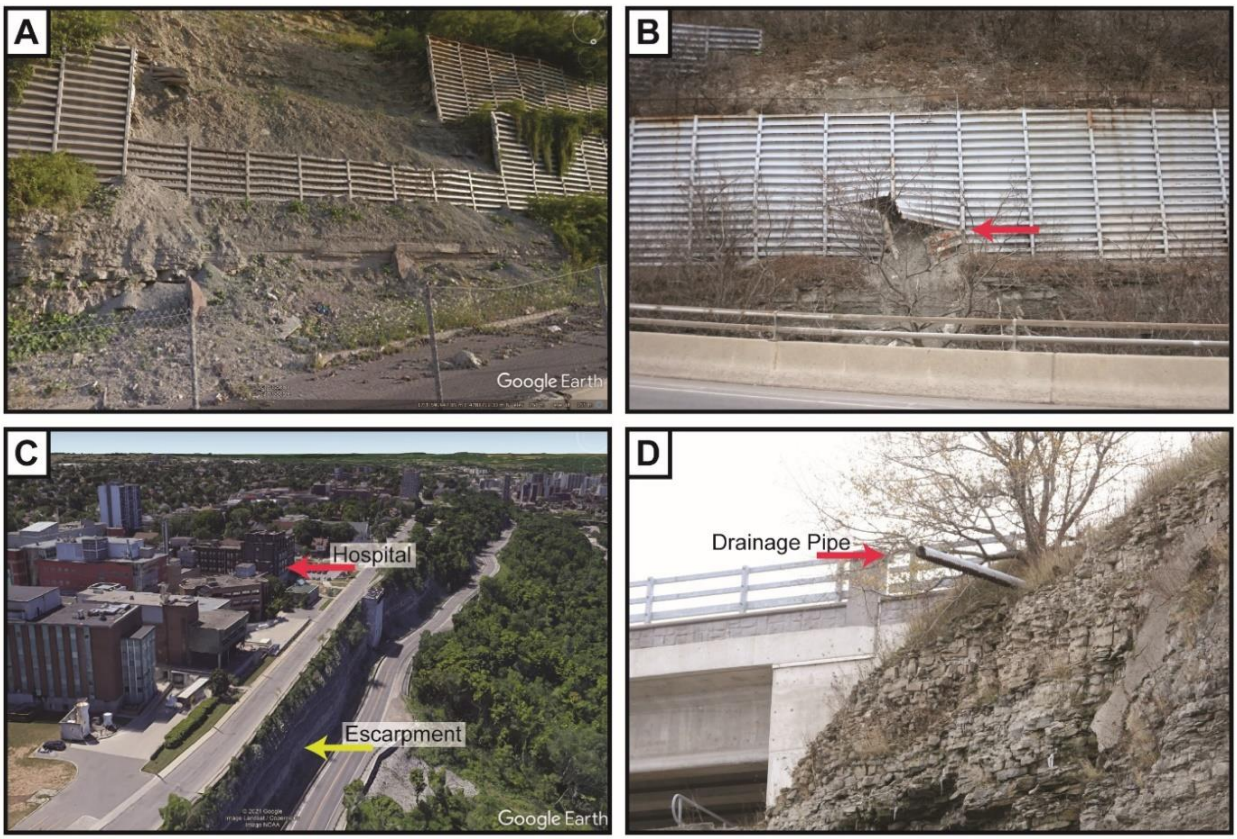

Figure 3.2: A) Image of a small rockfall and broken retaining walls along the Claremont Access in 2020 (Google, 2021a); B) Broken retaining wall indicated by red arrow on Claremont Access caused by slope movement; C) Proximity of buildings to the escarpment edge (Google, 2021b); D) Drainage pipe extending over a metre from the escarpment edge at Sherman Access.

Although erosion and rock falls are of significant concern to residents of the city of Hamilton, little is known about the exact nature of erosional processes, their rates, or of the spatial variability of factors contributing to failure of the rock face along the escarpment. These factors include lateral and vertical lithological variability, fracture density and distribution, climatic factors (including seasonal temperature changes), and surface and groundwater movement. To begin to address this issue, this study focuses on identification of factors related to lithological variability along the Niagara Escarpment within the city of Hamilton and their effect on erosion processes and rates. A series of eleven study sites on the escarpment were selected for investigation (Figure 3.3).

Figure 3.3: Map of study sites (blue dots) along the Niagara Escarpment (shown in red) within Hamilton, Ontario (Google Earth 2019).

3.1.1 Geological Background

The Niagara Escarpment is a significant geological feature crossing southern Ontario with a maximum height of 266 m at 'The Caves' near Craigleith and a local maximum height of approximately 100 m in Hamilton (Hewitt, 1971). The escarpment extends from Niagara Falls, through Hamilton, continuing northwards to form the eastern shoreline of the Bruce Peninsula (Figure 3.4A; Hewitt, 1971). The lithologic units exposed along the Niagara Escarpment are Paleozoic sedimentary rocks, deposited in shallow epeiric seas contained within the Appalachian and Michigan Basins during the Late Ordovician and Silurian Periods (Tepper et al., 1990; Armstrong & Dodge, 2007; Brunton & Brintnell, 2020); these lithological units are relatively flat lying, with a dip of approximately 5.5 m/km to the south in the region of the Niagara Peninsula (Figure 3.4B; Brigham, 1971; Feenstra, 1981; Tepper et al., 1987).

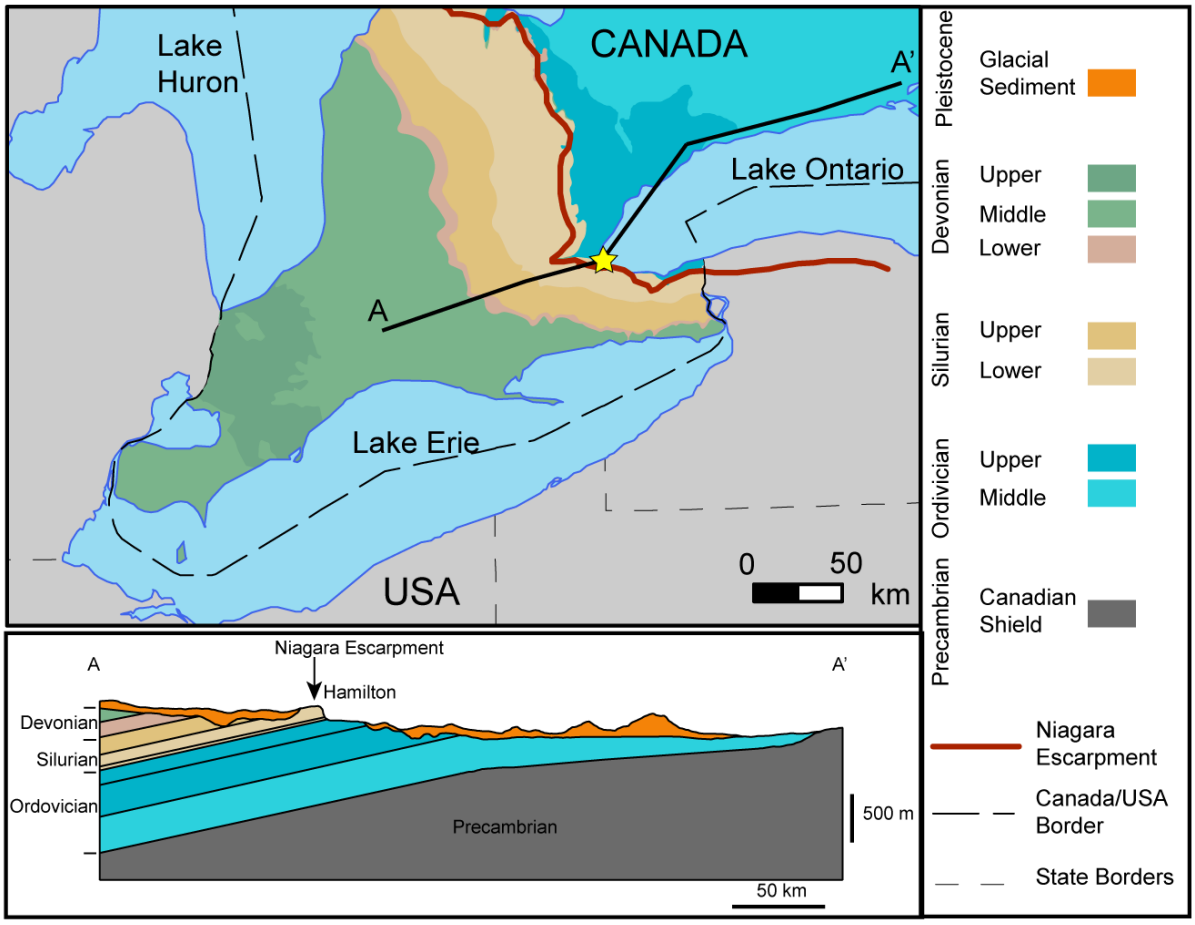

Figure 3.4: Bedrock geological map of southern Ontario (Ontario Geological Survey 2006). The cross-section A-A' highlights the gentle dip of the Paleozoic bedrock to the southwest. Glacial sediments of variable thickness deposited during the last glaciation overlie the bedrock. Hamilton is located at the yellow star, at the western end of Lake Ontario. Niagara Escarpment is shown by the red line (adapted from Eyles 2002).

The Paleozoic stratigraphy exposed along the Niagara Escarpment varies significantly across its length and results from changes in depositional conditions, changing sediment supply, and topographical variability, caused primarily by the presence and uplift of the Algonquin Arch north of Lake Ontario (Figure 3.4A; Bolton, 1957; Brett, Goodman, & LoDuca, 1990). The lowermost lithological units exposed at the base of the Niagara Escarpment along the Niagara Peninsula are composed of deltaic and marine sediments eroded from the uplifting Taconic Mountains (Bolton, 1957; Hewitt, 1971; Brett et al., 1990). The late Ordovician Queenston Formation, can be found throughout southern Ontario, thinning from 335 m beneath Lake Erie to approximately 45 m on the Bruce Peninsula to the northwest (Figure 3.5; Caley 1940; Johnson et

al. 1990; Armstrong and Dodge 2007). The overlying Medina Group, consisting of the Whirlpool Formation, Manitoulin Formation, Cabot Head Formation, Grimsby Formation, and Thorold Formation, was deposited during the lower Silurian (Figure 3.6). The Whirlpool unconformably overlies the Queenston Shale, thins towards the west and north, and was deposited in fluvial to storm influenced shallow marine environments (Figures 3.5 and 3.6; Brett et al., 1990; Barlow, 2002). In Hamilton, the Whirlpool is overlain by dolostones of the Manitoulin, and dark grey shales of the Cabot Head; both formations have a southern limit in eastern Hamilton and thicken towards the north (Figure 3.6; Anastas & Coniglio, 1993). The uppermost units of the Medina Group are red shales of the Grimsby, and sandstones of the Thorold Formations which extend from Niagara Falls in the east to northwest of Hamilton (Figure 3.5; Hewitt, 1971; Brintnell et al., 2009).

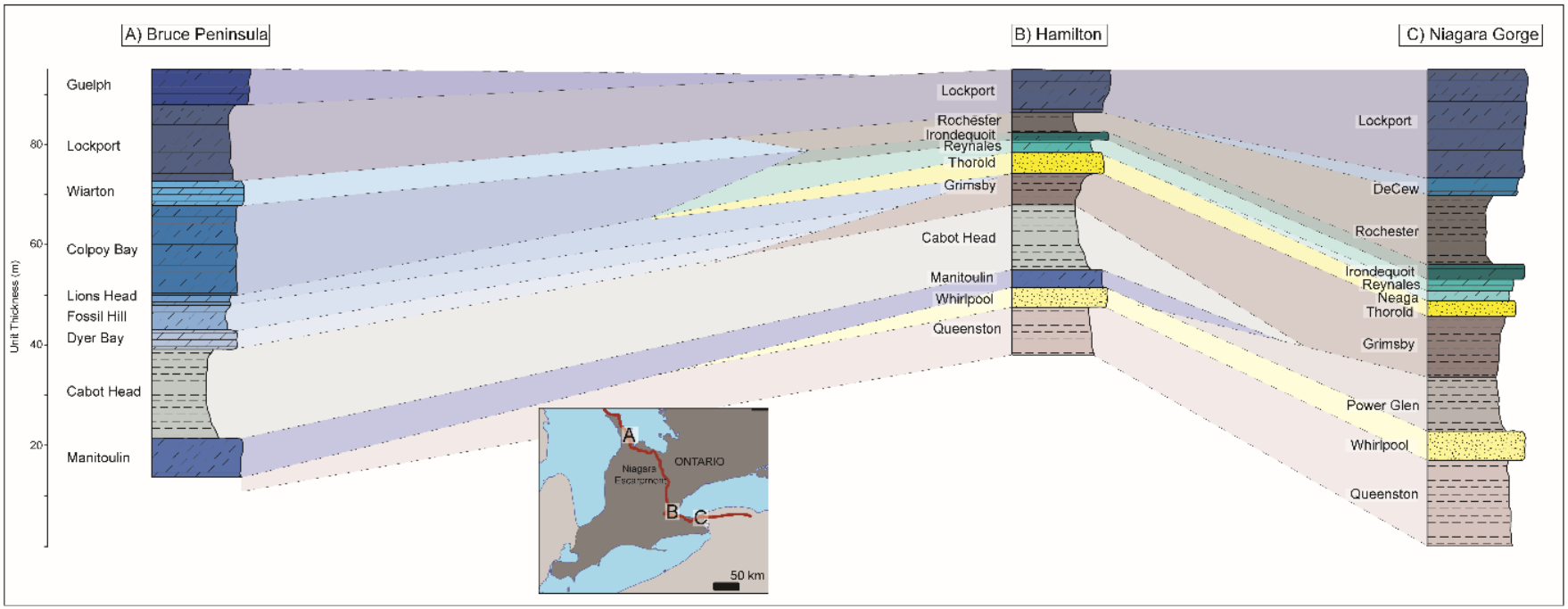

Figure 3.5: Schematic logs showing lithological changes along the Niagara Escarpment in southern Ontario, from the Bruce Peninsula in the northwest to the Niagara Gorge in the southeast. Composite graphic logs based on information from Bolton 1957 (A); this study (B); Hewitt 1971(C). There are significant changes in lithological characteristics, unit thicknesses, and the type of sedimentary structures preserved and now exposed along the escarpment resulting from variations in sediment supply, topography, and paleoenvironmental conditions during deposition.

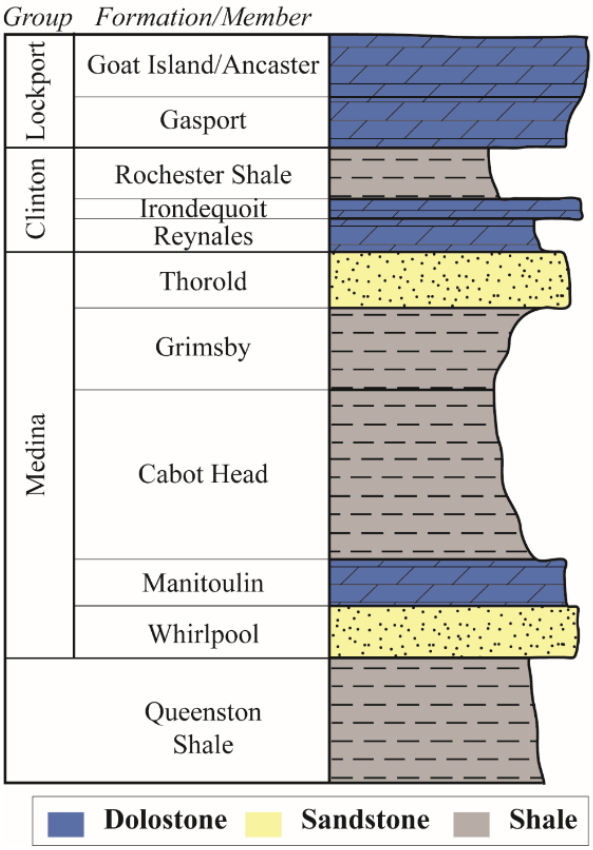

Figure 3.6: Schematic sedimentary log of the Niagara Escarpment in the Hamilton region showing dominant lithologies.

The Clinton Group overlies the Medina Group and consists of the Reynales Formation, Irondequoit Formation, Rochester Formation and DeCew Formation which each thin from Niagara Falls toward Hamilton (Figures 3.5 and 3.6; Caley, 1940; Johnson et al., 1992; Armstrong & Carter, 2009). Across the 22km length of the Niagara Escarpment in Hamilton, significant changes in the thickness of these units can be observed; for example, the Rochester Shale thins from approximately 10 m in eastern Hamilton to 3 m in the northwest (Johnson et al., 1992). The uppermost lithological units forming the resistant caprock of the Niagara Escarpment belong to the dolomitic Lockport Group which includes the Gasport Formation, Goat Island Formation and Eramosa Formation (Figures 3.5 and 3.6; Hewitt, 1971; Armstrong & Dodge, 2007; Brunton & Brintnell, 2020; Carter et al., 2021).

Many of the units exposed along the Niagara Escarpment show considerable spatial variability in terms of their lithological characteristics and thicknesses in the Hamilton area (Figure

3.5). It has been suggested that these changes may be related to the development of a relative topographic high in the Hamilton area at the time of deposition (Crowley, 1973; Brett et al., 1990). This spatial lithological variability also creates considerable complexity for the identification and interpretation of factors that control erosional processes active along the escarpment, and how they differ from one area of the city to another.

3.1.2 Erosion of the Niagara Escarpment

Although timing of the initial formation of the Niagara Escarpment is unknown, its development was undoubtedly enhanced by scouring and erosion of exposed Paleozoic bedrock by glacial and fluvial processes during the Pleistocene (Straw, 1968); many of these erosional processes have continued to operate since deglaciation, approximately 12 500 years ago, up to the present day. Erosion rates caused by fluvial erosion of the Horseshoe Falls, creating the Niagara Gorge, are estimated to be approximately 1 m/year since deglaciation (Hayakawa & Matsukura, 2009); these rates are probably higher than most, due to the aggressive force of the fast-flowing Niagara River.

3. 2 Methods

To address the concerns of escarpment stability it is necessary to understand the influence of geology on processes affecting erosion rates and erosion risk along the escarpment face. As previously discussed, there is significant spatial variability in the thickness, distribution, and characteristics of the lithologic units exposed along the Niagara Escarpment in the Hamilton region. The main characteristics considered in this study to have direct impact on erosional processes are the vertical lithological variation at each study site, the horizontal lithological variation between sites, and the geotechnical properties of the rocks exposed along the escarpment face. A workflow process was designed to integrate primary field data collected for this study with additional, mostly geotechnical, information from previously published reports (Figure 3.7). To examine the lateral variability of the lithologies exposed along the escarpment within Hamilton, eleven study sites located over 22 km were selected (Figure 3.3). At each site imagery was collected using a DSLR camera and, in appropriate locations, a Phantom 4 Advanced unpiloted aerial vehicle (UAV) was used. Sedimentological and geomorphological characteristics of the outcrops were recorded, and detailed sedimentological logs were created for selected sites (Figures 3.7 and 3.8). Photomosaics compiled from collected imagery were used for sediment logging when outcrops were inaccessible.

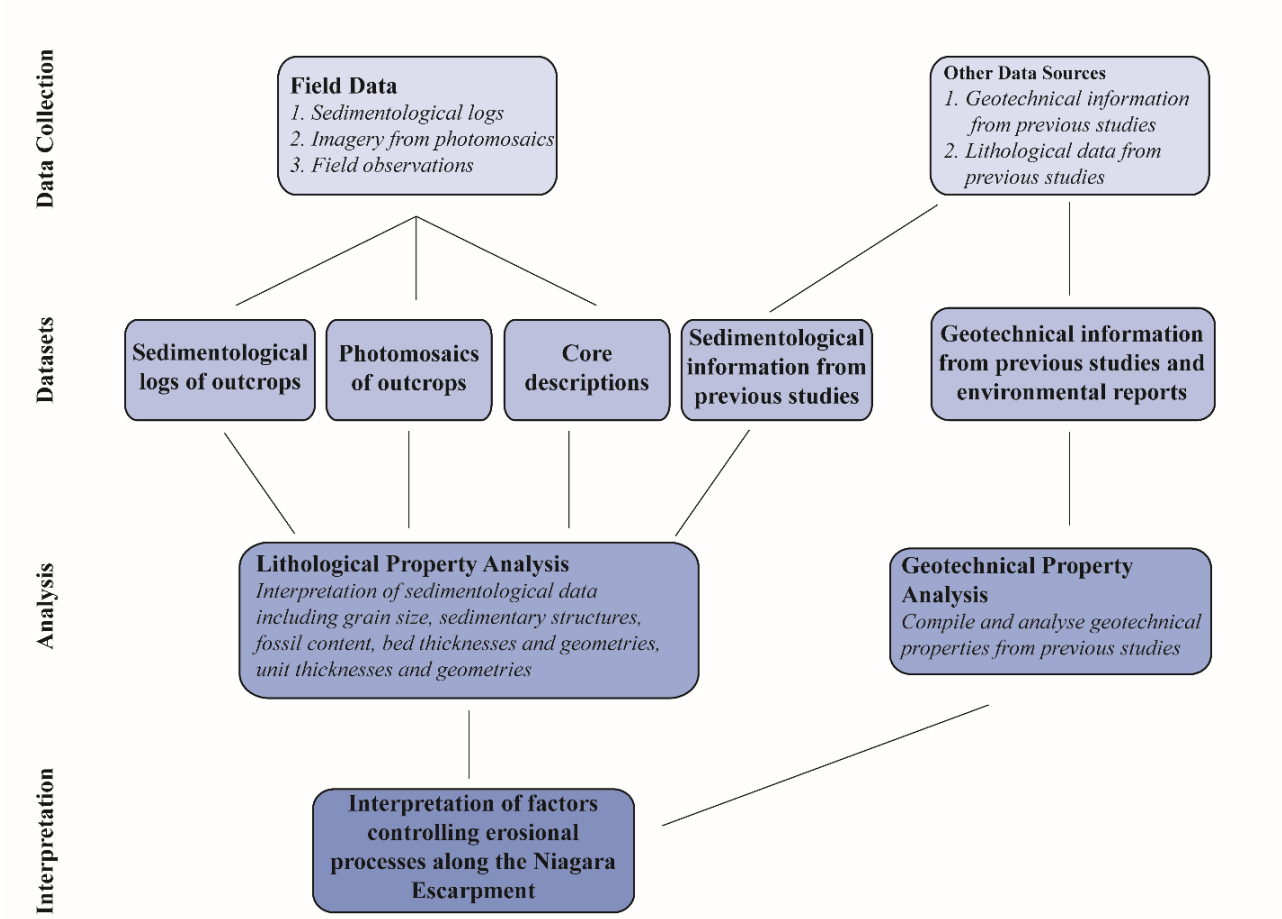

Figure 3.7: Flow diagram of the methodology used within this study.

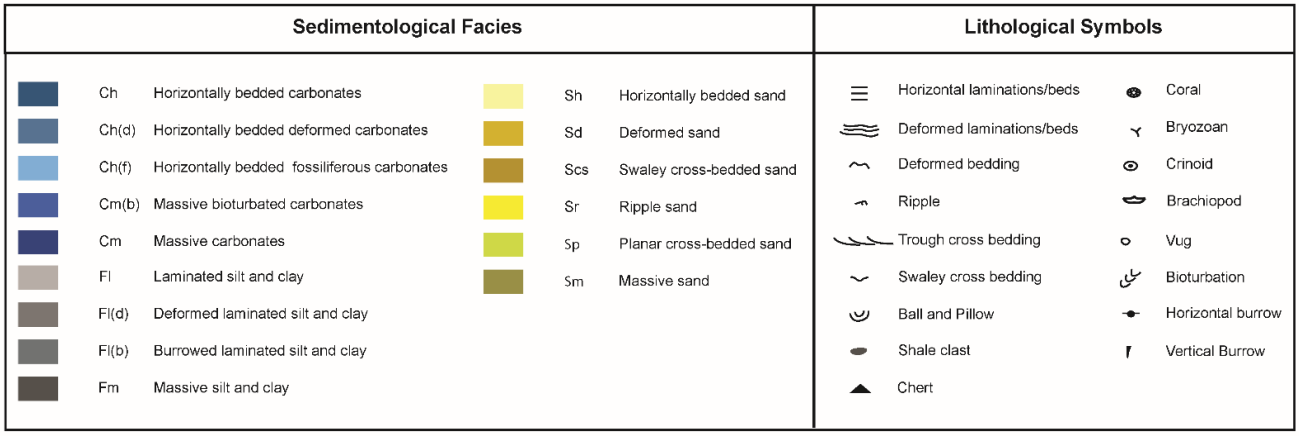

Figure 3.8: Symbology and facies codes used in this study.

Lithological characteristics of the deposits recorded during this process focused on documenting the type of rock (including grain size and sedimentary structures), unit thickness and geometry, and bed thickness and geometry. Facies codes were used to describe both the clastic and carbonate deposits exposed along the escarpment (Figure 3.8). In addition to the field data collected, a 46 m long core, obtained from a borehole drilled close to the Claremont Access route for hydrogeological investigations, and which contained each of the lithological units exposed along the escarpment, was examined and logged.

To complement the lithological analysis, a review of previous studies describing the geotechnical properties of rock types exposed along the Niagara Escarpment (e.g. Palmer and Lo, 1976; ; Lo et al., 1978; Lo, 1978, 1989Lo and Hori, 1979; Lo and Lee, 1990; Lam et al., 2007; Hayakawa and Matsukura, 2009; Al-Maamori et al., 2014; Perras et al., 2014) was completed to evaluate the variability of rock strength. When discussing the mechanical strength of rock, a common metric used is the unconfined compressive strength (UCS), a measure of the maximum axial stress, a cylindrical sample of rock under unconfined conditions is able to withstand (Agustawijaya, 2007). Integrated analysis of lithological characteristics and geotechnical properties allows for a more complete understanding of factors that may be influencing erosional processes along the Niagara Escarpment.

3. 3 Lithological Descriptions

The lithological units exposed along the escarpment will be described starting from the base and moving upwards through the stratigraphy. These descriptions are based on outcrop and core data collected from field sites in the city of Hamilton (Figure 3.3).

3.3.1 Queenston Formation

The Queenston Formation is exposed at the base of the escarpment in the Hamilton region, and although it is covered in most locations, it does outcrop at the Claremont Access route and at Devil's Punchbowl (Sites 6, 10; Figure 3.9), and can be seen in core (Site 6a; Figures 3.9, 3.10 and 3.11A). The Queenston is composed primarily of finely laminated brick red shale (Fl), with thin interbeds of siltstone (Figures 3.10 and 3.12), and appears to show an increase in silt up-section in core (Figure 3.10). The upper 25 cm – 50 cm of this formation is composed of a grey-green shale, in contrast to the distinctive red colour below (Figures 3.11A and 3.13A). A sharp upper contact exhibiting well developed mudcracks separates the Queenston from the overlying Whirlpool Formation (Figure 3.13B). The Queenston Formation is interpreted to have formed in a shallow

muddy shoreline environment on a delta influenced by tides and waves; after deposition, the region experienced periods of subaerial exposure, indicated by the development of mudcracks, and the erosion of fluvial channels (Sanford et al., 1972; Brogly et al., 1998).

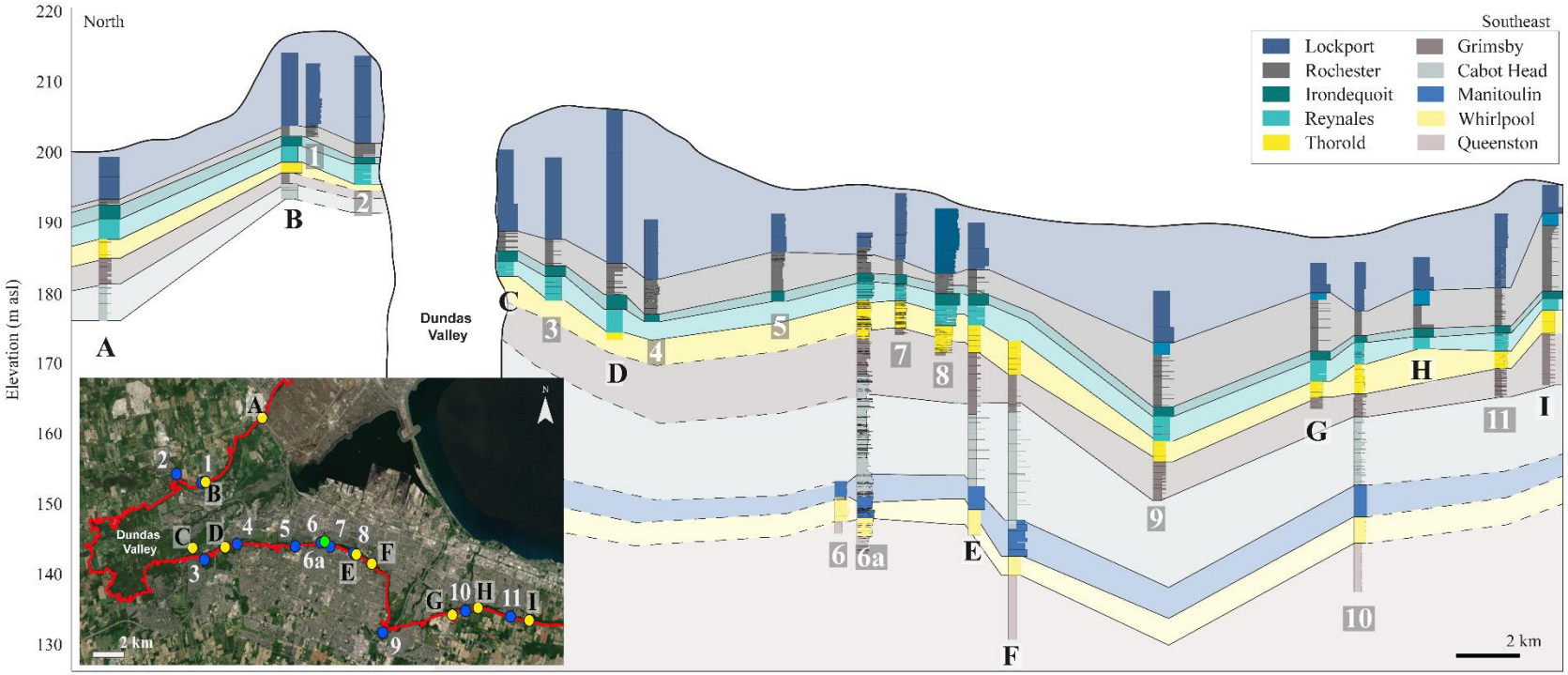

Figure 3.9: Cross section showing the geometry of lithological units exposed along the Niagara Escarpment from Clappison's Corner (Site A) in the northwest to Fruitland Road (Site I) in eastern Hamilton. Locations of the sites are indicated on the inset map, with the brow of the Niagara Escarpment shown as a red line. Sedimentological logs based on outcrop data are indicated by blue markers on the inset map and white numbering. Sedimentological log based on core data is indicated by a green marker on the inset map and white numbering (6a). Sedimentological logs based on data reported by Bolton (1957) are indicated using yellow markers on the inset map and black letters.

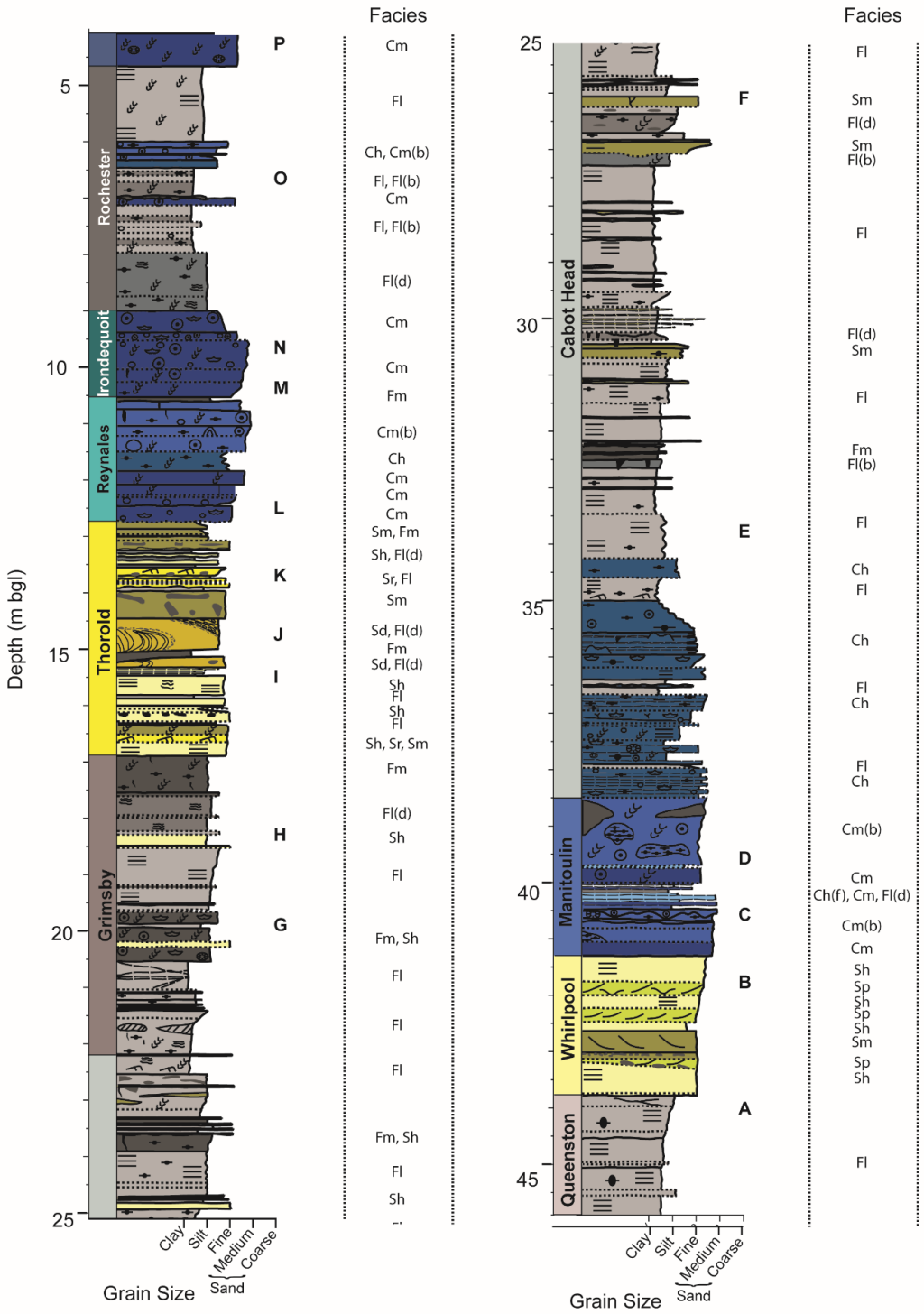

Figure 3.10: Sedimentological log of the 45.67m-long core taken close to the Claremont Access route (Site 6a; Figure 3.9) with formation names indicated on left of log. Top of core at upper left of figure, base at lower right. Note that most of the Lockport Group is missing from the top of the core. Location of images shown in Figure 3.11 indicated by letters to right of log. Refer to Figure 3.8 for symbology.


A
B
Wave Ripples
Crossbeds
C
Coral
D
Shale
Dolostone
Burrows
Brachiopod
E
F
Shale
Sandstone
G
Burrows
Brachiopod
H
Shale
Sandstone
I
J
K
L
Burrows
Vugs
M
N
Fossils
O
Burrows
P

Figure 3.11: A) Contact between red and grey shale at the top of the Queenston Formation; B) Crossbeds and wave ripples in the fine-grained sandstone of the Whirlpool Formation; C) Heavily bioturbated dolostone-dominated base of the Manitoulin Formation with coral fossil; D) Shale and dolostone interbeds of the Manitoulin Formation; E) Grey shale of the Cabot Head Formation; F) Sandstone and shale interbeds of the uppermost unit of the Cabot Head Formation; G) Abundant burrows in the red shale at the base of the Grimsby Formation; H) Shale and sandstone interbeds at the top of the Grimsby Formation; I, J) Deformation structures present in the Thorold Formation; K) Sandstone interbedded with deformed shale layers in the Thorold Formation; L) Vugs and burrows in the dolostones of the Reynales Formation; M) Calcite filled vug in the Irondequoit Formation; N) Oxidized fossil fragment rich section of the Irondequoit Formation; O) Burrows and bioturbation within the shales of the Rochester Formation; P) Large coral fragments and vugs in the dolostone of the Gasport Formation. Location of core sections indicated on Figure 3.10.

3.3.2 Whirlpool Formation

Lying unconformably above the Queenston is the Whirlpool Formation, a fine-grained quartz sandstone containing ripples, low angle trough and planar crossbeds, and channel structures that often protrude from the escarpment face when exposed (Figures 3.10, 3.11B and 3.12). Bed thickness changes from predominantly thick beds at the base (up to 2 m) to thinner sandstone beds (1 cm - 5 cm) interbedded with thin shale beds in the upper part of the formation (Figure 10; Hewitt, 1971; Armstrong & Carter, 2009). The Whirlpool does not outcrop frequently in Hamilton but is well exposed at the Claremont Access route and the Devil's Punchbowl (Sites 6, 10, Figure 3.9) and can be examined in core (Figure 3.10). In core, the Whirlpool includes interbedded units of horizontally bedded (Sh), crossbedded (Sp), and massive (Sm) fine- to very fine-grained sandstone (Figures 3.10 and 3.11B). Channel structures and planar crossbeds are visible at both exposed outcrops within Hamilton (Figures 3.12 and 3.13C).

The Whirlpool Formation shows significant lithological variation across the Hamilton region and thins from approximately 3.6 m in the east to 2.4 m in the west (Figure 3.9; Caley, 1940; Johnson et al., 1992; Armstrong & Carter, 2009). In the west, bedding within the Whirlpool appears to be thicker, with channelized sandstone units up to 2m thick (Figure 3.13C, D); in contrast, bedding is thinner and more irregular in the east, with more crossbedding and ripple structures (Figure 3.13E). The prevalence of channelized and cross-bedded facies within the Whirlpool Formation indicates that the primary environment of deposition was fluvial or shallow marine, representing a significant lowering of sea level from the time of deposition of the Queenston Formation shale (Brett et al., 1990)

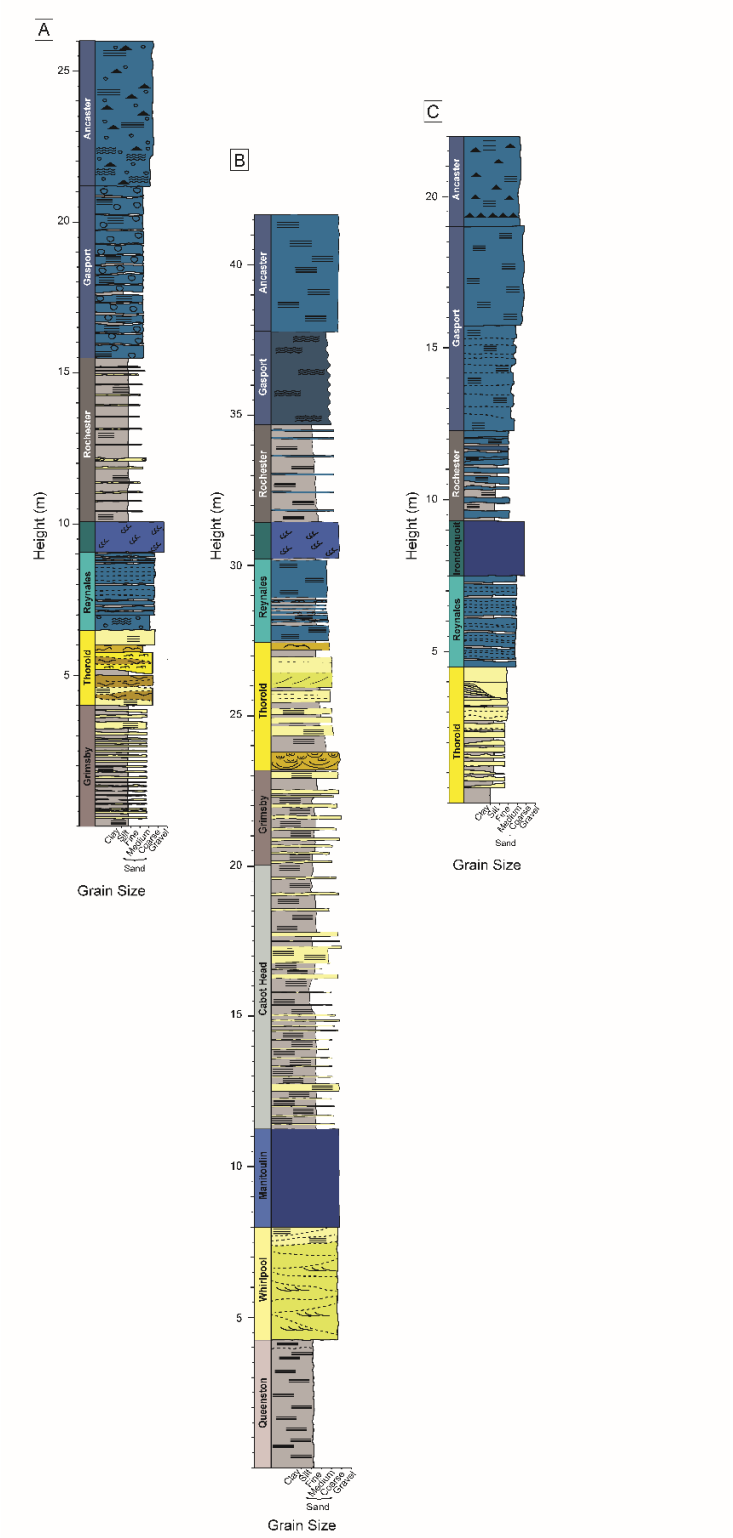

Figure 3.12: Detailed sedimentological logs based on A) Outcrop at Dewitt Road (Site 11); B) Outcrop and photomosaics of the Devil's Punchbowl (Site 10); C) Outcrop at Sherman Access (Site 8). The relative vertical position of the logs is based on the location of the top of the Irondequoit Formation. Refer to Figure 3.8 for symbology, Figure 3.9 for site location.

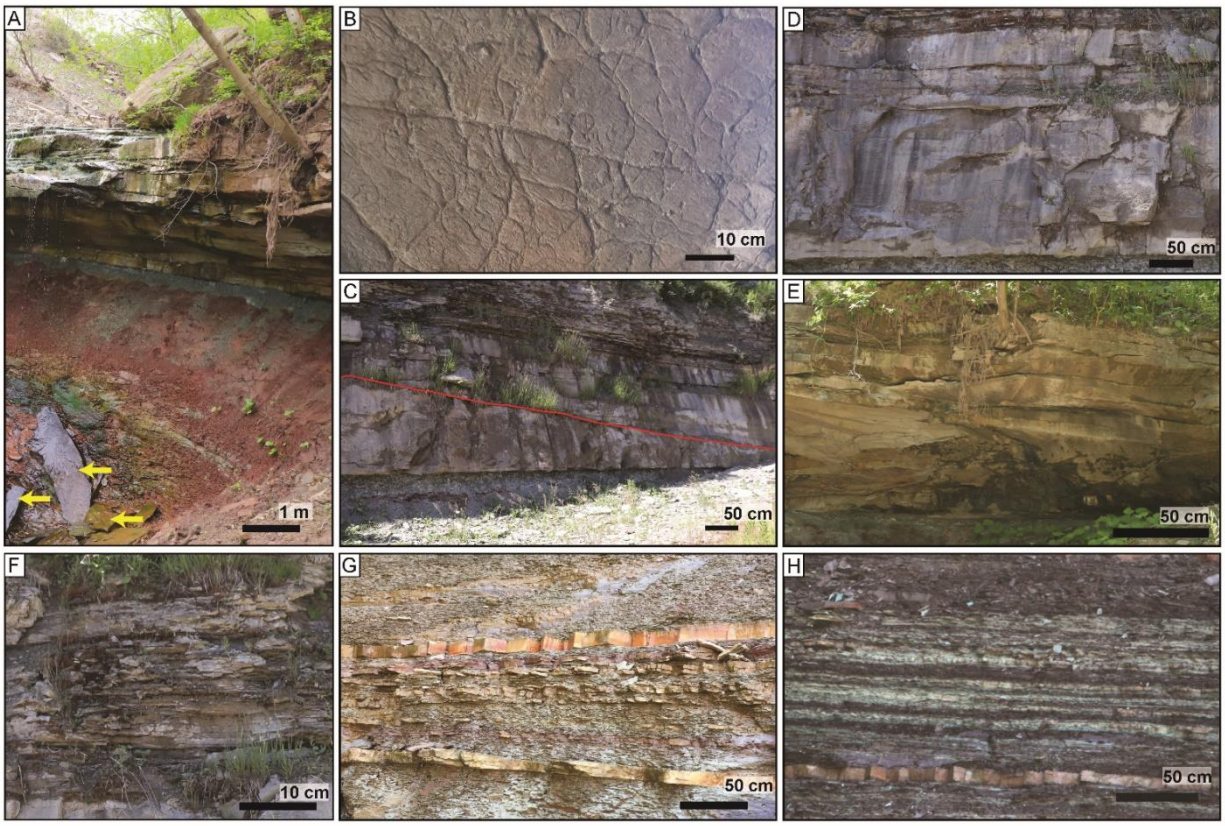

Figure 3.13: : A) Undercutting of Whirlpool Formation sandstones by erosion of the underlying Queenston Formation, composed primarily of red shale, with a band of grey-green shale in the upper 30 cm. Large sandstone blocks from the Whirlpool can be observed at the base of the rock face (indicated with yellow arrows); B) Underside of the Whirlpool formation showing the cast of mudcracks found on the upper surface of the Queenston Shale; C) Image from Claremont Access (Site 6) showing the Whirlpool Formation; outlined in red is a channel cut and fill; D) Whirlpool Formation at Site 6 which exhibits thickly bedded (0.5 m – 1 m), structureless sandstone; E) Whirlpool Formation at Site 10 (consists of thin beds (0.1 m – 0.3 m) of cross bedded and rippled sandstone; F) Thin bedded dolostone and shale of the Manitoulin Formation at Site 6; G) Cabot Head Formation at the Devil's Punchbowl (Site 10) showing the interbeds of shale with dolostone and sandstone; H) Grimsby Formation at the Devil's Punchbowl (Site 10) dominated by shale with thin interbeds of sandstone and dolostone, Location of sites shown in Figure 3.9.

3.3.3 Manitoulin Formation

The dolostone-rich Manitoulin Formation is well exposed in two areas of Hamilton, at Claremont Access and the Devil's Punchbowl (Site 6 and 10; Figure 3.9) and can also be viewed in core (Site 6a). At the eastern end of Hamilton (e.g., Site 10), the Manitoulin is composed primarily of massive dolostone (Cm), whereas in central Hamilton, the formation appears as a thinly bedded dolostone with frequent shale interbeds (Figure 3.13F).

In core, the Manitoulin is characterized by irregular beds of massive and horizontally bedded dolostone (Cm, Ch, Ch(f); 2-5 cm thick) interbedded with thin shale beds (Fl; Fl(d);1-3 cm) which become increasingly common up-section (Figures 3.10 and 3.11C, D). The Manitoulin increases in thickness across the city, from approximately 1.3 m in eastern Hamilton to 3.4 m in western Hamilton; this trend of increasing thickness to the northwest is continued across southern Ontario (Figure 3.9; Hewitt, 1971; Armstrong & Carter, 2009). Based on the fossil types identified in core, massive to thin bedding, and carbonate rock type, the Manitoulin Formation is interpreted to have been deposited in a warm, shallow marine environment, likely formed along a southern dipping carbonate ramp (Anastas & Coniglio, 1993)

3.3.4 Cabot Head Formation

The overlying Cabot Head Formation is composed of grey-green shales with thin interbeds of dolostone and sandstone (Figures 3.9, 3.12, and 3.13G). The basal contact with the Manitoulin is transitional, as evidenced by the abundance of dolostone interbeds in the lower section (Figure 3.12). In core, the Cabot Head can be broadly divided into two units, the lower unit consisting predominantly of interbedded dolostone and shale (Ch; 1 – 15 cm; Fl, Fl(b); 0.5 cm – 25 cm; Figure 3.10), with a decreasing proportion of dolostone up-section (Figure 3.11E), and the upper unit composed of primarily grey shale (Fl, Fl(d), Fm(b)) with thin interbeds of fine-grained sandstone (Sh, Sm; 3 cm – 15 cm) and siltstone (Fl; 1 cm – 5 cm; Figures 3.10 and 3.11F).

The Cabot Head Formation appears to show consistent lithological characteristics across the Hamilton region (Caley, 1940; Bolton, 1957; Johnson et al., 1992; Armstrong & Carter, 2009), but thins from west to east, pinching out just east of the city and transitioning into the Power Glen Formation found at Niagara Falls (Figures 3.5 and 3.9). Based on the abundance of shale within the unit, and the interbeds of sandstone, siltstone and dolostone, the Cabot Head Formation likely formed in a relatively deep, open marine setting. A notable change in the environment is recorded through the change from dolostone interbeds at the base to sandstone and siltstone interbeds at the top of the formation, indicating an increase in clastic sediment supply.

3.3.5 Grimsby Formation

The Grimsby Formation consists of interbedded fine-grained sandstone, siltstone, and shale, and has a gradational lower contact with the underlying Cabot Head Formation (Figures 3.10, 3.12 and 3.13H). The Grimsby is frequently distinguished on the basis of its rich, distinctive red colour which contrasts with the grey-green colour of the underlying Cabot Head (Caley, 1940;

Bolton, 1957; Johnson et al., 1992; Armstrong & Carter, 2009), although the uppermost 60 cm of the Grimsby Formation is composed of grey-green shale and siltstone, similar in appearance to the Queenston Formation shale. The Grimsby is characterized by a general coarsening upwards trend with the proportion of sandstone and siltstone beds increasing up-section (Fl(d), Fl, Fm, Sm, Sh; e.g. Site 6a; Figures 3.10 and 3.11F, G). The thickness of the Grimsby Formation also varies significantly across the Hamilton region, thinning slightly towards the west and north, where it eventually pinches out (Figures 3.9 and 3.12; Caley, 1940; Armstrong & Dodge, 2007). Similar to the Cabot Head, the Grimsby was likely formed in an open marine environment, with sea level lowering and/or an increase in sediment supply during its deposition, resulting in the increase in sandstone beds up-section.

3.3.6 Thorold Formation

The Thorold Formation is a grey, fine-grained quartz sandstone with interbeds of shale. In outcrop, the lower contact is sharp, distinguished from the underlying Grimsby by the change in colour, increase in grain size and presence of wave ripples and swaley crossbedding (SCS) (Figure 3.12; Caley, 1940; Armstrong & Dodge, 2007; Perras et al., 2014). In core the contact is sharp and undulating and is overlain by a 1.5 m thick unit of horizontally laminated and rippled fine-grained sandstone (Sh, Sr, Sp) and siltstone (Fl, Fm; Figure 3.10). This is followed by a 1 m thick unit containing soft-sediment deformation structures, including folds in the sandstone, siltstone and shale (Fl(d), Sd) (Figure 3.11I, J). This area of deformation is a notable feature of the Thorold Formation and can be seen at multiple locations in central to eastern Hamilton; elsewhere soft sediment structures are observed in a similar stratigraphic position (Site 11; Figure 3.14; Bolton, 1957; Sanford et al., 1972; Wallace & Eyles, 2015; Brunton & Brintnell, 2020). Undeformed interbeds of sandstone (Sh, Sh(d), Sr, Sm), siltstone and shale (Fl, Fl(d), Fm), overlie the deformed zone, although some laminations are irregular and undulating (Figure 3.11K).

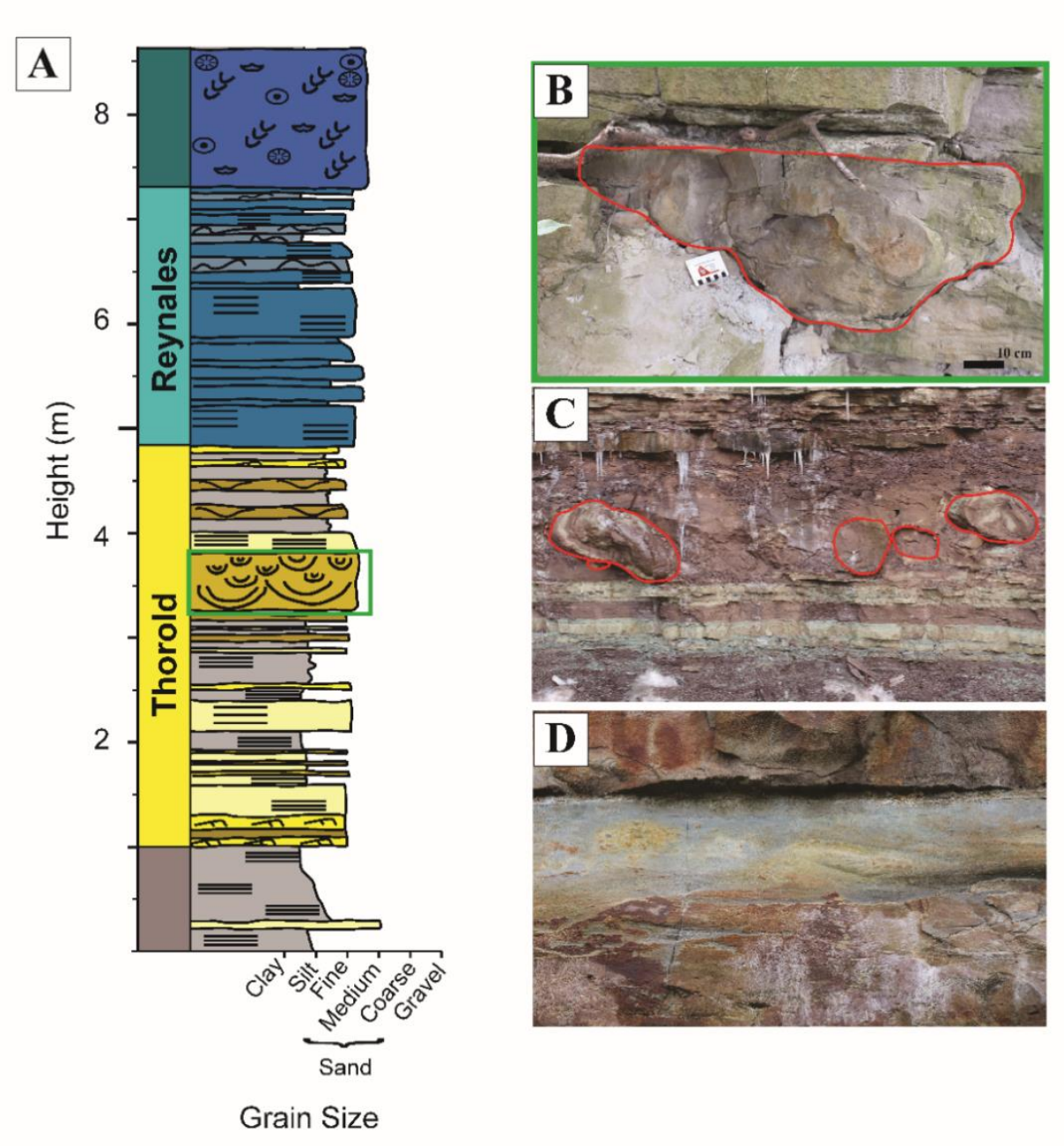

Figure 3.14: A) Lower section of the sedimentological log of the Jolley Cut (Site 7) showing the Grimsby (lower), Thorold, Reynales and Irondequoit (upper) Formations; B) Ball and pillow structure (outlined in red) observed at the Jolley Cut, location on log highlighted in the green box; C) Ball and pillow structures (outlined in red) observed at Devil's Punchbowl (Site 10); D) Layer of shale with soft sediment deformation structures at Dewitt Road (Site 11). Refer to Figure 3.8 for symbology. Figure 3.9 for site locations.

The proportion of sandstone beds in the upper section of the Thorold Formation varies across the city and there is an overall trend of increasing shale moving westward (Figure 3.9). The Thorold Formation thins towards the west and is not present past Clappison's Corner (Site A: Figure 3.9). The Thorold Formation includes planar beds and deformed beds as well as wave ripple cross-laminated fine-grained sandstone; these features, suggest deposition in a shallow marine environment influenced by storms and earthquake activity.

3.3.7 Reynales Formation

The Reynales Formation consists of beige to brown, fine crystalline dolostone with thin wavy or irregular beds of shale; there is a general decrease in bedding thickness and an increase in the number of shale beds and amount of bioturbation toward the top of the formation (Figures 3.10; 3.15A, B and 3.16; Bolton, 1957; Hewitt, 1971; Armstrong & Dodge, 2007). In core, the basal part of the formation consists of moderately bioturbated massive dolostone (Cm) with thin shale interbeds (Fl, Fm; Figure 3.10), overlain by highly bioturbated fossil-rich (crinoid, brachiopod) dolostone (Cm(b); Figure 3.11L). Abundant small scale vugs infilled with minerals occur throughout the formation. The Reynales Formation is consistent in its thickness and lithological characteristics across the Hamilton region (Figure 3.9). The Reynales is interpreted to have formed in an environment changing from one dominated by clastic sediment deposition (e.g. the Cabot Head, Grimsby and Thorold formations) to one dominated by carbonate deposition (Figures 3.10 and 3.12). The Reynales Formation has previously been interpreted to record a period of transgression in which sea level was rising, allowing the accumulation of increasing amounts of shale up-section (Brett et al., 1990).

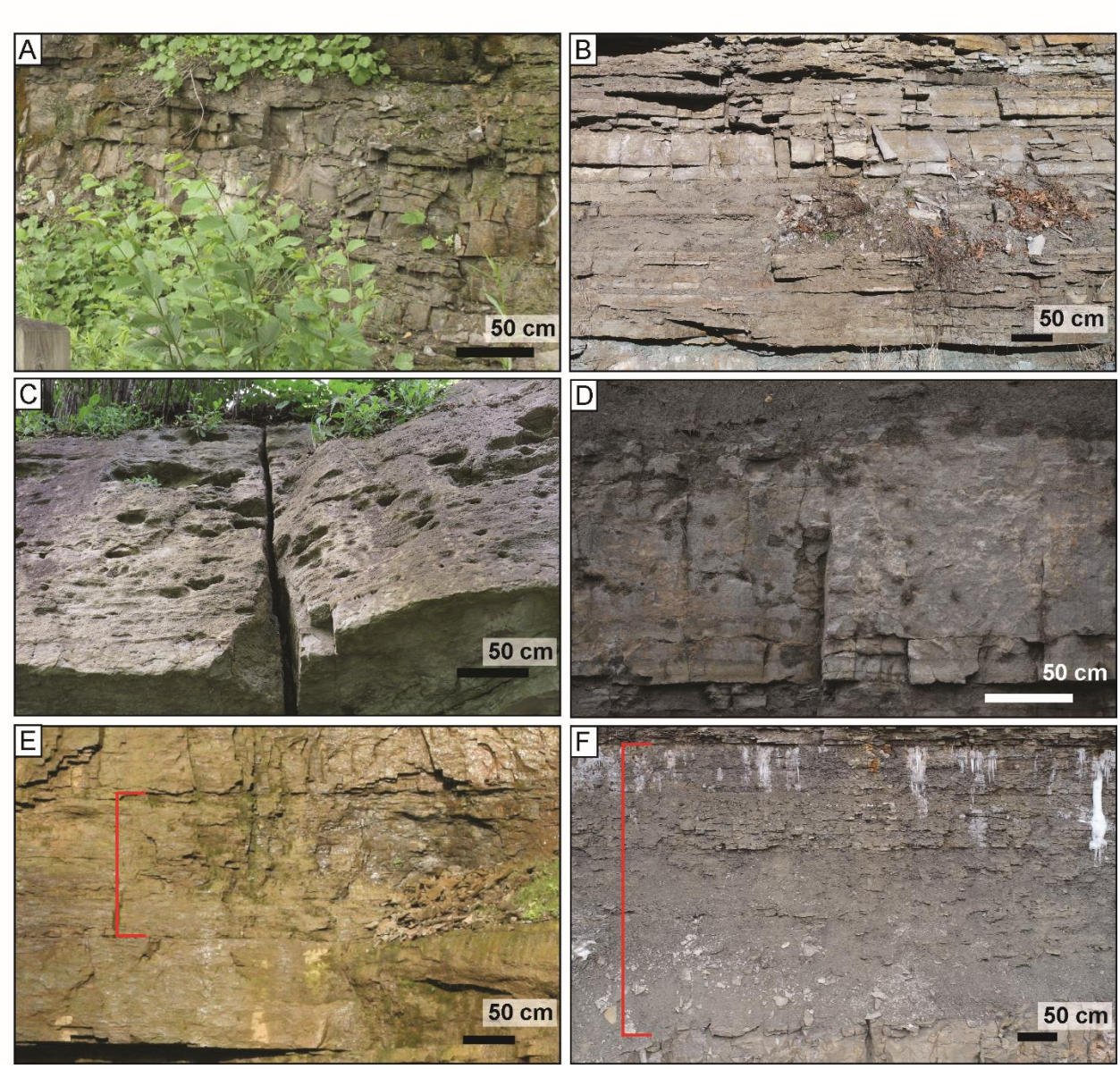

Figure 3.15: A and B) The Reynales Formation, showing bedded dolostone with thin shale layers at Site 9 (A) and Site 11 (B); C and D) The Irondequoit Formation composed of massive dolostone with abundant vugs (C: Site 7, D: Site 8); E) Rochester Shale at the most northwestern location in the city (Site 2) in which the formation is dominated by dolostone with thin shale layers; F) In comparison, the Rochester Shale in one of the most eastern locations in the city (Site 10) is dominated by a dark grey shale with few interbeds of dolostone. Extent of the Rochester Formation indicated in red on E and F. Location of sites shown in Figure 3.9.

3.3.8 Irondequoit Formation

The Irondequoit Formation is a 1 to 1.75 m thick, massive, vuggy, and highly bioturbated fossiliferous dolostone which is easily identifiable at outcrops across the city (Figures 3.11M, 3.15C, D and 3.16; Bolton, 1957; Hewitt, 1971; Johnson et al., 1992; Armstrong & Carter, 2009). The base of the Irondequoit is sharp, slightly undulating, and frequently shows evidence of bioturbation (Figure 3.15C, D). In core, some shaley dolostone can be seen in the basal 60 cm of the formation and fossil content increases up section (Figure 3.11N). The Irondequoit Formation is remarkably consistent in thickness and lithology across Hamilton (Figures 3.9 and 3.16). It is interpreted to record relatively slow deposition in a shallow marine environment in which organisms thrived.

3.3.9 Rochester Formation

The Rochester Formation consists of laminated and massive dark grey shales (Fm, Fl) interbedded with fossiliferous shaley dolostone beds (Cm) and occasional sandstone beds (Sh) (Figures 3.10, Figure 3.15 and 3.16). Small individual burrows are visible in core, although these are not visible in outcrop (Figure 3.11O). The thickness and frequency of dolostone interbeds increases upwards at most locations across the city (Figures 3.10 and 3.16). The high proportion of dolostone in the upper section of this formation makes delineating the contact between the Rochester and the overlying Gasport Formation difficult in some locations. The basal contact of the Rochester with the underlying Irondequoit is sharp and undulating (Figure 3.15D, E, F).

The lithological characteristics of the Rochester Formation vary significantly across Hamilton, transitioning from primarily shale in the eastern part of the city to more dolostone-rich in the central and western part of the city (Figures 3.9 and 3.15E, F). The Rochester also thins from 9 m in the east (Site I; Figure 3.9) to 0.75 m at Clappison's Corner in the northwest (Site A; Figure 3.9). The Rochester records deposition in a low energy marine environment supplied with abundant fine-grained sediment, which was probably sourced from the southeast. The dolostone interbeds may record episodes of clastic sediment starvation while the formation is generally interpreted to represent a highstand system (Brett et al., 1990).

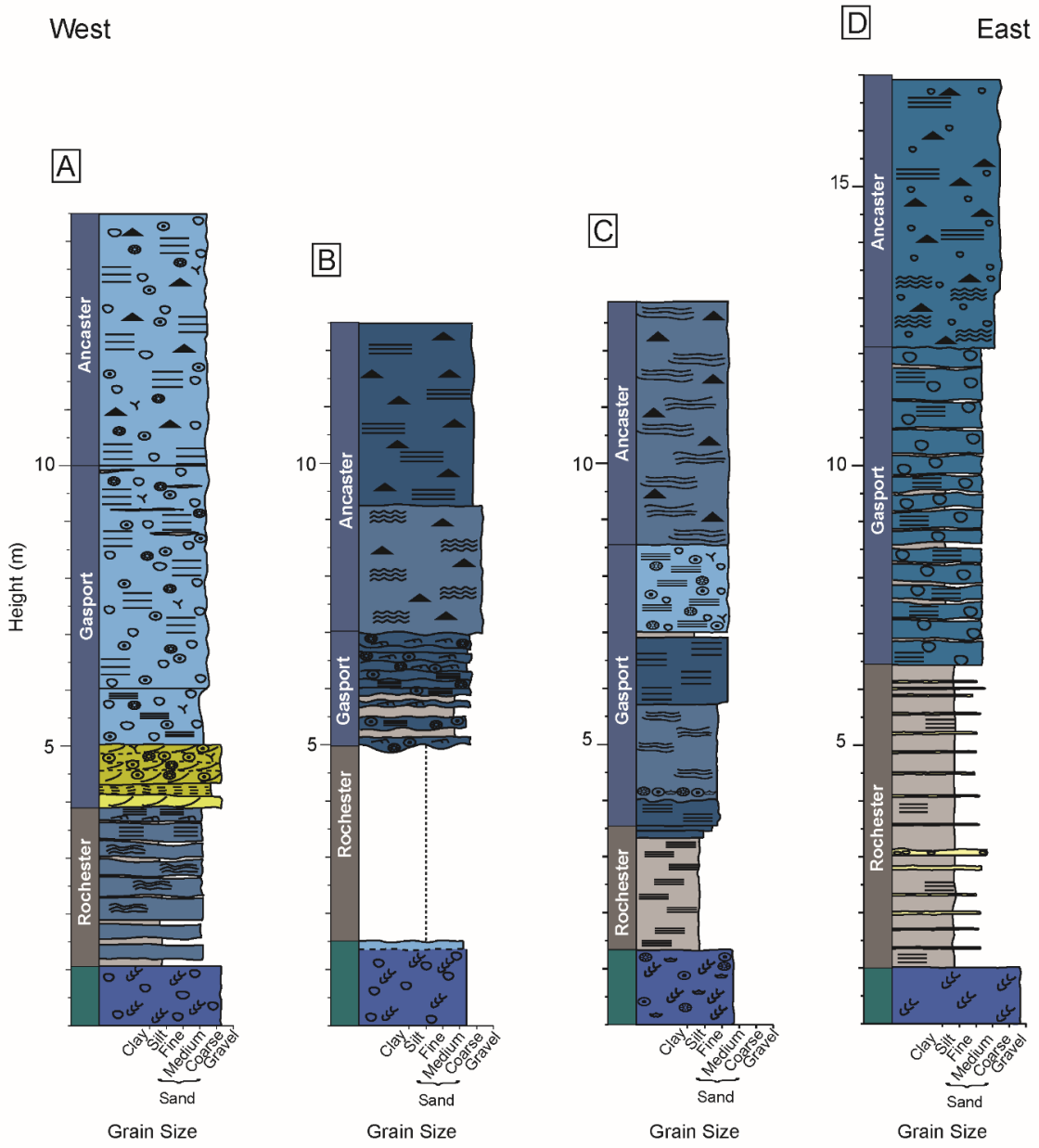

Figure 3.16: Sedimentological logs of the uppermost formations exposed along the Niagara Escarpment in Hamilton at Chedoke Radial Trail (Site 3) (A), Bruce Trail Outcrop (Site 5) (B), Jolley Cut (Site 7) (C), and Dewitt Road (Site 11) (D). Base of logs shows the highly bioturbated, massive dolostone of the Irondequoit Formation. A decrease in the ratio of dolostone to shale can be seen moving west to east across the city. The Gasport Formation is composed of dolostone interbedded with some shale, and there are lateral changes in fossil abundance and types of sedimentary structures. The Ancaster Member of the Goat Island Formation at top is a thinly bedded dolostone, rich in chert. Refer to Figure 3.8 for symbology. Location of sites shown in Figure 3.9.

3.3.10 Gasport Formation

The Gasport Formation is a bedded, highly fossiliferous vuggy dolostone (Ch(f)), containing abundant crinoid, coral and bryozoa fossils and has a gradational lower contact with the underlying Rochester Formation (Figure 3.10). The Gasport has a relatively uniform thickness of approximately 5 m across the city, but does show considerable variability in lithological properties (Figures 3.9 and 3.16) with thicker beds (30-50 cm), and smaller vugs in outcrops to the west (Figures 3.16 and 3.17A, B, C). A highly fossiliferous laminated to cross-bedded unit, composed primarily of crinoid fragments, can be observed at several sites (Site 4, 7 and 9; Figure 3.17D, E). The dolomitic composition and abundant fossil content of the Gasport Formation indicates a return to carbonate-rich depositional environments that dominate in the upper portion of the Niagara Escarpment. However, the Gasport does contain shale interbeds indicating that some clastic sediment was still being delivered to the region. The coarse-grained, cross-bedded units composed primarily of crinoid fragments suggest the depositional environment was also subject to episodic high energy storms that destroyed colonies of crinoids on the sea floor (Sites 4, 7 and 9; Figure 3.17D, E).

3.3.11 Goat Island Formation (Ancaster Member)

The Ancaster Member of the Goat Island Formation overlies the Gasport Formation and consists of a light beige to white, thin bedded, vuggy dolostone with abundant chert nodules (Figures 3.10, 3.16 and 3.17F). The bedding in this unit is irregular, showing pinch and swell geometry and wavy bedding. Chert nodules frequently lie parallel to bedding, with distinctive nodule layers present at some locations (e.g. Site 12; Figure 3.16; Bolton, 1957). Although the Ancaster Member has a consistent thickness of approximately 4.5 m across Hamilton, it varies from being highly fossiliferous in some locations (Site 4; Figure 3.16) to relatively fossil poor in other locations (Site 9; Figure 3.16), and also shows variation in the proportion of vugs within the unit. A very distinctive feature of the Ancaster is its blocky appearance in outcrop (Figure 3.17G) as it is thin bedded and highly fractured. The Ancaster Member is distinguished from the underlying Gasport Formation, by its thinner bedding, the absence of shale, variable fossil content, and abundance of chert nodules (Figure 3.17). This lithological unit was likely deposited in an offshore, low energy shelf environment, starved of clastic sediment (Brett et al., 1990)

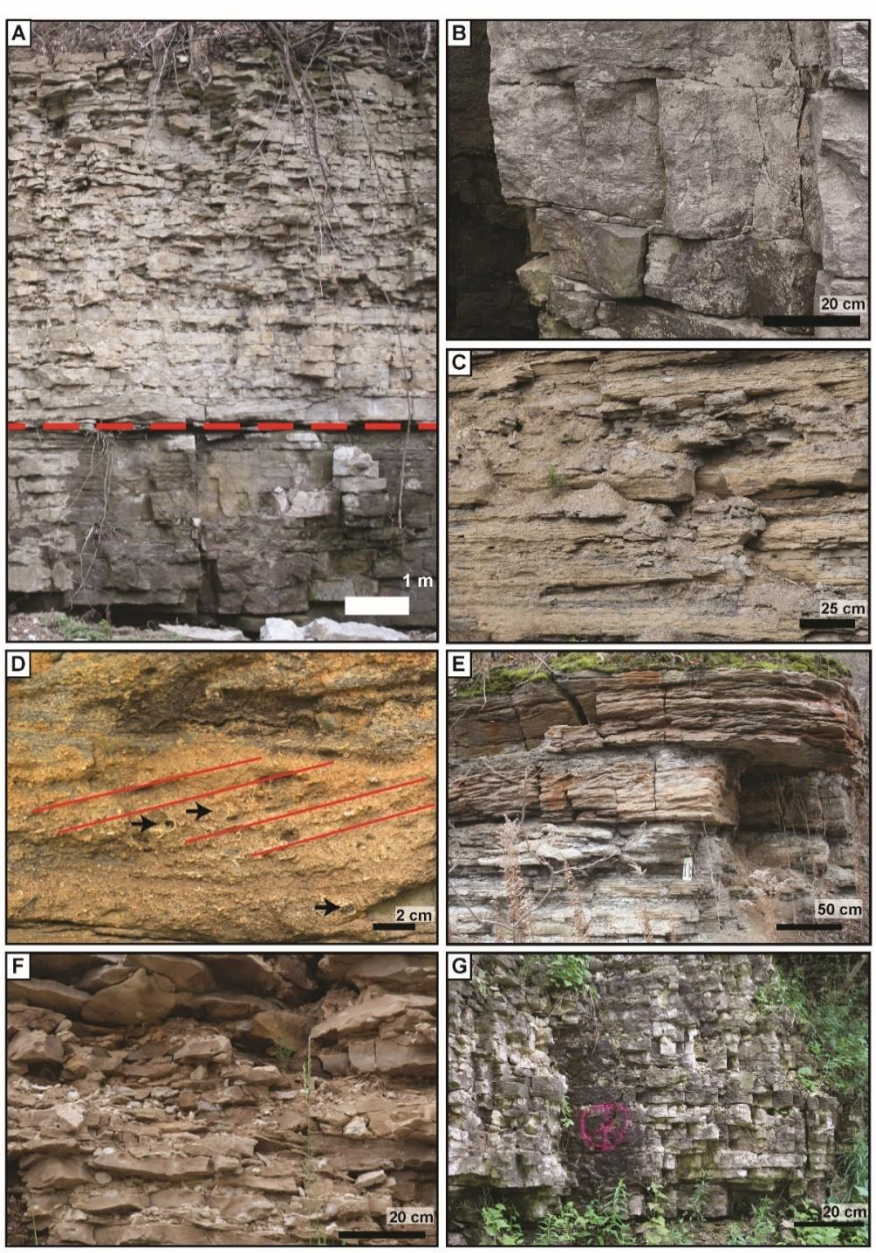

Figure 3.17: A) Contact between the Gasport Formation (below red line) and Ancaster Member of the Goat Island Formation (above red line), both dolostones of the Lockport Group in Hamilton. The thicker bedded dolostone of the Gasport contrasts with the overlying thinner bedded dolostone of the Ancaster. (B) Variability in lithological characteristics of the Gasport Formation, showing thick bedded dolostone at site 4 and (C) thin bedded dolostone at site 11; D) Close up of cross-bedded, oxidized layer with abundant fossil fragments (crinoids, corals indicated by black arrows) located at site 4. Crossbeds shown in red; E) Location of the crossbedded and oxidized layer at the base of the Gasport at site 4; F) Thin bedded, highly fractured dolostone with abundant chert nodules of the Ancaster Member at site 7; G) Blocky, fractured nature of the Ancaster Member at site 7. Location of sites shown in Figure 3.9.

3. 4 Geotechnical Rock Properties

The average unconfined compressive strength (UCS) values of each of the lithological formations exposed along the Niagara Escarpment in the Hamilton area were obtained from previously published reports and compiled to allow a comparison of the rock strength of these units (Table 3.1; Figure 3.18). The dominant lithology is an important factor in determining the UCS of a formation. As such, the values will be discussed in relation to the dominant rock type present in the formations, which are classified as either shale-, sandstone-, or dolostone-dominated.

Table 3.1: Average, minimum, and maximum unconfined compressive strength (UCS) values for rock types exposed along the Niagara Escarpment (values obtained from Palmer and Lo, 1976; ; Lo et al., 1978; Lo, 1978, 1989Lo and Hori, 1979; Lo and Lee, 1990; Lam et al., 2007; Hayakawa and Matsukura, 2009; Al-Maamori et al., 2014; Perras et al., 2014).

		Unconfined Compressive Strength (mPa)		
Formation	**Dominant Rock Types**	**Average**	**Minimum**	**Maximum**
Ancaster/Goat Island	Dolostone	200	137	282
Gasport	Dolostone	133	27	255
Rochester	Shale	50.9	21.6	83.7
Irondequoit	Dolostone	103	89	123.6
Reynales	Dolostone	107	97	129
Thorold	Sandstone	82.7	38.6	129
Grimsby	Shale	65.3	24	146
Cabot Head	Shale	94.7	20	115.9
Manitoulin	Dolostone	84.2	61.7	106.7
Whirlpool	Sandstone	159	107	190
Queenston	Shale	47	30	65

Shale-dominated formations: The shale-dominated formations, consisting of the Queenston, Cabot Head, Grimsby and Rochester formations, have significantly lower UCS values (average 20-95 mPa) compared to the dolostone-dominated (average 84-200 mPa), and sandstone-dominated formations (average 83-159 mPa) with the exception of the Cabot Head (Figure 3.18; Table 3.1). There are limited UCS values available from the Cabot Head, and the common presence of dolostone interbeds near the base of the formation may have increased the UCS values obtained

for this shale-dominated unit. The Rochester, Cabot Head and Grimsby formations show a significant variation in the values of UCS reported in the literature which may be related to the presence of interbeds of sandstone, siltstone, and dolostone which increase the overall rock strength.

Dolostone – dominated formations: The synthesized data presented in Table 3.1 show the dolostone-dominated formations to have generally high UCS and associated rock strength (Figure 3.18; Table 3.1); the highest UCS values are reported for the dolostones of the Ancaster Member /Goat Island Formation of the Lockport Group, which forms the caprock of the escarpment in the Hamilton area. Other dolostone-dominated units such as the Gasport, Reynales, and Manitoulin formations, have lower average UCS and a wide range of reported values (Table 3.1). This is likely due to the presence of shale interbeds which lower the overall rock strength. Unexpectedly, the Irondequoit, a massive crystalline dolostone, has one of the lowest UCS of the dolostone-dominated formations. The reason for this is unknown.

Sandstone-dominated formations: The two sandstone-dominated formations identified in Table 3.1, the Whirlpool and the Thorold, show significant differences in UCS values (Figure 3.18). The Whirlpool Formation, which has a high UCS, is dominated by thick beds of quartz sandstone, with thin shale layers restricted to the top 50 cm of the unit. In contrast, the Thorold Formation contains abundant shale layers, and displays pervasive deformation which may have reduced the overall integrity of the unit resulting in lower UCS values (Table 3.1).

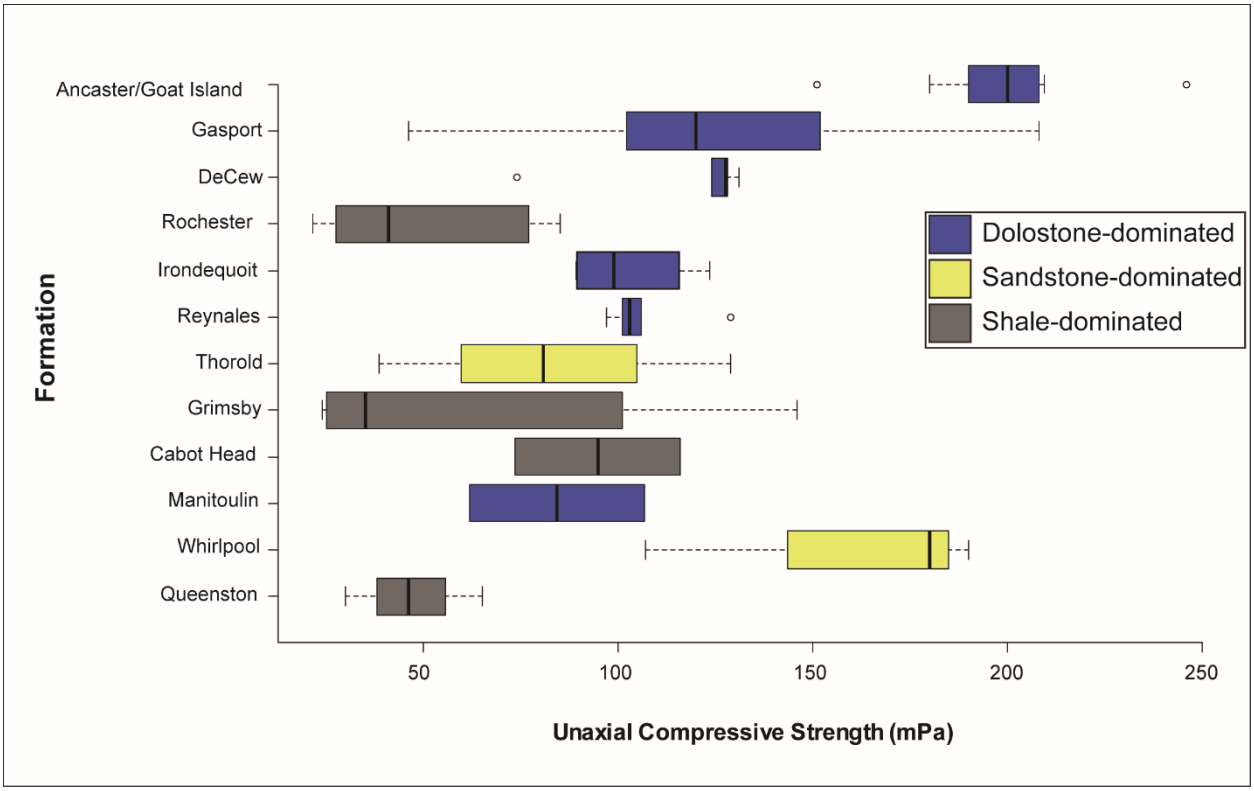

Figure 3.18: Chart showing unconfined compressive strength (UCS) of lithological units exposed along the Niagara Escarpment based on data from previous studies (Palmer & Lo, 1976; Lo, 1978, 1989; Lo et al., 1978; Lam et al., 2007; Hayakawa & Matsukura, 2009; Al-Maamori et al., 2014; Perras et al., 2014).

3. 5 Factors affecting erosion processes and rates:

There are many factors that can impact the rate and characteristics of erosion processes acting on an exposed rock face such as the Niagara Escarpment, many of which are influenced by lithological characteristics. These factors include the mechanical strength of the unit, the stratigraphic arrangement and frequency of lithological types, deformation and rock creep, and fracture characteristics (Gilbert, 1890; Lo & Hori, 1979; Barlow, 2002; Agustawijaya, 2007; Hayakawa & Matsukura, 2009; Al-Maamori et al., 2014; Zhou et al., 2016; Roy et al., 2017; Scott & Wohl, 2019 Formenti et al. 2021). In addition to these factors associated with lithology, climatic and hydrological factors also play a significant role (Fahey & Lefebure, 1988; Agustawijaya, 2007; Hayakawa and Matsukura, 2009; Bayram 2012; Miščević and Vlastelica, 2014; Wang et al. 2016).

3.5.1 Mechanical Strength

The grain size, composition, and structure of a lithological unit are important factors in determining its strength and resistance to erosion. Previous work has demonstrated an inverse relationship between UCS and the susceptibility of a rock to erosion and its overall rate of erosion (Budetta et al., 2000; Walker, 2004; Hayakawa & Matsukura, 2009). In fact, UCS has been proposed as one of the best single indicators of the resistance of bedrock to erosion (Hayakawa & Matsukura, 2009). However, there is considerable variation in the measured UCS for lithological units exposed along the Niagara Escarpment, and UCS cannot be used alone to determine the erodibility of the escarpment face (Figure 3.18; Palmer and Lo, 1976; Lo, 1978, 1989; Lo et al., 1978; Lo and Hori, 1979; Lo and Lee, 1990; Lam et al., 2007; Hayakawa and Matsukura, 2009; Al-Maamori et al., 2014; Perras et al., 2014) .

Additionally, the measured UCS of an intact rock sample can differ significantly from the *in situ* rock strength, due to other factors such as water saturation, bedding, and the presence of fractures on the rock face (Lo & Hori, 1979; Agustawijaya, 2007; Kaiser & Kim, 2014; Zhou et al., 2016; Roy et al., 2017). The UCS determined for the formations exposed along the Niagara Escarpment are strongly influenced by the dominant lithologies they contain, as discussed above.

3.5.2 Distribution of lithological units and undercutting

A critical factor affecting erosion of the Niagara Escarpment is that it is composed of alternating layers of relatively resistant rock types, primarily dolostone and sandstone, and less resistant shales (Figure 3.5). This alternation of lithological types results in an unstable system, in which the easily erodible shales break down more rapidly than the more resistant rocks, resulting in undercutting of overlying units. Undercutting has long been suggested as a major contributor to both the formation and ongoing erosion of the escarpment face (Gilbert, 1890; Hayakawa & Matsukura, 2009).

3.5.3 Deformation and Rock Creep

Exacerbating the process of undercutting, rock creep, the process in which shales deform and expand due to gravitational stresses, further destabilizes the overlying layers (Roegiers et al., 1979; Barlow, 2002). The dilation of joints close to the rock face, tilting of the caprock, and shale deformation caused by the removal of confining pressures are thought to impact erosion of the escarpment face, although the severity of this process is unknown (Quigley et al., 1978; Roegiers et al., 1979; Barlow, 2002). Rock creep occurs in rocks susceptible to plastic deformation, such as

shale, and does not commonly occur in rocks with higher UCS strength (Radbruch-Hall, 1978), such as the dolostones and sandstones in the escarpment.

In addition to the factors affecting erosion processes caused by lithological variations, there are large-scale morphological and regional issues that may also influence erosion rates along the escarpment. The bedrock in southern Ontario, especially near the shore of Lake Ontario, is subjected to high horizontal compressive stresses, residual stresses from the last glaciation or prior tectonism (Lam et al., 2007; Al-Maamori et al., 2014; Perras et al., 2014). This high stress field in the rock itself will add to the deformation of lithological units, as has been observed in tunnels bored through the escarpment rocks (Bowen et al., 1976; Lo, 1978). This type of deformation occurs when rocks are initially exposed, and stresses are released, but can continue for long periods of time, particularly in shales, causing further weakening of shale units as well as destabilizing more resistant layers through mechanisms of tilting and joint dilation (Al-Maamori et al., 2014).

3.5.4 Fracture characteristics

Bedrock fractures exert a major control on the rate and spatial distribution of erosional processes and can control the way in which geomorphic features evolve on exposed rock faces (Scott & Wohl, 2019). It has been suggested that the rate of glacial plucking, a potentially important process in the initial creation of the escarpment, was heavily influenced by the orientation of jointing and fractures in the rock (Straw, 1968; Gross & Engelder, 1991; Eyles et al., 1997; Gao, 2011). There are many clear relationships between fracture density, orientation, and size and the rate and risk of erosion. More densely fractured rocks erode more easily when compared with massive, unfractured rock types, and more densely fractured hillslopes are less stable and prone to failure (Kirby & Ouimet, 2011; Loye et al., 2012; Scott & Wohl, 2019). Instability and erosion caused by fractures are of concern in Hamilton, as there are abundant fractures both horizontally along bedding planes, and vertically in the dolostone units, such as the Ancaster Member which is exposed along most road cuts (Figure 3.17F, G; Formenti et al. 2021). In the Hamilton region, fracture propagation and expansion is likely to be influenced by the growth of ice during the winter months, further increasing the rate of erosion of the escarpment face. Other processes, such as chemical weathering through dissolution and the impact of vegetation through root expansion and tree throw may also be occurring in this region, although mechanical weathering processes are likely the dominant factors impacting rate and risk of erosion.

3.5.5 Climate and Hydrology

Hamilton is located in a temperate climatic region which has a mean annual temperature of approximately 7.8 °C and a mean annual precipitation of approximately 895 mm (data from 1981-2010; Environment Canada, 2019). This temperate climatic regime will likely result in elevated erosion rates, as high mean annual precipitation and mean annual temperatures of ~ 10°C have been associated with enhanced erosion rates (Portenga & Bierman, 2011). Enhanced weathering generated by hydrological processes is especially effective when rocks are saturated, which results in significant decreases in rock strength (40 - 80% reduction), and increases the erodibility of the material (Agustawijaya, 2007; Hayakawa and Matsukura, 2009; Miščević and Vlastelica, 2014). Precipitation can also directly cause erosion of a rock face, through water moving over the surface as overland flow or in waterfalls (Miščević & Vlastelica, 2014). In clay-rich rocks, the presence of water can lead to expansion of clay minerals and disintegration of the rock, a process referred to as slaking. During wetting-drying and freeze-thaw cycles, clay minerals in the shales exposed on the escarpment face are highly susceptible to swelling causing the shales to become increasingly friable, rapidly destabilized, and easily eroded (Tinkler & Stenson, 1992).

Water moving as either surface or ground water across the escarpment face will impact the rate of erosion and stability of the face. The amount of groundwater seeping from the escarpment face, and the amount of surficial flow over the escarpment varies significantly between the different sites across the city. Site specific hydrological processes are influenced by factors such as land use above the escarpment, slope gradient, proximity to a waterfall, or the presence of other anthropogenic changes (e.g., quarrying of the caprock). It is interesting to note that an area of the escarpment exposed along the Claremont Access route shows particularly rapid erosion of the shale units and more abundant water seeps than elsewhere; this area was formerly utilized as a quarry in which the majority of the overlying dolostone caprock (the Lockport Group) was removed and the rate of groundwater percolation changed substantially.

The location of water seeps on the escarpment face is most clearly observed during winter, when icicles form (Figure 3.19). There is evidence of significant water seepage at the top of the Grimsby (Site 7), top of the Rochester Shale (Site 3, Site 10), and the base of the Cabot Head (Site 6) (Figure 3.19). The groundwater emerging at these locations flows down and across the rock face loosens the surficial layer and transports debris which then accumulates at the base of the slope (Figure 3.20A, B). Most of the accumulated debris is fine-grained material sourced from the

shales, with larger blocks (> 5 cm diameter) sourced from thin sandstone and dolostone interbeds or one of the dolostone-dominated units.

In addition to the impact of high precipitation amounts on erosion processes, the fluctuation of temperature in Hamilton around the freezing point, facilitates cyclic freeze-thaw weathering processes (Wang et al., 2016; Environment Canada, 2019). Freeze- thaw weathering occurs when pore water in the rocks expands through freezing, causing an increase in hydraulic pressure, the expansion of cracks and pores, and the creation of micro fractures (McGreevy, 1981; Dredge, 1992; Wang et al., 2016). The degree of water saturation, the porosity of the rock unit, grain size, the presence of joints and/or fractures, and climatic variation are all factors that will impact the rate of freeze-thaw processes (Dredge 1992; Nicholson et al. 2000; Bayram 2012; Wang et al. 2016). Freeze-thaw weathering along the Niagara Escarpment is often suggested as a significant process in determining the timing and extent of erosion (Fahey & Lefebure, 1988), although few studies have been conducted in similar temperate climates to substantiate this claim.

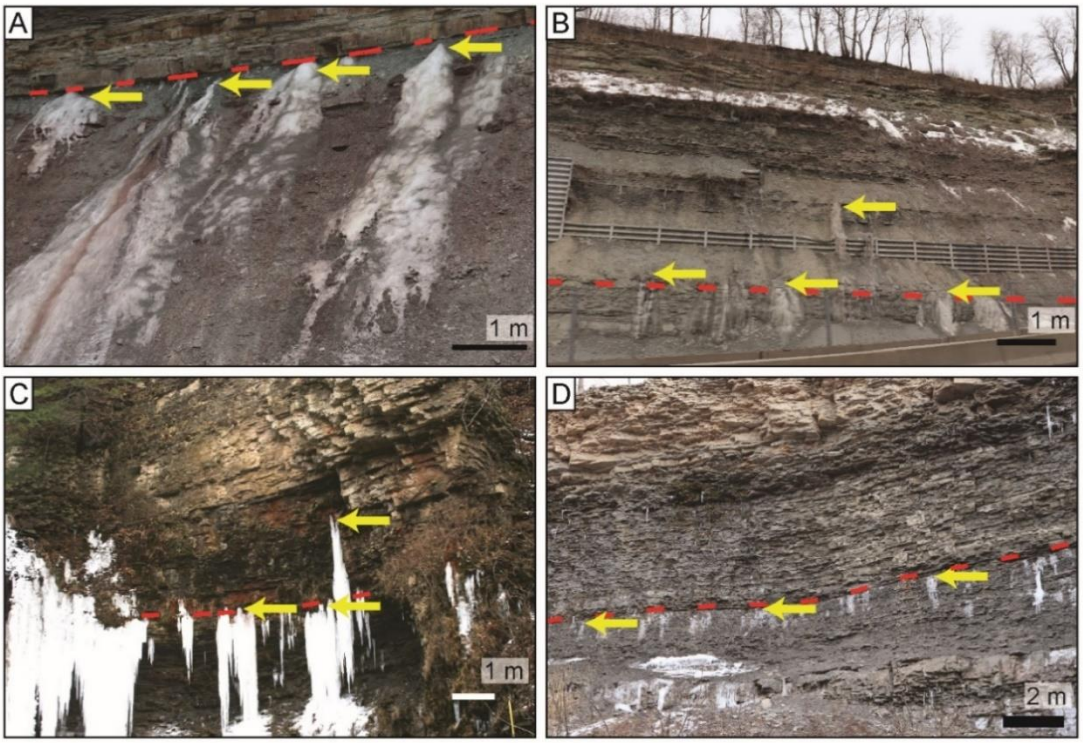

Figure 3.19: Frozen water seeps (yellow arrows) in shale-dominated formations on the escarpment face during winter. A) Seeps located at the top of the Grimsby Formation (Site 7); B) Seeps located at the base of the Cabot Head Formation (Site 6); C, D) Seeps located at the top of the Rochester Formation (Site 3, Site 10). Location of sites shown in Figure 3.9.

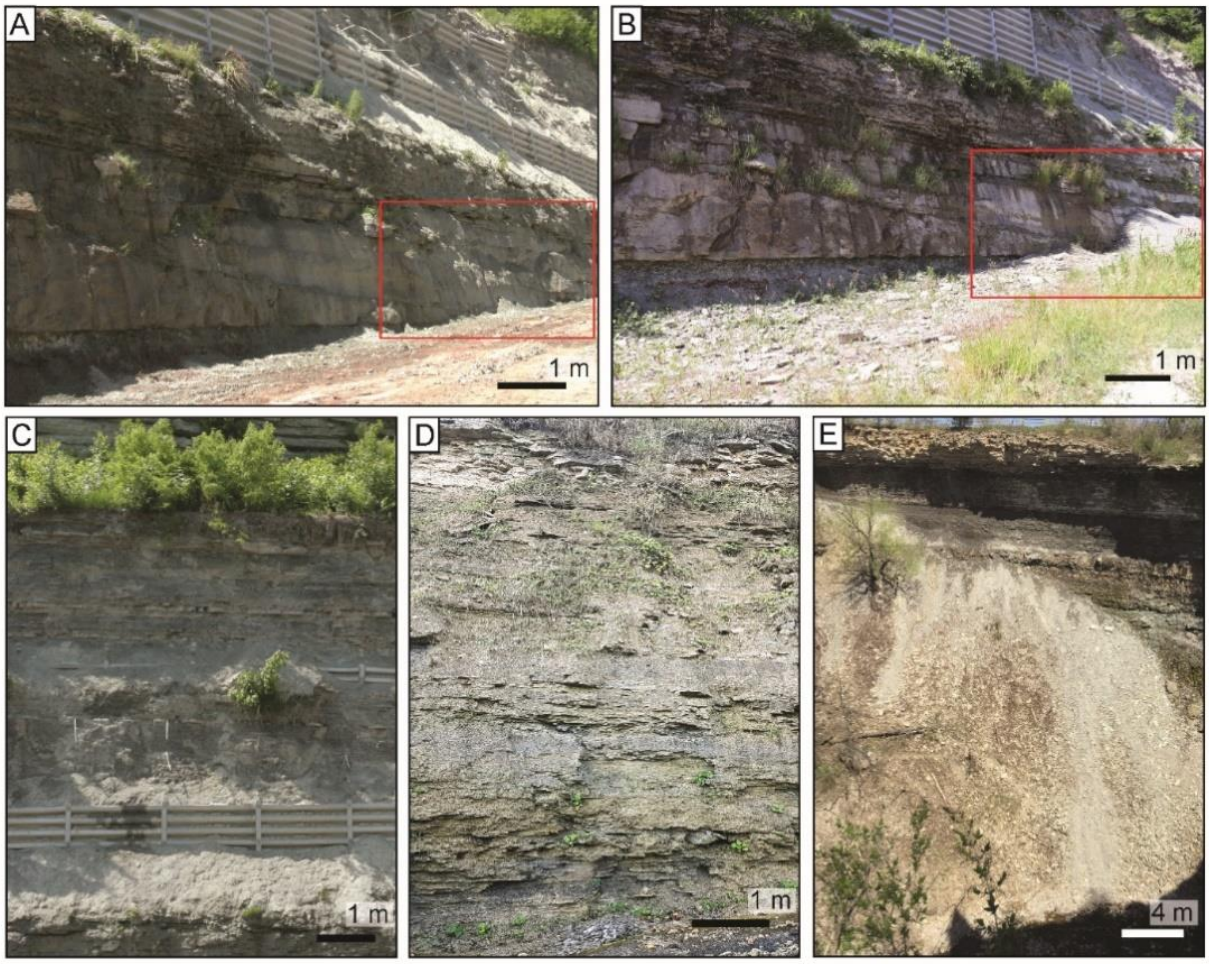

Figure 3.20: Slope debris accumulating at the base of the escarpment face. A) Base of escarpment at Claremont Access (Site 6) after debris has been cleared, taken in June 2018; B) Base of escarpment at Claremont Access, taken in May 2019, showing accumulation of slope debris (red box); Near vertical slope of the exposed shale-dominated formations including: C) the Cabot Head Formation at Claremont Access (Site 6) and D) the Rochester Shale Formation at Dewitt Road (Site 11); E) Natural debris slope located at the Devil's Punchbowl (Site 10). Location of sites shown in Figure 3.9.

Many factors influence the rate and mechanisms by which an outcrop erodes over time. Some of the most important factors have been discussed above including mechanical strength, distribution of lithological units, deformation, fracture characteristics, climate and hydrology. The relative impact of these factors will vary depending on the season, the rock type involved, the steepness of the slope, and the proximity to water bodies.

3. 6 Discussion

Each of the factors discussed above is impacting the type and rate of erosion of the Niagara Escarpment within Hamilton. However, the degree to which the rocks are affected by these processes is controlled primarily by their lithology and their stratigraphic position in the rock face. Lithological properties influence how the rock face fractures, whether rock creep and deformation can occur, the type of slope failures that occur, the size of slope debris released, and the overall rate of erosion. Hence, erosion processes affecting the lithological units exposed along the Niagara Escarpment will be discussed below in terms of how they affect shale-dominated, sandstone-dominated, or dolostone-dominated formations (Table 3.2).

Table 3.2: Factors influencing erosion of shale-, dolostone-, and sandstone -dominated formations.

	Shale-dominated Formations	**Dolostone-dominated Formations**	**Sandstone-dominated Formations**
Mechanical Strength	Low UCS; More susceptible to erosion	High but variable UCS; Less susceptible to erosion	High but variable UCS; Less susceptible to erosion
Potential for undercutting	Thick shale units have potential to erode rapidly and undercut overlying units	Interbedded shale units decrease formation stability	Interbedded shale units decrease formation stability
Deformation and Rock Creep	Release of horizontal stress causes deformation and rock creep	----------	----------
Climate and Hydrology	Wetting-drying and freeze-thaw cycles cause slaking and swelling of clay minerals	Dolostones with lower UCS will erode more rapidly when saturated	Sandstones with lower UCS will erode more rapidly when saturated
Fracture Characteristics	Highly fractured – horizontally and vertically	Dense fracture networks increase erosion rate; fractures oblique to rock face cause instability	Dense fracture networks increase erosion rate; fractures oblique to rock face cause instability
Implications for Erosion and Escarpment Stability in Hamilton	High risk of erosion and undercutting of overlying more resistant units. The well exposed and shale-rich Grimsby and Rochester formations are of particular concern in the eastern part of the city.	High risk of block release and toppling due to undercutting by shales and fracturing The Lockport Group and Reynales Formation are of particular concern as they are well exposed, underlain by shales, and highly fractured.	High risk of block release and toppling due to undercutting by shales and fracturing The Thorold Formation is of particular concern in the eastern part of the city as it is well exposed, underlain by shales, and highly fractured.

3.6.1 Shale-dominated formations

The shale-dominated formations, including the Queenston, Cabot Head, Grimsby, and Rochester formations, are key to the overall strength of the escarpment (Figure 3.22). Shale-dominated formations are strongly impacted by their mechanical strength, the degree of fracturing, and also climatic and hydrological factors (Table 3.2). In particular, shale lithologies are

influenced by the swelling of included clays, and by rock creep (Table 3.2; Franklin, 1981; Barlow, 2002; Miščević and Vlastelica, 2014). Enhanced erosion of shale layers in a heterogenous stratigraphy allows undercutting and block toppling of more resistant lithologies. It is therefore essential to determine the susceptibility of the shale-dominated formations to erosion in an exposure in order to evaluate the stability of the entire rock face.

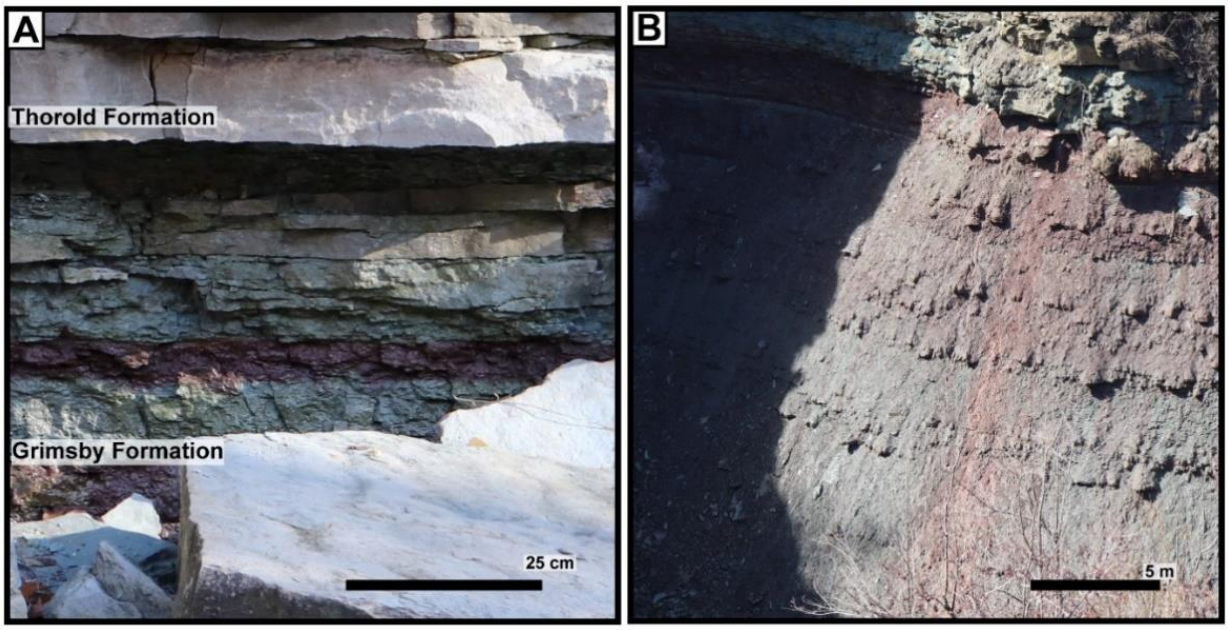

Figure 3.21: A) Undercutting of the Thorold Formation by the Grimsby Formation at Albion Falls (Site 9). B) Stepped appearance of the Grimsby and Cabot Head Formations exposed at the Devil's Punchbowl (Site 10).

Shale-dominated formations have low UCS and are more easily eroded compared to the dolostone- and sandstone-dominated formations in the escarpment (Table 3.2; Figures 3.18 and 3.22). Although these formations are dominated by shale, they each contain interbeds of more resistant rock types such as siltstone, sandstone, and dolostone. The Cabot Head Formation contains numerous resistant interbeds, which strengthen and lend stability to the formation and reduce the rate of erosion. The resistant beds also protect the shales from runoff and reduce the amount of undercutting that occurs (Figure 3.21B; Shakoor and Rodgers 1992; Niemann 2009). Thick, shale-dominated units, such as the Rochester Formation, that outcrop close to the slope crest, experience the highest amount of undercutting as they expose the greatest amount of shale to weathering and erosion processes (Admassu et al., 2012).

Shale-dominated lithological units have also been observed to be susceptible to deformation when excavated for tunneling operations in Hamilton (Table 3.2; Quigley et al., 1978; Roegiers et al., 1979) and rock creep as observed in the Guelph region (Barlow, 2002). It is unclear how much this process impacts the Niagara Escarpment in Hamilton. Rock creep in the shale layers can cause cambering in overlying dolostone or sandstone dominated units resulting in a less stable system.

Finally, the temperate climate of Hamilton impacts erosion processes operating on the shale-dominated lithologies through mechanisms related to temperature variations and hydrological processes (Table 3.2). Shales that have a higher silt to clay ratio are more durable and less susceptible to swelling, slaking and rock creep (Shakoor & Rodgers, 1992; Niemann, 2009). Along the Niagara Escarpment, the Queenston Shale has the highest content of swelling clays, while the Rochester Formation has the lowest (Lo & Lee, 1990; Al-Maamori et al., 2014). Swelling of the clay minerals in the shale not only leads to degradation of the shale, but also acts to increase the amount of fracturing in the escarpment face.

3.6.1.1. Implications for Stability and Erosion of the Niagara Escarpment

When considering the influence of shale-dominated formations on escarpment stability, the Queenston and the Cabot Head formations are of minor concern due to their limited exposure. However, both units outcrop at the Claremont Access route (site 6), a site that has experienced multiple major failures in recent years; these failures may be due to the relative thickness (~16m) of the Cabot Head at this site. These two formations are also likely to experience relatively high erosion rates based on their low UCS values, the dominance of shale, and the high degree of fracturing common in the shales (Figure 3.22).

Processes affecting erosion of the overlying Grimsby and Rochester formations are of greater importance to escarpment stability as these shale-dominated formations are exposed at most sites, and along almost every road cut in Hamilton (Figure 3.9). The Grimsby Formation often undercuts the overlying Thorold Formation (Figure 3.21A), although the interbeds of sandstone in the Thorold lend some stability to the unit. The uppermost shale-dominated formation, the Rochester, shows considerable lithological variability across the city, passing from almost entirely shale with few dolostone interbeds in the east to almost entirely dolostone with minor shale in the west (Figures 3.9 and 3.16). This variability affects erosion processes acting

upon the shale with higher amounts of swelling and slaking in the east and greater amounts of material loss through fracturing and collapse of the dolostone interbeds in the west.

Overall, the shale-dominated formations exposed along the Niagara Escarpment play a critical role in determining the stability of the rockface (Figure 3.22). The engineered slope of the rock face exposed along road cuts is much steeper than would exist in a natural system (Figure 3.20C, D, E; Franklin, 1981); the oversteepened rock face is therefore constantly attempting to reach a state of equilibrium and areas of shale exposure are particularly prone to failure and erosion through the processes described above (Table 3.1).

3.6.2 Dolostone-dominated formations

The dolostone-dominated formations exposed along the escarpment in Hamilton include the Manitoulin, Reynales, Irondequoit, Gasport and Goat Island formations (Figure 3.22). Although these dolostone-dominated formations are more resistant to weathering than the shale-dominated formations, the types of rock failure that can occur, and their magnitude, are of concern to the safety of infrastructure near the rock face (Table 3.2).

The mechanical strength (measured as UCS) of the dolostone-dominated formations varies significantly between the Manitoulin (lowest average 84.2 mPa) and the Ancaster Member of the Goat Island Formation (highest average 200 mPa; Table 3.1). The difference in UCS values between formations impacts their susceptibility to failure and collapse, particularly if the rock units are water saturated (Agustawijaya, 2007). It is thus likely that the dolostones of the Manitoulin Formation, which lie lower in the stratigraphy and allow groundwater transmission, will be affected more by weathering processes than the uppermost, well drained dolostones of the Ancaster Member.

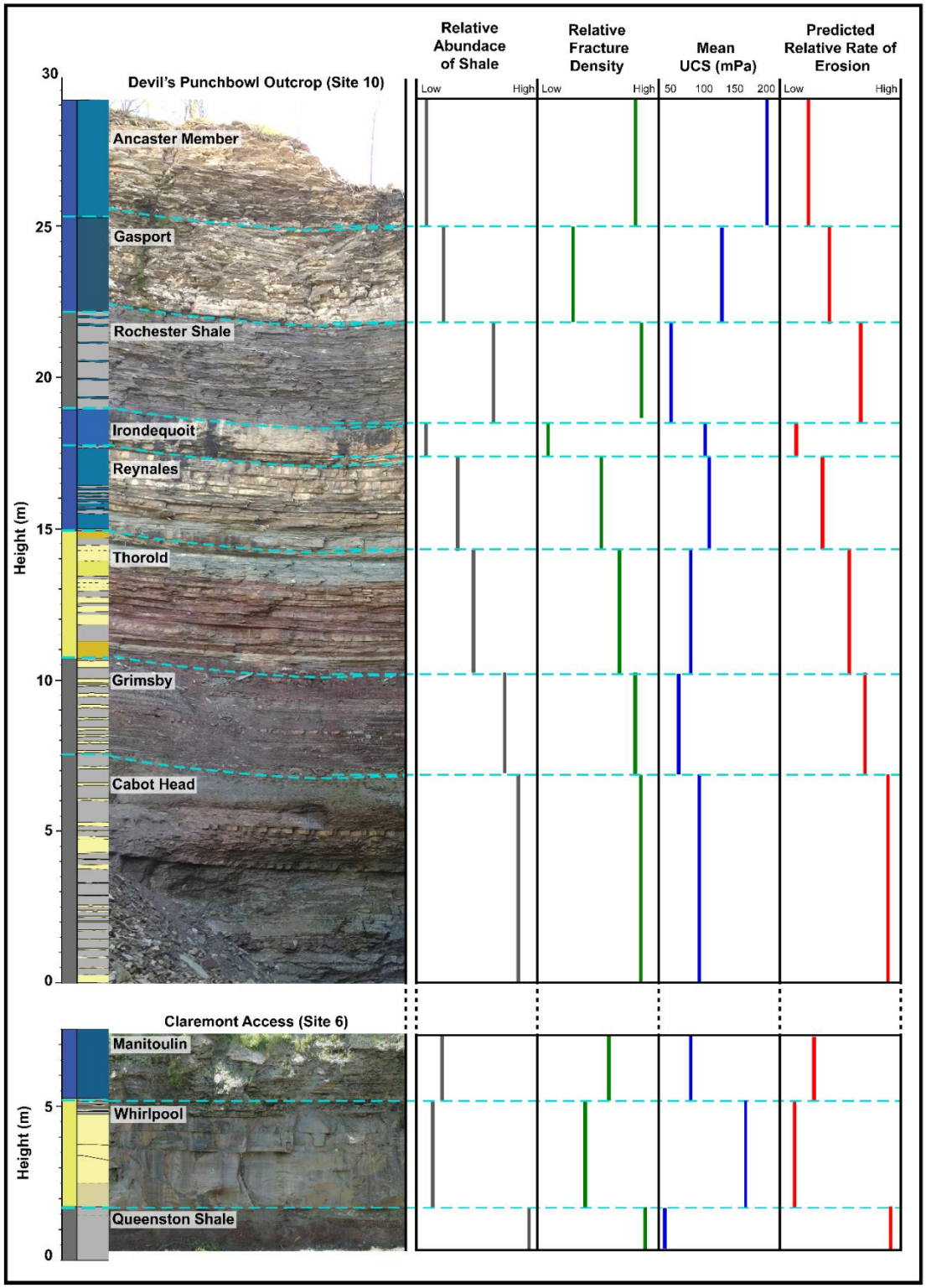

Figure 3.22: Summary diagram showing the vertical variation in factors that affect stability of the escarpment face including the relative abundance of shale, the relative fracture density, and the mean unconfined compressive strength. The predicted relative rate of erosion of each of the formations is indicated on the right, based on their lithological characteristics.

Although the Manitoulin, Reynales and Gasport formations are dominated by dolostone, in many locations they are interbedded with thin shale layers (Figures 3.10, 3.12 and 3.22); the presence of shale impacts the overall strength and stability of these lithological units and affects unit permeability which may instigate zones of groundwater seepage. Dolostone is particularly susceptible to erosion when exposed to acidic precipitation which can cause dissolution and increase porosity (Reddy, 1988; Bonazza et al., 2009; Eyssautier-Chuine et al., 2016), widen fractures and joints, and permit the release, toppling and sliding of blocks from the escarpment face. Dolostone can also contain clay minerals, which are susceptible to swelling and can contribute towards rock creep (Lo, 1978; Al-Maamori et al., 2014). However, despite the presence of shale and clay minerals in these units, the principal erosional processes affecting dolostone-dominated formations along the escarpment are those caused by fracturing, freeze thaw, and undercutting; water plays an important role in all these processes.

The density, intensity, and length of fractures in dolostone-dominated lithological units are critical for determining the nature and extent of erosion on exposed rock surfaces and those formations with a greater density of fractures are predicted to produce less stable rock faces that experience more rapid erosion through block failures (Table 3.2; Scott & Wohl, 2019). The repeated freezing and thawing of water infiltrating fractures and joints can also cause their expansion and growth; this is a particularly important process toward the base of the Gasport Formation where dolostone beds overlie the shales of the Rochester Formation and are likely to be water saturated.

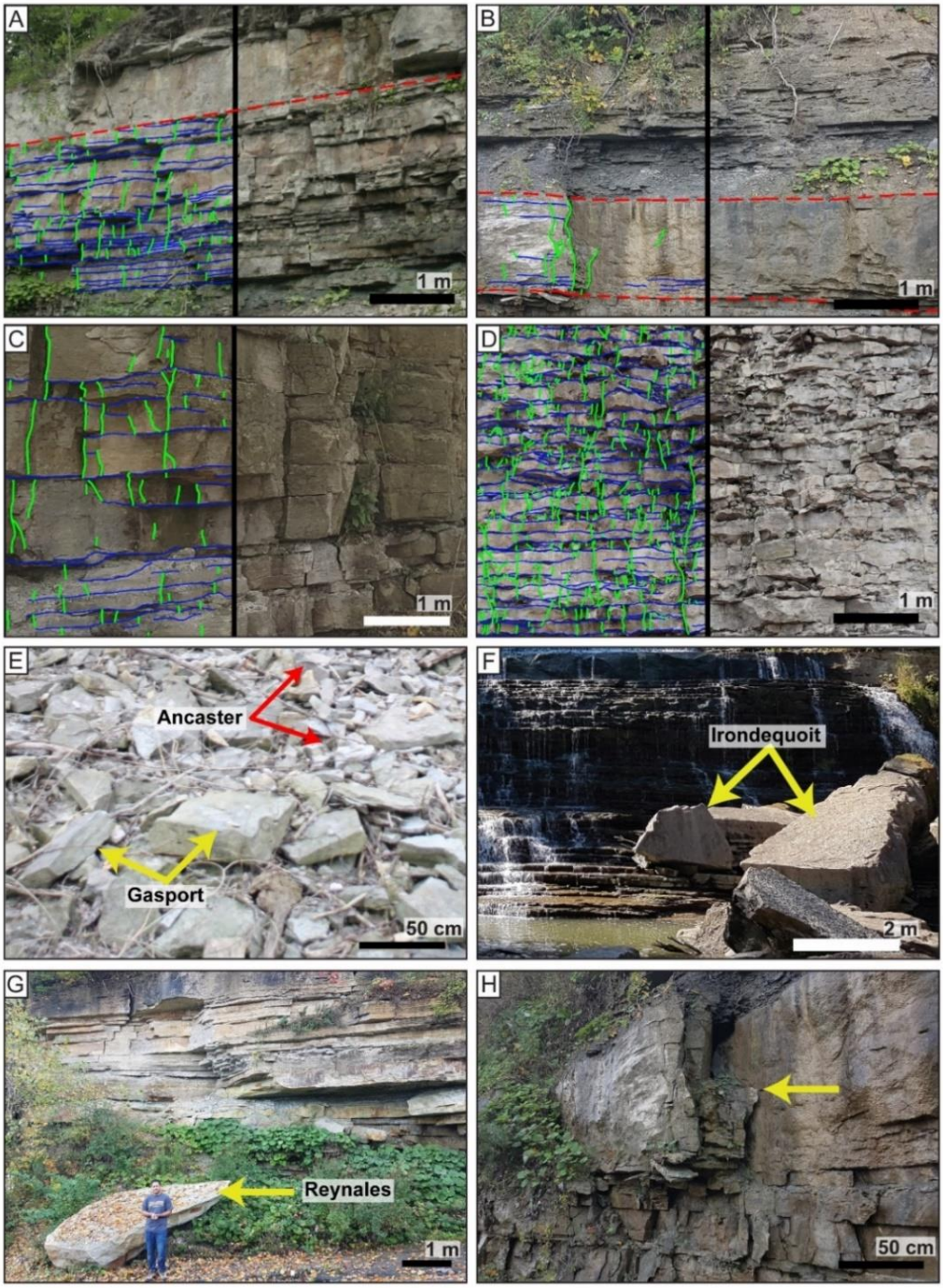

Figure 3.23: A-D) Images that highlight the differences in the density and intensity of fracturing of the dolostone dominated units exposed along the Niagara Escarpment. The left half of the images shows fracture traces, with horizontal fractures indicated in blue and vertical fractures indicated in green, while the right half shows the unit without traces. A) Ancaster Member of the Goat Island Formation (Site 7); B) Gasport Formation (Site 4); C) Irondequoit Formation (Site 11); D) Reynales Formation (Site 7); E-G) Size of debris released from the Ancaster and Gasport (E), Irondequoit (F) and Reynales (G); H) Fracture running obliquely to the rock face (yellow arrow), creating plane of weakness.

The dolostone-dominated lithological units comprising the Manitoulin, Reynales, Irondequoit, and Gasport Formations, and the Ancaster Member of the Goat Island Formation (Figure 3.22), show varying amounts of fracturing (Figure 3.23A-D; Formenti et al. 2021). Fracture density has a major control on the size of blocks released from the escarpment face as block size is largely determined by bed thickness and fracture spacing; this can be observed through examination of debris at the base of the escarpment slope. At most locations in Hamilton, slope debris is composed predominantly of small dolostone blocks (2-10 cm) released from the thinly bedded and highly fractured Ancaster Member (Figure 3.23E) with occasional, much larger blocks (>1m) from the massive and largely unfractured Irondequoit Formation (Figure 3.23F); debris released from the Reynales Formation and Gasport Formation is intermediate in size (15 – 50 cm) (Figure 3.23G, H). Most fractures visible on the escarpment face have limited length, and are often restricted to a single layer or bed (Figure 3.23A-D); however, occasional larger fractures propagate through multiple beds and may reflect a more regional pattern of jointing, potentially important for long term stability of the escarpment.

Each of the lithological units exposed along the escarpment displays fractures that run both perpendicular and obliquely, almost parallel, to the rock face (Figure 3.23I). The obliquely oriented fracture sets act as planes of weakness and failure, allowing the release of blocks which may then slide or topple from the rock face. In some areas, partially released blocks appear to camber away from the rock face, suggesting the action of rock creep in underlying shales, causing the overlying dolostone blocks to lean towards the edge.

3.6.2.1. Implications for Escarpment Stability

In general, the dolostone-dominated formations exposed along the Niagara Escarpment, with their higher UCS values, are more resistant to erosion than the shale-dominated formations which can often cause undercutting and failure of the escarpment slope (Figure 3.22). Although the dolostone-dominated Manitoulin Formation has relatively low UCS, it is likely to have little impact on escarpment stability in the Hamilton region as it has limited exposure in road cuts (Figure 3.9). The Manitoulin also shows considerable variation in lithological characteristics across the city, and the most easily eroded areas are likely to be the interbedded thinly bedded dolostone and shale units exposed in central Hamilton (Figure 3.9).

The remainder of the dolostone-dominated formations are exposed across the city (Figure 3.9) and are therefore more important for determining slope stability. The Reynales and Irondequoit formations have similar mean UCS values, and theoretically should experience similar erosion rates; however, the Reynales is heavily fractured, contains thin shale interbeds (Figures 3.9, 3.15A,B and 3.23A), and erodes much more rapidly than the massive, unfractured Irondequoit (Figure 3.23B), which is erosion resistant and usually protrudes from the escarpment face.

The Gasport Formation and Ancaster Member of the Goat Island Formation show significant variation in their properties and rate of erosion across the Hamilton region. The Gasport Formation has lower UCS than the Ancaster due to the presence of shale interbeds and is therefore more susceptible to erosion in areas of higher shale content (Figure 3.17C, E). The Gasport varies from being thick-bedded in the east to thin-bedded in the west where it has a higher shale content; this may lead to enhanced rates of erosion in the western part of the city. The Ancaster Member has the highest UCS of all the dolostone-dominated units on the escarpment, likely related to the absence of shale and abundance of chert, a highly resistant rock type. Despite its high resistance to erosion through ravelling, the highly fractured nature of the Ancaster (Figure 3.23D), facilitates block release from the escarpment face; this is evidenced by the abundance of blocks of Ancaster dolostone at the base of the escarpment face.

The dolostone-dominated lithological units that form the upper part of the escarpment play a critical role in determining the safety of the slope, as they commonly release blocks which can topple or slide onto adjacent roadways and undermine infrastructure (Table 3.2). These resistant units are particularly susceptible to undercutting by the shale-dominated units, and their stability is compromised by the presence of fractures which facilitate block release on various scales. Ensuring the stability of these units is extremely important for the management of access routes across the escarpment.

3.6.3 Sandstone-dominated formations

There are only two sandstone-dominated lithological units exposed along the escarpment in Hamilton, the Whirlpool and the Thorold formations. The strength properties of these units are determined by factors such as fabric, grain size, and mineralogy (Table 3.2). When grains within a sandstone are coarse and arranged to allow high levels of grain contact, or cementation has occurred, the rock tends to be relatively stable and resistant to erosion (Figure 3.22; Bruthans et al., 2014). Sandstones composed of resistant minerals, such as quartz, are likely to be more difficult

to erode than those composed of carbonate grains, as they do not undergo processes of dissolution or swelling. The effect of these factors on rock strength is observable through comparison of the high UCS values of fine- to medium-grained, cemented sandstones of the Whirlpool Formation compared to lower UCS values of fine-grained sandstones and interbedded shales of the Thorold. In the field, the resistant Whirlpool commonly forms a prominent ledge that protrudes significantly from the escarpment face (Figure 3.24A). The Whirlpool also experiences significant undercutting (Figures 3.13A and 3.24A) caused by the preferential erosion of the underlying Queenston Formation. In contrast, the sandstone-dominated but shale-rich Thorold Formation, is less prominent on the escarpment face as shale interbeds create areas of weakness that allow undercutting and destabilization of individual sandstone beds (Figure 3.24B).

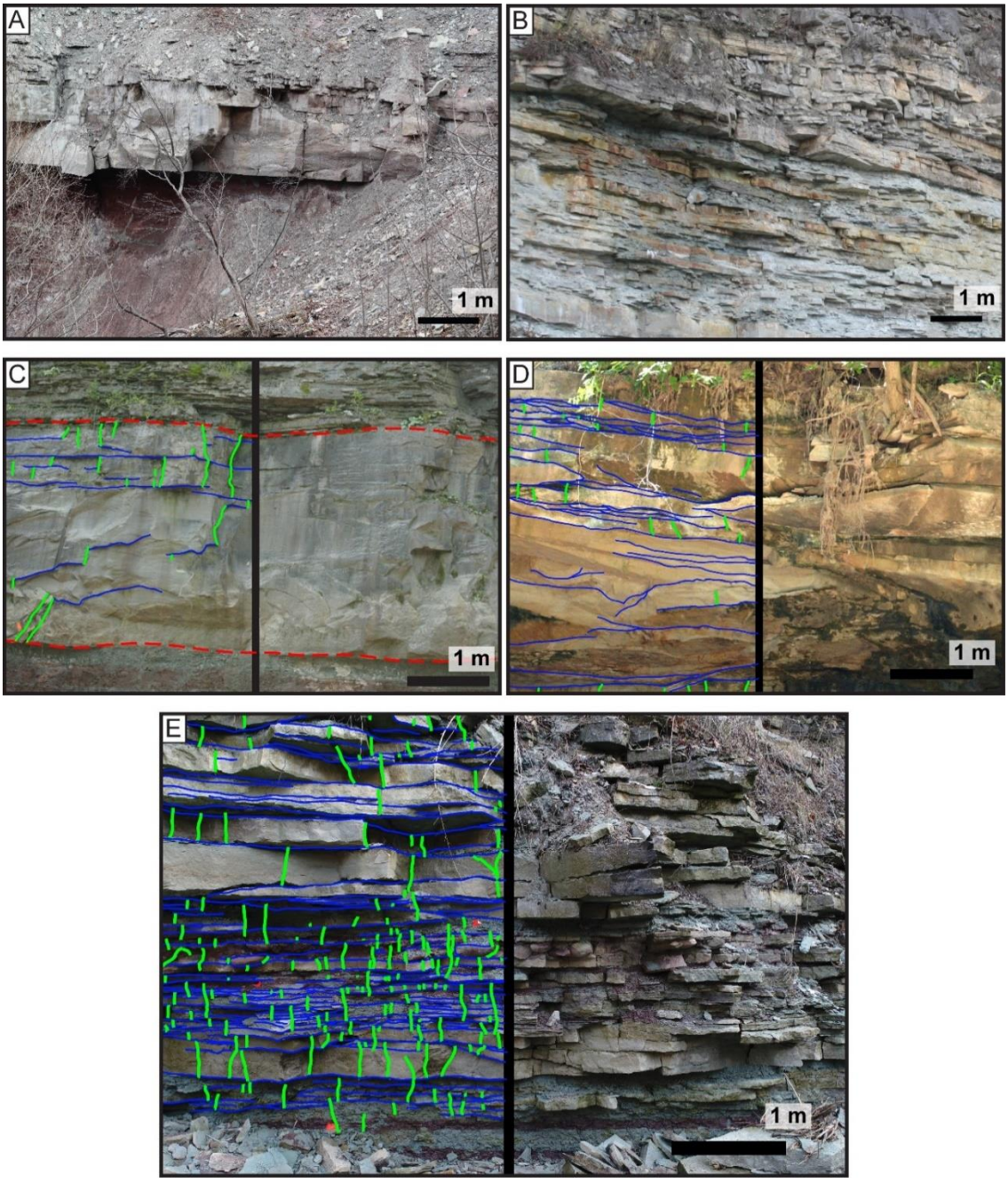

Figure 3.24: A) Undercutting of the Whirlpool by shales of the Queenston Formation at the Devil's Punchbowl (Site 10); B) Image of the undercutting of the Thorold at Albion Falls (Site 9); C-E) Differences in the density and intensity of fracturing of the sandstone dominated units of the Niagara Escarpment. The left half of the images shows fracture traces, with horizontal fractures indicated in blue and vertical fractures indicated in green, while the right half shows the units without traces. C) Western exposure of the Whirlpool Formation (Site 6); D) Eastern exposure of the Whirlpool Formation (Site 10); E) Thorold Formation (Site 9).

The sandstone-dominated units are also susceptible to the effects of wetting and drying cycles that promote the swelling and shrinking of clay minerals within the rocks (Table 3.2; Ruedrich et al., 2011).These processes will affect the Thorold Formation most significantly as clay minerals are contained within interbedded shales. The overall stability of the Whirlpool and Thorold formations will also be impacted by the presence of fractures within the units, similarly to the dolostone-dominated units.

3.6.4 Implications for Escarpment Stability

Based on its lithological characteristics and high UCS (Table 3.1) the Whirlpool Formation is expected to be relatively resistant to erosion (Figure 3.22). The unit does show some variability in the amount of fracturing between exposures in the eastern part of Hamilton (e.g. Site 10; Figure 3.24D) which are heavily fractured, and those in the west (e.g. Site 6; Figure 3.24C) where the fracturing is minimal (Figure 3.24C, D). Exposures of the Whirlpool in the east are likely to erode more rapidly through dilation of fractures through moisture infiltration and freeze-thaw processes which can initiate block toppling.

The Thorold Formation consists of fine-grained sandstone with common, heavily fractured shale interbeds, included shale clasts, and has a low UCS value (Figure 3.18); it also contains irregularly shaped sandstone ball and pillow deformation structures which form potential areas of weakness in the unit (Figure 3.24E). Hence, the Thorold is quite susceptible to erosion and commonly undercuts the overlying dolostone-dominated Reynales Formation (Figures 3.22 and 3.24B). Both the Whirlpool and Thorold formations thin to the west of the city, where their impact on escarpment stability becomes less significant.

3. 7 Conclusions and Future work

The heterogenous stratigraphy of the Niagara Escarpment shows lateral variability across the city of Hamilton that impacts processes and rates of erosion along the escarpment face. The nature of erosional processes affecting the escarpment is controlled fundamentally by the lithological characteristics of the exposed units and it is important to fully understand their lateral and vertical variability to predict areas of the escarpment face most susceptible to material loss.

Eleven lithologic units are exposed along the escarpment in Hamilton, four of which are shale-dominated, five dolostone-dominated, and two sandstone-dominated. The shale-dominated units are likely to play a significant role in determining the stability of the rock face, as these units tend to erode more rapidly due to their lower UCS; ongoing deformation and rock creep; and

susceptibility to erosion through freeze-thaw and wetting-drying cycles. Erosion of the dolostone- and sandstone-dominated units is controlled primarily by undercutting, the amount of interbedded shale, and the density and intensity of fracturing. Hence, dolostone-dominated units underlain by shales, specifically the Ancaster, Gasport and Reynales, undergo frequent block falls from the escarpment face and pose a serious risk to the safety of adjacent roads and trails. Sandstone-dominated units are not as well exposed in the Hamilton region and have less impact on erosion of the escarpment face. However, lateral variability in lithological characteristics, particularly within the Whirlpool, Grimsby, Thorold, and Rochester formations, will result in differential erosional processes and rates at different locations across the city.

In addition to their lithological characteristics, the variable thickness of lithological units and their amount of exposure along the escarpment face will also influence erosion processes and rates. Areas of the escarpment exposing greater thickness of the shale-dominated units are likely to experience higher rates of erosion. More gently sloping natural exposures of the escarpment face are often covered and protected by surface debris and vegetation, but artificially steepened road cuts are not, and experience much higher rates of material loss. These factors should be taken into consideration when identifying and mapping areas of the escarpment most at risk from erosion.

This investigation has identified the major lithological factors that can influence erosion of the exposed escarpment face across the city of Hamilton. However, there are many other factors that are also involved, including surface and subsurface hydrological conditions, climatic factors, and anthropogenic influences. These are beyond the scope of the current study but need to be incorporated into a comprehensive analysis of erosion processes along the escarpment. In addition, it is still necessary to quantify rates of erosion along the escarpment face, both in the city of Hamilton and elsewhere. This will allow the city of Hamilton to develop better informed policy and planning approaches to the maintenance and protection of this important landscape feature. fractures in the escarpment would aid in understanding the dominant erosional processes in this area. Utilizing novel techniques, such as UAV-based photogrammetry, to complete multi-year study of outcrop development is necessary to quantify the rate of erosion in the city.

3. 8 References

Admassu, Y., Shakoor, A., & Wells, N. A. (2012). Evaluating selected factors affecting the depth of undercutting in rocks subject to differential weathering. *Engineering Geology*, *124*(1), 1–11. https://doi.org/10.1016/j.enggeo.2011.09.007

Agustawijaya, D. S. (2007). The uniaxial compressive strength of soft rock. *Civil Engineering Dimension*, *9*(1), 9–14.

Al-Maamori, H. M. S., El Naggar, M. H., & Micic, S. (2014). A Compilation of the Geo-Mechanical Properties of Rocks in Southern Ontario and the Neighbouring Regions. *Open Journal of Geology*, *4*, 210–227. https://doi.org/10.4236/ojg.2014.45017

Anastas, A. S., & Coniglio, M. (1993). Sedimentology of an early Silurian carbonate ramp: the Manitoulin Formation, southern Ontario. *Canadian Journal of Earth Sciences*, *30*(12), 2453–2464. https://doi.org/10.1139/e93-212

Armstrong, D. K., & Carter, T. K. (2009). *The subsurface Paleozoic stratigraphy of southern Ontario* (Special Vo). Ontario Geological Survey.

Armstrong, D. K., & Dodge, J. E. P. (2007). Paleozoic Geology of Southern Ontario - Project Summary and Technical Document. In *Ontario Geological Survey, Miscellaneous Release Data 219*.

Barlow, J. (2002). Rock creep and the development of the Niagara Cuesta. *Earth Surface Processes and Landforms*, *27*(10), 1125–1135. https://doi.org/10.1002/esp.401

Bolton, T. E. (1957). Silurian stratigraphy and palaeontology of the Niagara Escarpment in Ontario.

Bonazza, A., Messina, P., Sabbioni, C., Grossi, C. M., & Brimblecombe, P. (2009). Mapping the impact of climate change on surface recession of carbonate buildings in Europe. *Science of the Total Environment*, *407*(6), 2039–2050.

Bowen, C. F. P., Hewson, F. I., Macdonald, D. H., & Tanner, R. G. (1976). Rock Squeeze At Thorold Tunnel. *Canadian Geotechnical Journal*, *13*(2), 111–138. https://doi.org/10.1139/t76-013

Brett, C. E., Goodman, W. M., & LoDuca, S. T. (1990). Sequences, cycles, and basin dynamics in the Silurian of the Appalachian Foreland Basin. *Sedimentary Geology*, *69*(3–4), 191–244. https://doi.org/10.1016/0037-0738(90)90051-T

Brigham, R. J. (1971). *Structural geology of southwestern Ontario and southeastern Michigan*. Ontario Department of Mines and Northern Affairs.

Brintnell, C., Brunton, F. R. R., Brett, C. E. E., & Jin, J. (2009). Characterization of the Fossil Hill–Cabot Head formational disconformity between Tobermory and Guelph, Niagara Escarpment region, southern Ontario. In *Ontario Geological Survey, Open File Report 6240* (Vol. 32, Issue 26, pp. 10–26). Ontario Geological Survey. https://doi.org/10.1016/0148-9062(95)00021-8

Brogly, P. J., Martini, I. P., & Middleton, G. V. (1998). The Queenston Formation: Shale-dominated, mixed terrigenous-carbonate deposits of Upper Ordovician, semiarid, muddy shores in Ontario, Canada. *Canadian Journal of Earth Sciences*, *35*(6), 702–719. https://doi.org/10.1139/e98-021

Brunton, F. R., & Brintnell, C. (2020). Early Silurian Sequence Stratigraphy and Geological Controls on Karstic Bedrock Groundwater-Flow Zones, Niagara Escarpment Region and the Subsurface of Southwestern Ontario.

Bruthans, J., Soukup, J., Vaculikova, J., Filippi, M., Schweigstillova, J., Mayo, A. L., Masin, D., Kletetschka, G., & Rihosek, J. (2014). Sandstone landforms shaped by negative feedback

between stress and erosion. *Nature Geoscience*, *7*(8), 597–601. https://doi.org/10.1038/ngeo2209

Budetta, P., Galietta, G., & Santo, A. (2000). A methodology for the study of the relation between coastal cliff erosion and the mechanical strength of soils and rock masses. *Engineering Geology*, *56*(3–4), 243–256. https://doi.org/10.1016/S0013-7952(99)00089-7

Caley, J. F. (1940). Palaeozoic geology of teh Toronto-Hamilton area, Ontario.

Carter, T. R., Fortner, L. D., Russell, H. A., Skuce, M. E., Longstaffe, F. J., & Sun, S. (2021). A Hydrostratigraphic Framework for the Paleozoic Bedrock of Southern Ontario. *Geoscience Canada*, 48(1), 23–58. https://doi.org/10.12789/geocanj.2021.48.172

CBC. (2014, May 23). The escarpment is falling and it's costing Hamilton thousands. *CBC News*. https://www.cbc.ca/news/canada/hamilton/headlines/the-escarpment-is-falling-and-it-s-costing-hamilton-thousands-1.2622273

Crowley, D. J. (1973). Middle Silurian Patch Reefs in Gasport Member (Lockport Formation), New York. *AAPG Bulletin*, *57*(2), 283–300. https://doi.org/10.1306/819a426a-16c5-11d7-8645000102c1865d

Dredge, L. A. (1992). Breakup of Limestone Bedrock by Frost Shattering and Chemical Weathering , Eastern Canadian Arctic Author (s): L . A . Dredge Source : Arctic and Alpine Research , Vol . 24 , No . 4 (Nov ., 1992), pp . 314-323 Published by : INSTAAR , University of Co. *Arctic and Alpine Research*, *24*(4), 314–323.

Environment Canada. (2019). *Canadian Cliamte Norals 1981-2010 Hamilton RBG Stations Data*. https://climate.weather.gc.ca/climate_normals/results_1981_2010_e.html?stnID=4937&autofwd=1

Eyssautier-Chuine, S., Marin, B., Thomachot-Schneider, C., Fronteau, G., Schneider, A., Gibeaux, S., & Vazquez, P. (2016). Simulation of acid rain weathering effect on natural and artificial carbonate stones. *Environmental Earth Sciences*, *75*(748), 1–19. https://doi.org/10.1007/s12665-016-5555-z

Fahey, B. D., & Lefebure, T. H. (1988). The freeze-thaw weathering regime at a section of the Niagara escarpment on the Bruce Peninsula, Southern Ontario, Canada. *Earth Surface Processes and Landforms*, *13*(4), 293–304. https://doi.org/10.1002/esp.3290130403

Feenstra, B. H. (1981). Quaternary geology and industrial minerals of the Niagara-Welland Area, southern Ontario (p. 260). Ontario Geological Survey - Open File Report 5361.

Formenti, S., Peace, A. Eyles, C. H., Lee, R. & Waldron, J.W.F. (2021). Fractures in the Niagara Escarpment in ontario, Canada: Distribution, Connectivity and geohazard implications. *Geological Magazine (submitted).*

Franklin, J. A. (1981). A shale rating system and tentative applications to shale performance. *Transportation Research Record*, *790*(3), 2–12.

Gao, C. (2011). Buried bedrock valleys and glacial and subglacial meltwater erosion in Southern Ontario, Canada. *Canadian Journal of Earth Sciences*, *48*(5), 801–818. https://doi.org/10.1139/e10-104

Gilbert, G. K. (1890). *The history of the Niagara River*. James Lyon.

Google. (2021a). *Claremont Access Streetview*. https://www.google.ca/maps/@43.2457819,-79.8670018,3a,75y,214.92h,99.24t/data=!3m6!1e1!3m4!1sipoOqWHwXDqWtzLaFf3okw!2e0!7i16384!8i8192

Google. (2021b). Terrain view of Sherman Access in Hamilton, Ontario. Google Earth.

Gross, M. R., & Engelder, T. (1991). A case for neotectonic joints along the Niagara Escarpment. *Tectonics*, *10*(3), 631–641. https://doi.org/10.1029/90TC02702

Eyles, N., Arnaud, E., Scheidegger, A. E., & Eyles, C. H. (1997). Bedrock jointing and geomorphology in southwestern Ontario, Canada: an example of tectonic predesign. Geomorphology, 19(1-2), 17-34.

Hayakawa, Y. S., & Matsukura, Y. (2009). Factors influencing the recession rate of Niagara Falls since the 19th century. *Geomorphology*, *110*(3–4), 212–216. https://doi.org/10.1016/j.geomorph.2009.04.011

Hewitt, D. F. (1971). *The Niagara Escarpment* (Industrial). Ontario Department of Mines and Northern Affairs - Report No. 35.

Johnson, M. D., Armstrong, D. K., Sanford, B. V., Telford, P. G., & Rutka, M. A. (1992). Paleozoic and Mesozoic Geology of Ontario. In *Geology of Ontario* (Special Vo, pp. 907–1010). Ontario Geological Survey.

Kaiser, P. K., & Kim, B. H. (2014). Characterization of Strength of Intact Brittle Rock Considering Confinement-Dependent Failure Processes. *Rock Mechanics and Rock Engineering*, *48*(1), 107–119. https://doi.org/10.1007/s00603-014-0545-5

Kirby, E., & Ouimet, W. (2011). Tectonic geomorphology along the eastern margin of Tibet: Insights into the pattern and processes of active deformation adjacent to the Sichuan Basin. *Geological Society Special Publication*, *353*, 165–188. https://doi.org/10.1144/SP353.9

Lam, T., Martin, D., & McCreath, D. R. (2007). Characterising the geomechanics properties of the sedimentary rocks for the DGR excavations. *Canadian Geotechnical Conference OttawaGeo2007*, *January*, 636–644.

Lo, K. Y. (1978). Regional Distribution of in Situ Horizontal Stresses in Rocks of Southern Ontario. *Canadian Geotechnical Journal*, *15*(3), 371–381. https://doi.org/10.1139/t78-034

Lo, K. Y. (1989). Recent advances in design and evaluation of performance of underground structures in rocks. *Tunnelling and Underground Space Technology Incorporating Trenchless*, *4*(2), 171–183. https://doi.org/10.1016/0886-7798(89)90050-3

Lo, K. Y., & Hori, M. (1979). Deformation and Strength Properties of Some Rocks in Southern Ontario. *Can Geotech J*, *16*(1), 108–120. https://doi.org/10.1139/t79-010

Lo, K. Y., & Lee, Y. N. (1990). Time-dependent deformation behaviour of Queenston shale. *Canadian Geotechnical Journal*, *27*(4), 461–471. https://doi.org/10.1139/t90-061

Lo, K. Y., Wai, R. S. C., Palmer, J. H. L., & Quigley, R. M. (1978). Time-Dependent Deformation of Shaly Rocks in Southern Ontario. *Canadian Geotechnical Journal*, *15*(4), 537–547. https://doi.org/10.1139/t78-057

Loye, A., Pedrazzini, A., Theule, J. I., Jaboyedoff, M., Liébault, F., & Metzger, R. (2012). Influence of bedrock structures on the spatial pattern of erosional landforms in small alpine catchments. *Earth Surface Processes and Landforms*, *37*(13), 1407–1423. https://doi.org/10.1002/esp.3285

Luczaj, J. A. (2013). Geology of the Niagara Escarpment in Wisconsin. *Geoscience Wisconsin*, *22*(1), 1–34.

Mann, K. (2019, May 14). Rockslide closes Hamilton mountain access, sports fields remain closed due to soggy conditions. *Global News*. https://globalnews.ca/news/5276437/rockslide-closes-hamilton-mountain-access/

McGreevy, J. P. (1981). Some perspectives on frost shattering. *Progress in Physical Geography*, *5*(1), 56–75. https://doi.org/10.1177/030913338100500103

Miščević, P., & Vlastelica, G. (2014). Impact of weathering on slope stability in soft rock mass. *Journal of Rock Mechanics and Geotechnical Engineering*, *6*(3), 240–250. https://doi.org/10.1016/j.jrmge.2014.03.006

Niemann, W. L. (2009). Lessons learned from rates of mudrock undercutting measured over two time periods. *Environmental and Engineering Geoscience*, *15*(3), 117–131. https://doi.org/10.2113/gseegeosci.15.3.117

Palmer, J. H. L., & Lo, K. Y. (1976). In situ stress measurements in some near-surface rock formations - Thorold, Ontario. *Canadian Geotechnical Journal*, *13*(1), 1–7.

Perras, M. A., Diederichs, M. S., & Besaw, D. (2014). Geological and geotechnical observations from the Niagara Tunnel Project. *Bulletin of Engineering Geology and the Environment*, *73*, 1303–1323. https://doi.org/10.1007/s10064-014-0633-5

Philbrick, S. S. (1970). Horizontal Configuration and the Rate of Erosion of Niagara Falls. *Geological Society of America Bulletin*, *81*, 3723–3732.

Portenga, E. W., & Bierman, P. R. (2011). Understanding earth's eroding surface with 10Be. *GSA Today*, *21*(8), 4–10. https://doi.org/10.1130/G111A.1

Quigley, R. M., Thompson, C. D., & Fedorkiw, J. P. (1978). A pictorial case history of lateral rock creep in an open cut into the Niagara Escarpment rocks at Hamilton, Ontario. *Canadian Geotechnical Journal*, *15*(1), 128–133. https://doi.org/10.1139/t78-011

Radbruch-Hall, D. H. (1978). Gravitational creep of rock masses on slopes. *Developments in Geotechnical Engineering*, *14*, 607–657.

Reddy, M. M. (1988). Acid rain damage to carbonate stone: a quantitative assessment based on the aqueous geochemistry of rainfall runoff from stone. *Earth Surface Processes and Landforms*, *13*(4), 335–354.

Roegiers, J.-C., Thompson, J. C., & McLennan, J. D. (1979). Rock movements induced by the construction of the Hamilton Mountain trunk sewer (stage 4). *Canadian Geotechnical Journal*, *16*(4), 651–658. https://doi.org/10.1139/t79-075

Roy, D. G., Singh, T. N., Kodikara, J., & Das, R. (2017). Effect of water saturation on the fracture and mechanical properties of sedimentary rocks. *Rock Mechanics and Rock Engineering*, *50*(10), 2585–2600. https://doi.org/https://doi.org/10.1007/s00603-017-1253-8

Ruedrich, J., Bartelsen, T., Dohrmann, R., & Siegesmund, S. (2011). Moisture expansion as a deterioration factor for sandstone used in buildings. *Environmental Earth Sciences*, *63*(7), 1545–1564. https://doi.org/10.1007/s12665-010-0767-0

Sanford, J. T., Martini, I. ., & Mosher, R. E. (1972). *Niagaran stratigraphy: Hamilton, Ontario*.

Scott, D. N., & Wohl, E. E. (2019). Bedrock fracture influences on geomorphic process and form across process domains and scales. *Earth Surface Processes and Landforms*, *44*(1), 27–45. https://doi.org/10.1002/esp.4473

Shakoor, A., & Rodgers, J. P. (1992). Predicting the rate of shale undercutting along highway cuts. *Bulletin of the Association of Engineering Geologists*, *29*(1), 61–75. https://doi.org/10.2113/gseegeosci.xxix.1.61

Straw, A. (1968). Late Pleistocene glacial erosion along the Niagara Escarpment of southern Ontario. *Geological Society of America Bulletin*, *79*(7), 889–910.

Tepper, D. H., York, N., Goodman, W. M., York, N., Gross, M. R., Kappel, W. M., York, N., & Yager, R. M. (1990). *Stratigraphy , structural geology, and hydrogeology of the Lockport Group : Niagara Falls area , New York* (pp. 1–25). Field Trip Guidebook.

Tinkler, K. J., & Pengelly, J. W. (1994). Protalus ramparts and related features along the Niagara Escarment, Niagara Peninsula, Ontario. *Permafrost and Periglacial Processes*, *5*, 171–184.

Tinkler, K. J., & Stenson, R. E. (1992). Sculpted bedrock forms along the Niagara Escarpment, Niagara Peninsula, Ontario. *Geographie Physique et Quaternaire*, *46*(2), 195–207. https://doi.org/10.7202/032904ar

Van Dongen, M. (2017, December 28). Experts begin 'painstaking' study of failing Claremont Access walls. *The Hamilton Spectator*. https://www.thespec.com/news-story/7040741-experts-begin-painstaking-study-of-failing-claremont-access-walls/

Walker, P. J. (2004). Strength and erosion characteristics of earth blocks and earth block masonry. *Journal of Materials in Civil Engineering*, *16*(5), 497–506.

Wallace, K., & Eyles, N. (2015). Seismites within Ordovician-Silurian carbonates and clastics of Southern Ontario, Canada and implications for intraplate seismicity. *Sedimentary Geology*, *316*, 80–95. https://doi.org/10.1016/j.sedgeo.2014.12.004

Wang, S. L., Lv, Q. F., Baaj, H., Li, X. Y., & Zhao, Y. X. (2016). Volume change behaviour and microstructure of stabilized loess under cyclic freeze–thaw conditions. *Canadian Journal of Civil Engineering*, *43*(10), 865–874. https://doi.org/10.1139/cjce-2016-0052

Zhou, Z., Cai, X., Cao, W., Li, X., & Xiong, C. (2016). Influence of water content on mechanical properties of rock in both saturation and drying processes. *Rock Mechanics and Rock Engineering*, *49*(8), 3009–3025. https://doi.org/https://doi.org/10.1007/s00603-016-0987-z

Chapter Four: Accuracy of change detection and volume calculations using UAV-based imagery of sedimentary rock outcrops on the Niagara Escarpment, Hamilton, Ontario, Canada

Abstract

Steep sedimentary rock slopes, such as those found along coasts and road cuts, undergo continual erosion, and can threaten the stability and safety of nearby infrastructure. These risks necessitate a detailed understanding of the rate of erosion and the factors that influence it over time. The issue of slope erosion is becoming increasingly important in Hamilton, Ontario where the Niagara Escarpment divides the lower city and the upper city and agricultural areas. In Hamilton, the Niagara Escarpment is a steep-faced cuesta composed of Ordovician and Silurian (400 – 450 million years old) sedimentary rocks and is crossed by 19 access routes that link the upper and lower parts of the city. Recent slope activity on the rock face, including significant rockfalls onto the roads, has raised major concerns about the stability of the escarpment. To address these concerns, and to provide more information on erosional processes active along the escarpment, a quantitative study to determine the rate of erosion using change detection methodologies, was conducted. Using an unpiloted aerial vehicle (UAV), imagery of a selected rock face on the escarpment was collected and used in a Structure from Motion (SfM) workflow to create detailed 3-D models. Following this initial photographic survey, blocks of a known size were removed from the site and a second survey was conducted. Agisoft Metashape software was used to create point clouds of the rock face from the two surveys. These were imported into CloudCompare, aligned, and the M3C2 algorithm was used to determine the distance of change detected from the removal of the blocks. The distances computed using the M3C2 algorithm were also used to estimate the volume of change which was compared to the known volume of the rock samples removed from the outcrop. The results of these calculations indicate that most of the removed blocks were detectable using M3C2, with a single small sample being missed. However, the volume of change estimates differed from the measured volume of the removed blocks, both over- and underestimating the change. This study demonstrates that the method used here for the detection of small-scale material loss from a rocky slope, provides a good estimate of the location

of eroded/lost blocks, but does not calculate volume losses accurately and should only be used as a guide for estimating amounts of rock lost when considering small-scale erosion events.

Keywords: Structure from Motion, close-range photogrammetry, change detection, erosion monitoring

4. 1 Introduction

The erosion of sedimentary rock slopes, coastal cliffs, and bedrock exposures through rockfalls and other slope failures near roadways and homes, pose a serious risk to the stability and integrity of urban infrastructure (Admassu et al., 2012; Miščević & Vlastelica, 2014; Clark, 2017; DiFrancesco et al., 2020). This potential for instability, the risks to health and safety, as well as the financial burden of repairs to infrastructure, create a need for an effective methodology to accurately determine the rate of slope erosion and how this rate is changing over time. Previous methodologies used to monitor slope erosion over long time periods include the installation of erosion pins, repetitive surveying over multiple years, and the construction of multiple slope profiles (Welch & Jordan, 1983; Barker et al., 1997; Gulyaev & Buckeridge, 2004). These methodologies are difficult to employ on steep, rocky cliffs, they have limited spatial resolution, and may not fully encapsulate the variety of erosional processes active on a heterogeneous rock face. The emplacement of erosion pins can also cause disruption to the surface of interest. Recently introduced non-invasive methodologies, utilizing remotely sensed data collected by terrestrial (or aerial) based LiDAR, has allowed the creation of high-resolution datasets (Welch & Jordan, 1983; Barker et al., 1997; Micheletti et al., 2015; Benjamin et al., 2016; Bonneau et al., 2019b). However, these methodologies are expensive, and require costly equipment and high degrees of technical skill to both collect and analyze the data (Micheletti et al., 2015; Letortu et al., 2018).

This study reports on the use of widely available, and relatively inexpensive, Unpiloted Aerial Vehicles (UAVs) to rapidly collect photographic data to be used for long-term slope erosion monitoring. Recent improvements in the accessibility, technological specifications and automation of UAVs, have resulted in their increased use in a number of geomorphological and environmental research fields, including landslide and erosion monitoring (Niethammer et al., 2012; Eltner et al., 2015; Hackney & Clayton, 2015; Stumpf et al., 2015; Bi et al., 2017; Duró et al., 2018; Nesbit & Hugenholtz, 2019; Schumann et al., 2019; Giordan et al., 2020; Javadnejad et al., 2021; Letortu et al., 2018). In addition to the enhanced ease of data collection with UAVs, the development of

Structure from Motion (SfM) software has enabled data collection using non-metric cameras; this allows the creation of detailed 3-D datasets with limited user supervision and less extensive expertise in stereophotogrammetric processing (Szeliski, 2011; Fonstad et al., 2013; Micheletti et al., 2015; Stumpf et al., 2015). SfM software utilizes the principles of stereoscopic photogrammetry, identifying common features from a series of overlapping images to establish spatial relationships between the features in an arbitrary 3-D space (Westoby et al., 2012; Fonstad et al., 2013; Micheletti et al., 2015; Javadnejad et al., 2021). This facilitates multi-temporal studies designed to analyze the development and erosion of cliffs, landslides and debris flows (Olsen et al., 2015; DiFrancesco et al., 2020; Giordan et al., 2020). The combined use of UAVs and SfM provides a unique opportunity to conduct high spatial resolution surveys, quickly and on a high temporal scale, in order to both observe and quantify erosion rates on an unstable slope.

The issue of sedimentary rock slope erosion has become increasingly important in the City of Hamilton, located at the western end of Lake Ontario, as the Niagara Escarpment extends through the city, dividing the downtown core from adjacent suburban and agricultural areas above the escarpment brow (Figure 4.1B; CBC, 2014; Van Dongen, 2017b, 2017a). The Niagara Escarpment is a significant geomorphological feature in the region, extending from New York State through southern Ontario, into Michigan and Wisconsin (Figure 4.1A). It varies in form and appearance along its length, changing from a steep rock face in parts of southern Ontario, to a more gentle-sloped feature buried beneath glacial deposits and not observable at the surface (Hewitt, 1971; Tinkler & Pengelly, 1994; Luczaj, 2013). In Hamilton, a city of over 500 thousand people, nineteen access roads cross the escarpment, ranging from single-lane one-way roads to provincial highways (Figure 4.1B). Dozens of pedestrian hiking trails (including the Bruce Trail; Pearson, 2019) follow the base of the escarpment or climb it, often leading users to picturesque waterfalls (Hamilton is known as the city of Waterfalls; McCann, 1987) important for tourism in the city (Figure 4.1B and Figure 4.2A,B; Berezin, 2012). Understanding the stability of the escarpment is critical for the city to maintain the safety of access roads and trails, to predict and reduce infrastructure costs, and to protect the natural landscape of the escarpment.

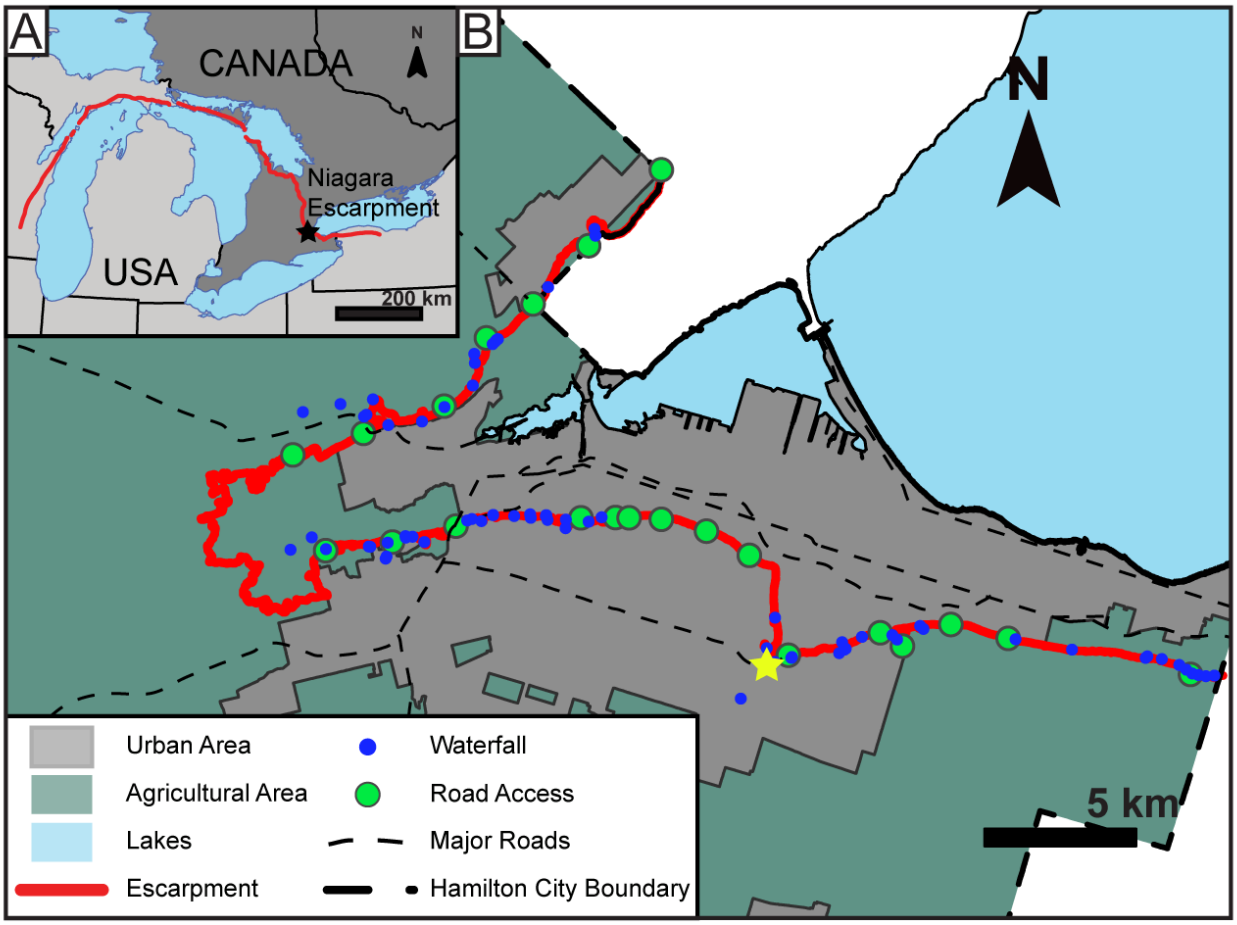

Figure 4.1: A) Location of the Niagara Escarpment (indicated with a red line) extending though New York State, southern Ontario, Michigan, and Wisconsin. Location of Hamilton, Ontario indicated with the black star. B) Extent of the Niagara Escarpment within Hamilton; the distribution of urban and agricultural areas in Hamilton are shown. The location of the waterfalls (blue dots) found on the escarpment and the road accesses (green dots) are indicated. Location of the study site at Albion Falls is shown with a yellow star.

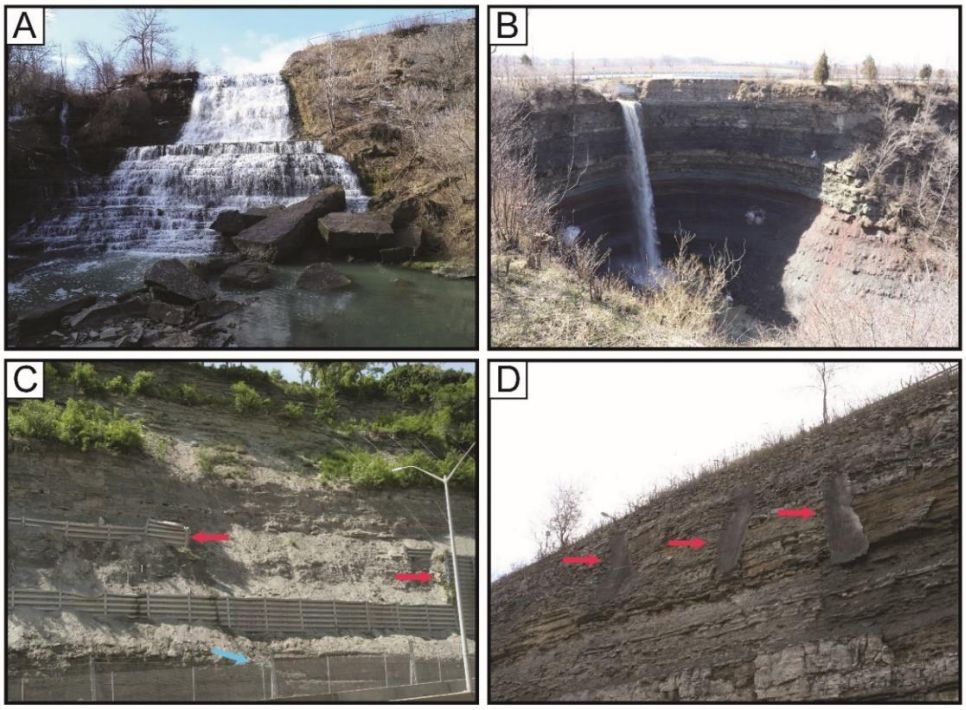

Figure 4.2: A) Albion Falls, a two-tiered waterfall, which cascades over the escarpment. This waterfall is located immediately south of the study site; B) Waterfall at the Devil's Punchbowl; this 36 m waterfall has eroded the sedimentary rocks of the Niagara Escarpment; C) Failed retaining walls at the Claremont Access (indicated with red arrows). A fence and barrier (blue arrow) have been installed to protect traffic on the road (in foreground) from rockfall debris; D) Remains of shotcrete used to support rock face at the Sherman Access (red arrows); rock fences have been installed at this location to reduce risks of falling rock to traffic.

Limited research has been conducted, or published, on erosion of the Niagara Escarpment in Hamilton, despite decades of issues with massive rock and mud slides that have closed roadways and damaged infrastructure (Van Dongen, 2017b; Mann, 2019). While research quantifying rates of erosion and determining key factors controlling erosion processes has not been pursued, many erosion control measures have been implemented in an attempt to reduce failure of the escarpment face (e.g. rock fences, barriers, scaling of the face), with variable success (Figure 4.2C,D). This clearly demonstrates the need to pursue long term erosion monitoring of the escarpment in the Hamilton area, to help quantify the rate of erosion occurring on slopes adjacent to access roads and natural sites, and to predict areas where enhanced erosion rates may be expected in the future. The application of UAV-based photography, combined with SfM 3-D modelling and analysis, provides an excellent methodology with which to monitor short- and long-term erosion rates and processes on the Niagara Escarpment in Hamilton. The purpose of the study reported here is to use

staged erosional events, involving the removal of rock blocks from the escarpment face, to determine the accuracy of the methodology which may be applied to other regions where similar erosion problems are encountered. As many erosional events along the Niagara Escarpment are characterized by single rockfalls and the loss of relatively small volumes of material, the focus of this study was the removal of relatively small blocks (<30 cm) from the escarpment face to determine the lower limit of detection using these methods.

4.1.1 Study Area

The Niagara Escarpment is composed of sedimentary rocks, primarily shales, dolostones, and sandstones deposited during the Late Ordovician and Silurian periods when the region was covered by a shallow epeiric sea (Tepper et al., 1990; Armstrong & Dodge, 2007; Brunton & Brintnell, 2020). These Paleozoic sedimentary rocks have been exposed at surface since the late Neogene to Quaternary and have a shallow dip of about 5.5m/km to the south (Brigham, 1971; Feenstra, 1981). The escarpment has formed through differential erosion of predominantly shale and dolostone lithologies by fluvial and glacial erosion processes over the past several million years and is progressively migrating toward the southwest. In southern Ontario, the escarpment reaches a maximum height of approximately 266 m, with a local maximum in Hamilton of 100 m (Hewitt, 1971; Perras et al., 2014).

The study site selected for erosion monitoring on the escarpment was an almost vertical exposure through several lithological units at Albion Falls in eastern Hamilton (Figure 4.3A). This location was selected as it exhibits considerable vertical variation in lithology and contains areas of undercutting and vegetation cover which are potential obstacles to obtaining detailed images and creating an accurate 3-D model of the escarpment face. The methods used in this study are intended to be applied to other sites of interest in Hamilton which range from a few metres to more than 50 metres in height. In addition, the site lies within a small valley more than 60 m from the nearest roadway; this allows detailed study of the area using a UAV and minimizes access and safety risks. The rock face of interest contains three distinct lithological units with differing sedimentological characteristics; the Grimsby Formation composed of interbeds of shale and sandstone; the Thorold Formation dominated by sandstone with thin shale layers; and the Reynales Formation, a dolostone unit with thin shale layers (Figure 4.3B). These formations are representative of the sedimentary rock types that are exposed elsewhere along the escarpment in the Hamilton area.

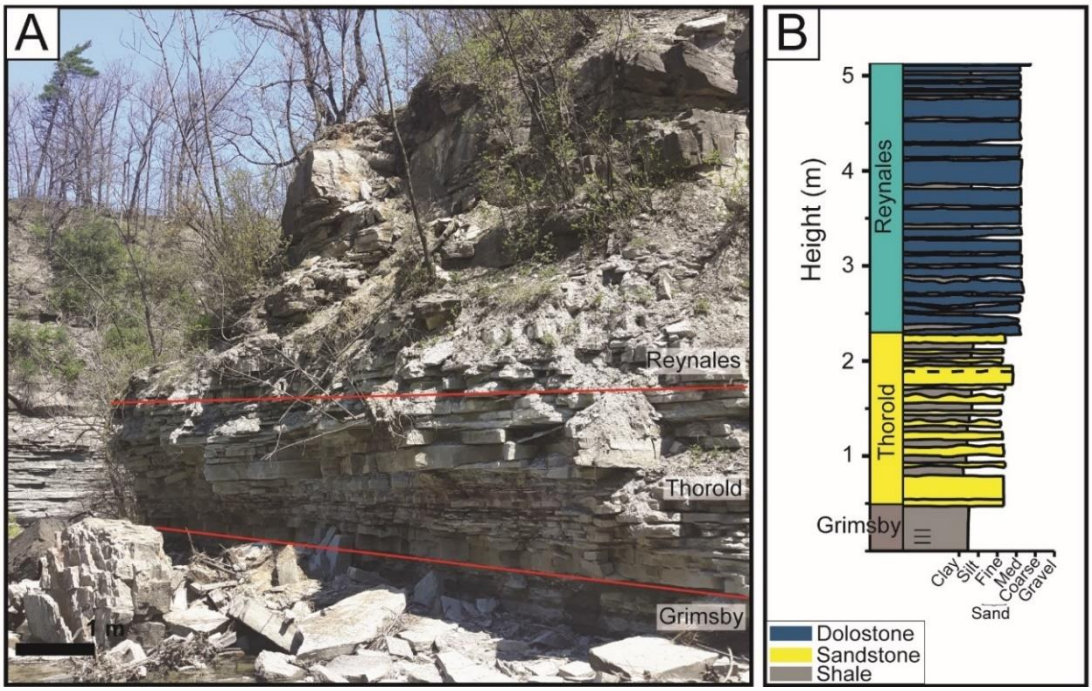

Figure 4.3: A) Image of the near vertical face selected as the Albion Falls study site, showing sparse vegetation cover, areas of shadow and undercutting. This exposure shows considerable vertical variation in lithology ranging from shale at the base (Grimsby Fm.) through interbedded sandstones and shales (Thorold Fm.) to dolostone with thin shale interbeds (Reynales Fm.). B) Schematic sedimentological log of the outcrop showing vertical lithological variation.

4. 2 Methods

4.2.1 Field Data Collection

Data collection occurred in December 2018 and February 2020. To test the accuracy of the methodology, and the lower limit of erosion that can be determined, two surveys of the study site were completed during each field visit (Figure 4.4). Survey 1 was conducted with the rock face intact, to create a baseline for the study. Survey 2 was completed following approximately the same flight path after blocks of a documented size and location were manually removed from the rock face (Figure 4.5). The removed blocks represent material eroded from the outcrop face through block toppling and fall. Both the surface area and volume of each removed block was calculated. The removed samples frequently contained additional slope debris, for example loose shale fragments, which were included in the volume calculation as they were also lost from the rock face. In recognition of the difficulty of determining the volume of irregular rock blocks in the field, each measured block volume includes a 20% error to encapsulate possible issues with the volume measurements.

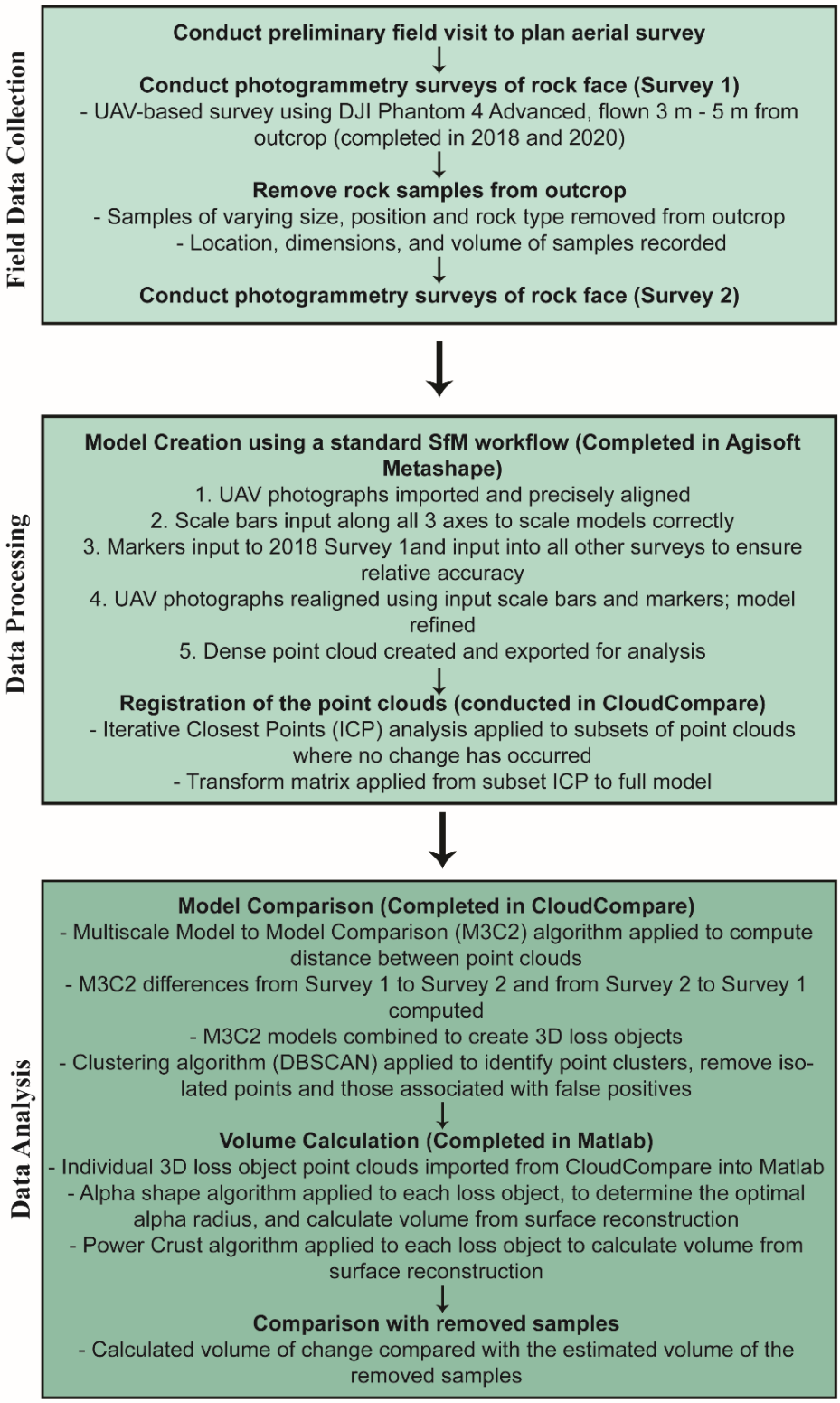

Figure 4.4: Detailed workflow used for collection of data, production of models, and change detection used within this study .

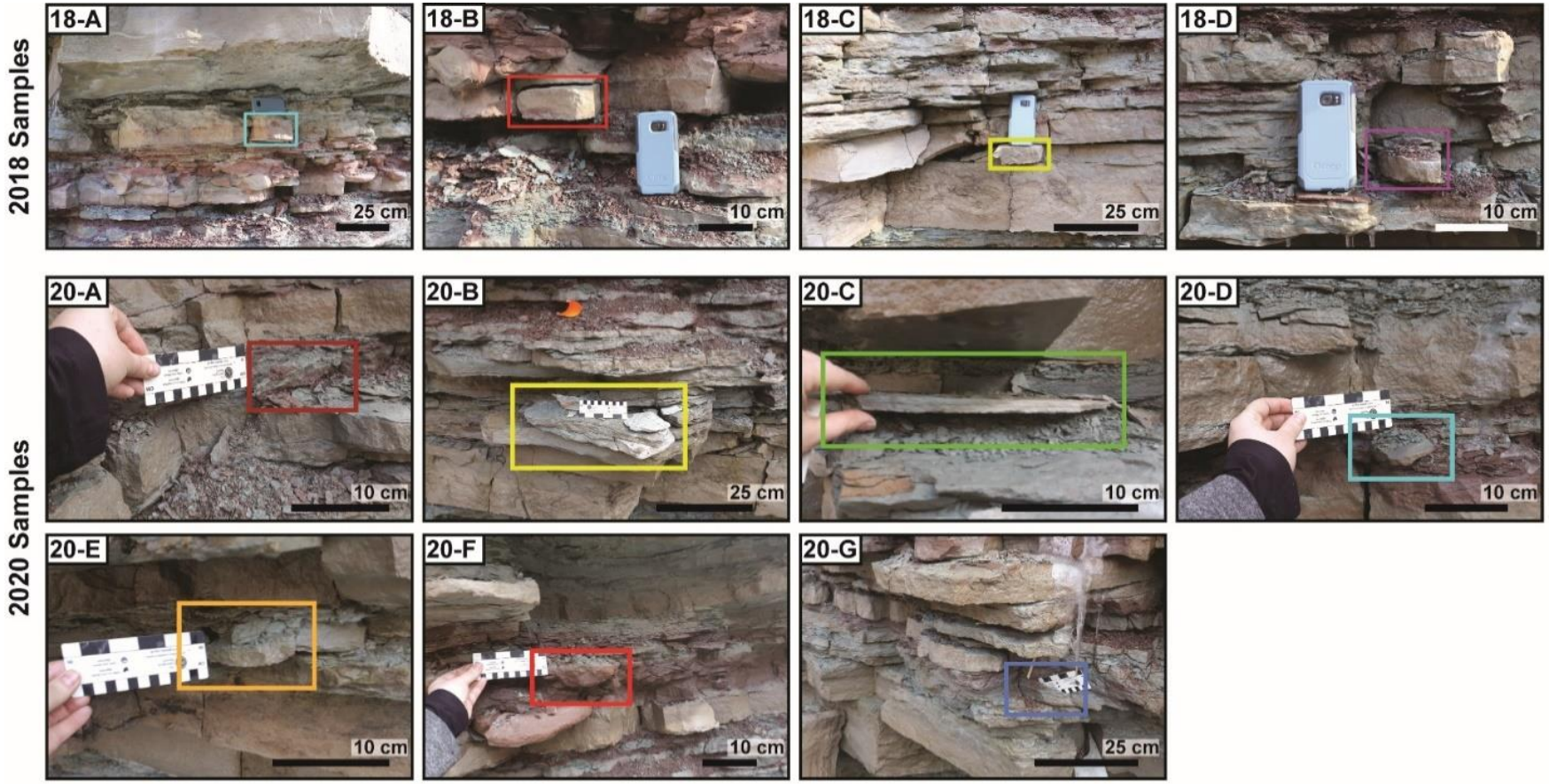

Figure 4.5: Images of sample blocks removed from the outcrop at Albion Falls in 2018 and 2020. Samples removed in 2018 (upper images) are composed of beige sandstone and were removed from the Thorold Formation in areas variably impacted by undercutting and shadow. The 2020 samples (lower two rows of images) are from both the Grimsby and Thorold formations and are composed of sandstone and shale of various colours and with variable impact from shadow and undercutting.

UAV-based imagery of the rock face was collected for both Survey 1 and Survey 2 in each of the field visits. Planning of data acquisition to ensure low error, high-resolution models was based on previous studies that outline best practices for photogrammetry data collection (James & Robson, 2012; Westoby et al., 2012; Micheletti et al., 2015; Letortu et al., 2018). Image overlap of 75% or higher was used to ensure the best 3-D reconstruction (Micheletti et al., 2015). The UAV-based imagery was collected using a DJI Phantom 4 Advanced, which has an equivalent focal length of 24 mm and 20-megapixel resolution. The built-in GPS receiver of the UAV, which has an error up to 1.5 m in the horizontal plane, was used to constrain the geometry of the outcrop for model creation. The UAV was flown 3 to 4 m from the rock face and completed multiple passes of the face at different elevations and at different angles to the cliff face (nadir and ~20 degrees off nadir). Ground control points (GCPs) were established at the site using a SxBlue II GNSS receiver but had large errors (> 1 m) due to locational issues resulting from the site lying in a narrow valley in a city, under a cover of vegetation, and proximal to a vertical cliff face. To overcome this issue and to aid in the creation of high-quality models, distances between multiple reference points identified on the rock face were measured using a measuring tape and recorded; these points were used to constrain model geometry in the model generation process and to ensure consistency in model positioning over time. The data collection methodology outlined above (Figure 4.4) was used in both field visits in December 2018 and February 2020.

4.2.2 Model Creation and Refinement

Using Agisoft Metashape (Agisoft Metashape, 2020) a standard Structure from Motion (SfM) workflow (Westoby et al., 2012; Micheletti et al., 2015; Ely et al., 2017; Javadnejad et al., 2021), was applied to each of the photogrammetric surveys collected during each field visit (Figure 4.4). Photos were aligned with the highest precision achievable; all points aligned with a reprojection error greater than 0.5 pixels were removed from the model and camera optimization was performed. The tie points used in this stage of model creation were features in the rock face which could be observed in multiple photos and allowed calculation of the geometry of the face (Lowe, 2004; Snavely et al., 2008; Micheletti et al., 2015). Vegetation at the site was relatively sparse, as the surveys were collected in winter when there is little foliage; masking of the vegetation was therefore not necessary in the modeling process. From the initial tie points, a dense point cloud was created using high precision and moderate depth filtering to help address and remove any images of vegetation on the rock face (Figure 4.6A).

The use of low-quality GCPs, such as those collected at the site, can cause significant errors in the model (James & Robson, 2012; Jaud et al., 2016). To address these concerns and to ensure model accuracy, scale bars were created along multiple axes in Metashape, using known distances between the reference points recorded in the field. This ensured accurate scaling of the digital representation of the rock face. Following this, 20 artificial markers were input to the 2018 Survey 1 UAV model in Metashape at identifiable locations; these locations acted as artificial control points (CPs) when the 2018 Survey 2 UAV model was run. The use of 20 markers was found to reduce the reprojection error and resulted in acceptable alignment of the Survey 1 and Survey 2 models. For this application, the size of the outcrop and the position of the models are the most critical components; the workflow used here (Figure 4.4) therefore focusses on maximizing the accuracy between models and not on global accuracy.

The location of the scale bars and artificial CPs of the 2018 Survey 1 model were applied to each of the other models (2018 Survey 2 model, 2020 Survey 1 and 2 models). This ensured limited model-generated error allowing direct comparison of the rock outcrop between surveys, and qualitative and quantitative determination of the amount of change on the outcrop face between surveys. The edges of the model, where there was most discrepancy in the spacing, roughness, and quality of the points in the point cloud, were removed from each of the models maintaining a consistent extent and area of study (~13 m by 5 m). The average number of points in each model ranges from 9.9 million to 22.5 million with an average point spacing of 0.0022 m to 0.0033 m (Appendix A). To assess the error of the models, additional measured distances between points on the rock face were compared to their corresponding model lengths. The same 10 locations were chosen for each model with the average difference between the actual length and model length being ±0.8 cm.

4.2.3 Model registration and alignment

CloudCompare (CloudCompare, 2020) was used to compare the photogrammetric models (Survey 1 and Survey 2) created from the repeated UAV surveys of the outcrop completed before and after the removal of rock samples in 2018 and 2020 (Figure 4.4). Multiple comparisons were conducted to determine the scale of block removal that could be defined using this methodology. Co-registration of the point clouds from each of the surveys (Survey 1 and Survey 2) in 2018 and 2020 was necessary to ensure that there was minimal difference in the clouds caused by error in the spatial location of points, unrelated to real-world change. These errors can occur due to issues

associated with data collection or processing, and include inaccuracies in reference point location, impact of shadows and lighting on model geometry, and the quality of the initial imagery (Lague et al., 2013; Tonkin et al., 2014).

Initial registration was completed through manual registration, picking points on areas of no change in the full model. Iterative Closest Points (ICP) is one of the most common methods of point cloud registration where no change has occurred between the collection of the models (Zhang, 1994; Rajendra et al., 2014). The ICP algorithm iteratively transforms a point cloud (Survey 2) based on a reference point cloud (Survey 1) by minimizing the square error between the neighbouring points of the two clouds (Zhang, 1994; Rajendra et al., 2014). As there are changes expected in the Survey 1 and Survey 2 models, ICP cannot be applied to the full point clouds; however, previous research has shown that ICP can be effectively applied to ensure best fit if completed on a subset of the point cloud data (Micheletti et al., 2015; Stumpf et al., 2015). In this instance, ICP was applied to a subset of the point cloud data where change had not occurred, a transformation matrix was determined, and the full point cloud was transformed using the resulting matrix (Micheletti et al., 2015; Stumpf et al., 2015); this ensured the best spatial fit of the Survey 1 and Survey 2 point clouds for each field season (Figure 4.4).

4.2.4 M3C2 Change Detection

The point cloud models created for the escarpment face are complex and include features such as vertical and sub-vertical slopes and overhangs making simple DEM of difference comparisons difficult. To address these complexities, the Multiscale Model to Model Cloud Comparison (M3C2) algorithm, which computes the local distance between two point clouds based on the surface orientation, was used (Figure 4.4; Lague et al., 2013). This is a commonly applied algorithm to evaluate change in 3-D features, such as rock outcrops (DiFrancesco et al., 2020). It is effective in determining change on complex vertical faces and provides reasonable estimates of uncertainty in model comparisons (Barnhart & Crosby, 2013; Lague et al., 2013; Stumpf et al., 2015; DiFrancesco et al., 2020). In addition to calculating areas of change based on two 3-D point clouds, the algorithm also provides a confidence interval for each of the distance measurements based on the cloud roughness and the registration error (Lague et al., 2013).

To address changes in point spacing between the models, subsampling at 0.01 m was conducted as this represents the maximum point spacing of the models. Based on prior studies, a projection diameter of one to two times the point spacing (Williams et al., 2018; DiFrancesco et

al., 2020), 0.02 m was used in this study. This projection diameter is likely to identify most rockfalls and smaller rockfall events as it reduces the impact of spatial averaging (Williams et al., 2018; DiFrancesco et al., 2020). The registration error used in this study, based on errors in the initial models and the ICP registration, was ~1.5 cm; however, a higher registration error of 5 cm was used in the modelling process to account for other unquantifiable errors in the models. In this study, a 95% confidence interval was chosen, wherein any changes identified with a confidence of less than 95% were removed and assumed to represent change caused by small differences in modelled point locations between the surveys (Figure 4.6). The confidence interval allows the user to determine whether or not the change between models represents real change or is reflective of small variations in the point locations of the models.

Following the methodologies used by other researchers (Bonneau et al., 2019a; Benjamin et al., 2020; DiFrancesco et al., 2020), the M3C2 algorithm was run twice for both the 2018 and 2020 field seasons; firstly comparing the change from Survey 1 to Survey 2 where the negative M3C2 values represent erosion and the shape of the outcrop after rockfall (block removal); and secondly from Survey 2 to Survey 1 where positive values represent the shape of the front of the rock block which was removed between Survey 1 and 2. These point clouds are merged to represent the 3-D loss objects (i.e. the removed blocks).

From the M3C2 point cloud, areas of change representing minor variations in the location of vegetation and shadows between models were removed manually. Clustering analysis was performed on the cleaned M3C2 point clouds to identify and remove any remaining isolated points from the clouds and identify the individual rock blocks which were removed from the outcrop. This was completed using the density-based spatial clustering of applications with noise (DBSCAN) algorithm, as suggested in prior studies (Tonini & Abellan, 2014; Bonneau et al., 2019b; Benjamin et al., 2020; DiFrancesco et al., 2020), and used a search radius of 15, chosen based on the k-nearest neighbours method (Kurumalla & Srinivasa Rao, 2016; MathWorks, 2021) and a minimum of 12 points. Points identified as ‘not part of clusters’ were removed from the point cloud and a final manual check of the point cloud was completed to ensure the clusters represented actual change in the face.

4.2.5 Volume Calculations

Two common methodologies, applying the alpha shape and power crust algorithms (Amenta et al., 2001; van Veen et al., 2017; Bonneau et al., 2019b; DiFrancesco et al., 2020, 2021),

were used to reconstruct the surface form of the blocks and to calculate the volume of identified areas of change in the models. Both surface reconstruction methodologies were completed in MATLAB. When completing surface reconstruction, appropriate parameters were chosen to ensure that each surface model is manifold and watertight (van Veen et al., 2017; Bonneau et al., 2019b; DiFrancesco et al., 2021).

An alpha shape algorithm generalizes the convex hull of a point set which is defined as the union of all simplices covered by its alpha complex. The alpha complex is a subcomplex of the Delaunay triangulation of the point set which includes all Delaunay tetrahedra (including faces, edges and points) which have empty spheres with radii less than the set alpha radius. Alpha radii were determined separately for each of the defined clusters in order to find the smallest radius that creates a manifold, watertight model to provide accurate volume measurements. The second surface reconstruction methodology utilized the power crust algorithm (Amenta et al., 2001) which computes an approximate medial axis transform (MAT) based on a subset of Voronoi vertices of the point set (Amenta et al., 2001; Bonneau et al., 2019b). From the MAT, a piecewise-linear approximation of the surface is created (Amenta et al., 2001; Bonneau et al., 2019b).

4. 3 Results

In the 2018 field study, following the collection of UAV imagery (Survey 1) of the exposed rock face, sample blocks of rock with lengths ranging from 9.2 cm to 28.4 cm were removed (Figure 4.7A) and the rock face was rephotographed (Survey 2). The M3C2 algorithm was able to identify the location of all four removed blocks by comparing 2018 Surveys 1 and 2 (Figure 4.7B, C). The shapes of the identified areas of change in the M3C2 point cloud represented the removed block shapes well and only differed slightly in one of the removed blocks (Sample 18-A); the overall location of the identified areas of change were accurate with the known sample locations. The sample blocks removed during the 2018 field season were composed primarily of beige-coloured sandstone of the Thorold Formation (Figure 4.5).

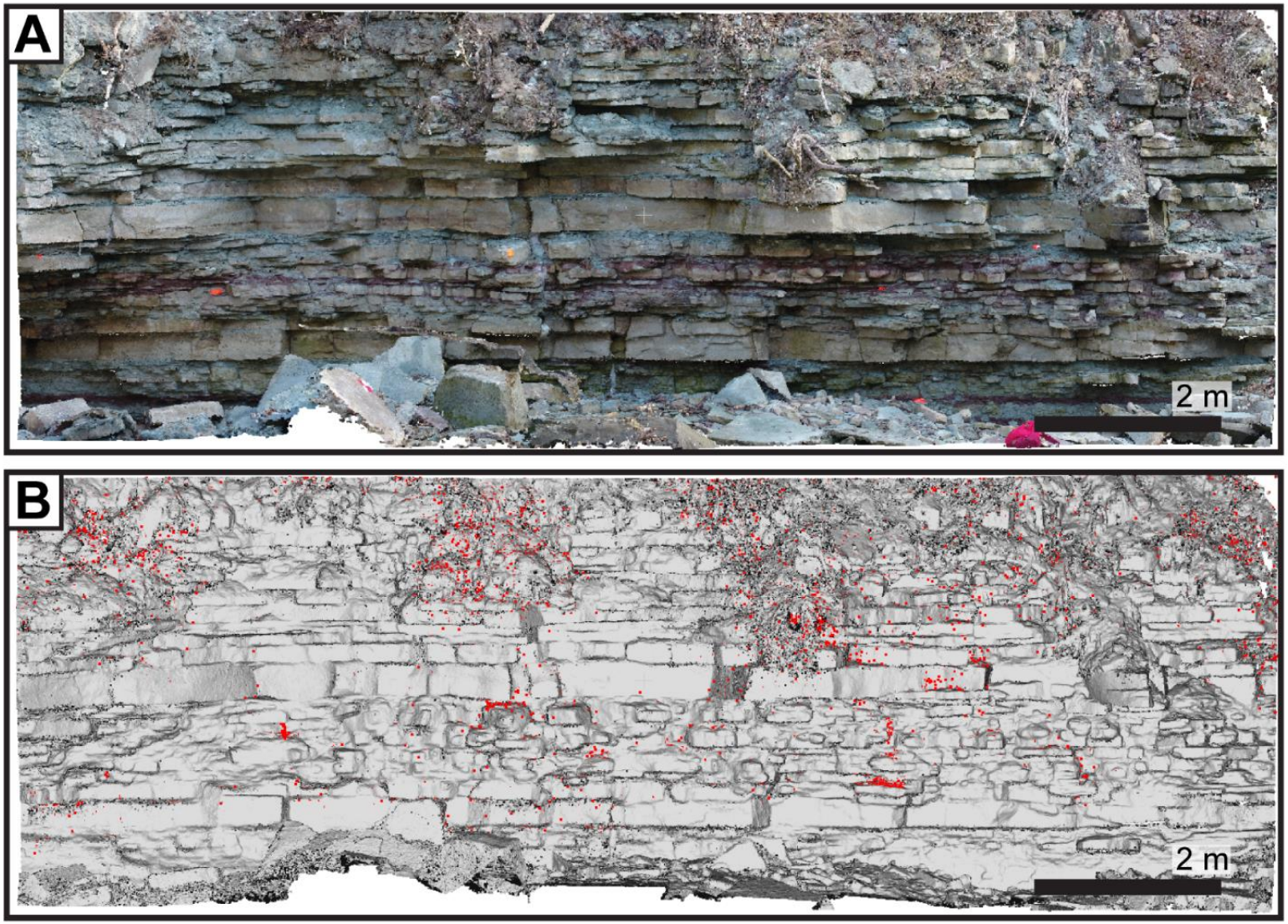

Figure 4.6: A) Example of a dense point cloud created in Agisoft Metashape (Agisoft Metashape, 2020) from the 2020 Survey 1; B) M3C2 calculated differences depicting the changes in the models from Survey 1 2020 to Survey 2 2020. The upper areas of identified change (red dots) result from the movement of vegetation between surveys.

In the 2020 field study, seven sample blocks were removed from the outcrop. These sample blocks were from a variety of locations on the outcrop face and included red and grey shale of the Grimsby Formation and red sandstone of the Thorold Formation (Figure 4.5). In the M3C2 comparison of 2020 Surveys 1 and 2, six of the seven samples were identifiable (Figure 4.8). The sample that was not identifiable on the M3C2 comparison (20-G) was a small block of grey shale, removed from an undercut area of the rock face. The shape of the M3C2 point clouds of two samples (Sample 20-E, Sample 20-F) were inaccurate compared to the shape of the removed block; however, most point cloud shapes represented the removed samples well.

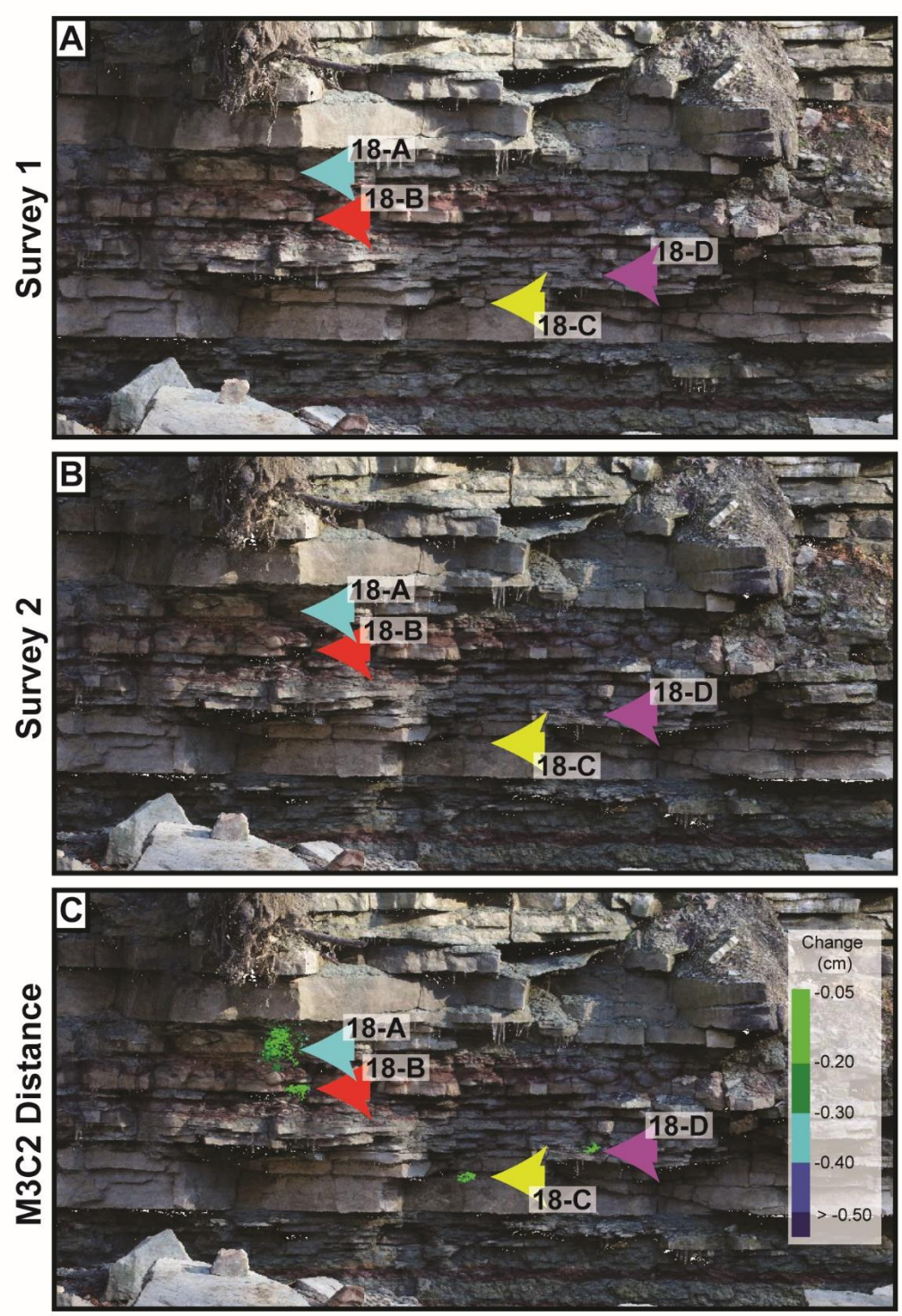

Figure 4.7: A) Initial 2018 survey of the outcrop with all sample locations indicated by coloured arrows (Survey 1: see Figure 4.5 for sample close-up); B) Survey 2 of the outcrop with the location of the removed samples indicated; C) Results of the M3C2 algorithm showing the calculated change for the four removed samples overlain on Survey 2 imagery. Each of the four removed samples was clearly identified using this algorithm.

Table 4.1: Summary of the measured volume and calculated volumes using the alpha-shape and power crust algorithms of the samples removed from the Niagara Escarpment outcrop and the difference between the measured and calculated volumes.

Year	**2018**				**2020**							
Sample	**18-A**	**18-B**	**18-C**	**18-D**	**20-A**	**20-B**	**20-C**	**20-D**	**20-E**	**20-F**	**20-G ***	**20-H ****
Measured volume (MV) (m^3)	0.0020	0.00061	0.012	0.00014	0.00024	0.0010	0.00037	0.00023	0.0010	0.0030	0.00012	---
Alpha-shape												
Calculated Volume (CV) (m^3)	0.0077	0.0010	0.00023	0.00034	0.0035		0.0031	0.000011	0.000046	0.00084	---	0.00072
Difference (10^{-3} m^3)	0.0057	0.00039	-0.012	0.00019	-0.00024	0.0025	0.0027	-0.00022	-0.00097	-0.0022	---	---
MV to CV difference (%)	289	64	-98	135	-98	244	749	-95	-95	-72	---	---
Power Crust												
Calculated Volume (CV) (10^{-3} m^3)	0.0059	0.00090	0.00026	0.00031	---	0.0031	0.0028	0.000034	0.00011	0.00075	---	0.00073
Difference (10^{-3} m^3)	0.0039	0.00029	-0.012	0.00017	---	0.0021	0.0024	-0.00020	-0.00091	-0.0022	---	---
MV to CV difference (%)	198	48	-98	115	---	205	667	-86	-89	-75	---	---

* Removed sample not identified using M3C2

** Sample not removed for study, icicles fell naturally from the outcrop

Approximate volumes of the removed rock samples were determined from the measured dimensions of the sample and an error of 20% of the volume was allowed to account for errors associated with determining the volume of an irregular shape; these values were compared with the calculated values using algorithms within M3C2 to determine the accuracy of volume calculations using this method (Table 4.1).

The volume of the loss objects calculated using the alpha-shape (AS) and power crust (PC) algorithms showed similar volume estimates and discrepancies with the measured volume (Figure 4.9; Table 4.1). A comparison of the two calculated volumes and the measured volume of the samples shows significant differences in the estimates, with the power crust estimates being slightly closer to the measured volumes in all samples except in sample 20-F. A volume estimate for sample 20-A was not possible using the power crust algorithm as there were inadequate points to complete the processing. Sample 20-G was not identifiable in the M3C2 point cloud and therefore volume calculations were not possible.

Of the 10 samples for which volumes were calculated, half of them over-estimated the measured volume with an average overestimation of 247% (PC volume) and 296% (AS volume; Figure 4.9; Table 4.1). Two samples showed a difference between calculated and measured volumes of less than 150% with the least difference found in Sample 18-B at 48% (PC volume) 64% (AS volume). Two of the calculated volumes showed between 150% and 300% difference with the measured volume and one sample, Sample 20-C, showed 667% difference between the measured volume of 3.6×10^{-4} m^3 and a PC calculated volume of 2.8×10^{-3} m^3.

The remaining five samples had calculated volumes that underestimated the measured volume of the rock samples with an average underestimation of 87% (PC volume) and 92% (AS volume; Figure 4.9; Table 4.1). All five of these calculated volumes had less than 100% difference with the measured rock volumes, with four of the calculated volume differences between 85% and 100%. Sample 20-F had the least difference between calculated and measured volumes (75% PC volume and 71% AS volume differences). For all removed sample blocks, the M3C2 calculated volumes (using both PC and AS algorithms) either underestimated or overestimated the measured volume; in general, the underestimated volumes were less than the overestimated volumes (Figure 4.9; Table 4.1).

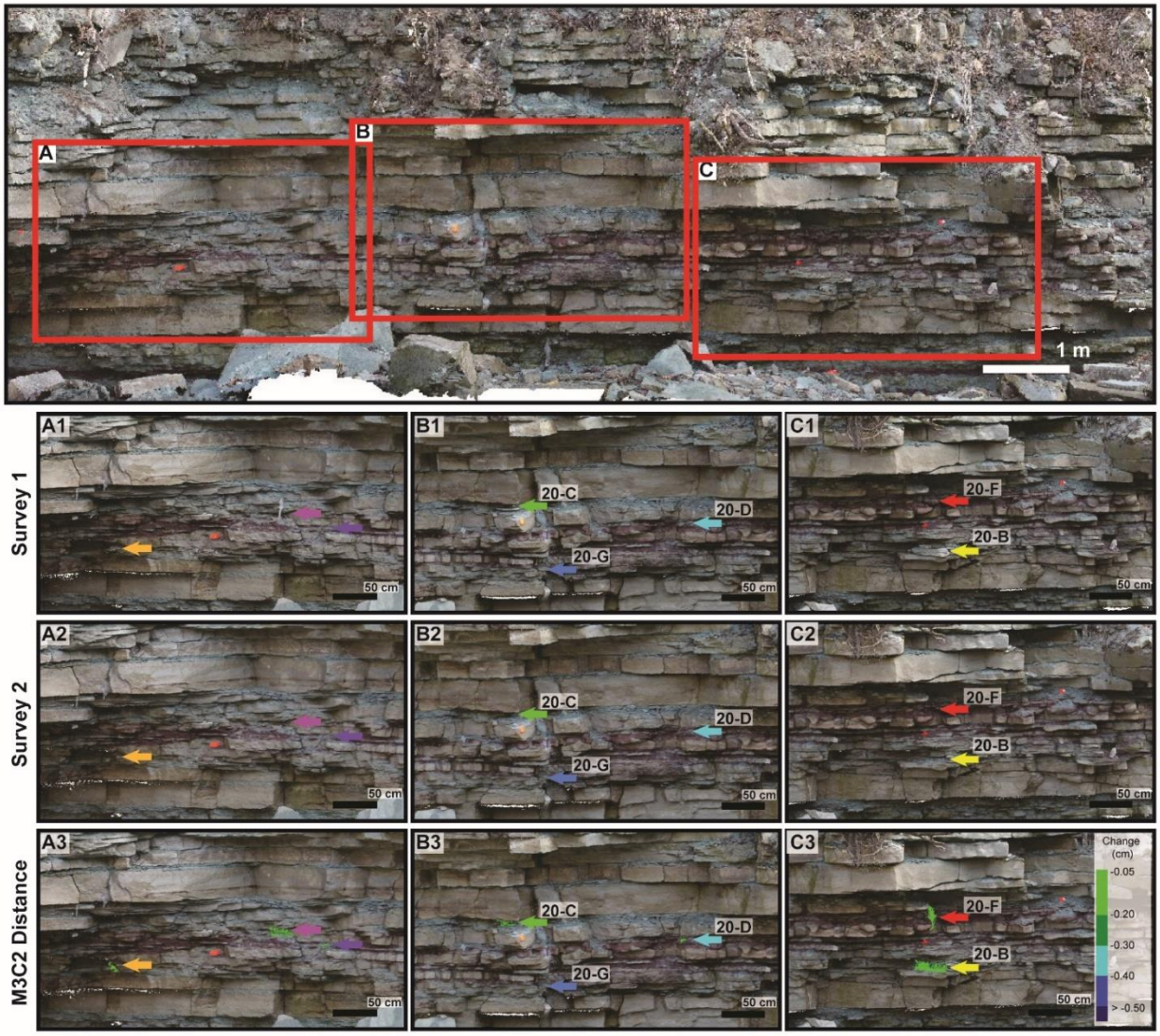

Figure 4.8: Top: Overview of the outcrop studied in 2020 showing the location of the three areas of sampling with images of areas of removed samples enlarged below. Survey 1 of the outcrop with all sample locations indicated by coloured arrows, see Figure 4.5 for sample close-up (A1; B1: C1); B) Survey 2 of the outcrop with the location of the samples indicated (A2; B2: C2). Sample 20-G (B3) did not register any change in the M3C2 point cloud; C) Results of the M3C2 algorithm showing the calculated change for the removed samples overlain on Survey 2 imagery (A3; B3: C3). Seven of the eight removed samples were identified using the algorithm, with Sample 20-G (B1-3) considered a false negative in this analysis.

4. 4 Discussion

4.4.1 Location of staged erosion events

Of the eleven samples removed from the rock face in the 2018 and 2020 field surveys, 10 were identified using the M3C2 methodology with a 95% confidence interval. This demonstrates the utility of the M3C2 methodology as a viable tool for mapping areas of erosion on vertical and lithologically complex rock faces (Stumpf et al., 2015; Leyland et al., 2017; Zimmer et al., 2018; Del Río et al., 2020; DiFrancesco et al., 2020;). The only unidentified area of change was associated with Sample 20-G, a relatively small sample measuring 3.7cm in thickness, 2.2 cm wide and 15 cm long (Figure 4.5G). This sample was removed from a recessed area and was partially hidden by rocks that were not removed. The relative obscurity of the sample may have prevented identification of the change after sample removal, resulting in false-negative identification of change on the face. The limitations of identification of change (erosion) events using the M3C2 algorithm are strongly linked to the quality of the input datasets and their inherent registration error caused by the alignment of the Survey 1 and 2 models. Based on the root mean square error (RMS) calculated during the ICP alignment of the two models, a registration error of 5 cm was used in the analysis. This registration error may have exceeded the recorded amount of change associated with removal of sample 20-G and therefore masked the location of the change event. It is possible to lower the registration error through the use of high-quality GCPs and/or the improved alignment of models, allowing small areas of change, such as that represented by removal of sample 20-G, to be more easily identified.

During the completion of the M3C2 analysis of the models created for this study, there were false positive identifications of change where real-world change did not occur. These locations were frequently linked to changes in the position of shadows on the outcrop, the movement of vegetation, and the presence/absence of icicles on the outcrop. Once the resultant point cloud was manually cleaned for individual points and small groupings through the DBSCAN clustering and removal of areas characterized by the growth of icicles, shadows and/or vegetation, there were very few false-positive identifications of areas of change; those that did exist were frequently located near the edges of the model. This emphasizes the importance of manually checking the validity of changes identified by the M3C2 methodology, even when using the 95% confidence interval, as small differences in the models caused by factors other than material loss, can be misinterpreted as areas of change.

4.4.2 Volume calculation differences

Once the locations of areas of change were identified using the M3C2 algorithm, the volume of these changes (erosion or deposition) were also calculated for each of the segmented patches (Olsen et al., 2015; Benjamin et al., 2016; Bonneau et al., 2019b; DiFrancesco et al., 2020). The measured volume of manually removed blocks, recorded in the field when the samples were removed, was compared with the volume of change calculated with the M3C2 algorithm. The comparisons showed large discrepancies between the measured and calculated volumes using two volume calculation algorithms (PC and AS); these differences are discussed here as a percentage difference between the two values as this most readily applies to rock samples of all sizes. This study shows there is no clear connection between the percent difference in measured and calculated values and the size of the sample block when all samples are taken into consideration (Figure 4.10), although possible reasons for the discrepancies in measured and calculated volumes need to be addressed.

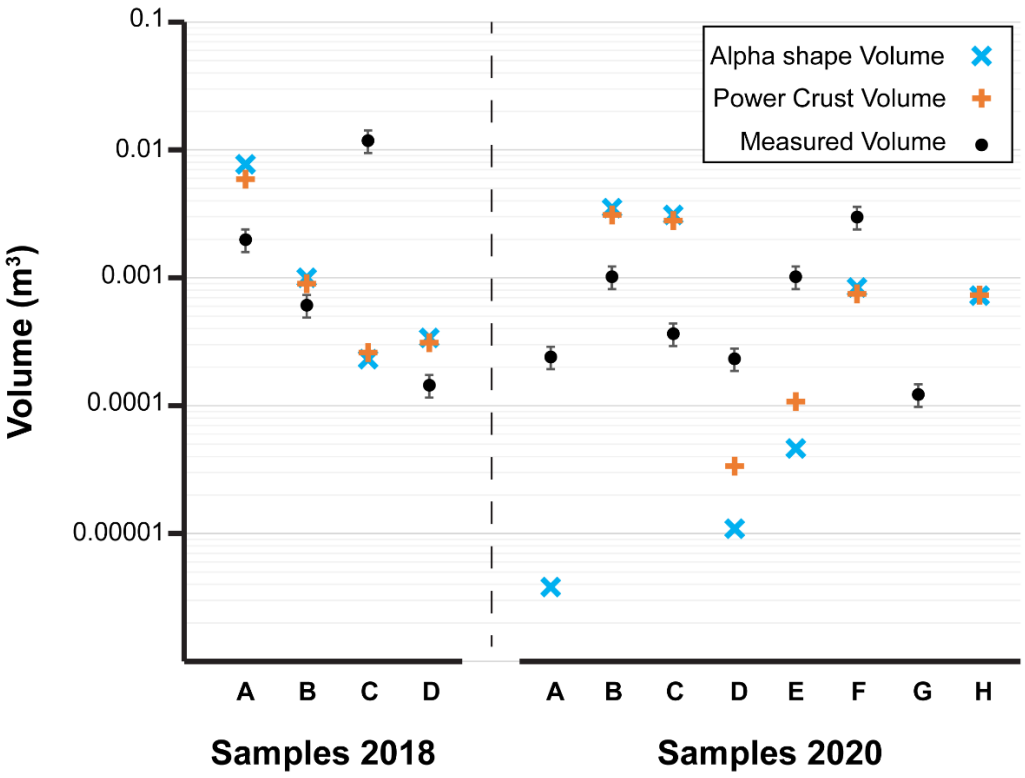

Figure 4.9: Comparison of the calculated volume of blocks removed in 2018 (left) and 2020 (right) using the alpha shape and power crust algorithms and the measured volume of the blocks. It is evident that the calculated volume either under or overestimates the volume of the blocks.

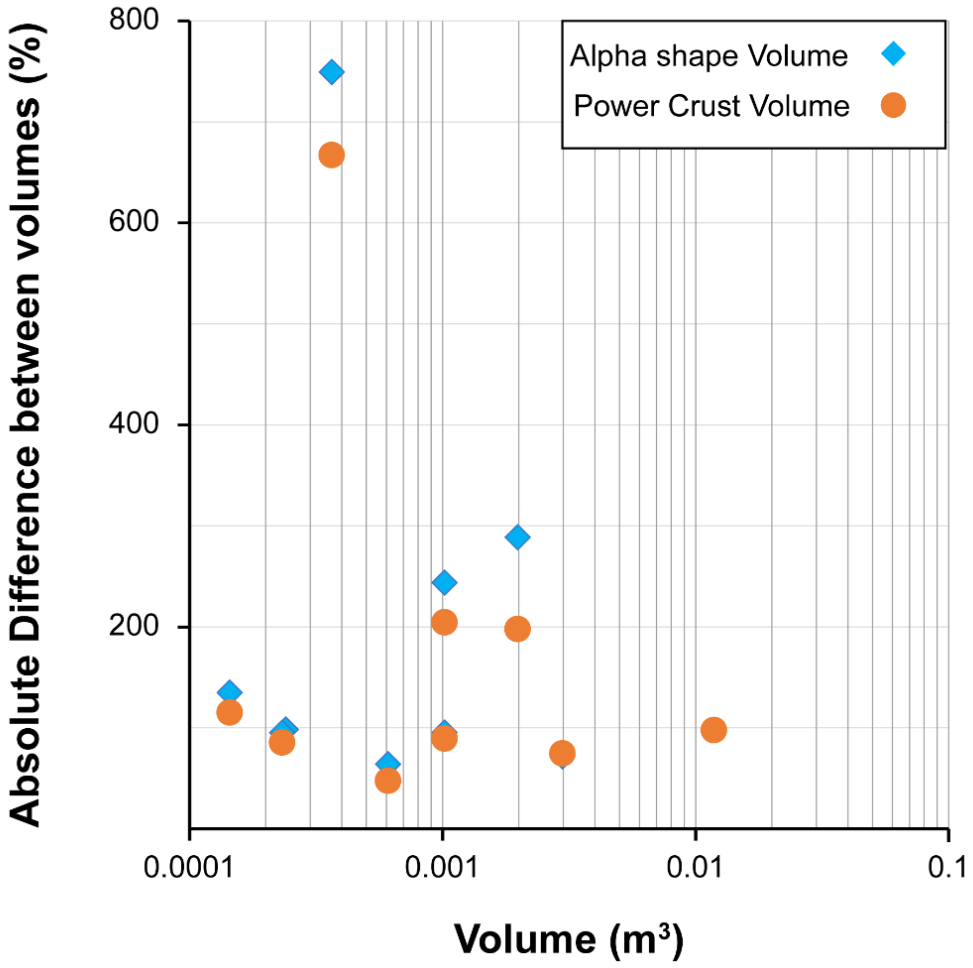

Figure 4.10: Relationship between the volume of the removed rock block and the absolute percent difference between the calculated and measured volumes. This indicates there is no clear relationship between the size of the block removed and the percentage difference between the measured and calculated volumes.

The location of the removed rock samples on the outcrop may have some impact on the accuracy of the M3C2 volume calculation as shadows on the rock face can affect the initial creation of the model (James & Robson, 2012; Bi et al., 2017; Del Río et al., 2020). However, the models created for this study were manually checked and did not appear to show any connection between the presence of shadows on a removed rock sample and discrepancies between measured and calculated sample volumes (Table 4.2). Sample 20-G, which was removed from the face but not identified in the M3C2 change detection, was not located in a shaded area; in contrast, the samples with both the largest (20-C) and the smallest (18-B) percentage difference in volume estimates

were both found in shadow. Four of the samples with overestimated volumes and only two of the samples with underestimated volumes were located in areas of shadow.

In areas of undercutting, where more and less resistant lithologies are juxtaposed, the topography of the face is complicated by the overhanging rocks, which can impede the comparison model if the SfM workflow creates different geometrical profiles for these features in different models. Five of the removed rock samples were taken from areas of undercutting, including 20-G, which was not identified by the M3C2 change detection, and 20-C, which had the highest percentage difference in the measured and calculated volumes; however, sample 20-F was also removed from beneath overhanging rocks and shows smaller volume differences between measured and calculated values (Table 4.2). There appears to be no clear relationship between samples removed in areas of undercutting, and overestimations or underestimations of sample volume calculation.

Table 4.2: Qualitative assessment of key characteristics of each of the rock samples removed for the study. These characteristics may affect the initial creation of the rock face model or the M3C2 comparison algorithm, impacting the accuracy of the final volume calculations.

Year	Sample	Alpha-shape Volume difference (%)	Power Crust Volume difference (%)	Shadow	Colour	Rock type	Undercut	Contrast
2018	18-A	289	198	Yes	Pink-beige	Sandstone	Yes	Medium
	18-B	64	48	Yes	Beige-red	Sandstone	Partially	Medium
	18-C	-98	-98	yes	Beige-red	Sandstone	No	Low
	18-D	135	115	Yes	Beige	Sandstone	No	Low
2020	20-A	-98	---	No	Mottled red-grey	Shale	No	Medium
	20-B	244	205	No	Grey	Sandstone	No	Low to Medium
	20-C	749	667	Yes	Grey	Sandstone	Yes	High
	20-D	-95	-86	No	Grey and red	Sandstone	No	Low to medium
	20-E	-95	-89	Yes	Grey	Sandstone	Yes	Low
	20-F	-72	-75	Minimal	Mottled red/grey	Sandstone	Yes	High
	20-G *	---	---	No	Grey	Shale	Yes	Low

* Removed sample not identified using M3C2

The colour of the sample and its contrast with the surrounding rocks could also affect discrimination of the boundaries of the removed sample and its subsequent volume calculation. If the sample block is removed from an area where the block and the surrounding rocks have similar colour and low contrast, it may not register as an area of change by the SfM workflow when removed from the face (James & Robson, 2012; Stumpf et al., 2015; Bi et al., 2017). Most of the samples removed from the face in this study consisted of sandstone ranging in colour from grey to beige-red; only two samples were composed of mottled red-grey and grey shale (Table 4.2). The colour and the relative contrast of the sample was visually assessed using the sample images taken (Figure 4.5). Only one of the samples (20-F) was considered to have a high degree of contrast with the surrounding rocks; it was removed from an area of variably coloured and textured rock types (Table 4.2). This ‘high contrast’ rock sample has the second lowest percent difference between the

measured and calculated volumes. However, the sample with the highest percent difference between its measured and calculated volume (20-C) has a 'moderate contrast' with the surrounding rock and multiple samples with 'low contrast' have relatively low differences between measured and calculated volumes. The relationship between the contrast of the sample with the surrounding rock and the ability of the M3C2 algorithms to estimate volume loss is unclear, although higher contrast between the removed sample and the rock face may enhance delineation of margins of the rock blocks.

The large difference between measured and estimated volumes for Sample 20-C was likely caused by the shape of the removed rock and its location within an alcove. This sample was a thin sheet of sandstone, approximately 0.84 cm thick, and was located within a significantly shaded undercut region of the cliff face. The combination of the shape of the removed block, the significant shadowing, and location in an area of undercutting most likely contributed to inaccuracies in the volume calculation.

The removed sample blocks had relatively small volumes, less than 0.01 m^3 in all but one of the samples (Sample 18-C) and represent single small rock fall events. These small-scale events can be difficult to reconcile on models and identifying small areas of change can lead to inaccuracies (Olsen et al., 2015). However, along the Niagara Escarpment, there is considerable interest in identifying and recording these small-scale rockfall events as they pose a danger to individuals hiking along escarpment trails and to vehicles driving on access roads.

In this study, the small size of the removed sample blocks allowed a limited number of points in the point cloud to record the change and, although the change was identifiable using M3C2, the volume estimates of the blocks removed were compromised by the limited number of points available. With larger block falls and larger sections of rock loss, the ability to quantify volume loss using M3C2 algorithms may be improved as more points will be available to constrain the block morphology and volume.

Although the methodology for identifying areas of change (location of erosion events) and estimating volumes of change (amount of erosion) used here, using a combination of UAV photogrammetry and M3C2 change detection, does show some areas of inaccuracy, it does provide a quantitative and time-efficient process for monitoring erosion processes and rates on exposed rocky cliffs such as the Niagara Escarpment. The errors encountered in the testing conducted here are mostly associated with volume loss calculations and are likely the result of a combination of

factors including the inconsistent recording of shadows on the cliff face, obscuring of portions of the face by overhanging rocks, and contrast between the removed rock samples and the adjacent rocks. Further refinement of the model creation process (including more accurate locational data), photographing at consistent times of day or year to reduce shadows, and identifying cliff faces with heterogenous lithologies with high degrees of contrast, may improve the accuracy of this methodology, particularly the change detection process and volume loss calculations. Despite the inaccuracies identified here, the methodology has provided an effective way to identify the location of small-scale erosion events and quantify amount of erosion on heterogenous vertical cliff faces.

4. 5 Conclusions

The methodology utilized in this study involving UAV photogrammetry and application of a SfM workflow provides a baseline for further study of erosion along the Niagara Escarpment. The study site at Albion Falls in the Hamilton region is located in an area with good access allowing for the removal of blocks without potential danger to others and was an ideal experimental site to test out the new methodology proposed here. The methodology allowed effective and efficient determination and quantification of areas of erosion on the cliff face and can be applied to other locations along the Niagara Escarpment with greater obstacles to access. While many steep exposures of the escarpment lie adjacent to trails and roadways in Hamilton, access is often limited due to the height and steepness of the cliff face; the use of UAVs to obtain high resolution images facilitates access to the entirety of the cliff faces with limited risk. The methodology employed at the Albion Falls study site can be applied at other key exposures in Hamilton and elsewhere to quantify the rate of erosion, as well as to determine regions of the escarpment most at risk from erosion. With frequent rock falls affecting roadways and trails crossing the escarpment, the capacity to collect high resolution data that can be used to identify small-scale erosional events such as those replicated here, is extremely valuable. In addition, quantification of the changing form of the escarpment face is critical to effective future policy and planning of infrastructure and transportation corridors in the region.

The M3C2 algorithm used in this study was able to identify the location of >90% of the samples removed from the outcrop in the 2018 and 2020 field experiments reported here. This consistency in the identification of small-scale change from UAV imagery makes this a robust methodology for identifying areas of localized, or more widespread, erosion on a vertical cliff face.

The shape of the M3C2 cloud representing the removed blocks was remarkably representative of the block samples, with the exception of a few examples (e.g. 18-A, 20-F).

However, the volume of the removed rocks calculated using this methodology consistently over- and underestimated the volume of the removed rock. Despite these shortcomings, the methodology used here does provide an approximation of the volume of change, which can be used to inform future decision-making regarding erosion control and monitoring of complex sedimentary cliff faces, such as the Niagara Escarpment.

Further refinement of the methodology applied in this study will improve the model outputs and will facilitate longer term, multi-year assessments of erosion along rocky cliff faces. Critical to further refinement is the collection of high resolution GCPs using differential GPS units which can reduce point location error caused by the interference of the rock face, vegetation, and surrounding buildings. Additionally, ensuring photogrammetric surveys are completed at approximately the same time of year and day will reduce the effects of differences in lighting, shadows, and vegetation cover, and will further reduce possible sources of model generation error.

The time-efficient and non-invasive methodology presented in this paper can be applied to erosion studies of near vertical outcrops of sedimentary rock in both urban and rural settings, to reliably identify areas of change, and to provide an estimate of the volume and rate of erosion occurring on the rock face. The ability to identify even small-scale erosional events is critical in some areas, such as the Niagara Escarpment, where large-scale slope failures are less common, and the focus is smaller failures which threaten the safety of people and infrastructure. Identifying areas of high rates of erosion and erosion risk allows insight into the factors controlling these processes and will allow more informed planning and design of erosion control strategies where they are required.

4. 6 References

Admassu, Y., Shakoor, A., & Wells, N. A. (2012). Evaluating selected factors affecting the depth of undercutting in rocks subject to differential weathering. *Engineering Geology*, *124*(1), 1–11. https://doi.org/10.1016/j.enggeo.2011.09.007

Agisoft Metashape. (2020). *Agisoft Metashape Professional* (Version 1.6.2). https://www.agisoft.com/downloads/installer/

Amenta, N., Choi, S., & Kolluri, R. K. (2001). The power crust. *Proceedings of the Symposium on Solid Modeling and Applications*, 249–260. https://doi.org/10.1145/376957.376986

Armstrong, D. K., & Dodge, J. E. P. (2007). Paleozoic Geology of Southern Ontario - Project Summary and Technical Document. In *Ontario Geological Survey, Miscellaneous Release Data 219*.

Barker, R., Dixon, L., & Hooke, J. (1997). Use of terrestrial photogrammetry for monitoring and measuring bank erosion. *Earth Surface Processes and Landforms*, *22*(13), 1217–1227. https://doi.org/10.1002/(SICI)1096-9837(199724)22:13<1217::AID-ESP819>3.0.CO;2-U

Barnhart, T. B., & Crosby, B. T. (2013). Comparing two methods of surface change detection on an evolving thermokarst using high-temporal-frequency terrestrial laser scanning, Selawik River, Alaska. *Remote Sensing*, *5*(6), 2813–2837. https://doi.org/10.3390/rs5062813

Benjamin, J., Rosser, N. J., & Brain, M. J. (2016). Rockfall detection and volumetric characterisation using LiDAR. *Landslides and Engineered Slopes. Experience, Theory and Practice*, *2*(July), 389–395. https://doi.org/10.1201/b21520-38

Benjamin, J., Rosser, N. J., & Brain, M. J. (2020). Emergent characteristics of rockfall inventories captured at a regional scale. *Earth Surface Processes and Landforms*, *45*(12), 2773–2787. https://doi.org/10.1002/esp.4929

Berezin, A. A. (2012). Aquatic realms and running water in sustainable tourism. In C. A. Brebbia & T.-S. Chon (Eds.), *Environmental Impact* (pp. 447–458). WIT Press.

Bi, H., Zheng, W., Ren, Z., Zeng, J., & Yu, J. (2017). Using an unmanned aerial vehicle for topography mapping of the fault zone based on structure from motion photogrammetry. *International Journal of Remote Sensing*, *38*(8–10), 2495–2510. https://doi.org/10.1080/01431161.2016.1249308

Bonneau, D., DiFrancesco, P. M., & Jean Hutchinson, D. (2019). Surface reconstruction for three-dimensional rockfall volumetric analysis. *ISPRS International Journal of Geo-Information*, *8*(12). https://doi.org/10.3390/ijgi8120548

Bonneau, D., Hutchinson, D. J., DiFrancesco, P.-M., Coombs, M., & Sala, Z. (2019). Three-dimensional rockfall shape back analysis: Methods and implications. *Natural Hazards and Earth System Sciences*, *19*(12), 2745–2765. https://doi.org/10.5194/nhess-19-2745-2019

Brigham, R. J. (1971). *Structural geology of southwestern Ontario and southeastern Michigan*. Ontario Department of Mines and Northern Affairs.

Brunton, F. R., & Brintnell, C. (2020). Early Silurian Sequence Stratigraphy and Geological Controls on Karstic Bedrock Groundwater-Flow Zones, Niagara Escarpment Region and the Subsurface of Southwestern Ontario.

CBC. (2014). *The escarpment is falling and it's costing Hamilton thousands*. CBC News. https://www.cbc.ca/news/canada/hamilton/headlines/the-escarpment-is-falling-and-it-s-costing-hamilton-thousands-1.2622273

Clark, A. (2017). Small unmanned aerial systems comparative analysis for the application to coastal erosion monitoring. *GeoResJ*, *13*, 175–185. https://doi.org/10.1016/j.grj.2017.05.001

CloudCompare. (2020). *CloudCompare* (Version 2.10.2). http://www.cloudcompare.org/

Del Río, L., Posanski, D., Gracia, F. J., & Pérez-Romero, A. M. (2020). A comparative approach of monitoring techniques to assess erosion processes on soft cliffs. *Bulletin of Engineering Geology and the Environment*, *79*(4), 1797–1814. https://doi.org/10.1007/s10064-019-01680-2

DiFrancesco, P.-M., Bonneau, D. A., & Hutchinson, D. J. (2021). Computational Geometry-Based Surface Reconstruction for Volume Estimation: A Case Study on Magnitude-Frequency Relations for a LiDAR-Derived Rockfall Inventory. *ISPRS International Journal of Geo-Information*, *10*(3), 157. https://doi.org/10.3390/ijgi10030157

DiFrancesco, P. M., Bonneau, D., & Hutchinson, D. J. (2020). The implications of M3C2 projection diameter on 3-D semi-automated rockfall extraction from sequential terrestrial laser scanning point clouds. *Remote Sensing*, *12*(11). https://doi.org/10.3390/rs12111885

Duró, G., Crosato, A., Kleinhans, M. G., & Uijttewaal, W. S. J. (2018). Bank erosion processes measured with UAV-SfM along complex banklines of a straight mid-sized river reach. *Earth Surface Dynamics*, *6*(4), 933–953. https://doi.org/10.5194/esurf-6-933-2018

Eltner, A., Baumgart, P., Maas, H. G., & Faust, D. (2015). Multi-temporal UAV data for automatic measurement of rill and interrill erosion on loess soil. *Earth Surface Processes and Landforms*, *40*(6), 741–755. https://doi.org/10.1002/esp.3673

Ely, J. C., Graham, C., Barr, I. D., Rea, B. R., Spagnolo, M., & Evans, J. (2017). Using UAV acquired photography and structure from motion techniques for studying glacier landforms: application to the glacial flutes at Isfallsglaciären. *Earth Surface Processes and Landforms*, *42*(6), 877–888. https://doi.org/10.1002/esp.4044

Feenstra, B. H. (1981). Quaternary geology and industrial minerals of the Niagara-Welland Area, southern Ontario (p. 260). Ontario Geological Survey - Open File Report 5361.

Fonstad, M. A., Dietrich, J. T., Courville, B. C., Jensen, J. L., & Carbonneau, P. E. (2013). Topographic structure from motion: A new development in photogrammetric measurement. *Earth Surface Processes and Landforms*, *38*(4), 421–430. https://doi.org/10.1002/esp.3366

Giordan, D., Adams, M. S., Aicardi, I., Alicandro, M., Allasia, P., Baldo, M., De Berardinis, P., Dominici, D., Godone, D., Hobbs, P., Lechner, V., Niedzielski, T., Piras, M., Rotilio, M., Salvini, R., Segor, V., Sotier, B., & Troilo, F. (2020). The use of unmanned aerial vehicles (UAVs) for engineering geology applications. *Bulletin of Engineering Geology and the Environment*, *79*(7), 3437–3481. https://doi.org/10.1007/s10064-020-01766-2

Gulyaev, S. A., & Buckeridge, J. S. (2004). Terrestrial Methods for Monitoring Cliff Erosion in an Urban Environment. *Journal of Coastal Research*, *203*(3), 871–878. https://doi.org/10.2112/1551-5036(2004)20[871:tmfmce]2.0.co;2

Hackney, C., & Clayton, A. I. (2015). Unmanned Aerial Vehicles (UAVs) and their application in geomorphic mapping. *Geomorphological Techniques*, *7*, 1–12. http://www.geomorphology.org.uk/sites/default/files/geom_tech_chapters/2.1.7_UAV.pdf

Hewitt, D. F. (1971). *The Niagara Escarpment* (Industrial). Ontario Department of Mines and Northern Affairs - Report No. 35.

James, M. R., & Robson, S. (2012). Straightforward reconstruction of 3-D surfaces and topography with a camera: Accuracy and geoscience application. *Journal of Geophysical Research: Earth Surface*, *117*(3), 1–17. https://doi.org/10.1029/2011JF002289

Jaud, M., Passot, S., Le Bivic, R., Delacourt, C., Grandjean, P., & Le Dantec, N. (2016). Assessing the accuracy of high resolution digital surface models computed by PhotoScan® and MicMac® in sub-optimal survey conditions. *Remote Sensing*, *8*(6). https://doi.org/10.3390/rs8060465

Javadnejad, F., Slocum, R. K., Gillins, D. T., Olsen, M. J., & Parrish, C. E. (2021). Dense Point Cloud Quality Factor as Proxy for Accuracy Assessment of Image-Based 3-D Reconstruction. *Journal of Surveying Engineering*, *147*(1), 04020021. https://doi.org/10.1061/(asce)su.1943-5428.0000333

Kurumalla, S., & Srinivasa Rao, P. (2016). K-nearest neighbor based dbscan clustering algorithm for image segmentation. *Journal of Theoretical and Applied Information Technology*, *92*(2), 395–402.

Lague, D., Brodu, N., & Leroux, J. (2013). Accurate 3-D comparison of complex topography with terrestrial laser scanner: Application to the Rangitikei canyon (N-Z). *ISPRS Journal of Photogrammetry and Remote Sensing*, *82*, 10–26. https://doi.org/10.1016/j.isprsjprs.2013.04.009

Letortu, P., Jaud, M., Grandjean, P., Ammann, J., Costa, S., Maquaire, O., Davidson, R., Le Dantec, N., & Delacourt, C. (2018). Examining high-resolution survey methods for monitoring cliff erosion at an operational scale. *GIScience and Remote Sensing*, *55*(4), 457–476. https://doi.org/10.1080/15481603.2017.1408931

Leyland, J., Hackney, C. R., Darby, S. E., Parsons, D. R., Best, J. L., Nicholas, A. P., Aalto, R., & Lague, D. (2017). Extreme flood-driven fluvial bank erosion and sediment loads: direct process measurements using integrated Mobile Laser Scanning (MLS) and hydro-acoustic techniques. *Earth Surface Processes and Landforms*, *42*(2), 334–346. https://doi.org/10.1002/esp.4078

Lowe, D. G. (2004). Distinctive image features from scale-invariant keypoints. *International Journal of Computer Vision*, *60*(2), 91–110.

Luczaj, J. A. (2013). Geology of the Niagara Escarpment in Wisconsin. *Geoscience Wisconsin*, *22*(1), 1–34.

Mann, K. (2019, May 14). Rockslide closes Hamilton mountain access, sports fields remain closed due to soggy conditions. *Global News*. https://globalnews.ca/news/5276437/rockslide-closes-hamilton-mountain-access/

MathWorks. (2021). *DBSCAN*. https://www.mathworks.com/help/stats/dbscan-clustering.html

McCann, S. B. (1987). Physical landscape of the Hamilton region. In Dear, M. J., Drake, J. J., & Reeds, L. G. (Eds.) *Steel City: Hamilton and Region* (pp. 9–33). University of Toronto Press.

Micheletti, N., Chandler, J. H., & Lane, S. N. (2015). Structure from Motion (SfM) Photogrammetry (Section 2.1.3). In L. E. Clarke & J. M. Nield (Eds.), *Geomorphological Techniques (Online Edition)*. British Society for Geomorphology. https://doi.org/10.1002/esp.3767

Miščević, P., & Vlastelica, G. (2014). Impact of weathering on slope stability in soft rock mass. *Journal of Rock Mechanics and Geotechnical Engineering*, *6*(3), 240–250. https://doi.org/10.1016/j.jrmge.2014.03.006

Nesbit, P. R., & Hugenholtz, C. H. (2019). Enhancing UAV-SfM 3-D model accuracy in high-relief landscapes by incorporating oblique images. *Remote Sensing*, *11*(3), 1–24. https://doi.org/10.3390/rs11030239

Niethammer, U., James, M. R., Rothmund, S., Travelletti, J., & Joswig, M. (2012). UAV-based remote sensing of the Super-Sauze landslide: Evaluation and results. *Engineering Geology*, *128*, 2–11. https://doi.org/10.1016/j.enggeo.2011.03.012

Olsen, M. J., Wartman, J., McAlister, M., Mahmoudabadi, H., O'Banion, M. S., Dunham, L., & Cunningham, K. (2015). To fill or not to fill: Sensitivity analysis of the influence of resolution

and hole filling on point cloud surface modeling and individual rockfall event detection. *Remote Sensing*, *7*(9), 12103–12134. https://doi.org/10.3390/rs70912103

Pearson, N. (2019). The Bruce Trail. In *A Naturalist's Guide to Ontario* (pp. 63–67). University of Toronto Press.

Perras, M. A., Diederichs, M. S., & Besaw, D. (2014). Geological and geotechnical observations from the Niagara Tunnel Project. *Bulletin of Engineering Geology and the Environment*, *73*, 1303–1323. https://doi.org/10.1007/s10064-014-0633-5

Rajendra, Y. D., Mehrotra, S. C., Kale, K. V., Manza, R. R., Dhumal, R. K., Nagne, A. D., & Vibhute, A. D. (2014). Evaluation of Partially Overlapping 3-D Point Cloud's Registration by using ICP variant and CloudCompare. *The International Archives of Photogrammetry, Remote Sensing and Spatial Information Sciences*, *40*(8), 891–897.

Schumann, G. J. P., Muhlhausen, J., & Andreadis, K. M. (2019). Rapid mapping of small-scale river-floodplain environments using UAV SfM supports classical theory. *Remote Sensing*, *11*(8). https://doi.org/10.3390/rs11080901

Snavely, N., Seitz, S. M., & Szeliski, R. (2008). Modeling the world from internet photo collections. *International Journal of Computer Vision*, *80*, 189–210.

Stumpf, A., Malet, J. P., Allemand, P., Pierrot-Deseilligny, M., & Skupinski, G. (2015). Ground-based multi-view photogrammetry for the monitoring of landslide deformation and erosion. *Geomorphology*, *231*, 130–145. https://doi.org/10.1016/j.geomorph.2014.10.039

Szeliski, R. (2011). Structure from motion. In *Computer Vision: Algorithms and Applications* (pp. 303–334). Springer London. https://doi.org/10.1007/978-1-84882-935-0_7

Tepper, D. H., York, N., Goodman, W. M., York, N., Gross, M. R., Kappel, W. M., York, N., & Yager, R. M. (1990). *Stratigraphy , structural geology, and hydrogeology of the Lockport Group : Niagara Falls area , New York* (pp. 1–25). Field Trip Guidebook.

Tinkler, K. J., & Pengelly, J. W. (1994). Protalus ramparts and related features along the Niagara Escarment, Niagara Peninsula, Ontario. *Permafrost and Periglacial Processes*, *5*, 171–184.

Tonini, M., & Abellan, A. (2014). Rockfall detection from terrestrial lidar point clouds: A clustering approach using R. *Journal of Spatial Information Science*, *8*(1), 95–110. https://doi.org/10.5311/JOSIS.2014.8.123

Tonkin, T. N., Midgley, N. G., Graham, D. J., & Labadz, J. C. (2014). The potential of small unmanned aircraft systems and structure-from-motion for topographic surveys: A test of emerging integrated approaches at Cwm Idwal, North Wales. *Geomorphology*, *226*, 35–43. https://doi.org/10.1016/j.geomorph.2014.07.021

Van Dongen, M. (2017a, October 13). Cracks in the foundation: The price of living on the edge. *Hamilton Spectator*. https://www.thespec.com/news/hamilton-region/2017/10/13/cracks-in-the-foundation-the-price-of-living-on-the-edge.html

Van Dongen, M. (2017b, December 28). Experts begin 'painstaking' study of failing Claremont Access walls. *The Hamilton Spectator*. https://www.thespec.com/news-story/7040741-experts-begin-painstaking-study-of-failing-claremont-access-walls/

van Veen, M., Hutchinson, D. J., Kromer, R., Lato, M., & Edwards, T. (2017). Effects of sampling interval on the frequency - magnitude relationship of rockfalls detected from terrestrial laser scanning using semi-automated methods. *Landslides*, *14*(5), 1579–1592. https://doi.org/10.1007/s10346-017-0801-3

Welch, R., & Jordan, T. R. (1983). Analytical non-metric close-range photogrammetry for monitoring stream channel erosion. *Photogrammetric Engineering & Remote Sensing*, *49*(3), 367–374.

Westoby, M. J., Brasington, J., Glasser, N. F., Hambrey, M. J., & Reynolds, J. M. (2012). "Structure-from-Motion" photogrammetry: A low-cost, effective tool for geoscience applications. *Geomorphology*, *179*, 300–314. https://doi.org/10.1016/j.geomorph.2012.08.021

Williams, J. G., Rosser, N. J., Hardy, R. J., Brain, M. J., & Afana, A. A. (2018). Optimising 4-D surface change detection: An approach for capturing rockfall magnitude-frequency. *Earth Surface Dynamics*, *6*(1), 101–119. https://doi.org/10.5194/esurf-6-101-2018

Zhang, Z. (1994). Iterative point matching for registration of free-form curves and surfaces. *International Journal of Computer Vision*, *13*(2), 119–152.

Zimmer, B., Liutkus-Pierce, C., Marshall, S. T., Hatala, K. G., Metallo, A., & Rossi, V. (2018). Using differential structure-from-motion photogrammetry to quantify erosion at the Engare Sero footprint site, Tanzania. *Quaternary Science Reviews*, *198*, 226–241. https://doi.org/10.1016/j.quascirev.2018.07.006

Appendix A

Table 1: Characteristics of the survey collection and model creation for the surveys completed in this study.

	Number of pictures	**Number of points**	**Average Surface density (points/area) (r= 0.1m)**	**Average Point Spacing**	**Average Roughness (m)**
2018 – Survey 1	**82**	**9 912 791**	**90 115**	**0.0033**	**0.0095**
2018 – Survey 2	**90**	**11 946 937**	**117 159**	**0.0029**	**0.0096**
2020 – Survey 1	**147**	**20 649 674**	**183 710**	**0.0023**	**0.011**
2020 – Survey 2	**167**	**22 544 833**	**202 748**	**0.0022**	**0.011**

Chapter Five: Application of change detection to the analysis of erosion processes in an urban environment, Hamilton, Ontario, Canada

Abstract

The Niagara Escarpment is a significant geomorphological feature extending from New York, through southern Ontario and into Michigan and Wisconsin. In Hamilton, Ontario the escarpment is a steep-sloped rock face which divides the city and is traversed by 19 access routes. The escarpment is undergoing continual erosion and recent rockfalls onto the access routes have caused concerns over the safety of surrounding infrastructure, although little is currently known about erosion processes or rates in this urban setting. To address this issue, the rate and volume of erosion loss at a specific site at Albion Falls in Hamilton, and the factors impacting the amount and characteristics of the erosional events over a 14-month time period are documented. An unpiloted aerial vehicle (UAV) was used to collect imagery of the face in 2018 and 2020 and a Structure from Motion (SfM) workflow was used to create dense point clouds of the outcrops in each year. The models were compared using the M3C2 algorithm and the location and volume of change calculated. The sedimentological and fracture characteristics of the slope were also documented as these are considered to be as factors that impact the rate of erosion. Over the 14-month period approximately 30% of the study site experienced material loss (erosion) and approximately 3% of the site gained material (deposition). Many areas of erosion were clearly associated with undercutting of sandstone or dolostone layers by preferential removal of shale and in areas of dense fracturing; however, other areas of the outcrop with similar characteristics experienced minimal erosion. It appears that undercutting and the propagation of fractures do enhance the potential for material loss from an exposed rock face but exposure time is a dominant control on the effectiveness of these processes.

Keywords: Structure from Motion, close-range photogrammetry, change detection, erosion monitoring

5. 1 Introduction

The Niagara Escarpment is a significant geomorphological feature which varies in appearance along its length with areas characterized by either steep-faced cliffs or gentle debris covered slopes (Hewitt, 1971; Johnson et al., 1992; Brunton & Brintnell, 2020). The landform extends through southern Ontario and the neighbouring states of New York, Michigan, and Wisconsin (Figure 5.1A). In Hamilton, Ontario the escarpment is a steep-faced cliff up to 100 m high which separates the lower city on the shore of Lake Ontario from the upper city (Figure 5.1B). Having an escarpment fragment the city presents a number of issues, most notably the potential for rock falls onto access roads crossing the escarpment and the stability of homes located close to the escarpment edge (Figure 5.1C; e.g. Admassu et al., 2012; Miščević and Vlastelica, 2014). Large rockfalls in the recent past (Figure 1C; Van Dongen, 2017; Mann, 2019) have cemented a need to understand the erosional processes affecting the escarpment, how these processes differ across the city, and the overall rate of erosion. Determining which areas of the escarpment are likely to experience catastrophic rockfalls and which are likely to have the greatest rates of erosion, through slow persistent erosion processes or episodic failures, is important to allow city planners to make informed decisions regarding urban growth and the emplacement of infrastructure protection works.

Although erosion of the Niagara Escarpment is recognized to be a critical issue in Hamilton, there are limited studies documenting erosion processes or rates, the factors affecting these rates, and the spatial variability of erosion processes. To date, methodologies used to monitor slope erosion over multi-year time periods have involved the difficult and time-consuming installation of erosion pins, repetitive surveying, and the construction of multiple cross-profiles (Welch & Jordan, 1983; Barker et al., 1997; Gulyaev & Buckeridge, 2004). These methodologies have limited spatial resolution, can be disruptive to the rock face, and are often difficult to quantify. Hence, a more efficient and accurate method of erosion monitoring is required.

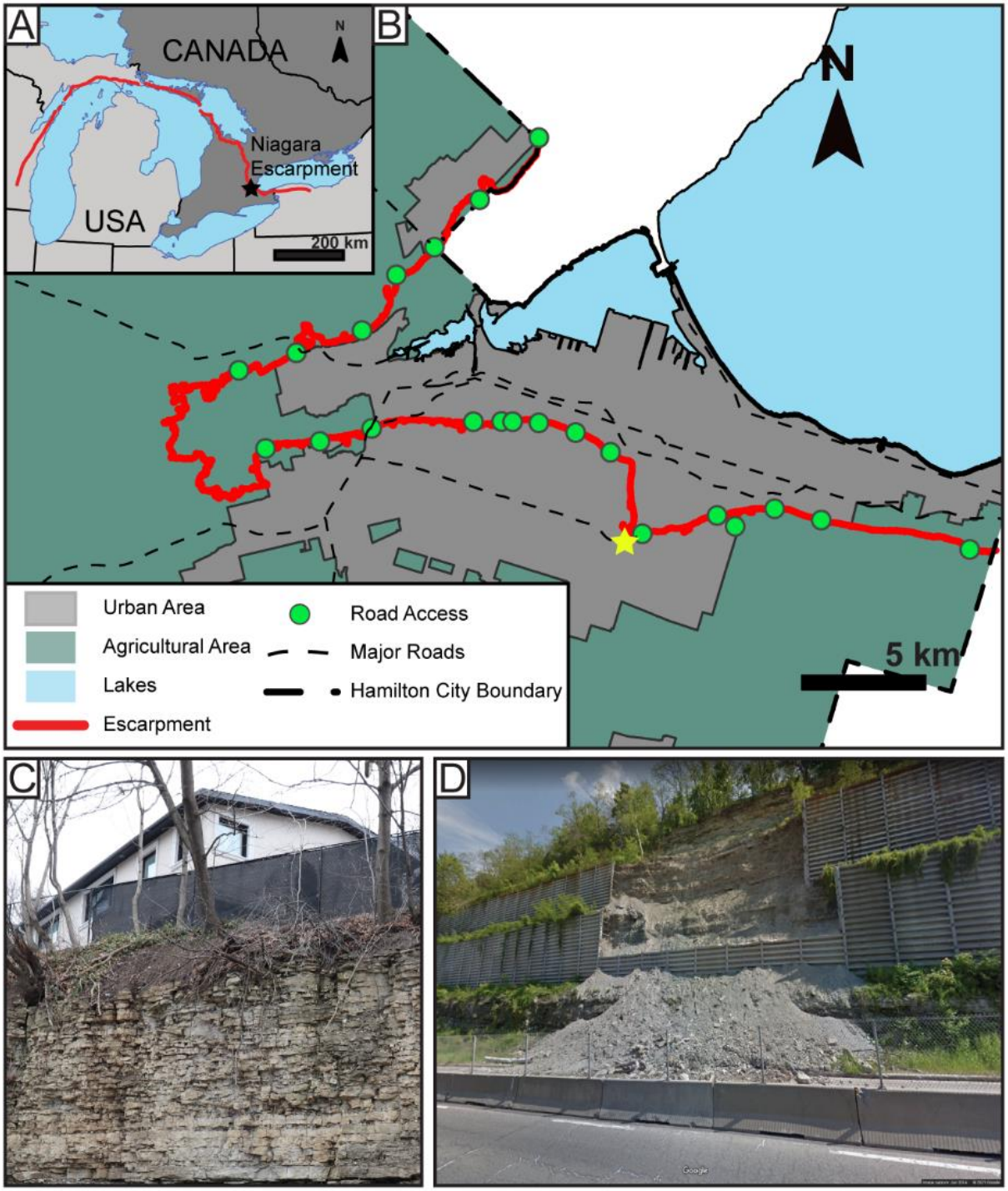

Figure 5.1: A) Location of the Niagara Escarpment extending from New York State, through southern Ontario into Michigan and Wisconsin. Hamilton shown with a black star; B) Location of the Niagara Escarpment (red) within the city of Hamilton, Ontario and access routes crossing the escarpment (green dots). Study site depicted with a yellow star; C) House located near the escarpment edge; D) Rockfall onto a road access (Google 2021).

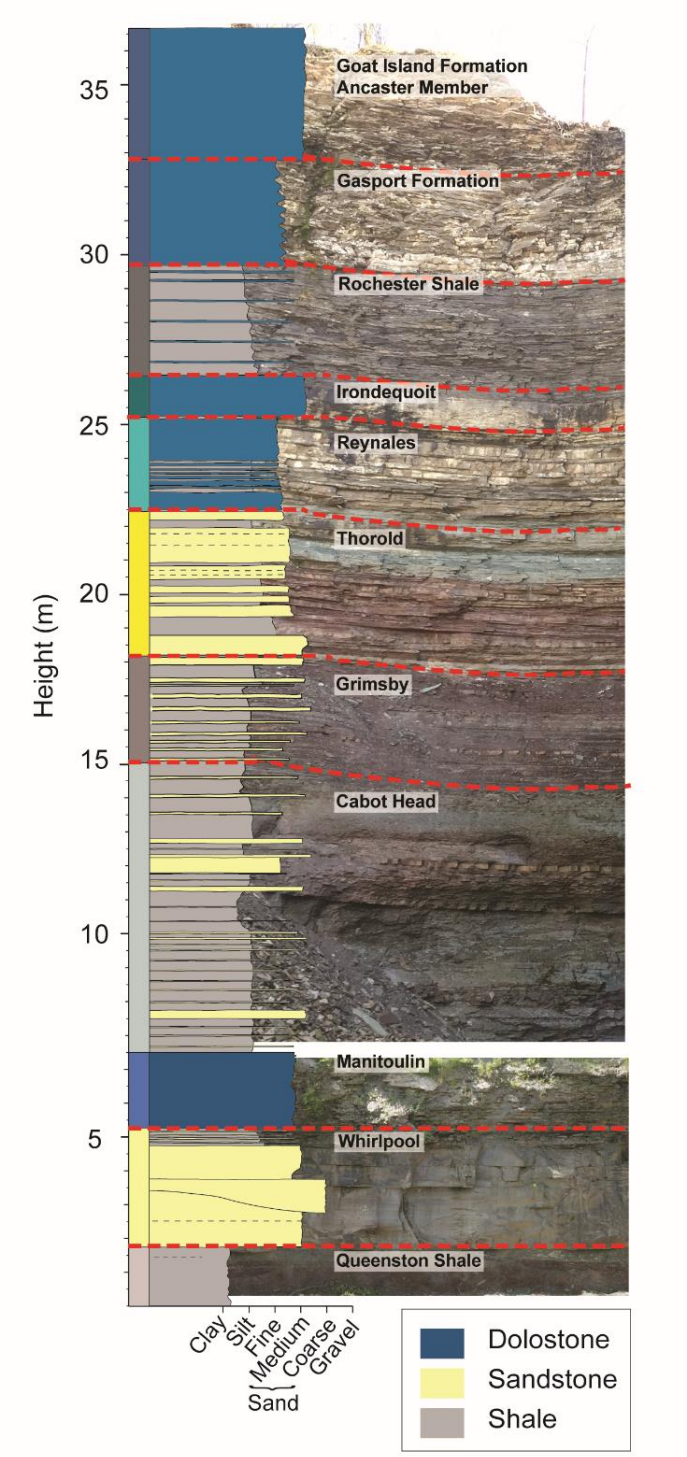

Figure 5.2: Simplified sedimentological log (left) and photograph (right) depicting the lithological characteristics of stratigraphic units exposed along the Niagara Escarpment in Hamilton, Ontario. The major units (named formations separated by red dashed lines) are dominated by three lithologies; dolostone, sandstone and shale.

This study utilizes a relatively new methodology to monitor erosion processes and rates along the Niagara Escarpment in Hamilton using photogrammetry collected from an unpiloted aerial vehicle (UAV) and analyzed using Structure from Motion (SfM) software. Most erosion occurring along the escarpment in Hamilton is relatively small-scale, composed of near continuous single block failures from the escarpment face. To document this, UAV imagery of an outcrop exposing rocks of the Niagara Escarpment at Albion Falls in Hamilton (Figure 5.1) was collected in two field surveys, the first in 2018 and a second in 2020. Structure from Motion (SfM) software was then used to create high resolution point clouds (models) from the input imagery, which were then compared over time to quantify the change caused by erosion (e.g. Stumpf et al., 2015; Duró et al., 2018; Letortu et al., 2018). High temporal and spatial resolution models produced in this way are becoming increasingly important for mapping the erosion of a rock face such as the Niagara Escarpment and for determining the characteristics of areas showing most change (e.g. Eltner et al., 2015; Stumpf et al., 2015; Clark, 2017; Duró et al., 2018; Letortu et al., 2018; Giordan et al., 2020).

5.1.1 Background

Many factors impact the rate of erosion occurring on a steeply sloping rock face including rock strength, distribution of lithological types and fracturing (Roegiers et al., 1979; Weissel & Seidl, 1997; Budetta et al., 2000; Barlow, 2002; Walker, 2004; Hayakawa & Matsukura, 2009; Kirby & Ouimet, 2011; Loye et al., 2012; Scott & Wohl, 2019). There is a direct correlation between the strength of a rock, as measured by its unconfined compressive strength (UCS), and its resistance to erosion; the lower a rock's strength, the greater its susceptibility to erosion (Hayakawa & Matsukura, 2009). The Niagara Escarpment is composed of Paleozoic sedimentary rocks with variable strength and resistance to erosion (Figure 5.2). Three lithological types with distinctive strength characteristics dominate the stratigraphy exposed along the escarpment; dolostone-dominated units (e.g. the Goat Island, Gasport, Irondequoit, Reynales and Manitoulin formations; Figure 5.2); sandstone-dominated units (e.g. the Thorold and Whirlpool formations; Figure 5.2); and shale-dominated units (e.g. the Rochester, Grimsby, Cabot Head and Queenston formations; Figure 5.2). Relatively resistant dolostone-dominated formations form the cap rocks to the escarpment and are underlain by more easily eroded shale-rich lithologies with lower UCS values (Al-Maamori et al., 2014; Perras et al., 2014). Undercutting of the rock face by the preferential erosion of shales destabilizes overlying layers and is considered to be an important

mechanism causing rockfalls and erosion of the escarpment (Gilbert, 1890; Moss & Nickling, 1980).

The sedimentary rocks exposed along the Niagara Escarpment in Hamilton are also extensively fractured, particularly the upper lithological units (e.g. Rochester, Gasport and Ancaster Member of the Goat Island; Figure 5.2). The orientation, density and intensity of fractures influences the size of erosive blocks and frequency of rockfalls and ultimately affects the rate of erosion (Loye et al., 2012; Scott & Wohl, 2019). A higher density of fractures (the measure of the number of fractures per unit area) in a rock face is generally associated with a decrease in rock stability (Kirby & Ouimet, 2011; Loye et al., 2012).

Fractures can be enlarged through many processes including ice growth, which is likely to occur in this region due to the temperate climate and winter months with average temperatures below 0°C (Fahey & Lefebure, 1988; Hales & Roering, 2007; Anderson & Lines, 2008; Kellerer-Pirklbauer, 2017). Fractures develop over time as weathering processes, such as freeze-thaw (Potts, 1970; Nicholson & Nicholson, 2000; Sass, 2005; Agustawijaya, 2007; McGreevy & Whalley, 2018; Draebing & Krautblatter, 2019), chemical weathering through groundwater acidity and salinity (Reddy and Youngdahl 1987; Webb et al. 1992; Goudie, 1999; Williams et al., 1999; Ruiz-Agudo et al., 2007; Meriano et al., 2009; Perera et al., 2013) and tree root weathering processes (Zwieniecki and Newton, 1995; Phillips et al., 2008; Gabet et al. 2010; Phillips et al. 2016; Pawlik et al. 2016; Malik et al. 2019), occur at the surface and near surface to lengthen and widen the fractures known as propagation. Each of these processes begins when the rock is first exposed where the pre-existing fractures in the rock create the conditions for many of these processes which act to propagate the fractures over time (Nicholson & Nicholson, 2000; Meriano et al., 2009; Gabet et al. 2010; Perera et al., 2013; Malik et al. 2019)

Climatic, hydrological, hydrogeological, and biophysical factors can substantially affect rates of erosion on an exposed rock face (Fahey & Lefebure, 1988; Agustawijaya, 2007; Portenga & Bierman, 2011; Miščević & Vlastelica, 2014).

5.1.2 Study Area

The Niagara Escarpment extends over 725 km across southern Ontario with a maximum height of 266 m (Hewitt, 1971; Perras et al., 2014). It is composed of relatively flat lying sedimentary rocks of late Ordovician and Silurian age, dipping approximately 5.5 m/km to the south. The escarpment is primarily composed of dolostone, sandstone and shale and the feature

has developed through progressive erosion of a resistant dolomitic scarp edge during the Paleogene, Neogene and Quaternary (Figure 5.2; Feenstra 1981; Tepper et al. 1990; Armstrong and Dodge 2007; Brunton and Brintnell 2020). The lower units exposed along the Niagara Escarpment are primarily sandstones and shales deposited during the late Ordovician and early Silurian periods during the uplift of the Taconic Mountains to the east (e.g. Queenston, Whirlpool, Cabot Head, Grimsby and Thorold formations; Figure 5.2; Bolton 1957; Brett, Goodman, and LoDuca 1990; Brogly, Martini, and Middleton 1998; Brunton, Turner, and Armstrong 2009). When uplift of the mountains ceased, the amount of clastic material supplied to the area was reduced and reefs and carbonate secreting organisms thrived, depositing carbonates and carbonaceous shale containing abundant fossils (e.g. the Reynales, Irondequoit, Rochester and Lockport formations; Figure 5.2) (Bolton, 1957; Hewitt, 1971; Johnson et al., 1992; Anastas & Coniglio, 1993; Armstrong & Carter, 2009).

The site selected for this study lies in the Red Hill Valley on the eastern side of Hamilton, opposite Albion Falls, a 19 m tiered waterfall fed by the Red Hill Creek (Figure 5.3). The studied outcrop runs approximately northeast to southwest and is approximately 13 m wide and 3.5 m tall (Figure 5.3B). This specific site was chosen for study as it is some distance away from high traffic walking trails or roads which limits the impact of people altering the rock face. The outcrop also exposes all major sedimentary rock types of the escarpment including dolostone-dominated, sandstone-dominated and shale-dominated lithologies of the Grimsby, Thorold, and Reynales formations.

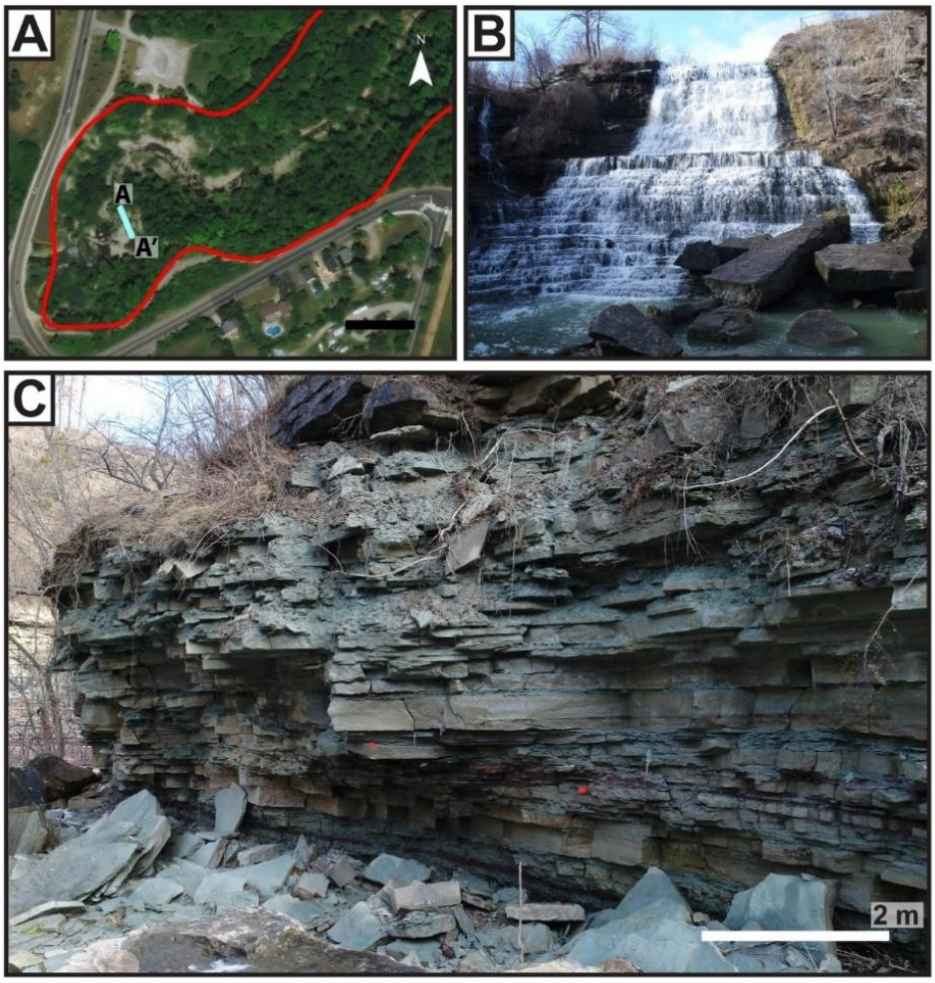

Figure 5.3: A) Study site at Albion Falls (see Figure 5.1 for location in Hamilton), location of outcrop in blue; Niagara Escarpment shown by red curved line; B) Albion Falls, a 19 m tiered waterfall fed by the Red Hill Creek; C) Outcrop used in this study.

5. 2 Methods

5.2.1 Model generation

Data were collected in two field surveys completed in December 2018 and February 2020 using the methodology outlined in Chapter 4 of this thesis. A DJI Phantom 4 was used to collect imagery of the outcrop using the built-in camera with an equivalent focal length of 24 mm and 20 MPix resolution. Data collection included a minimum 75% overlap of images and multiple passes of the outcrop from different distances and different angles (nadir and ~25 degrees off nadir) following best practices proposed by others (James & Robson, 2012; Micheletti et al., 2015; Letortu et al., 2018; Jaud et al., 2019). The UAV was flown 3 m to 4 m from the rock face. The

built-in GPS on the UAV, which has a horizontal error of 1.5 m, was used to provide basic locational constraints on the geometry of the model produced from the imagery. Unfortunately, due to the irregular form of the rock face, and the presence of surrounding vegetation and buildings, reliable ground control points could not be established with GPS; those points that were collected had an unacceptable error of > 1 m in all directions. To address this issue, the distances between established reference points on the outcrop were measured and input into the final models to ensure consistency in the model geometry.

The collected imagery was input into Agisoft Metashape software and, using a standard SfM workflow (e.g. Westoby et al. 2012; Ely et al. 2017; Javadnejad et al. 2021), point clouds were created for each of the two surveys (Figure 5.4). The images were aligned using the highest accuracy settings and points with a reprojection error of greater than 0.5 were removed. The dense point clouds were generated using moderate filtering to remove points created by vegetation and to create models of the outcrop that allowed comparison between the 2018 and 2020 surveys. The final models have 9.9 million points (2018) and 22.5 million points (2020) with an average point spacing of 0.0033 m and 0.0022 m in 2018 and 2020 respectively (Figure 5.5); differences in point spacing are due to differences in the number of images collected in each of the two surveys. To assess the error of the models, additional known lengths on the rock face were compared to their corresponding model lengths. On each model, the same 10 locations were chosen with the average difference between the actual length and model length of ±0.85 cm.

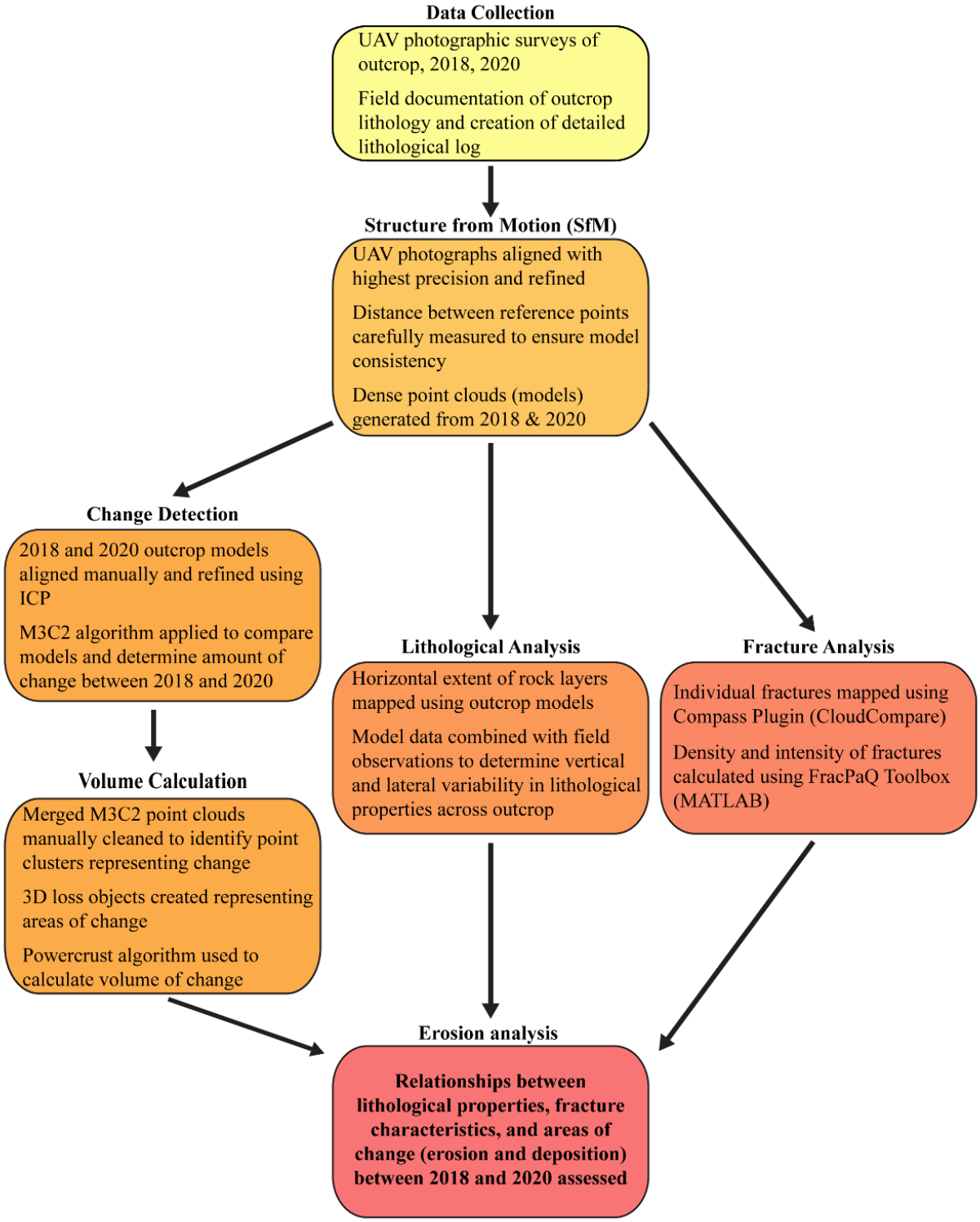

Figure 5.4: Workflow utilized in this study.

5.2.2 Change Detection

To allow comparison between the outcrop models created for the 2018 and 2020 surveys and to identify areas of erosion (change) they were each imported into CloudCompare and the two models registered using manual coarse alignment and refined using Iterative Closest Points (ICP) (Zhang, 1994; Rajendra et al., 2014; Micheletti et al., 2015; Stumpf et al., 2015). Due to the complex nature of the rock face which included areas of overhang, the Multiscale Model to Model Cloud Comparison (M3C2) algorithm was used to compare the models (Figure 5.4), a commonly used algorithm for this type of comparison in rockfall analysis (Lague et al., 2013; Benjamin et al., 2016; DiFrancesco et al., 2020). The M3C2 algorithm determines the amount of change (either erosion or deposition) by computing the local distance between two point cloud models based on surface orientation (Lague et al., 2013). To address the discrepancy in point spacing between the models, a subsample of the point clouds was used with a point spacing of 0.01 m. Best practices suggest a projection diameter of one to two times the point spacing is appropriate to delineate rockfalls (Williams et al., 2018; DiFrancesco et al., 2020), and a M3C2 projection diameter of 0.02 m was used in this study; a registration error of 0.05 was also applied to account for issues in initial imagery capture, errors in the initial models, and in the ICP registration (Figure 5.5).

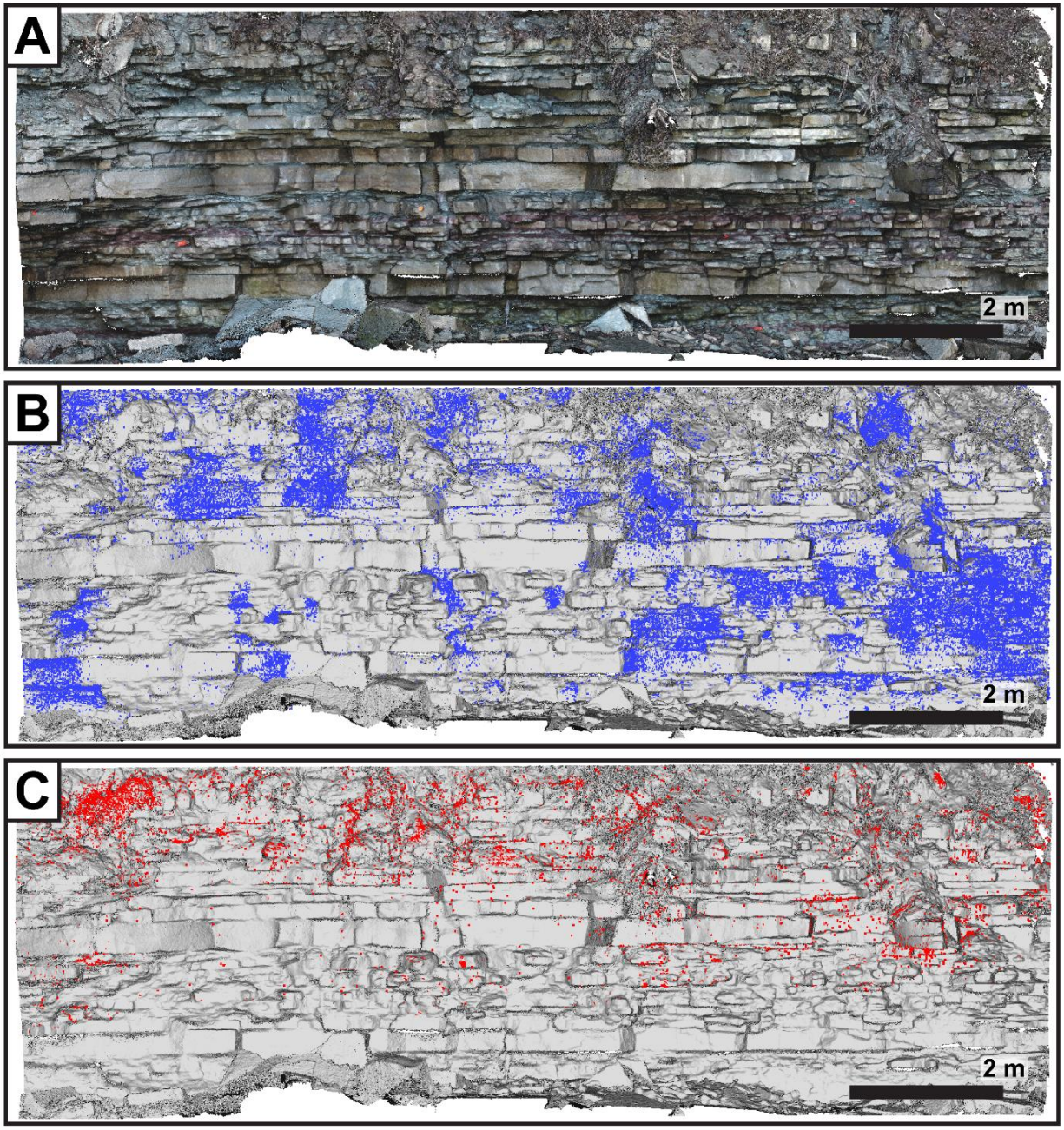

Figure 5.5: A) Dense point cloud created from the 2020 survey images in Agisoft Metashape (Agisoft Metashape, 2020); B) Areas determined as significant negative change in the M3C2 algorithm overlain on the 2020 survey (blue points); C) Areas determined as significant positive change in the M3C2 algorithm overlain on the 2020 survey (red points).

The M3C2 algorithm was applied twice, comparing the 2018 model to the 2020 model to find the geometry of the rock face subsequent to any erosional events, and between 2020 and 2018 to delineate the initial geometry of the rock face (Hutchinson, et al., 2019; Benjamin et al., 2020; Bonneau, DiFrancesco et al., 2020). Based on the confidence interval calculated during creation of the M3C2 models, only points with a confidence interval of 95% or above were retained, with the remainder of the points removed and assumed to represent change recorded due to minor differences in the modelled point locations (Lague et al., 2013; Stumpf et al., 2015). The merged point clouds create the 3-D shapes of the material lost from the outcrop face (rockfalls) which can then be used to determine the volume of material lost.

The merged M3C2 point clouds were manually cleaned of any points in which the detected change was caused by minor variations between the models, the movement of vegetation, or from shadows on the rock face. Clustering of the point clouds was determined using the density-based spatial clustering of applications with noise (DBSCAN) algorithm, completed in MATLAB (Tonini & Abellan, 2014; Bonneau, Hutchinson, et al., 2019; Benjamin et al., 2020; DiFrancesco et al., 2020).

Areas of change identified in this way represented areas of loss (erosion) and areas of gain (deposition) on the escarpment face between 2018 and 2020 (Figure 5.5). Using the power crust algorithm developed by Amenta et al. (2001) surface reconstruction of the areas of loss and gain was completed in MATLAB. The power crust algorithm creates an approximation the surface of a set of 3-D points by calculating the medial axis transform (MAT) which incorporates the medial axis, the centre of a set of disks which maximally fit into the shape, and their corresponding radii (Choi & Han, 2002). The MAT is determined based on the Voronoi vertices of the point set, based on the corresponding Voronoi Diagram and representing locations in which the vertices are equidistant to three or more points from the original point set (Vleugels et al., 1996). The final output of the power crust algorithm is an approximation of the shape of the erosional block from which the volume can be calculated (Amenta et al., 2001; Bonneau et al., 2019a).

Based on the results of a previous test of this methodology elsewhere on the Niagara Escarpment (this thesis, Chapter 4), rock volumes calculated this way are likely to both over and underestimate the size of rock block falls. Therefore, the estimates of volume change presented in this study should be taken as an approximation of the relatively small-scale rock falls and erosional events expected in this environment.

5. 3 Lithological Analysis

To assess if areas of change detected between the two models are related to lithological characteristics of the outcrop, a detailed sedimentological log of the outcrop was constructed recording information on lithology, bedding characteristics, sedimentary structures, and fossils (Figure 5.6). The base of the outcrop is composed of fissile grey and red mottled shale with thin 2 cm to 5 cm irregular beds of fine-grained sandstone belonging to the Grimsby Formation (Figure 5.6 and 5.7). This is overlain by a fine-grained massive sandstone bed with sharp upper and lower contacts that records the sharp transition from the Grimsby to the Thorold Formation (Figure 5.6). The overlying Thorold Formation is characterized by interbedded fine to medium-grained sandstones containing wave ripples, burrows, planar crossbedding, swaley crossbedding, and thin beds of laminated shale (Figure 5.6); one notable sandstone bed contains ball and pillow structures, a characteristic feature of the Thorold Formation in this area (Figure 5.6). The upper part of the outcrop is composed of thickly bedded (5-20 cm) dolostone units, interbedded with thin shale layers (< 2 cm) of the Reynales Formation (Figure 5.6 and 5.7). The lateral continuity of the dominant lithological units can be clearly seen over approximately 13 metres.

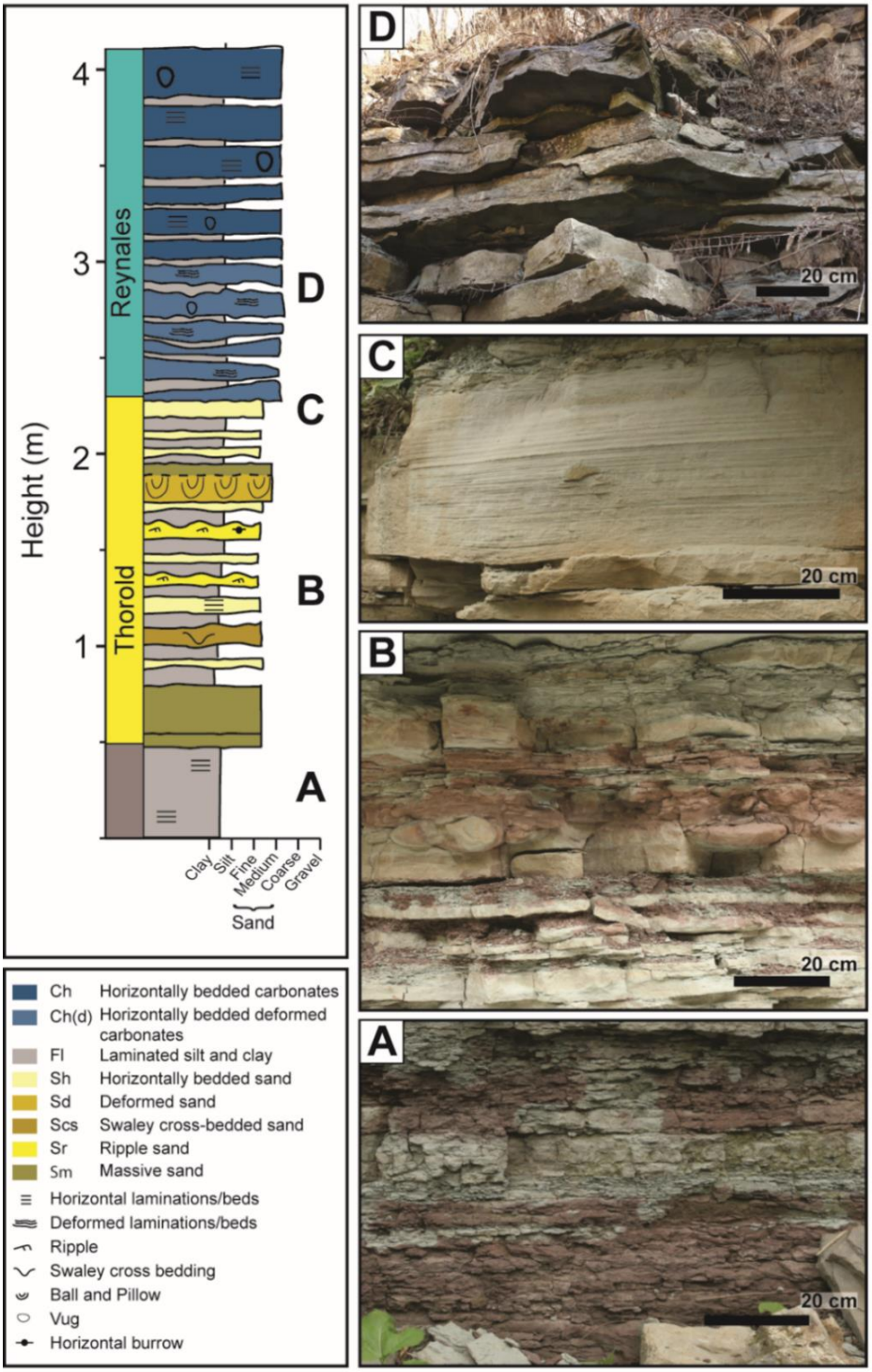

Figure 5.6: Upper left: Detailed sedimentological log of the outcrop at Albion Falls. A) Mottled red and grey shale of the Grimsby Formation; B) Interbedded sandstone and shale beds of the Thorold Formation. Small scale, 5 cm to 15 cm, ball and pillow structures are visible in the centre of the image; C) 30 cm laminated sandstone bed within the Thorold Formation; D) Interbedded dolostone and shale of the Reynales Formation.

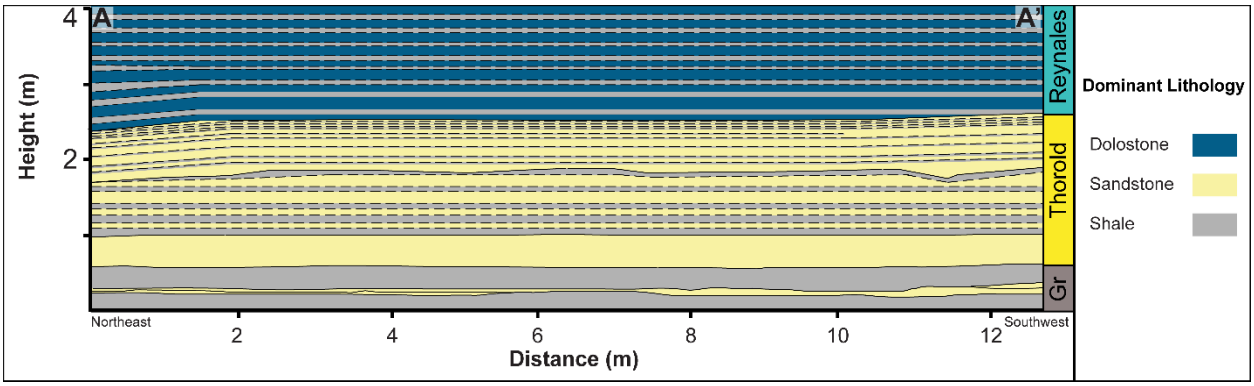

Figure 5.7: Simplified sedimentological map depicting the lateral continuity of the dominant rock types across the outcrop. The lowest formation is the Grimsby (Gr) followed by the Thorold and the Reynales Formations.

5. 4 Fracture Analysis

The relative density and intensity of fractures in dolostone and sandstone lithologies on the outcrop face were recorded using photogrammetric models (e. g. Bemis et al. 2014; Bi et al. 2017; Piras et al. 2017); individual fractures in the shale layers were not mapped due to their small size and extremely high density. Using the Compass plugin (Thiele et al., 2017) in CloudCompare, a preliminary map of fractures on the 2018 outcrop model was created (Figure 5.8A). The Compass plugin is a semi-automated method of fracture mapping that applies user-specified start and end points identified on a fracture and applies a least-cost-path method to create a fracture trace based on the contrast of pixel values (Thiele et al., 2017); a consistent magnification of the model was used during fracture identification, to ensure consistency in the size of fractures mapped (Healy et al., 2017). This methodology has been used in several other studies to map fractures on vertical and horizontal rock faces (e.g. Sayab et al. 2018; Menegoni et al. 2018; Samsu et al. 2020). The mapped fractures were then exported from CloudCompare into Adobe Illustrator where the traces were simplified by combining trace segments that represented single continuous fractures and smoothed of any artifacts found in the traces caused by the least-cost paths analysis; the simplified fracture traces were used in the fracture pattern analysis.

The MATLAB FracPaQ toolbox (Healy et al., 2017) was utilized to calculate the density and intensity of fractures on the outcrop. This toolbox uses established quantitative methods to examine density, intensity, connectivity, and orientation of fractures (Healy et al., 2017). During processing, 15 scan circles were used with a diameter of approximately 0.33 m to create the

fracture density and intensity maps (Figure 5.8 B,C). These maps of the rock face were exported and used to assess the potential impact of fracturing on erosion.

On the outcrop 737 fractures were mapped, including 279 horizontal bedding plane fractures and 458 vertical fractures (Figure 5.8A). Along horizontal bedding planes, the longest fracture is 12.15 m long, extending along most of the rock face, and the smallest fracture is 0.07 m; the average length of horizontal fractures is 0.84 m (Figure 5.8A). The vertical fractures are smaller, ranging from 0.04 m to 0.73 m and averaging 0.16 m in length; many vertical fractures terminate at the intersection with horizontal fractures, limiting their length. There is considerable variation between areas of high and low density of fracturing across the outcrop, with an average density of 16.47 fracture segments/m^2 (Figure 5.8B). More high-density areas of fracturing are found in the lower 2 m of the outcrop (Thorold Formation; see right hand side of Figure 5.8B) and fewer in the upper left (Reynales Formation; see left hand side of Figure 5.8B). Analysis of fracture intensity also shows higher values in the lower part of the outcrop in the Thorold Formation (Figure 5.8C). The lowest intensity of fractures occurs in the Reynales (shown in the upper left of Figure 5.8C), indicating that the fractures in this area are shorter. In the lowest parts of the outcrop, areas that do not show fracturing are dominated by shale (Grimsby), where the fractures are below the size threshold of fracture mapping. These areas are assumed to have high fracture density and low fracture intensity as the fractures are usually small in size.

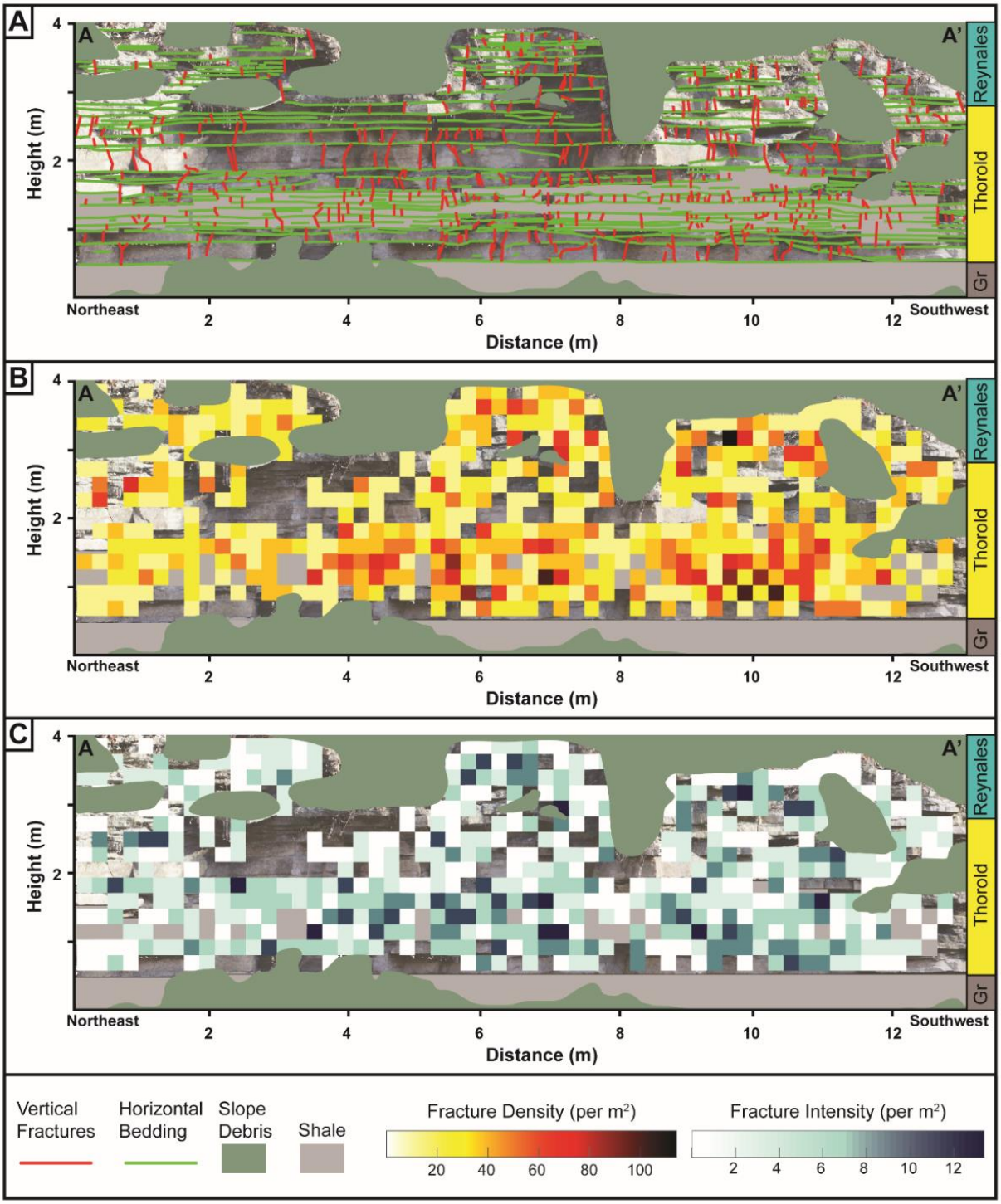

Figure 5.8: A) Map of the vertical (red) and horizontal (green) fractures on the outcrop, areas of slope debris indicated by green shading; B) Density map depicting the number of fractures within a scanning circle and C) Intensity map depicting the average length of fractures which pass through each scanning circle. B and C created using FracPaQ Matlab Toolbox (Healy et al., 2017).

5. 5 Change Detection Analysis

The two models created from UAV imagery collected in 2018 and 2020 were compared to determine the location and volume of change on the rock face that occurred over the 14-month period (Figure 5.9A, B). A visual inspection of the two models shows a significant amount of change on the outcrop with both erosion and deposition occurring (Figure 5.9A, B). Using the M3C2 algorithm, similar areas of both positive and negative are identified. Areas of negative change (erosion) occur across the entire outcrop and are not limited to any one area or lithological unit (Figure 5.9D), although certain areas (e.g. southwest side of the outcrop) experienced more volume loss than others.

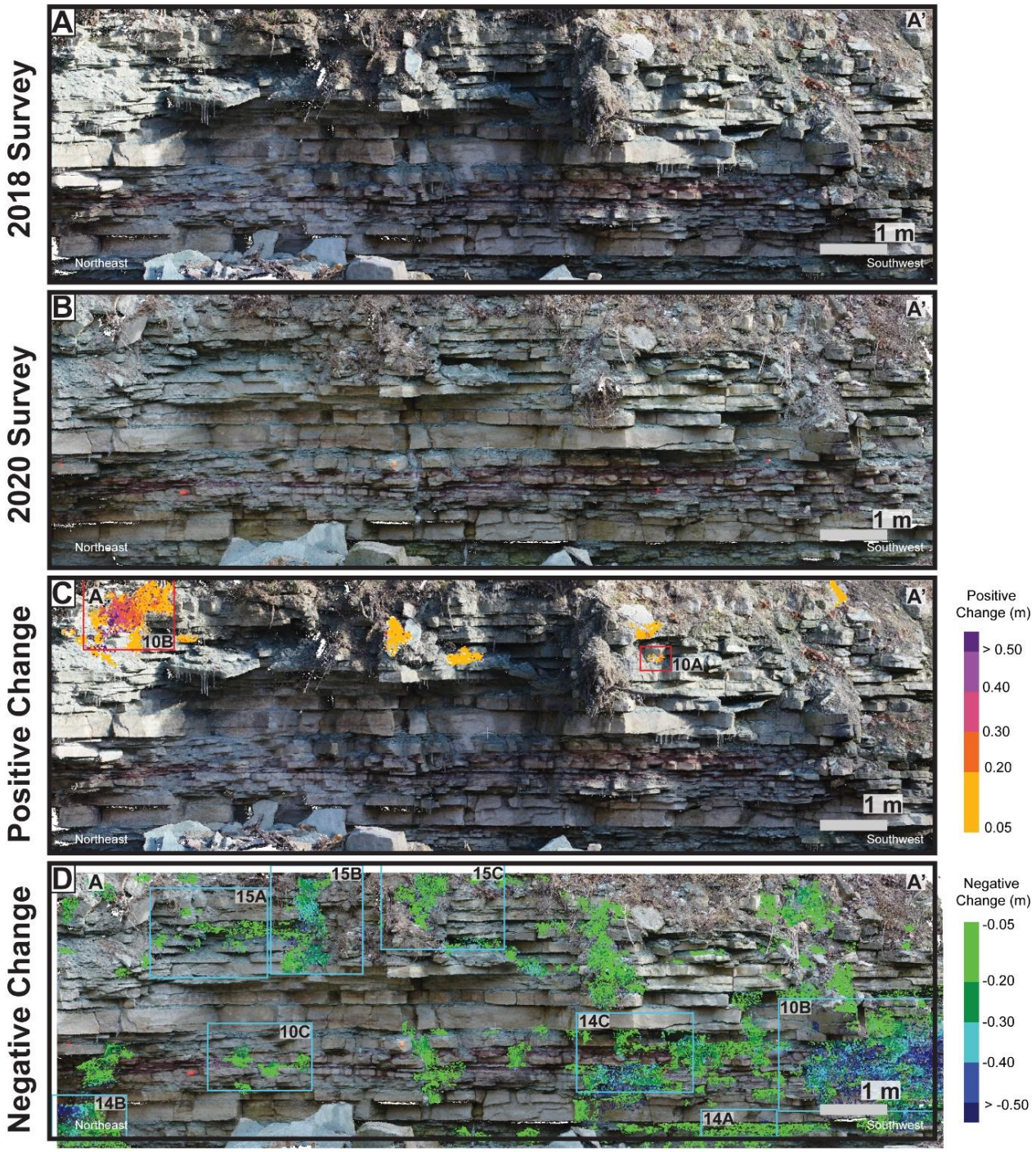

Figure 5.9: A) 2018 model of the outcrop; B) 2020 Model of the outcrop; C); D) Results of the M3C2 algorithm applied to the 2018-2020 models, showing areas of positive change (C) and negative change (D).

Thirteen distinct areas of positive change (deposition) can be identified in the upper 1.25 m of the rock outcrop (Figure 5.9C). Each of these regions was isolated to determine the average distance of change, representing the thickness of deposition, and the volume of change. Regions of deposition record the accumulation of slope debris (Figure 5.10A) and the slow movement of blocks on the face that have changed position but not yet fallen (Figure 5.10B). The accumulated debris is composed primarily of soil and clay sediments from the slope above. The ground surface at the base of the outcrop was not included in the change detection and volume calculations; however, based on a visual comparison between survey images, this area experienced significant deposition of material lost from the outcrop face during the period of study.

In total, depositional changes were recorded over approximately 2.5% of the surveyed outcrop. Most of regions of deposition record thicknesses of deposited material between 0.1 and 0.59 m (Figure 5.11A) and volumes of between 0.001 m^3 and 0.1 m^3 (Figure 5.12A). The total calculated volume of deposited material was 0.22 m^3.

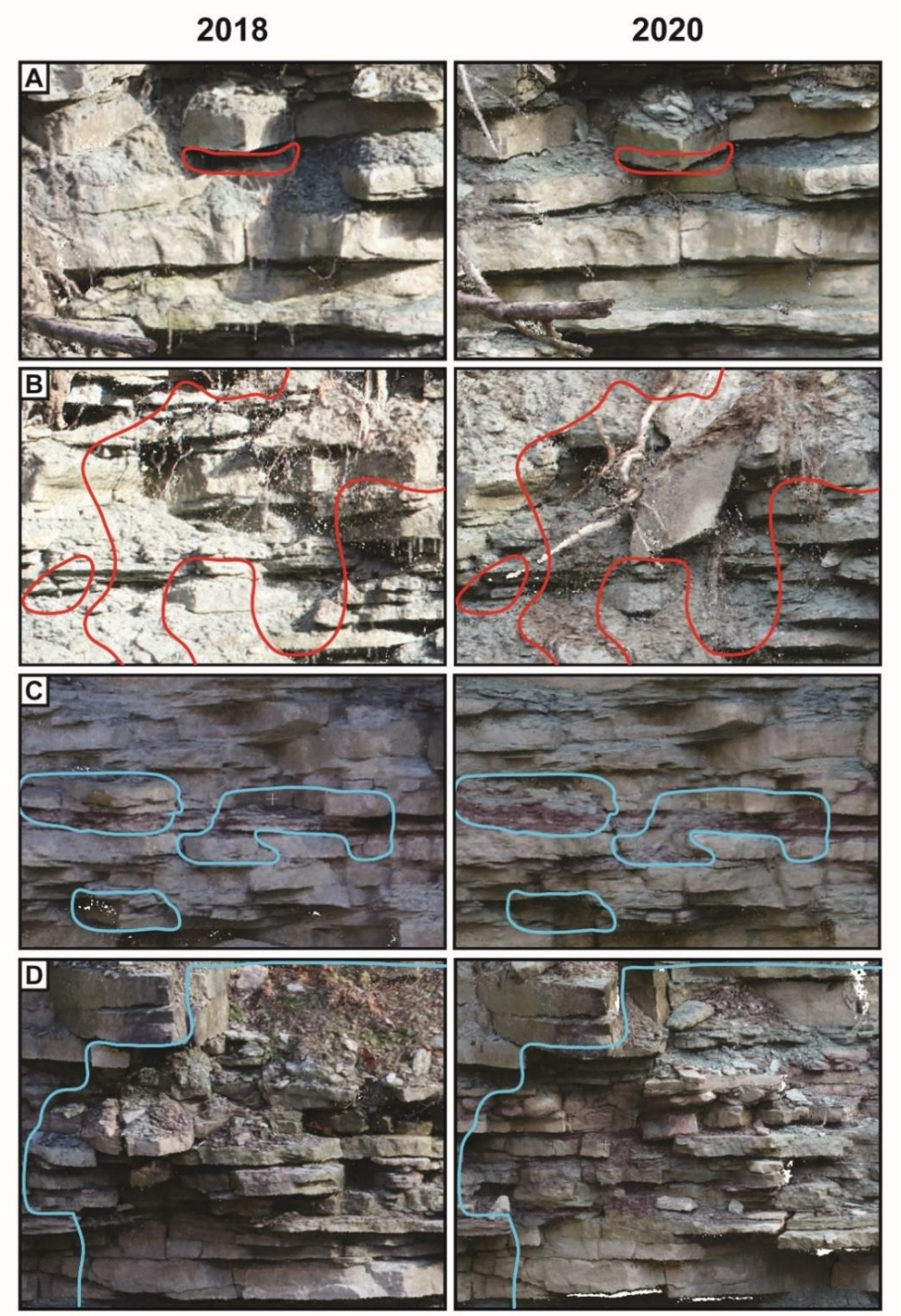

Figure 5.10: A) Example of positive change caused by the slow movement of blocks on the outcrop; areas of change (deposition) identified by M3C2 analysis outlined in red; B) Deposition of slope debris on the upper part of the outcrop; areas of change (deposition) identified by M3C2 analysis outlined in red. C) Single rock blocks released from the interbedded sandstone and shales of the Thorold Formation; areas of change (loss) identified by M3C2 analysis outlined in blue; D) Large area of rockfall on the southwestern side of the outcrop; areas of change (loss) identified by M3C2 outlined in blue. Location of the images shown in Figure 5.9.

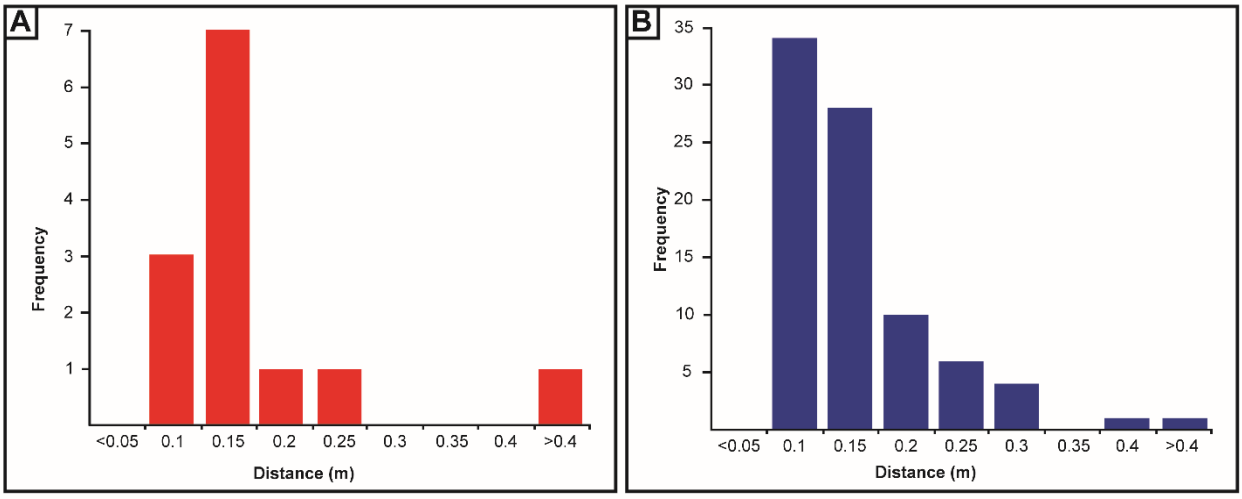

Figure 5.11: Histogram depicting the average distance of change in the M3C2 results which represent thickness of material added through deposition (positive change) (A) and lost through erosion (negative change) (B).

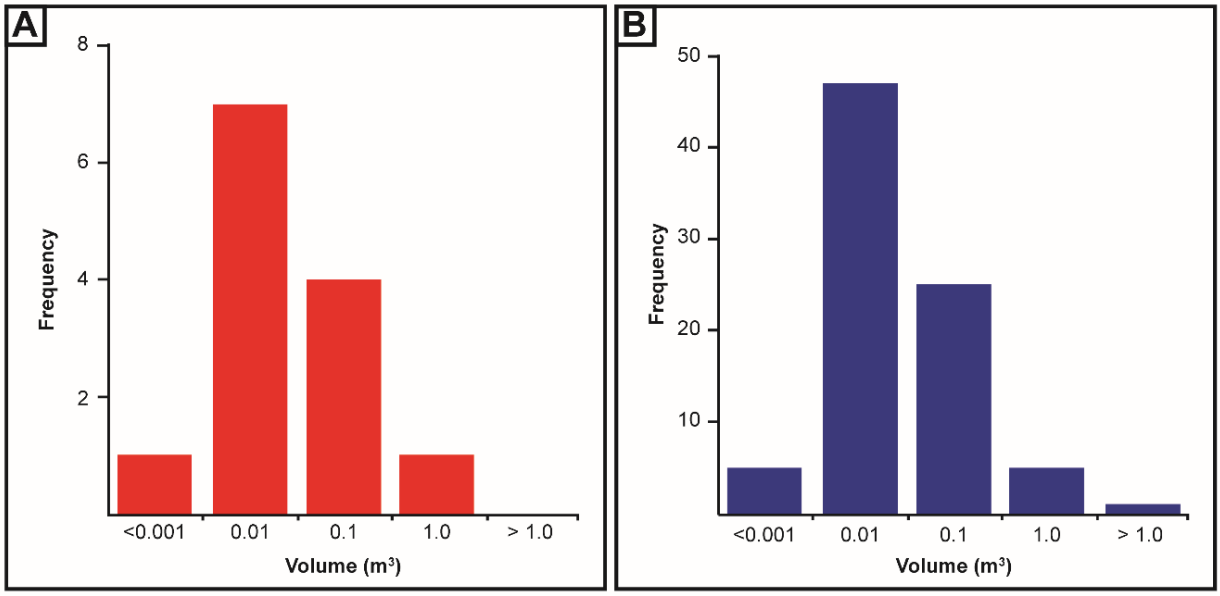

Figure 5.12: Histogram depicting the average volume of change calculated by M3C2 which represent the volume of deposited material (positive change) (A) and the volume of material lost through erosion (negative change) (B).

In contrast, when the outcrop models from 2018 and 2020 are compared, approximately one-third of the outcrop (83 separate regions) can be identified as having negative change recording material loss or erosion (Figure 5.9D); this includes single blocks that have fallen from the outcrop (Figure 5.10C), and larger areas of more significant losses (Figure 5.10D). The average thickness of material lost from these areas was 0.14 m (ranging from 0.06 m to 0.63 m) and approximately 73% of the areas of erosion lost between 0.05 and 0.15 m of material from the rock face (Figure 5.11B); this suggests that most blocks that fell from the rock face were within that thickness range.

The total volume of material lost to erosion on the outcrop is approximately 3.35 m^3. The average volume of material lost from regions on the rock face that experienced erosion is 0.04 m^3 and approximately 57% of these regions documented losses between 0.001 m^3 and 0.01 m^3 (Figure 5.12B); this also suggests that the majority of eroded block were within this volume range. For M3C2 calculations of change identifying the size and volume of material lost and deposited, a lower limit of 0.05 m was used; hence, any changes in the models below this size would not be detected and smaller events that occurred on the outcrop may not be registered.

5. 6 Discussion

Three distinct lithological units are present in the studied outcrop, the Grimsby, Thorold, and the Reynales formations. The Reynales Formation lies at the top of the studied outcrop and experienced both erosion and deposition of material whereas the underlying Thorold Formation experienced only erosion, particularly on the southwestern side of the outcrop (Figure 5.13). The Grimsby Formation lies at the base of the outcrop and shows the least amount of erosion; this may in part be due to the fine-grained nature of this unit and the release of small blocks below the threshold of detection used in this study. The severity of erosion/material loss experienced by each of these lithological units over the study period is likely related to their specific properties including sediment type, stratigraphic position, and fracture patterns (Budetta et al., 2000; Agustawijaya, 2007; Hayakawa & Matsukura, 2009; Kirby & Ouimet, 2011; Loye et al., 2012; Scott & Wohl, 2019).

5.6.1 Influence of Sediment Type and Stratigraphy

Each of the lithological units exposed on the outcrop are dominated by different sedimentary rock types and each type experienced some degree of erosion (Figure 5.13). Lithological variability in an outcrop is known to impact both the rate and location of erosion.

Shale is a considered to have a high susceptibility to erosion through processes such as slaking and rock creep (Budetta et al., 2000; Hayakawa & Matsukura, 2009), resulting in more rapid retreat of shale-dominated units and destabilization of overlying resistant layers in the stratigraphy (Roegiers et al., 1979; Shakoor & Rodgers, 1992; Barlow, 2002; Admassu et al., 2012). Sandstone and dolostone-dominated units are less susceptible to erosion (Agustawijaya, 2007; Hayakawa & Matsukura, 2009) but are prone to block loss through falling and toppling.

Along the Niagara Escarpment, the stratigraphic distribution of more and less resistant rocks has played a critical role in its formation; more rapid erosion of less resistant rock types has resulted in undercutting and the creation of unsupported overhangs which can fail causing significant rockfall events (Hayakawa & Matsukura, 2009; Niemann, 2009; Admassu et al., 2012). This process is documented close to the base of the studied outcrop where shales of the Grimsby Formation and those interbedded in the Thorold Formation, have undercut overlying sandstone beds causing block failure and overall slope erosion (Figure 5.13, 5.14).

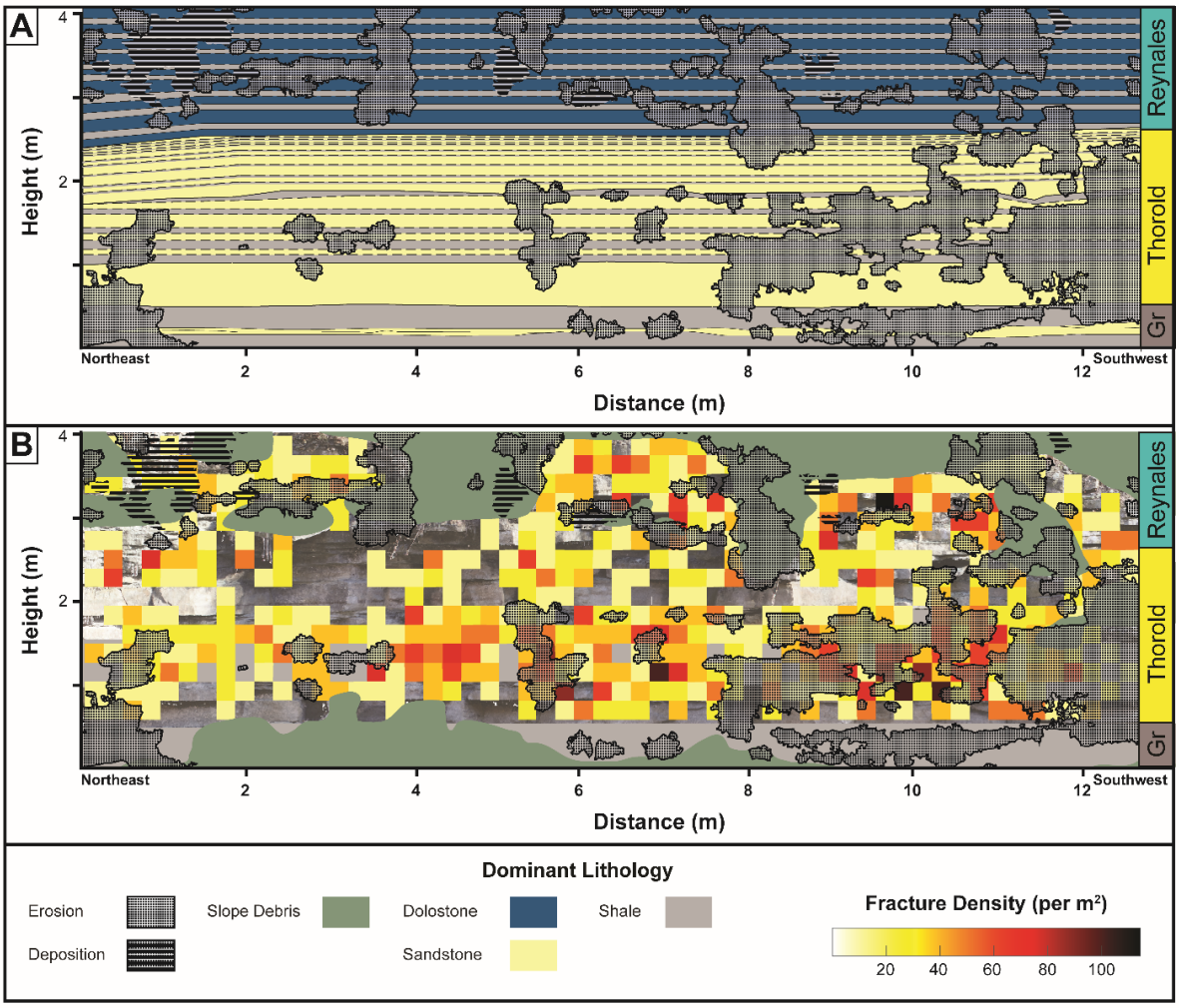

Figure 5.13: A) Location of areas of change (representing areas of erosion and deposition) superimposed on the map of outcrop lithology; B) Location of areas of change (representing areas of erosion and deposition) superimposed on the fracture density map of the rock face.

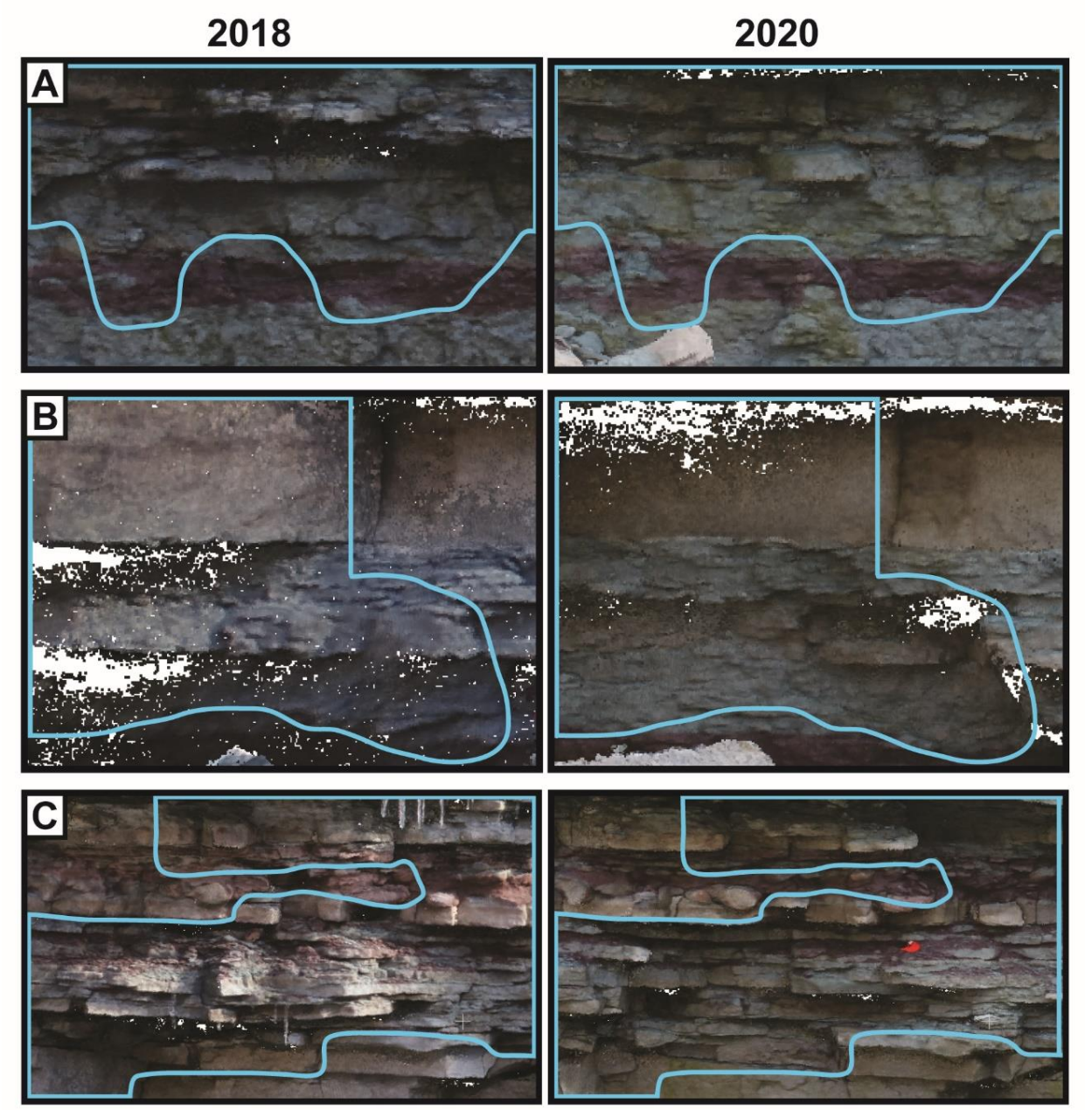

Figure 5.14: A) Shale of the Grimsby Formation with overlying sandstone bed that failed between 2018 and 2020(failed block at lower left on 2020 image); B) Thick sandstone bed (upper) at base of Thorold Formation. 2018 model shows undercutting by underlying shales; in 2020 model the sandstone block has fallen (lower left of image); C) Interbedded sandstone and shale of the Thorold Formation with multiple areas of rock fall. For each image, areas of erosion are fully outlined in blue.

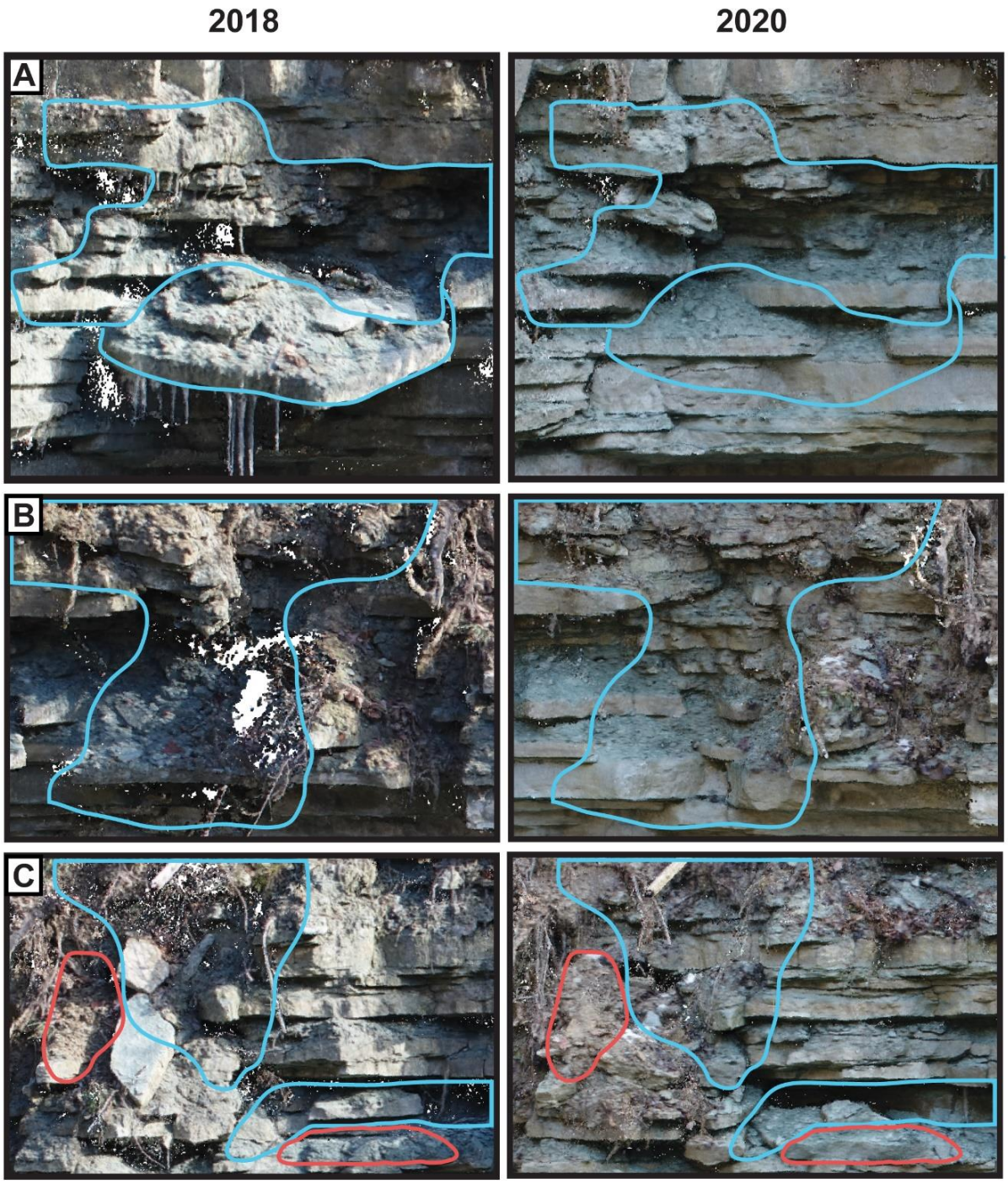

Figure 5.15: A) Interbedded dolostone and shale of the Reynales Formation which has undergone significant rockfall between surveys; B) Loss of slope debris from the surface of the Reynales Formation; C) Area of the outcrop which experienced both erosion and deposition during the study period. For each image, areas of erosion are fully outlined in blue and areas of deposition fully outlined in red.

Near the top of the Thorold Formation, the sandstone beds are relatively thick (5-8cm), and are interbedded with much thinner shale beds (0.5-1cm); this area of the rock face shows less erosion than elsewhere, with the majority occurring on the southwest side of the face which was destabilized by a large failure of the underlying interbedded shale and sandstone unit (Figure 5.14C).

The upper 1.5 m of the Reynales Formation is covered by a substantial amount of slope debris released from overlying units and trapped on prominent ledges of underlying thick bedded dolostone (Figure 5.15B,C). Movement of this material by small debris slides accounts for areas of both positive (deposition) and negative (erosion) change on the outcrop face (Figure 5.15C).

Interbedding of resistant dolostones or sandstones with more easily eroded shale occurs across the entire studied outcrop face and does appear to have a significant influence on slope stability. However, the stratigraphic arrangement of sediment types does not explain all of the variability in the amount of erosion that occurred during the time frame of the study; some lithological units, with the same sedimentological characteristics, show significant differences between the amount of erosion on the southwestern and northeastern parts of the outcrop (Figure 5.9).

5.6.2 Influence of Fractures

The density, intensity and orientation of fractures is commonly linked to slope instability, the size of blocks that will topple from the face, and the type of erosion that occurs on an exposed rock face (Dühnforth et al., 2010; Gutierrez & Youn, 2015; Scott & Wohl, 2019). The orientation of fractures relative to the rock face is also known to impact the rate of erosion (Lane et al., 2016; Scott & Wohl, 2019). On the studied outcrop, vertical and horizontal fractures in sandstone and dolostone-dominated units run relatively parallel to each other and therefore at this location variability in fracture orientation is unlikely to impact the rate of erosion across the face (Figure 5.3, 5.8 and Figure 5.9).

The shale of the Grimsby Formation is highly friable and contains abundant fractures which are below the limits of identification using the methodology outlined here (Figure 5.5 and Figure 5.14A). There is evidence of material loss (erosion) across almost all of the Grimsby Formation outcrop, although the connection to fracture abundance is difficult to quantify given the difficulty of delineating individual fractures. However, the high density of fractures in this unit likely increases water penetration and significantly increases its rate of deterioration.

The overlying Thorold Formation is also fractured throughout the outcrop with a slight increase in the concentration of fractures in the centre of the outcrop (Figure 5.8). The density of fractures in sandstone units within the Thorold does not show a direct correlation with areas that experienced high amounts of erosion, despite the known connection between these two factors (Figure 5.13B; Kirby& Ouimet 2011; Scott & Wohl 2019). Some thick-bedded sandstones within the Thorold Formation are unfractured (e.g. at 0.5 m and 1.75 m from the base of the outcrop) and have not experienced any erosion over the studied time interval (Figure 5.13B). Thorold sandstones exposed in the central portion of the outcrop are highly fractured but also did not experience significant erosion (Figure 5.14A); however, high amounts of erosion toward the southwestern side of the outcrop occurred in units with a lower density of fractures but a higher proportion of fractured shale beds (Figure 5.10B). The Thorold Formation in the central portion of the outcrop may also have experienced less erosion due to the protection from surface water runoff provided by the overlying, significantly protruding, Reynales Formation (Figure 5.9, 6.3C). The southwestern part of the outcrop is not protected by similar overhanging rocks.

There are two minimally fractured thick-bedded sandstone layers of the Thorold which have experienced limited erosion; these help to highlight the impact of fracture density on the amount of erosion occurring in this formation as the limited fractures reduce erosion of these two layers (Figure 5.13B). The thick-bedded sandstone layers, found at 0.5 m and 1.75 m from the base of the face, have many areas which have no fractures with no erosion of the face. Therefore, it can be said that the absence of fractures limits erosion on the rock (Scott & Wohl, 2019). As the density of fractures in a lithological unit does not directly relate to the amount of erosion that occurred on the outcrop, additional factors must be considered.

The Reynales Formation shows less intensity and density of fracturing than the Thorold (Figure 5.8) with the highest amounts found in the central part and the southwestern side of the outcrop (shown in the upper middle part of Figure 5.8C,D). Unfortunately, outcrop mapping of fractures was difficult in this unit due to the amount of slope debris (Figure 5.13B) which obscures the rock surface and is also prone to movement creating areas of both positive (deposition) and negative (erosion) change (Figure 5.13B and Figure 5.15B, C).

5.6.3 Influence of temporal changes on outcrop stability

It is important to consider that this study reports on observations made in a single, short (14-month) time period and not all factors contributing to future development of the studied

outcrop may have been active during this period (Figure 5.16). While it is impossible to determine exactly how the rock face may evolve in the future there are changes affecting its stability that occur over time and impact the location of current and future erosional events. On the basis of findings from this study, it is clear that the sedimentological characteristics or fracture patterns of individual units do not necessarily indicate where erosion will occur on a rock face, although they do clearly impact the location of broad regions of an outcrop that will be more susceptible to erosion. Areas of the studied outcrop with similar lithological characteristics do show differences in the amount of erosion experienced over the study period. The long-term development of various characteristics of the rock face will ultimately determine its stability.

Undercutting is an iterative process, whereby more easily eroded material progressively undermines overlying more resistant materials until the overlying unit becomes unstable and fails (Figure 5.16; Shakoor and Rodgers 1992; Niemann 2009; Admassu, Shakoor, and Wells 2012). Over the short timeframe of this study, multiple small-scale areas of undercutting were observed in the Thorold Formation on the southwest side of the outcrop in 2018 which ultimately led to a more substantial collapse of the rock face prior to 2020 (Figure 5.9 and Figure 5.10B). This process of undercutting occurs over longer time periods than those covered by this study; it takes some considerable time for undercutting to fully redevelop and destabilize a slope once collapse of overlying layers has occurred (Figure 5.16). The amount of time required is dependent on factors such as the specific properties of the undercutting unit (e.g. shale), the thickness of both the underlying (shale) and overlying (sandstone/dolostone) units, the hydrological properties of the rock face, the presence of vegetation, and/or the presence of a protective barrier such as an overhang; these factors will all influence how the slope develops over time.

The thicker beds of sandstone within the Thorold Formation in this study are relatively resistant to erosion but will be prone to failure as undercutting of underlying shale-rich units destabilizes them, potentially causing catastrophic slope failures. Large scale failure events caused by undercutting is episodic in nature, although the timeframe of recurrent events at any one site is unknown, as many factors impact the stability of these beds.

The more resistant lithological units exposed along the outcrop are also prone to fracturing and development of the fracture network over time must also be taken into consideration. The rate of fracture propagation relative to the rate of erosion occurring on the outcrop face impacts the erosion rate over time (Scott & Wohl, 2019). After a rockfall event, such as occurred in the

southwest section of the studied outcrop, the fractures exposed on the rock face may be smaller in aperture, length and less developed as they were previously protected from many physical weathering processes. Over time, weathering processes will occur on the surface and near surface of the rock face acting to widen and lengthen the fractures, once again starting the processes that lead to destabilization and failures (Figure 5.16; Hancock et al., 1998; Chatanantavet & Parker, 2009). The rate of fracture propagation is impacted by processes, such as frost cracking, the length of time of exposure, and other chemical and biological weathering processes which impact the fractures (Scott & Wohl, 2019).

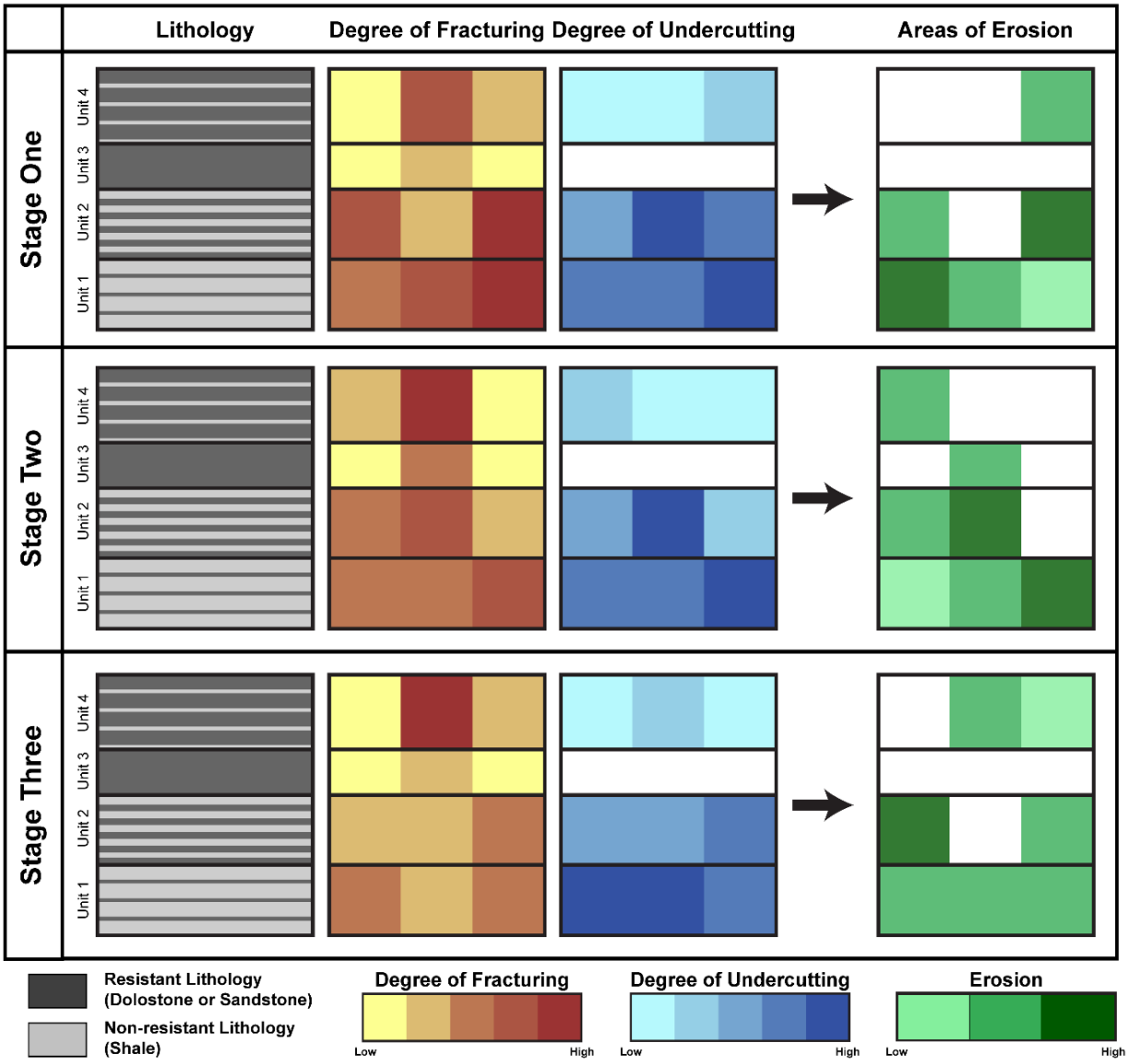

Figure 5.16: Schematic diagram showing the evolution of a rock face over time (Stage 1 – Stage 3). This assumes rock units are fractured, and undercutting occurs between units. Both undercutting and fracturing are processes that develop iteratively over time, becoming more severe until a rock face becomes unstable and failure occurs. The rate of these processes is dependent on many factors. Once failure has occurred the amount of undercutting and fracture size will be reduced and will require further time to develop.

The left column for each stage shows a simplified stratigraphy with different proportions of resistant rock types (e.g. dolostone and sandstone) and those susceptible to erosion (e.g. shale). In the initial stage of rock face development (Stage 1), there are more fractures in the shale rich units (unit 1 and unit 2) compared with the units with more resistant rock types (unit 3 and unit 4). The amount of fracturing and undercutting differs within the same unit due to variations in the amount of vegetation present and hydrological properties. Areas of abundant fracturing and undercutting will experience the highest amounts of erosion (unit 2, right side); areas with few

fractures and limited undercutting will experience less erosion (unit 3). In stage 2, areas that experienced erosion during stage 1 will experience less severe undercutting and fracturing (unit 2, right side), as the rock face is now more stable and will require further time to develop these features. Areas in which erosion did not occur in Stage 1 continue to develop higher amounts of undercutting and fracturing (unit 2, centre). This pattern of the development of fractures and undercutting is likely to continue, (as shown in Stage 3), causing variable erosion across the outcrop face over time. To determine the overall rate of erosion across the outcrop face, a long-term study is required.

5. 7 Conclusions

This study has demonstrated the utility of using UAV collected imagery and Structure from Motion (SfM) analytical tools to monitor erosion processes and rates on an outcrop of heterogenous sedimentary rocks along the Niagara Escarpment in Hamilton. The study has compared outcrop models created from the UAV imagery to detect both positive changes (representing deposition) and negative changes (representing erosion) on the outcrop face over a period of 14 months. Analysis of the models indicates there is significant variability in erosion rates across the outcrop over the study period; individual lithological characteristics such as sedimentary rock type or fracture characteristics do not adequately account for the location of erosional events and a combination of these factors, including time, need to be taken into consideration. In general, it appears that areas of the outcrop dominated by interbedded shales and more resistant sandstone and dolostone lithologies experienced the most extensive erosion over the study period. However, the extent of this erosion was not consistent across the outcrop face with more extensive erosion of interbedded units of the Thorold Formation on the southwestern side of the outcrop, and limited erosion of the same unit elsewhere on the outcrop. The degree of fracturing of the more resistant sandstone and dolostone units does also appear to have some control on the location of erosional events on the outcrop and unfractured units are unlikely to experience significant erosion.

The most apparent control on the location of erosional events on the studied outcrop appears to be linked to undercutting of resistant units by shale-dominated lithologies exposed on the outcrop face. This iterative process creates instability by removing support from overlying units and promotes slope failure. Once slope failure has occurred it takes time to redevelop an unstable undercut slope and to further propagate fractures in newly exposed rock surfaces. It is probable that the timing of significant rockfalls may be controlled in part by the amount of time it

takes for the combined processes of undercutting and fracture propagation to significantly weaken the rock face. Further erosion of the studied outcrop is likely to include the failure of additional areas of interbedded sandstone and shale of the Thorold Formation that may experience large, cascading rock falls in areas where little to no erosion occurred during the 14 months of this study.

The factors dictating the location and amount of erosion occurring on the studied outcrop face are complex, and dependent not only on properties of the rock face, but also how the face has developed over time. Using UAV photogrammetry and change detection analysis of an outcrop over a 14-month period, the general pattern of erosion of three of the major lithological units (the Grimsby, Thorold and Reynales formations) exposed along the Niagara Escarpment in Hamilton has been documented. However, the Niagara Escarpment exposes heterogenous lithological units that show large vertical and spatial variability, and the broader applicability of these findings needs to be tested. The creation of high temporal and spatial resolution models from UAV photography in this study allowed detailed mapping of an extremely complex rock face and the clear identification of areas of change on this face over time. This methodology has the potential to be effectively used to document erosion processes and rates on a much larger scale.

5. 8 References

Admassu, Y., Shakoor, A., & Wells, N. A. (2012). Evaluating selected factors affecting the depth of undercutting in rocks subject to differential weathering. *Engineering Geology*, *124*(1), 1–11. https://doi.org/10.1016/j.enggeo.2011.09.007

Agisoft Metashape. (2020). *Agisoft Metashape Professional* (Version 1.6.2). https://www.agisoft.com/downloads/installer/

Agustawijaya, D. S. (2007). The uniaxial compressive strength of soft rock. *Civil Engineering Dimension*, *9*(1), 9–14.

Al-Maamori, H. M. S., El Naggar, M. H., & Micic, S. (2014). A Compilation of the Geo-Mechanical Properties of Rocks in Southern Ontario and the Neighbouring Regions. *Open Journal of Geology*, *4*, 210–227. https://doi.org/10.4236/ojg.2014.45017

Amenta, N., Choi, S., & Kolluri, R. K. (2001). The power crust. *Proceedings of the Symposium on Solid Modeling and Applications*, 249–260. https://doi.org/10.1145/376957.376986

Anastas, A. S., & Coniglio, M. (1993). Sedimentology of an early Silurian carbonate ramp: the Manitoulin Formation, southern Ontario. *Canadian Journal of Earth Sciences*, *30*(12), 2453–2464. https://doi.org/10.1139/e93-212

Anderson, P. F., & Lines, L. R. (2008). A comparison of inversion techniques for estimating Vp/Vs from 3-D seismic data. *Estimating Vp/Vs CREWES Research Report —*, *20*(1997).

Armstrong, D. K., & Carter, T. K. (2009). *The subsurface Paleozoic stratigraphy of southern Ontario* (Special Vo). Ontario Geological Survey.

Armstrong, D. K., & Dodge, J. E. P. (2007). Paleozoic Geology of Southern Ontario - Project Summary and Technical Document. In *Ontario Geological Survey, Miscellaneous Release Data 219*.

Barker, R., Dixon, L., & Hooke, J. (1997). Use of terrestrial photogrammetry for monitoring and measuring bank erosion. *Earth Surface Processes and Landforms*, *22*(13), 1217–1227. https://doi.org/10.1002/(SICI)1096-9837(199724)22:13<1217::AID-ESP819>3.0.CO;2-U

Barlow, J. (2002). Rock creep and the development of the Niagara Cuesta. *Earth Surface Processes and Landforms*, *27*(10), 1125–1135. https://doi.org/10.1002/esp.401

Benjamin, J., Rosser, N. J., & Brain, M. J. (2016). Rockfall detection and volumetric characterisation using LiDAR. *Landslides and Engineered Slopes. Experience, Theory and Practice*, *2*(July), 389–395. https://doi.org/10.1201/b21520-38

Benjamin, J., Rosser, N. J., & Brain, M. J. (2020). Emergent characteristics of rockfall inventories captured at a regional scale. *Earth Surface Processes and Landforms*, *45*(12), 2773–2787. https://doi.org/10.1002/esp.4929

Bolton, T. E. (1957). Silurian stratigraphy and palaeontology of the Niagara Escarpment in Ontario.

Bonneau, D., DiFrancesco, P. M., & Jean Hutchinson, D. (2019a). Surface reconstruction for three-dimensional rockfall volumetric analysis. *ISPRS International Journal of Geo-Information*, *8*(12). https://doi.org/10.3390/ijgi8120548

Bonneau, D., Hutchinson, D. J., DiFrancesco, P.-M., Coombs, M., & Sala, Z. (2019b). Three-dimensional rockfall shape back analysis: Methods and implications. *Natural Hazards and Earth System Sciences*, *19*(12), 2745–2765. https://doi.org/10.5194/nhess-19-2745-2019

Brett, C. E., Goodman, W. M., & LoDuca, S. T. (1990). Sequences, cycles, and basin dynamics in the Silurian of the Appalachian Foreland Basin. *Sedimentary Geology*, *69*(3–4), 191–244. https://doi.org/10.1016/0037-0738(90)90051-T

Brogly, P. J., Martini, I. P., & Middleton, G. V. (1998). The Queenston Formation: Shale-dominated, mixed terrigenous-carbonate deposits of Upper Ordovician, semiarid, muddy shores in Ontario, Canada. *Canadian Journal of Earth Sciences*, *35*(6), 702–719. https://doi.org/10.1139/e98-021

Brunton, F. R., & Brintnell, C. (2020). Early Silurian Sequence Stratigraphy and Geological Controls on Karstic Bedrock Groundwater-Flow Zones, Niagara Escarpment Region and the Subsurface of Southwestern Ontario.

Brunton, F. R., Turner, E., & Armstrong, D. K. (2009). A Guide to the Paleozoic Geology and Fossils of Manitoulin Island and northern Bruce Peninsula, Ontario, Canada. In *Canadian Paleontology Conference Field Trip Guildebook No. 14* (Issue September 2009).

Budetta, P., Galietta, G., & Santo, A. (2000). A methodology for the study of the relation between coastal cliff erosion and the mechanical strength of soils and rock masses. *Engineering Geology*, *56*(3–4), 243–256. https://doi.org/10.1016/S0013-7952(99)00089-7

Chatanantavet, P., & Parker, G. (2009). Physically based modeling of bedrock incision by abrasion, plucking, and macroabrasion. *Journal of Geophysical Research: Earth Surface*, *114*(4), 1–22. https://doi.org/10.1029/2008JF001044

Choi, H. I. & Han, C. Y. (2002). The Medial Axis Transform. In Farin, G., Hoschek. J & Kim M. -S. (Eds.s), *Handbook of Computer Aided Geometric Design* (pp. 451-471). Elsevier Science.

Clark, A. (2017). Small unmanned aerial systems comparative analysis for the application to coastal erosion monitoring. *GeoResJ*, *13*, 175–185. https://doi.org/10.1016/j.grj.2017.05.001

DiFrancesco, P. M., Bonneau, D., & Hutchinson, D. J. (2020). The implications of M3C2 projection diameter on 3-D semi-automated rockfall extraction from sequential terrestrial laser scanning point clouds. *Remote Sensing*, *12*(11). https://doi.org/10.3390/rs12111885

Draebing, D., & Krautblatter, M. (2019). The Efficacy of Frost Weathering Processes in Alpine Rockwalls. *Geophysical Research Letters*, *46*(12), 6516–6524. https://doi.org/10.1029/2019GL081981

Duró, G., Crosato, A., Kleinhans, M. G., & Uijttewaal, W. S. J. (2018). Bank erosion processes measured with UAV-SfM along complex banklines of a straight mid-sized river reach. *Earth Surface Dynamics*, *6*(4), 933–953. https://doi.org/10.5194/esurf-6-933-2018

Eltner, A., Baumgart, P., Maas, H. G., & Faust, D. (2015). Multi-temporal UAV data for automatic measurement of rill and interrill erosion on loess soil. *Earth Surface Processes and Landforms*, *40*(6), 741–755. https://doi.org/10.1002/esp.3673

Ely, J. C., Graham, C., Barr, I. D., Rea, B. R., Spagnolo, M., & Evans, J. (2017). Using UAV acquired photography and structure from motion techniques for studying glacier landforms: application to the glacial flutes at Isfallsglaciären. *Earth Surface Processes and Landforms*, *42*(6), 877–888. https://doi.org/10.1002/esp.4044

Fahey, B. D., & Lefebure, T. H. (1988). The freeze-thaw weathering regime at a section of the Niagara escarpment on the Bruce Peninsula, Southern Ontario, Canada. *Earth Surface Processes and Landforms*, *13*(4), 293–304. https://doi.org/10.1002/esp.3290130403

Feenstra, B. H. (1981). Quaternary geology and industrial minerals of the Niagara-Welland Area, southern Ontario (p. 260). Ontario Geological Survey - Open File Report 5361.

Gabet, E. J., & Mudd, S. M. (2010). Bedrock erosion by root fracture and tree throw: A coupled biogeomorphic model to explore the humped soil production function and the persistence of hillslope soils. *Journal of Geophysical Research: Earth Surface*, *115*(F4).Gilbert, G. K. (1890). *The history of the Niagara River*. James Lyon.

Giordan, D., Adams, M. S., Aicardi, I., Alicandro, M., Allasia, P., Baldo, M., De Berardinis, P., Dominici, D., Godone, D., Hobbs, P., Lechner, V., Niedzielski, T., Piras, M., Rotilio, M., Salvini, R., Segor, V., Sotier, B., & Troilo, F. (2020). The use of unmanned aerial vehicles (UAVs) for engineering geology applications. *Bulletin of Engineering Geology and the Environment*, *79*(7), 3437–3481. https://doi.org/10.1007/s10064-020-01766-2

Goudie, A. S. (1999). A comparison of the relative resistance of limestones to frost and salt weathering. *Permafrost and Periglacial Processes*, *10*(4), 309-316.

Gulyaev, S. A., & Buckeridge, J. S. (2004). Terrestrial Methods for Monitoring Cliff Erosion in an Urban Environment. *Journal of Coastal Research*, *203*(3), 871–878. https://doi.org/10.2112/1551-5036(2004)20[871:tmfmce]2.0.co;2

Gutierrez, M., & Youn, D. J. (2015). Effects of fracture distribution and length scale on the equivalent continuum elastic compliance of fractured rock masses. *Journal of Rock Mechanics and Geotechnical Engineering*, *7*(6), 626–637. https://doi.org/10.1016/j.jrmge.2015.07.006

Hales, T. C., & Roering, J. J. (2007). Climatic controls on frost cracking and implications for the evolution of bedrock landscapes. *Journal of Geophysical Research: Earth Surface*, *112*(2), 1–14. https://doi.org/10.1029/2006JF000616

Hancock, G. S., Anderson, R. S., & Whipple, K. X. (1998). Beyond power: Bedrock river incision process and form. *Geophysical Monograph Series*, *107*(January), 35–60. https://doi.org/10.1029/GM107p0035

Hayakawa, Y. S., & Matsukura, Y. (2009). Factors influencing the recession rate of Niagara Falls since the 19th century. *Geomorphology*, *110*(3–4), 212–216. https://doi.org/10.1016/j.geomorph.2009.04.011

Healy, D., Rizzo, R. E., Cornwell, D. G., Farrell, N. J. C., Watkins, H., Timms, N. E., Gomez-Rivas, E., & Smith, M. (2017). FracPaQ: A MATLAB^{TM} toolbox for the quantification of fracture patterns. *Journal of Structural Geology*, *95*, 1–16. https://doi.org/10.1016/j.jsg.2016.12.003

Hewitt, D. F. (1971). *The Niagara Escarpment* (Industrial). Ontario Department of Mines and Northern Affairs - Report No. 35.

James, M. R., & Robson, S. (2012). Straightforward reconstruction of 3-D surfaces and topography with a camera: Accuracy and geoscience application. *Journal of Geophysical Research: Earth Surface*, *117*(3), 1–17. https://doi.org/10.1029/2011JF002289

Jaud, M., Letortu, P., Théry, C., Grandjean, P., Costa, S., Maquaire, O., Davidson, R., & Le Dantec, N. (2019). UAV survey of a coastal cliff face – Selection of the best imaging angle. *Measurement: Journal of the International Measurement Confederation*, *139*, 10–20. https://doi.org/10.1016/j.measurement.2019.02.024

Javadnejad, F., Slocum, R. K., Gillins, D. T., Olsen, M. J., & Parrish, C. E. (2021). Dense Point Cloud Quality Factor as Proxy for Accuracy Assessment of Image-Based 3-D Reconstruction. *Journal of Surveying Engineering*, *147*(1), 04020021. https://doi.org/10.1061/(asce)su.1943-5428.0000333

Johnson, M. D., Armstrong, D. K., Sanford, B. V., Telford, P. G., & Rutka, M. A. (1992). Paleozoic and Mesozoic Geology of Ontario. In *Geology of Ontario* (Special Vo, pp. 907–1010). Ontario Geological Survey.

Kellerer-Pirklbauer, A. (2017). Potential weathering by freeze-thaw action in alpine rocks in the European Alps during a nine year monitoring period. *Geomorphology*, *296*, 113–131. https://doi.org/10.1016/j.geomorph.2017.08.020

Kirby, E., & Ouimet, W. (2011). Tectonic geomorphology along the eastern margin of Tibet: Insights into the pattern and processes of active deformation adjacent to the Sichuan Basin. *Geological Society Special Publication*, *353*, 165–188. https://doi.org/10.1144/SP353.9

Lague, D., Brodu, N., & Leroux, J. (2013). Accurate 3-D comparison of complex topography with terrestrial laser scanner: Application to the Rangitikei canyon (N-Z). *ISPRS Journal of Photogrammetry and Remote Sensing*, *82*, 10–26. https://doi.org/10.1016/j.isprsjprs.2013.04.009

Lane, T. P., Roberts, D. H., Ó Cofaigh, C., Rea, B. R., & Vieli, A. (2016). Glacial landscape evolution in the Uummannaq region, West Greenland. *Boreas*, *45*(2), 220–234. https://doi.org/10.1111/bor.12150

Letortu, P., Jaud, M., Grandjean, P., Ammann, J., Costa, S., Maquaire, O., Davidson, R., Le Dantec, N., & Delacourt, C. (2018). Examining high-resolution survey methods for monitoring cliff erosion at an operational scale. *GIScience and Remote Sensing*, *55*(4), 457–476. https://doi.org/10.1080/15481603.2017.1408931

Loye, A., Pedrazzini, A., Theule, J. I., Jaboyedoff, M., Liébault, F., & Metzger, R. (2012). Influence of bedrock structures on the spatial pattern of erosional landforms in small alpine catchments. *Earth Surface Processes and Landforms*, *37*(13), 1407–1423. https://doi.org/10.1002/esp.3285

Malik, I., Pawlik, Ł., Ślęzak, A., & Wistuba, M. (2019). A study of the wood anatomy of Picea abies roots

and their role in biomechanical weathering of rock cracks. *Catena*, *173*, 264-275.

Mann, K. (2019, May 14). Rockslide closes Hamilton mountain access, sports fields remain closed due to soggy conditions. *Global News*. https://globalnews.ca/news/5276437/rockslide-closes-hamilton-mountain-access/

McGreevy, J. P., & Whalley, W. B. (2018). Rock Moisture Content and Frost Weathering under Natural and Experimental Conditions : A Comparative Discussion. *INSTAAR*, *17*(3), 337–346.

Menegoni, N., Meisina, C., Perotti, C., & Crozi, M. (2018). Analysis by UAV digital photogrammetry of folds and related fractures in the monte antola flysch formation (Ponte organasco, Italy). *Geosciences (Switzerland)*, *8*(8). https://doi.org/10.3390/geosciences8080299

Meriano, M., Eyles, N., & Howard, K. W. (2009). Hydrogeological impacts of road salt from Canada's busiest highway on a Lake Ontario watershed (Frenchman's Bay) and lagoon, City of Pickering. *Journal of Contaminant Hydrology*, *107*(1–2), 66–81.

Micheletti, N., Chandler, J. H., & Lane, S. N. (2015). Structure from Motion (SfM) Photogrammetry (Section 2.1.3). In L. E. Clarke & J. M. Nield (Eds.), *Geomorphological Techniques (Online Edition)*. British Society for Geomorphology. https://doi.org/10.1002/esp.3767

Miščević, P., & Vlastelica, G. (2014). Impact of weathering on slope stability in soft rock mass. *Journal of Rock Mechanics and Geotechnical Engineering*, *6*(3), 240–250. https://doi.org/10.1016/j.jrmge.2014.03.006

Moss, M. R., & Nickling, W. G. (1980). Geomorphological and vegetation interaction and its relationship to slope stability on the Niagara Escarpment, Bruce Peninsula, Ontario. *Geographie Physique et Quaternaire*, *34*(1), 95–106. https://doi.org/10.7202/1000386ar

Nicholson, D. T., & Nicholson, F. H. (2000). Physical deterioration of sedimentary rocks subjected to experimental freeze-thaw weathering. *Earth Surface Processes and Landforms*, *25*(12), 1295–1307. https://doi.org/10.1783/147118902101196171

Niemann, W. L. (2009). Lessons learned from rates of mudrock undercutting measured over two time periods. *Environmental and Engineering Geoscience*, *15*(3), 117–131. https://doi.org/10.2113/gseegeosci.15.3.117

Pawlik, Ł., Phillips, J. D., & Šamonil, P. (2016). Roots, rock, and regolith: Biomechanical and biochemical

weathering by trees and its impact on hillslopes—A critical literature review. *Earth-science reviews*, *159*, 142-159.

Perera, N., Gharabaghi, B., & Howard, K. (2013). Groundwater chloride response in the Highland Creek watershed due to road salt application : A re-assessment after 20 years. *Journal of Hydrology*, *479*, 159–168. https://doi.org/10.1016/j.jhydrol.2012.11.057

Perras, M. A., Diederichs, M. S., & Besaw, D. (2014). Geological and geotechnical observations from the Niagara Tunnel Project. *Bulletin of Engineering Geology and the Environment*, *73*, 1303–1323. https://doi.org/10.1007/s10064-014-0633-5

Phillips, J. D. (2008). Soil system modelling and generation of field hypotheses. *Geoderma*, *145*(3-4), 419-425.

Phillips, J. D. (2016). Biogeomorphology and contingent ecosystem engineering in karst landscapes. *Progress in Physical Geography*, *40*(4), 503-526.

Portenga, E. W., & Bierman, P. R. (2011). Understanding earth's eroding surface with 10Be. *GSA Today*, *21*(8), 4–10. https://doi.org/10.1130/G111A.1

Potts, A. S. (1970). Frost Action in Rocks : Some Experimental Data L. In *Transactions of the Institute of British Geographers* (Vol. 49).

Rajendra, Y. D., Mehrotra, S. C., Kale, K. V., Manza, R. R., Dhumal, R. K., Nagne, A. D., & Vibhute, A. D. (2014). Evaluation of Partially Overlapping 3-D Point Cloud's Registration by using ICP variant and CloudCompare. *The International Archives of Photogrammetry, Remote Sensing and Spatial Information Sciences*, *40*(8), 891–897.

Roegiers, J.-C., Thompson, J. C., & McLennan, J. D. (1979). Rock movements induced by the construction of the Hamilton Mountain trunk sewer (stage 4). *Canadian Geotechnical Journal*, *16*(4), 651–658. https://doi.org/10.1139/t79-075

Ruiz-Agudo, E., Mees, F., Jacobs, P., & Rodriguez-Navarro, C. (2007). The role of saline solution properties on porous limestone salt weathering by magnesium and sodium sulfates. *Environmental geology*, *52*(2), 269-281.

Samsu, A., Cruden, A. R., Micklethwaite, S., Grose, L., & Vollgger, S. A. (2020). Scale matters: The influence of structural inheritance on fracture patterns. *Journal of Structural Geology*, *130*(October 2019), 103896. https://doi.org/10.1016/j.jsg.2019.103896

Sass, O. (2005). Rock moisture measurements: Techniques, results, and implications for weathering. *Earth Surface Processes and Landforms*, *30*(3), 359–374. https://doi.org/10.1002/esp.1214

Sayab, M., Aerden, D., Paananen, M., & Saarela, P. (2018). Virtual structural analysis of Jokisivu open pit using "structure-from-motion" Unmanned Aerial Vehicles (UAV) photogrammetry: Implications for structurally-controlled gold deposits in Southwest Finland. *Remote Sensing*, *10*(8), 1–17. https://doi.org/10.3390/rs10081296

Scott, D. N., & Wohl, E. E. (2019). Bedrock fracture influences on geomorphic process and form across process domains and scales. *Earth Surface Processes and Landforms*, *44*(1), 27–45. https://doi.org/10.1002/esp.4473

Shakoor, A., & Rodgers, J. P. (1992). Predicting the rate of shale undercutting along highway cuts. *Bulletin of the Association of Engineering Geologists*, *29*(1), 61–75. https://doi.org/10.2113/gseegeosci.xxix.1.61

Stumpf, A., Malet, J. P., Allemand, P., Pierrot-Deseilligny, M., & Skupinski, G. (2015). Ground-based multi-view photogrammetry for the monitoring of landslide deformation and erosion. *Geomorphology*, *231*, 130–145. https://doi.org/10.1016/j.geomorph.2014.10.039

Tepper, D. H., York, N., Goodman, W. M., York, N., Gross, M. R., Kappel, W. M., York, N., & Yager, R. M. (1990). *Stratigraphy , structural geology, and hydrogeology of the Lockport Group : Niagara Falls area , New York* (pp. 1–25). Field Trip Guidebook.

Thiele, S. T., Grose, L., Samsu, A., Micklethwaite, S., Vollgger, S. A., & Cruden, A. R. (2017). Rapid, semi-automatic fracture and contact mapping for point clouds, images and geophysical data. *Solid Earth*, *8*(6), 1241–1253. https://doi.org/10.5194/se-8-1241-2017

Tonini, M., & Abellan, A. (2014). Rockfall detection from terrestrial lidar point clouds: A clustering approach using R. *Journal of Spatial Information Science*, *8*(1), 95–110. https://doi.org/10.5311/JOSIS.2014.8.123

Van Dongen, M. (2017, December 28). Experts begin 'painstaking' study of failing Claremont Access walls. *The Hamilton Spectator*. https://www.thespec.com/news-story/7040741-experts-begin-painstaking-study-of-failing-claremont-access-walls/

Vleugels, J., Ferrucci, V., Overmars, M. & Roa, A. Hunting voronoi vertices. *Computational Geometry*, 6(5), 329 – 354.

Walker, P. J. (2004). Strength and erosion characteristics of earth blocks and earth block masonry. *Journal of Materials in Civil Engineering*, *16*(5), 497–506.

Weissel, J. K., & Seidl, M. A. (1997). Influence of rock strength properties on escarpment retreat across passive continental margins. *Geology*, *25*(7), 631–634. https://doi.org/10.1130/0091-7613(1997)025<0631:IORSPO>2.3.CO;2

Welch, R., & Jordan, T. R. (1983). Analytical non-metric close-range photogrammetry for monitoring stream channel erosion. *Photogrammetric Engineering & Remote Sensing*, *49*(3), 367–374.

Westoby, M. J., Brasington, J., Glasser, N. F., Hambrey, M. J., & Reynolds, J. M. (2012). "Structure-from-Motion" photogrammetry: A low-cost, effective tool for geoscience applications. *Geomorphology*, *179*, 300–314. https://doi.org/10.1016/j.geomorph.2012.08.021

Williams, D. D., Williams, N. E., & Cao, Y. (2000). Road salt contamination of groundwater in a major metropolitan area and development of a biological index to monitor its impact. *Water research*, *34*(1), 127-138.

Williams, J. G., Rosser, N. J., Hardy, R. J., Brain, M. J., & Afana, A. A. (2018). Optimising 4-D surface change detection: An approach for capturing rockfall magnitude-frequency. *Earth Surface Dynamics*, *6*(1), 101–119. https://doi.org/10.5194/esurf-6-101-2018

Zhang, Z. (1994). Iterative point matching for registration of free-form curves and surfaces. *International Journal of Computer Vision*, *13*(2), 119–152.

Zwieniecki, M.A., Newton, M., 1995. Roots growing in rock fissures: their morphological adaptation. *Plant Soil*, 172, 181–187.

Chapter Six: Conclusions

6. 1 Introduction

This thesis aims to explore the utility of high-resolution spatial surveys involving UAVs in conjunction with geomorphological and sedimentological studies, for the delineation, analysis and interpretation of features and processes in glaciated terrains (Figure 6.1). The recent improvement in UAV technology and SfM processing allows the rapid collection of high-resolution spatial and temporal remotely sensed data at low cost and facilitates their use over more traditional methodologies of data collection and analysis (Hugenholtz et al., 2013; Clark, 2017; Bi et al., 2017; Ely et al., 2017; Chandler et al., 2020). To explore the utility of high-resolution spatial surveys, two separate study sites were selected. The first study site was in Iceland and utilized a planform survey style to examine the landforms on the forefields of surge-type glaciers in Iceland (Chapter 2) to identify and document geomorphological characteristics associated with fast-flowing ice. The second study site was on the Niagara Escarpment in southern Ontario (Chapters 3 – 5), where the sedimentological and structural features of the escarpment were analyzed to assess ongoing erosion processes. Together these investigations provide a robust understanding of the potential utility of high-resolution spatial surveys for geomorphological analysis in glaciated regions.

6. 2 Summary of Findings

The selection of two different study sites for this investigation provided an opportunity to collect and analyse high resolution spatial surveys in both vertical and horizontal perspectives, on actively eroding and previously formed landforms, and in two very different geological settings. The forefields of the surge-type glaciers Sléttjökull and Öldufellsjökull in southern Iceland were explored using a planform aerial survey technique (Chapter 2). Surge-type glaciers are commonly found in Iceland and represent an important method of ice movement in this region (Björnsson et al., 2003; Kjær et al., 2008; Ingólfsson et al., 2016); despite this importance there is limited information available to connect the surging behaviour with a suite of diagnostic landforms. In this study, a UAV was utilized to collect high resolution imagery in the forefields of Sléttjökull and Öldufellsjökull, to determine whether an imprint of the fast-ice flow regime was distinguishable. Based on a large-scale analysis of each of the forefields there were few landscape features that were similar to those attributed to the traditional surge-type glacier landsystem (Evans & Rea, 2003; Brynjólfsson et al., 2012; Ingólfsson et al., 2016). This discrepancy between the landforms observed in this study and those expected based on the landsystem models of surge-type glaciers

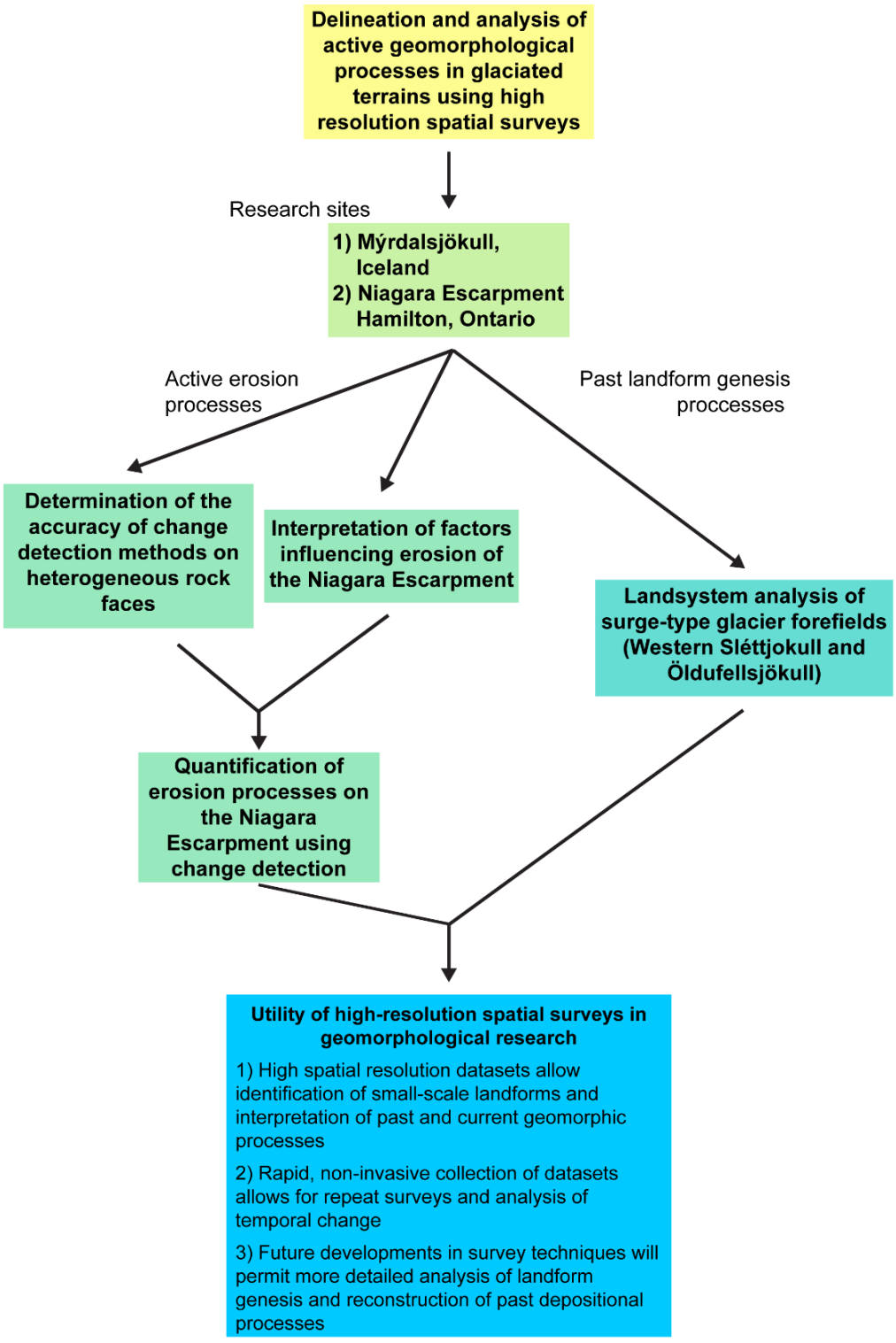

Figure 6.1:Visual summary of this thesis.

(e.g. Evans & Rea, 2003), highlights the complexity of these dynamic systems. The forefields of Sléttjökull and Öldufellsjökull may not show the typical features of a surge-type landsystem due to many factors. For example, surging events may have only recently started at these glaciers which limited the imprint of fast ice flow. In addition, the coarse-grained nature of the forefields and lack of supraglacial debris supply may not have allowed the development of the pervasive deformation features commonly associated with surging behaviour. The surge-type glacier landsystem model proposed by others (e.g. Evans & Rea, 2003) does represent the overall landform suite expected at glaciers with a long history of surging, but does not encapsulate all variability that may be encountered in glaciers with intermittent or short-term surging behaviour.

Analysis of the high-resolution UAV-based imagery from small survey areas in the surge zone at Öldufellsjökull, did however result in the identification of multiple features indicative of surge-type behaviour. These included areas of hummocky moraine, a concertina esker, and circular feature related to hydrologic overpressuring, most likely recording the impact of surge-related processes on the forefield. Using high-resolution datasets, low relief landforms reflective of surging behaviour were identifiable; if similar structures were found at other surge-type glaciers using high-resolution imagery, these features could be added to the Evans and Rea (2003) landsystems model.

The second study site investigated for this thesis was in Hamilton, Ontario where the Niagara Escarpment is well exposed and is subjected to ongoing erosion processes. To better understand the nature and rate of erosion along the exposed escarpment face, it was critical to determine the key factors controlling the location and nature of erosion processes (Chapter 3). The lithological characteristics of exposed units along the escarpment face exert a major control on erosional processes; lithological strength characteristics, the presence of undercutting, and fracturing, as well as stratigraphic positioning along the escarpment, were identified as the major controlling factors (Lo & Lee, 1990; Budetta et al., 2000; Barlow, 2002; Hayakawa & Matsukura, 2009; Kirby & Ouimet, 2011; Scott & Wohl, 2019). Some of the lithological units exposed along the escarpment in Hamilton show considerable vertical and lateral variability, likely related to the paleo landscape configuration at the time of their deposition (Hewitt, 1971; Sanford et al., 1972; Johnson et al., 1992; Armstrong & Carter, 2009); this variability can result in spatially variable erosion rates. The importance of lithological controls on erosion processes and rates is clearly

documented in Chapter 3, although site specific processes and rates required additional documentation and analysis.

A vertically oriented UAV-based survey was completed on a small rock outcrop on the Niagara Escarpment in Hamilton to test the applicability of change detection methodologies (Chapter 4) to determine the location and rate of erosion (Chapter 5). The escarpment face is complex, exposing heterogenous, vertically stacked, lithological units; this creates an uneven surface characterized by areas of significant undercutting, shadows, as well as patchy vegetation cover during the spring, summer and fall. To identify and determine the position and size of rockfall material lost from the escarpment face using change detection methodologies, an artificial erosion event was created through the removal of blocks from the face. The M3C2 method of change detection was used to determine the location and shape of blocks removed (Lague et al., 2013; Williams et al., 2018; DiFrancesco et al., 2020). This algorithm correctly identified the location of all, but one sample removed from the face, and in general, the shape of the point cloud that represented the removed sample was relatively accurate. However, when volume changes were calculated using the power crust and alpha shape algorithms (Amenta et al., 2001; van Veen et al., 2017; Bonneau et al., 2019; DiFrancesco et al., 2020, 2021), the calculated volumes created by the models both overestimated and underestimated the measured volumes of the removed blocks (Chapter 4).

Once a methodology that could reliably locate areas of change and provide an estimate of volume change on a lithologically complex outcrop face was determined, a comparison of the outcrop over a 14-month period was conducted (Chapter 5). Over this time period, approximately one third of the studied rock face experienced some form of erosion or mass gain through deposition. Greater amounts of erosion occurred in areas of the outcrop face where interbedded shale and more resistant lithologies (sandstone or dolostone) occurred, allowing undercutting. Despite lithology playing a major role in the control of erosional processes, there was significant variation in the amount of erosion recorded within a single unit with similar lithological characteristics. This suggests that a single factor, such as lithology or fracture density, does not determine the location and amount of erosion experienced on a rock face, and instead this likely results from a combination of interrelated factors. Both fracture propagation and undercutting are processes that evolve over time and are therefore more likely to cause failure when a slope has been exposed for an extended time period. Factors dictating the location and amount of erosion

occurring on the studied outcrop face are complex, and dependent, not only on current properties of the rock face, but also on how the face has developed in the past (Chapter 5).

Despite some issues with the accuracy of volume loss calculations using change detection methodologies, they provide a time-efficient and non-invasive methodology to use in erosion studies of near vertical outcrops of sedimentary rock in both urban and rural settings, to reliably identify areas of change, and to provide an estimate of the volume and rate of erosion occurring on the rock face.

The four substantive chapters presented in this thesis (Chapters 2-5) highlight the use of high-resolution spatial surveys in the study of geomorphological processes and landforms. The utility and importance of using UAV technology to collect high resolution data and change detection analytical tools to identify and quantify rates of material loss and gain, is clear.

6. 3 Future Work

The use of UAVs in data collection is still relatively new and innovative uses of the technology continue to be discovered. The discipline of geomorphology lends itself well to the use of UAVs as their primary benefit is the ability to rapidly collect high spatial and temporal resolution imagery which facilitates the monitoring of ongoing geomorphic processes and the delineation of small-scale features, both of which have been explored in this thesis.

In future, the use of high-resolution imagery in planform data collection and mapping in glacial forefields will allow more comprehensive mapping of features at multiple scales and in turn will provide more robust datasets with which to conduct various geomorphological studies. The use of UAVs in Iceland allowed for the delineation of small-scale features which may be diagnostic of fast-ice flow; it is now necessary to conduct similar studies in other regions where surging behaviour has occurred to determine whether similar features, such as the circular water escape structure, are present and whether these can be conclusively connected to surging and incorporated into the landsystem model.

While lithological characteristics are one of the key factors influencing erosion of the Niagara Escarpment (Chapter 3) there are other factors which must still be considered to fully understand the development of the feature, current erosion processes, and to protect the infrastructure located nearby. It is clear that hydrological characteristics and pathways likely contribute to erosion of the face through direct erosional processes and the impact of saturation on

the strength of rocks (Fahey & Lefebure, 1988; Dredge, 1992; Agustawijaya, 2007; Hayakawa & Matsukura, 2009; Wang et al., 2016); however, the hydrological properties of the lithological units exposed along the Niagara Escarpment and their variation across the city of Hamilton are not well understood. Further work to quantify surface and groundwater processes at different locations in the city are required to understand the impact of these processes on erosion of the escarpment and to determine the areas in Hamilton most likely to be impacted by them.

The methodology used to quantify erosion on the Niagara Escarpment (Chapters 4 and 5) can be widely applied to other areas. The use of a high accuracy DGPS or other system to collect high resolution ground control points (<5 cm), would help to refine the models and potentially reduce the error in the volume calculations found in the studies reported here. Conducting similar artificial erosional trials at other outcrops, which differ in their complexity and lithology, would further the understanding of the capabilities and limitations of these methods.

The study of erosion of the Niagara Escarpment in Hamilton found that approximately one third of the face underwent erosion in a 14-month period (Chapter 5); however, this approximation is site-specific and time-specific and would likely differ across the city and in different time periods. Therefore, to create an understanding of the overall development of the escarpment in the region, and to aid in the development of strategies to protect nearby infrastructure, studies using similar methodology should be completed at different locations and over longer time periods. These studies could provide information on local variability of erosion processes and rates, in addition to addressing the complexity of factors influencing erosion and how these may differ at other sites.

6. 4 Conclusions

The identification and analysis of small-scale geomorphological features and processes is extremely important for the reconstruction of past environmental conditions and the monitoring of current changes to inform policy, planning and mitigation strategies in the future. Despite the importance of dynamic geomorphological features in urban areas, their study has been difficult due to technological restrictions and the time-consuming nature of conducting quantitative geomorphological studies. Recent advancements in UAV technology and SfM software has permitted the study of geomorphic features and processes at a scale that would previously have been impossible. The thesis has explored the utility of high-resolution spatial surveys to conduct research on critical environmental processes and small-scale erosional events.

6. 5 References

Agustawijaya, D. S. (2007). The uniaxial compressive strength of soft rock. *Civil Engineering Dimension*, *9*(1), 9–14.

Amenta, N., Choi, S., & Kolluri, R. K. (2001). The power crust. *Proceedings of the Symposium on Solid Modeling and Applications*, 249–260. https://doi.org/10.1145/376957.376986

Armstrong, D. K., & Carter, T. K. (2009). *The subsurface Paleozoic stratigraphy of southern Ontario* (Special Vo). Ontario Geological Survey.

Barlow, J. (2002). Rock creep and the development of the Niagara Cuesta. *Earth Surface Processes and Landforms*, *27*(10), 1125–1135. https://doi.org/10.1002/esp.401

Bi, H., Zheng, W., Ren, Z., Zeng, J., & Yu, J. (2017). Using an unmanned aerial vehicle for topography mapping of the fault zone based on structure from motion photogrammetry. *International Journal of Remote Sensing*, *38*(8–10), 2495–2510. https://doi.org/10.1080/01431161.2016.1249308

Björnsson, H., Pálsson, F., Sigurdsson, O., & Flowers, G. E. (2003). Surges of glaciers in Iceland. *Annals of Glaciology*, *36*, 82–90. https://doi.org/10.3189/172756403781816365

Bonneau, D., Hutchinson, D. J., DiFrancesco, P.-M., Coombs, M., & Sala, Z. (2019). Three-dimensional rockfall shape back analysis: Methods and implications. *Natural Hazards and Earth System Sciences*, *19*(12), 2745–2765. https://doi.org/10.5194/nhess-19-2745-2019

Brynjólfsson, S., Ingólfsson, Ó., & Schomacker, A. (2012). Surge fingerprinting of cirque glaciers at the Tröllaskagi. *Jökull*, *62*(March 2014), 1–16.

Budetta, P., Galietta, G., & Santo, A. (2000). A methodology for the study of the relation between coastal cliff erosion and the mechanical strength of soils and rock masses. *Engineering Geology*, *56*(3–4), 243–256. https://doi.org/10.1016/S0013-7952(99)00089-7

Chandler, B. M. P., Evans, D. J. A., Chandler, S. J. P., Ewertowski, M. W., Lovell, H., Roberts, D. H., Schaefer, M., & Tomczyk, A. M. (2020). The glacial landsystem of Fjallsjökull, Iceland: Spatial and temporal evolution of process-form regimes at an active temperate glacier. *Geomorphology*, *361*, 107192. https://doi.org/10.1016/j.geomorph.2020.107192

Clark, A. (2017). Small unmanned aerial systems comparative analysis for the application to coastal erosion monitoring. *GeoResJ*, *13*, 175–185. https://doi.org/10.1016/j.grj.2017.05.001

DiFrancesco, P.-M., Bonneau, D. A., & Hutchinson, D. J. (2021). Computational Geometry-Based Surface Reconstruction for Volume Estimation: A Case Study on Magnitude-Frequency Relations for a LiDAR-Derived Rockfall Inventory. *ISPRS International Journal of Geo-Information*, *10*(3), 157. https://doi.org/10.3390/ijgi10030157

DiFrancesco, P. M., Bonneau, D., & Hutchinson, D. J. (2020). The implications of M3C2 projection diameter on 3-D semi-automated rockfall extraction from sequential terrestrial laser scanning point clouds. *Remote Sensing*, *12*(11). https://doi.org/10.3390/rs12111885

Dredge, L. A. (1992). Breakup of Limestone Bedrock by Frost Shattering and Chemical Weathering , Eastern Canadian Arctic Author (s): L . A . Dredge Source : Arctic and Alpine Research , Vol . 24 , No . 4 (Nov ., 1992), pp . 314-323 Published by : INSTAAR , University of Co. *Arctic and Alpine Research*, *24*(4), 314–323.

Ely, J. C., Graham, C., Barr, I. D., Rea, B. R., Spagnolo, M., & Evans, J. (2017). Using UAV acquired photography and structure from motion techniques for studying glacier landforms: application to the glacial flutes at Isfallsglaciären. *Earth Surface Processes and Landforms*, *42*(6), 877–888. https://doi.org/10.1002/esp.4044

Evans, D. J. A., & Rea, B. R. (2003). Surging glacier landsystem. In D. J.A. Evans (Ed.), *Glacial Landsystems* (pp. 259–288). Hodder Arnold.

Fahey, B. D., & Lefebure, T. H. (1988). The freeze-thaw weathering regime at a section of the Niagara escarpment on the Bruce Peninsula, Southern Ontario, Canada. *Earth Surface Processes and Landforms*, *13*(4), 293–304. https://doi.org/10.1002/esp.3290130403

Hayakawa, Y. S., & Matsukura, Y. (2009). Factors influencing the recession rate of Niagara Falls since the 19th century. *Geomorphology*, *110*(3–4), 212–216. https://doi.org/10.1016/j.geomorph.2009.04.011

Hewitt, D. F. (1971). *The Niagara Escarpment* (Industrial). Ontario Department of Mines and Northern Affairs - Report No. 35.

Hugenholtz, C. H., Whitehead, K., Brown, O. W., Barchyn, T. E., Moorman, B. J., LeClair, A., Riddell, K., & Hamilton, T. (2013). Geomorphological mapping with a small unmanned aircraft system (sUAS): Feature detection and accuracy assessment of a photogrammetrically-derived digital terrain model. *Geomorphology*, *194*, 16–24. https://doi.org/10.1016/j.geomorph.2013.03.023

Ingólfsson, Ó., Benediktsson, Í. Ö., Schomacker, A., Kjær, K. H., Brynjólfsson, S., Jónsson, S. A., Korsgaard, N. J., & Johnson, M. D. (2016). Glacial geological studies of surge-type glaciers in Iceland - Research status and future challenges. *Earth-Science Reviews*, *152*, 37–69. https://doi.org/10.1016/j.earscirev.2015.11.008

Johnson, M. D., Armstrong, D. K., Sanford, B. V., Telford, P. G., & Rutka, M. A. (1992). Paleozoic and Mesozoic Geology of Ontario. In *Geology of Ontario* (Special Vo, pp. 907–1010). Ontario Geological Survey.

Kirby, E., & Ouimet, W. (2011). Tectonic geomorphology along the eastern margin of Tibet: Insights into the pattern and processes of active deformation adjacent to the Sichuan Basin. *Geological Society Special Publication*, *353*, 165–188. https://doi.org/10.1144/SP353.9

Kjær, K. H., Korsgaard, N. J., & Schomacker, A. (2008). Impact of multiple glacier surges - a geomorphological map from Bruarjokull, East Iceland. *Journal of Maps*, *4*(1), 5–20. https://doi.org/10.4113/jom.2008.91

Lague, D., Brodu, N., & Leroux, J. (2013). Accurate 3-D comparison of complex topography with terrestrial laser scanner: Application to the Rangitikei canyon (N-Z). *ISPRS Journal of Photogrammetry and Remote Sensing*, *82*, 10–26. https://doi.org/10.1016/j.isprsjprs.2013.04.009

Lo, K. Y., & Lee, Y. N. (1990). Time-dependent deformation behaviour of Queenston shale. *Canadian Geotechnical Journal*, *27*(4), 461–471. https://doi.org/10.1139/t90-061

Sanford, J. T., Martini, I. ., & Mosher, R. E. (1972). *Niagaran stratigraphy: Hamilton, Ontario*.

Scott, D. N., & Wohl, E. E. (2019). Bedrock fracture influences on geomorphic process and form across process domains and scales. *Earth Surface Processes and Landforms*, *44*(1), 27–45. https://doi.org/10.1002/esp.4473

van Veen, M., Hutchinson, D. J., Kromer, R., Lato, M., & Edwards, T. (2017). Effects of sampling interval on the frequency - magnitude relationship of rockfalls detected from terrestrial laser scanning using semi-automated methods. *Landslides*, *14*(5), 1579–1592. https://doi.org/10.1007/s10346-017-0801-3

Wang, S. L., Lv, Q. F., Baaj, H., Li, X. Y., & Zhao, Y. X. (2016). Volume change behaviour and microstructure of stabilized loess under cyclic freeze–thaw conditions. *Canadian Journal of Civil Engineering*, *43*(10), 865–874. https://doi.org/10.1139/cjce-2016-0052

Williams, J. G., Rosser, N. J., Hardy, R. J., Brain, M. J., & Afana, A. A. (2018). Optimising 4-D surface change detection: An approach for capturing rockfall magnitude-frequency. *Earth Surface Dynamics*, *6*(1), 101–119. https://doi.org/10.5194/esurf-6-101-2018